Hybrid polyoxometalate – porphyrin materials : photovoltaic devices and photocatalysis

Yiming Liang

To cite this version:

Yiming Liang. Hybrid polyoxometalate – porphyrin materials : photovoltaic devices and photocatalysis. Other. Université de Strasbourg, 2020. English. NNT : 2020STRAF022 . tel-03626507

HAL Id: tel-03626507
https://theses.hal.science/tel-03626507

Submitted on 31 Mar 2022

UNIVERSITÉ DE STRASBOURG

ÉCOLE DOCTORALE DES SCIENCES CHIMIQUES

Institut de Chimie, UMR 7177

THÈSE présentée par :

Yiming LIANG

soutenue le : **1ème décembre 2020**

pour obtenir le grade de : **Docteur de l'université de Strasbourg**

Discipline/ Spécialité : Chimie

Matériaux hybrides polyoxométallate – (iso)porphyrine : dispositifs photovoltaïques et photo(électro)catalyse

THÈSE dirigée par :

M. RUHLMANN Laurent	Professeur, Université de Strasbourg

RAPPORTEURS :

M. MAISONHAUTE Emmanuel	Professeur, Sorbonne université
M. CADOT Emmanuel	Professeur, Université Versailles-Saint Quentin

---

EXAMINATEURS :

Mme. SAVINOVA Elena	Professeur, Université de Strasbourg
M. MELIN Frédéric	Maitre de conférences, Université de Strasbourg
M. ALOISE Stephane	Maitre de conférences, Université de Lille 1

Remerciements

Je tiens tout d'abord à remercier tous les membres du jury d'avoir accepté d'évaluer cette thèse :

- Prof. Laurent RUHLMANN, Université de Strasbourg
- Prof. Emmanuel MAISONHAUTE, Sorbonne Université
- Prof. Emmanuel CADOT, Université Versailles - Saint-Quentin
- Prof. Elena SAVINOVA, Université de Strasbourg
- Dr. Frédéric MELIN, Université de Strasbourg
- Dr. Stéphane ALOISE, Université de Lille 1

Je tiens à remercier le Conseil chinois des bourses d'études (Chinese Scholarship Council) qui a fourni le soutien financier pour étudier et vivre en France. Je remercie également l'Université de Strasbourg pour son soutien financier supplémentaire. Je n'aurais jamais pu terminer la thèse sans les supports financiers mentionnées.

Je tiens à exprimer ma gratitude à mon superviseur le Prof. Laurent Ruhlmann pour son aimable soutien lors de l'étude de cette recherche. Ses connaissances abondantes en électrochimie mais aussi en chimie des POM et des porphyrines sont une inspiration pour moi. Pendant l'étude, il me donne de la patience et de l'expérience pour m'aider à résoudre beaucoup de problèmes. Son attitude rigoureuse et son dévouement professionnel pour la recherche scientifique m'apprennent beaucoup et me donnent une meilleure vue d'ensemble de mes études et de ma vie.

Je tiens à exprimer ma gratitude au Dr Antoine Bonnefont pour son aide dans les expériences XPS et les mesures d’impédances (EIS) et dont les conseils et les commentaires m'ont grandement contribué. Il me donne beaucoup d'encouragements qui me rendent plus confiant.

Je suis très reconnaissant au Dr Vasilica Badets et au Dr Corinne Boudon qui m’ont donné gentiment des conseils et des encouragements pour m'aider dans le cadre de mes travaux de thèse et mêm au-delà de la chimie. La communication avec eux m’a donné une meilleure compréhension de la vie.

Je tiens à remercier la coopération de recherche avec Mesdames Sylvie Choua, etNolwenn Le Breton du groupe POMAM pour les mesures et résultats en Résonance Paramagnétique Electronique réalisées dans le cadre de cette thèse.

Je tiens à remercier tous mes collègues du groupe de recherche qui partageaient le même laboratoire avec moi, pour les précieuses discussions sur les aspects pratiques de la chimie.

Je tiens à remercier tous mes amis que j'ai rencontrés en France, qui m'aident beaucoup à faire face à différentes questions et à soulager la pression de ma vie et de mes études.

Je tiens à remercier ma famille et mon petit ami qui m'apporte un soutien et une préoccupation qui me poussent à insister. C'est un réconfort pour moi de communiquer avec eux chaque semaine.

Je tiens à remercier Mme Yang Tao, l'épouse du Prof. Laurent Ruhlmann. Elle m’a donné une grande quiétude pour ma vie. Ses grandes compétences culinaires me donnent le sentiment d'être chez moi.

Résumé

1) Introduction

Une isoporphyrine peut être définie comme une porphyrine avec deux substituants liés au même atome en position *méso* ce qui induit une perte de l'aromaticité du cycle.[1] Comme reporté dans la littérature, l'isoporphyrine présente une bande d'absorption caractéristique[2] dans la région du proche infrarouge entre 750 nm et 950 nm. La présence de cette bande peut être mise à mise à profit notamment pour la thérapie photodynamique.[3] En effet, l'illumination dans le proche infrarouge permettrait de generé l'oxygène singulet 1O2 à partir du dioxygène $^3O_2$.

Des poly-porphyrines peuvent être obtenus par électropolymérisation basée sur l'oxydation ou la réduction de substituants liés au cycle de porphyrine. Les isoporphyrines sont les principaux intermédiaires réactionnels décrits dans la littérature pour former ces polyporphyrines.[4]

Dans ce travail de thèse, le potentiel d'oxydation appliqué a été modulé dans le cadre du processus d'électropolymérisation pour former soit des copolymères à base de porphyrines, mais également des polymères à base d'isoporphyrines radicalaires stables. Ces isoporphyrines radicalaires n'avaient à ce jour pas été décrit dans la littérature, les isoporphyrines étant connues pour être relativement instables. Pour obtenir et étudier ces poly-isoporphyrines, plusieurs types de porphyrines et de nucléophiles avant au minimum deux groupements pyridyles pendants ont été employé. Les propriétés redox et physico-chimiques de ces nouvelles polyisoporphyrines radicalaires stables seront décrit dans cette thèse.

2) Résultats et discussions

2.1. Copolymères stables de porphyrine / isoporphyrine préparés à partir de divers ligands bipyridyliques

La β-octaéthyl porphyrine de zinc (**ZnOEP**), la 5-(4-methoxyphenyl)-10,20-di-p-tolylporphyrine de zinc (**ZnAT$_2$P**) et la 5,15-ditolyl-porphyrine de zinc (**ZnT$_2$P**) ont été utilisées pour préparer le copolymère de porphyrines avec des espaceurs du type viologène et double viologène. Ces poly-porphyrines ont été préparées en utilisant un potentiel assez élevé en oxydation permettant l'électrogénération de la porphyrine monomère (**Porp ; Porp = porphyrine**) en porphyrine dication (**Porp**$^{2+}$). Dans le cas d'une électropolymérisation à balayage itératif, si la limite de potentiel positive est réglée à une valure permettant uniquement la formation du radical cation de la porphyrine (**Porp**$^{+\bullet}$), aucun changement au niveau de l'allulre des voltammogrammes cycliques ne sont observés si on utilise des porphyrines de zinc du type **ZnOEP** et **ZnAT$_2$P**. , Cela signifie qu'aucun copolymère n'a été formé à l'électrode du type ITO indiquant l'absence d'électropolymérisation. Dans le cas de l'utilisation de la porphyrine **ZnT$_2$P**, présentant 2 côtés de la porphyrine à accès beaucoup plus aisé, c'est-à-dire occupé sur la position *méso* et et les quatre positions β par des atomes d'hydrogènes H, le radical cation porphyrine **ZnT$_2$P**$^{+\bullet}$ ainsi que la porphyrine de dication **ZnT$_2$P**$^{2+}$ électrogénérés sont de puissants électrophiles qui peuvent réagir rapidement avec des nucléophiles, par exemple du type 4,4'-bipyridyle ou bis-bipyridinium (py-py^{+}-$(CH_2)_3$-py^{+}-py .2PF_6^{-} que l'on peut écrire encore soula forme bpy^{+}-$(CH_2)_3$–$^{+}$bpy.2PF_6^{-}), pour former suivant le potentiel appliqué des copolymères contenant soit des unités radicalaires isoporphyrines stables (**poly-ZnT$_2$isoP**$^{\bullet}$) soit des unités porphyrines (**poly-ZnT$_2$P**) (Fig. 1) liées à des espaceurs viologènes ou dipyridinium.

Ces copolymères ont été caractérisés par spectroscopie UV-Visible-NIR, par spectroscopie photoélectronique aux rayons X (XPS), par microscopie à force atomique (AFM), par microbalance électrochimique à cristal de quartz (EQCM), par électrochimie (voltampérométrie cyclique) et enfin par spectroscopie d'impédance électrochimique (EIS). Les premiers résultats sont extrêmement prometteurs et un article a déjà été publié sur cette partie de la thèse :

M. Boudiaf, **Y. Liang,** R. Lamare, J. Weiss, H. Ibrahim, M. Goldmann, Embarek Bentouhami, V. Badets, S. Choua, N. Le Breton, A. Bonnefont, **L. Ruhlmann*** "Stable isoporphyrin copolymer: electrochemical mechanism and behaviour and photovoltaic properties", *Electrochimica Acta*, **2019**, *309*, 432-449. DOI: 10.1016/j.electacta.2019.04.050.

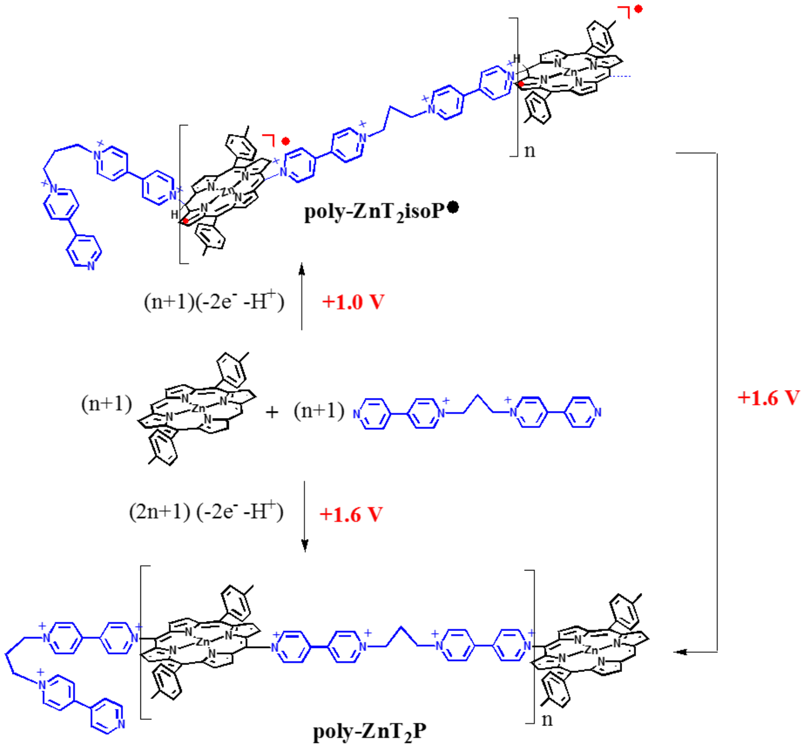

Figure 1. Schéma d'électropolymérisation expliquant la réactivité de bpy$^+$-(CH$_2$)$_3$–$^+$bpy.2PF$_6^-$ en présence du monomère **ZnT$_2$P** dans le cas de balayage itératif entre -1,0 V et 1,0 V ou entre -1,0 V et 1,6 V *vs.* ECS (ECS = Electrode au Calomel Saturé). Le balayage itératif entre -1,0 V et 1,0 V permet d'obtenir le copolymère contenant soit des unités radicalaires isoporphyrines stables (**poly-ZnT$_2$isoP$^\bullet$**) alors qu'un balayage itératif entre -1,0 V et 1,6 V permet d'obtenir le copolymère sous la forme de polyporphyrine (**poly-ZnT$_2$P**) toujours avec des espaceurs du type double viologène.

Pour les copolymères radicalaires d'isoporphyrine, la spectroscopie RPE a confirmé la présence des centres d'isoporphyrine radicalaire iso-ZnT$_2$P$^\bullet$. Le copolymère à base d'isoporphyrines radicalaires **poly-ZnT$_2$isoP$^\bullet$** présente également au niveau du spectre d'absorption UV-visible-NIR deux bandes additionnels par rapport au copolymère de porphyrines parent **poly-ZnT$_2$P** : un dédoublement de la bande Soret (bande B) au voisinage de 410 – 470 nm dans le visible et une bande d'absorption additionnel dans le proche infrarouge. On a établi et démontré lors de nos études sous illumination que la bande d'absorption NIR de la poly-isoporphyrine contribue de manière notable et importante à la génération de photocourants expliquant pourquoi l'efficacité de la conversion de la lumière est plus élevée pour le copolymère du type poly-isoporphyrine **poly-ZnT$_2$isoP$^\bullet$** comparé au copolymère poly-porphyrine **poly-ZnT$_2$P**. L'excitation de cette nouvelle bande NIR pour le copolymère radicalaire poly-isoporphyrine **poly-ZnT$_2$isoP$^\bullet$** conduit, dans les milieux aérés (en présence de $^3O_2$), à la formation et photogénération de l'état singulet du dioxygène $^1O_2$ (Fig. 2), qui est la première étape pour l'utilisation de tels matériaux dans le cadre de traitement du cancer par photothérapie. Sous une illumination uniquement dans le domaine du proche infra-rouge, l’intensité d'absorption du DPBF (1,3-diphénylisobenzofurane) qui est un piégeur de $^1O_2$)[5] diminue au cours du temps. Cela signifie que sous illumination proche infrarouge en présence de poly-isoporphyrines radicalaire en solution, l’oxygène signulet $^1O_2$ est photogénéré et que le DPBF réagit et piège le $^1O_2$ générés

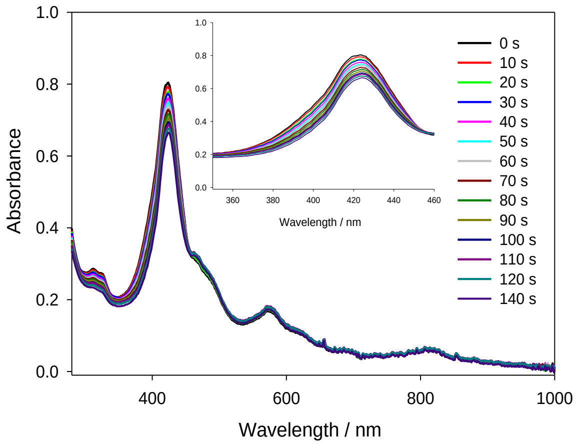

Figure 2. Evolution sous illumination proche infrarouge des spectres d'absorption normalisés de la Poly-isoporphyrine radicalaire **poly-ZnT$_2$isoP$^\bullet$** obtenue avec bpy$^+$-$(CH_2)_3$–$^+$bpy.$2PF_6^-$ en présence de **ZnT$_2$P** dans le cas d'un balayage itératif entre -1,0 V et 1,0 V *vs.* ECS en présence de la DPBF. Solvant : DMF. L'encart de la figure montre le zoom du spectre optique au niveau de la bande Soret entre 350 nm et 460 nm.

Un ligand du type 3-(2-(3-(2-(pyridin-3-yl)éthynyl)phényl)éthynyl) pyridine a été également utilisée pour l’obtention de copolymères de porphyrines ou d'isoporphyrines. L’idée initiale avait été l’étude de l’influence de la nature de l’espaceurs (long ou court, conjugué ou non conjugué) sur les propriétés photovoltaïques ou pour la production de l’oxygène singulet $^1O_2$.

De nombreux facteurs ont été étudiés de manière à obtenir des films de copolymères à base de de porphyrines ou d'isoporphyrines de bonne qualité. la vitesse de balayage, la plage de potentiel pour le balayage itératif, la concentration du monomère de porphyrine ainsi que la concentration du ligand dipyridyle, et enfin le rapport de concentration entre la porphyrine et le ligand dipyridyle.

Le résultat a montré que la meilleure condition pour l’électropolymérization est d'utiliser 3 fois plus de ligand dipyrididyle par rapport à la porphyrine. Dans ces conditions, les films obtenus avec des copolymères de porphyrines ou d’isoporphyrines redicalaire ont montré de bonnes propriétés électrochimiques mais également photoélectrochimiques. Les mesures de photocourant sous irradiation avec de la lumière visible et/ou proche IR ont montré que les films minces de poly-isoporphyrines radicalaires présentaient des performances significativement améliorées par rapport aux poly-porphyrines parents (Fig. 3). Les performances photovoltaïques atteignent un optimum en fonction du nombre de balayage itératifs n. Ce nombre obtimum n varie avec le type de ligand dipyridyle utilisé.

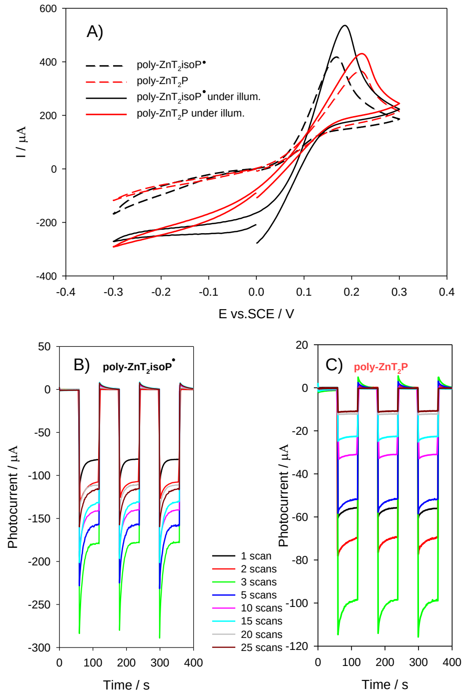

Figure 3. A) Courbes potentiel-courant pour le copolymère d'isoporphyrine radicalaires **poly-$ZnT_2isoP^{\bullet}$** et pour la polyporphyrine **poly-ZnT_2P**. B) et C) Réponse photoélectrochimique des films obtenus après différent nombre de balayages itératifs (entre 1 et 25 balayages).

2.2. Copolymère d'isoporphyrine stable préparé avec un cluster à base d'halogénure de molybdène (II) décoré à l'extrémité par six groupement pyridines

Les halogénures octaédriques pontées de Mo (II) et W (II) ont pour formule générale $[\{M_6(\mu_3\text{-}X)_8\}L_6]$ (M = Mo, W; X = Cl, Br, I; L = ligand inorganique acide ou espèce organique ; $\{M_6(\mu_3\text{-}X)_8\}^{4+}$ est le cluster central). Ils possèdent des propriétés photophysiques remarquables qui peuvent être utilisées pour le stockage et la transformation d'énergie.[6] En utilisant le polyiodométallate $((Bu_4N_2)$ $[\{Mo_6I_8\}(OOC\text{-}C_5H_4N)_6]$, abrégé **PIM(py)$_6$**) substitué par six ligands pyridyles pendants, comme nous nous y attendions, le copolymère d'isoporphyrine radicalaire avec l'incorporation des groupements **PIM(py)$_6$** dans le film a été obtenu avec succès par électropolymérisation. Néanmoins seule la formation de la poly-isoporphyrine semble possible, le copolymère poly-porphyrine n'a pas pu être synthétisé (Fig. 4) et ne semble pas stable.

En effet, pour obtenir le copolymère de poly-porphyrine, un potentiel appliqué plus élevé doit être appliqué de manière à oxyderl'isoporphyrine intermédiaire qui permet l'élimination du proton pendant en position méso et la réarromatisation de la porphyrine de zinc. Cependant, à ce potentiel, le ligand **PIM(py)$_6$** peut être également oxydé et n'est pas stable. Malgré cela, le copolymère poly-isoporphyrine radicalaire intermédiare stable incorporant le ligand **PIM(py)$_6$** peut être obtenu avec succès à partir de l'électrogénération du radical π cation porphyrine **$ZnT_2P^{+\bullet}$**. L'existence du radical pour le copolymère isoporphyrine a été démontré par spectroscopie de résonance paramagnétique électronique (RPE). Le copolymère obtenu a été caractérisé par spectroscopie UV-Visible-NIR, spectroscopie photoélectronique aux rayons X ainsi que par microbalance à crystal de quartz électrochimiques (EQCM). L'analyse de donnés obtenu par EQCM a premis de montrer que l'on obtient bien un copolymère en 3D où les six groupements pyridyls pendant porté par le ligand **PIM(py)$_6$** ont réagit avec le radical cation ditolyl porphyrine.

Ce copolymère a également présenté des propriétés électrochimiques et photochimiques remarquables. Les mesures en spectroscopie d'impédance électrochimique ont également été effectuées et modélisées confirmant les propriétés observées sous illumination.

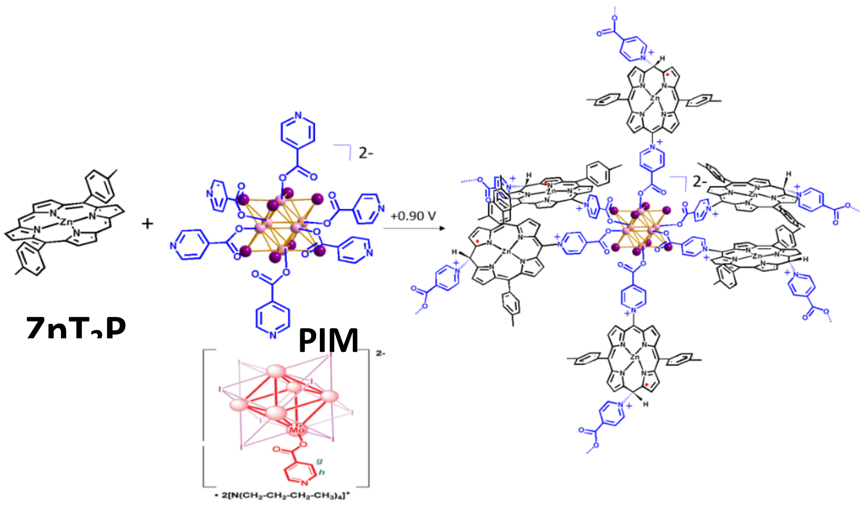

Figure 4. Processus d'électropolymérisation pour l'obtention de la poly-isoporphyrine avec une structure 3D en utilisant le ligand hexa-pyridylique **PIM(py)$_6$**.

2.3. Copolymère d'isoporphyrine stable préparé à partir de bis-diphosphine

Comme déjà montré par notre groupe, les bis-diphosphine et tris-diphosphine peuvent être subtituées au niveau des positions *β* du macrocycle porphyrinique $ZnTPP^{+\bullet}$ électrogénéré lors de l'oxydation de la poprhyrine ZnTPP pour former les dimères et trimères avec des espaceurs bisphosphonium ou tris-phosphonium.[7-8] Ainsi, des ligands du type diphosphine, tel que le 1,2-bis(diphénylphosphino)benzène, peuvent agir également en qualité de nucléophile à l'instar de la 4,4'-bipyridine permettant également la formation d'espaceurs biphosphonium. Ce type de ligand diphosphine a été utilisé avec succès pour former un nouveau type de copolymères d'isoporphyrine avec des espaceurs diphosphoniums et toujours à partir t de la porphyrine monomère du type **ZnT$_2$P** (Fig. 5). Des propriétés électrochimiques et photoélectrochimiques intéressantes ont été également mesurées. Ces résultats ouvrent une nouvelle voie pour former des copolymères originaux aux propriétés intéressantes pour des applications en photo(électro)catalyse.

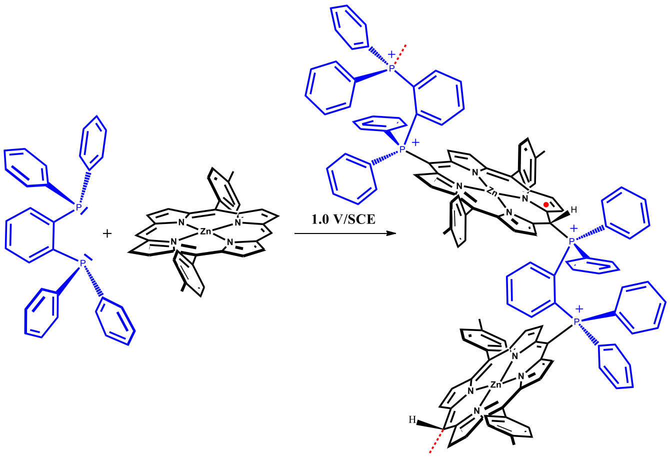

Figure 5. Processus de formation de la poly-isoporphyrine à partir de la porphyrine **ZnT$_2$P** et du 1,2-bis(diphénylphosphino)benzène.

3) Conclusion générale

Pour conclure, dans le cadre de cette thèse, les copolymères radicalaires de poly-isoporphyrines stables ont montré une meilleure efficacité pour la génération de photocourant comparé aux copolymères poly-porphyrine parents en milieu aqueux en présence d'un médiateur rédox réversible du type I_3^-/I^-.

La présence d'une bande d'absorption additionnel dans le proche IR pour le copolymère radicalaire poly-isoporphyrine a été mise à profit pour générer $^1O_2$ par illumination dans le domaine du proche IR en milieu aéré, c'est-à-dire en présence de $^3O_2$. Cette bande d'absorption explique également en partie la meilleure efficacité pour la génération d'un photocourant.

Cette propriété montre que de tels matériaux peuvent être utilisés pour la thérapie photodynamique.

Un matériau hybride avec de l'isoporphyrine et du polyoxométallate pourrait être également développé à l'avenir pour des applications en photochimiothérapie, certains polyoxométalates étant efficaces seuls pour le traitement de cancer en chimiothérapie, l'isoporphyrine étant sans doute un bon candidat pour des traitements en photothérapie.

Références

1. D. Dolphin, R. H. Felton, D. C. Borg, J. Fajer, *J. Am. Chem. Soc.* **1970**, 92, 743–745.
2. G. J. Abhilash, J. Bhuyan, P. Singh, S. Maji, K. Pal and S. Sarkar, *Inorg. Chem.*, **2009**, 48, 1790–1792.
3. S. C. Mwakwari, H. Wang, T. J. Jensen, M. Vicente, H. Graça, K. M. Smith, *J. Porphyrins Phthalocyanines*, **2011**, 15, 918–929.
4. A. Giraudeau, L. Ruhlmann, L. El-Kahef, M. Gross, *J. Am. Chem. Soc.* **1996**, 118, 2969–2979.
5. N. Adarsh, R. R. Avirah, D. Ramaiah, *Org. Lett.* **2010**, 12, 5720–5723.
6. M. N. Sokolov, M. A. Mihailov, E. V. Peresypkina, K. A. Brylev, N. Kitamura, V. P. Fedin, *Dalton Trans.*, **2011**, 40, 6375–6377.
7. L. Ruhlmann, A. Giraudeau, *Eur. J. Inorg. Chem.* **2001**, 13, 659–668.
8. L. Ruhlmann, M. Gross, A. Giraudeau, *Chem. Eur. J.* **2003**, 9, 5085–5096.

Contents

List of Abbreviations

AFM	**atomic force microscopy**
bpy	**4,4-bipyridine**
CV	**cyclic voltammogram**
DMF	**N,N-dimethylformamid**
DPBF	**1,3-diphenylisobenzofuran**
DSSCs	**Dye-Sensitized Solar Cells**
EQCM	**Electrochemistry Quartz Crystal Microbalance**
ESR	**Electron Spin Resonance**
EIS	**Electrochemical Impedance Spectroscopy**
GC	**Glassy Carbon**
H_2TPP	**5,10,15,20-tetraphenylporphyrin**
HOMO	**highest occupied molecular orbital**
H_2T_2P	**5,15-bis(p-tolyl)porphyrin**
ITO	**Indium Tin Oxide**
IR	**infrared**
LUMO	**lowest unoccupied molecular orbital**
L	**ligand**
M	**metal**
NMR	**Nuclear Magnetic Resonance**
PDT	**Photodynamic therapy**
POM	**polyoxometalate**
Porp	**porphyrin**

Ph	**phenyl**
PF_6^-	**hexafluorophosphate**
SCE	**Saturated Calomel Electrode**
TBA	**tetrabutylammonium**
UV	**Ultra Violet**
Vis	**visible**
V	**viologen**
XPS	**X-ray Photoelectron Spectroscopy**
ZnOEP	**zinc-*β*-cotaethylporphyrin**
$ZnAT_2P$	**5-(4-methoxyphenyl)-10,20-di-p-tolylporphyrin zinc**
ZnTPP	**zinc tetraphenylporphyrin**
ZnT_2P	**zinc-5,15-ditolyl-porphyrin**
ϕ_Δ	**singlet oxygen quantum yield**
Γ	**surface coverage**

Introduction générale

Les porphyrines avec des macrocycles aromatiques de 18 électrons ont montré des propriétés optiques, photochimiques, de coordination, catalytiques et électrocatalytiques riches et intéressantes. Les porphyrines sont les composants clés des processus biologiques tels que la photosynthèse des plantes ou des bactéries et du transport de l'oxygène dans les systèmes cardiovasculaires des humains et des animaux. Dans la technologie développée pour la thérapie photo-dynamique (PDT), les porphyrines et les dérivés de porphyrine peuvent être traités comme un photo-sensibilisateur efficace qui pourrait réagir avec l'oxygène triplet ($^3O_2$) et produire des espèces réactives de l'oxygène tel que l’oxygène singulet ($^1O_2$) sous une irradiation avec de la lumière visible.

La structure de base de la porphyrine est facile à modifier en incorporant des substituants à la périphérie du cycle.

Dans notre groupe de Strasbourg, nous avons montré que les copolymères à base de porphyrine pouvaient être obtenus par électropolymérisation en présence de nucléophile par exemple du type 4,4’-bipyridine.

La formation d'isoporphyrines peut tout d’abord être générée lors de l'attaque de nucléophile tel que le méthanol. D'autres nucléophiles tel que H_2O peut également réagir avec la porphyrine oxydée telle que la $ZnTPP^{+\bullet}$ pour former une isoporphyrine. Ces isopoporphyrines ont cependant un temps de vie limité et ne sont pas stables. Le spectre UV-visible-NIR d’une isoporphyrine présente une forte absorption caractéristique dans la région proche IR[1] entre 750 nm et 950 nm et un comportement redox remarquable ce qui en fait un bon candidat pour que thérapie photodynamique du fait d’une meilleure pénétration des rayonnements proche-infra-rouge dans les tissus.

Le chapitre I correspond à la description de la chimie des porphyrines, des isoporphyrines et des polyoxométalates, suivi par un état de l'art des assemblages hybrides porphyrine - polyoxométalate obtenus via des interactions covalentes ou non covalentes. Les polyoxométalates (POM) sont des cluster d'oxydes anioniques aux propriétés structurelles et électroniques diverses et remarquables.[2] En raison de leur robustesse et du grand nombre d'atomes de métaux de transition à haut état d'oxydation, les POM peuvent subir des processus de photorédox multi-électroniques sans décomposition. Les porphyrines[3] et les POM[4] ont été principalement étudiées séparément pour des applications telles que les matériaux photovoltaïques et supramoléculaires, les matériaux qui combinent à la fois une porphyrine et du POM sont beaucoup plus rares. Certains complexes POM-porphyrine ont été rapportés sur la base de l'interaction(s) de coordination entre les unités porphyriniquees et les POM.[5-7]

L. Ruhlmann[8] a démontré que l'on pouvait former des films covalents à base de POM-porphyrine en utilisant une méthode d'électropolymérisation basée sur l'attaque nucléophile de groupes pyridyle (greffé sur le POM) sur les dications de porphyrine électrogénérées. Cependant il est nécessaire de greffer deux groupements pyridyles pendant sur le polyoxométallate pour obtenir le copolymère avec alternance porphyrine et polyanion.

Les hybrides POM-porphyrine peuvent être utilisé pour le développement de cellules photovoltaïques et pour la génération de photocourant. Ces hybrides peuvent également être employés pour des applications en photocatalyse tel que la photoréduction des métaux nobles (Ag (I), Au (III) et Pt (IV)) présent en milieu aqueux comme par exemple dans les eaux usées industrielles. Les résultats ont prouvé que la présence du POM pouvait améliorer l'efficacité de la génération de photocourant ainsi que l'efficacité de ce type de photocatalyse.

Le chapitre II comprend des études sur la formation de polyisoporphyrine radicalaire stable en utilisant une porphyrine de zinc du type ditolylporphyrine et des ligands dipyridyle à structures variées. De tels copolymères de poly-isoporphyrine absorbent tout le domaine de la lumière (UV, Visible et proche IR) et peuvent être utilisés pour le développement de dispositifs photovoltaïques et la génération de photocourants. De plus, des études sur l'efficacité de la génération d'oxygène singulet $^1O_2$ à l'aide de la poly-isoporphyrine sous illumination visible et proche IR ou seulement sous illumination dans le proche IR ont été étudiées.

Le chapitre III correspond à l'optimisation de la préparation de copolymères stables à base de (iso)porphyrines face-à-face, c'est-à-dire de configuration cofaciale, à l'aide de la 5,15-ditolyl-porphyrine de zinc (**ZnT$_2$P**) et d'un ligand dipyridyle de géométrie adapté. Le but ultime était l'étude de l'inclusion de divers types de polyoxométallate dans les cavités porphyriniques via des interactions électrostatiques et de coordination. L'idée initiale était de moduler la distance entre les porphyrines via un contrôle de la topologie du ligand dipyridyle de départ.

L'objet du chapitre IV a porté sur la formation d copolymères d'(iso)porphyrines stables à partir d'un cluster d'halogénures octaédriques décorés de six groupement pyridyles (**PIM(py)$_6$** ; PIM = PolyIodoMétallate). Notre objectif était d'électrosynthétiser un copolymère 3D en utilisant un cluster d'halogénure de molybdène (II) du formule $(Bu_4N_2)[\{Mo_6I_8\}(OOC\text{-}C_5H_4N)_6]$ (abrégé (**PIM(py)$_6$**), possédant 6 groupes pyridyl pendants, dans le présence de ditolyporphyrine de zinc (**ZnT$_2$P**).

Comme déjà publié, des dimères et trimères de porphyrine ont été préparés avec des espaceurs diphosphonium connectés aux positions *β* de la tétraphényl porphyrine de zinc (**ZnTPP**) par synthèse électrochimique. L'oxydation facile des ligands bisphosphines (parfois appelé diphosphine) où le potentiel d'oxydation est inférieur au deuxième second potentiel d'oxydation de la porphyrine pose problème pour l'obtention de copolymère à base de porphyrines et d'espaceurs diphosphonium. L'objectif du dernier chapitre (chapitre V) est de préparer des copolymères de polyisoporphyrine qui nécessite une oxydation qu'au potentiel de première oxydation vers +1,0 V vs. ECS avec différents types d'espaceurs diphosphonium. L'emplois d'un faible potentiel appliqué lors de l'oxydation de la porphyrine a permi d'éviter l'oxydation du ligand diphosphine permettant l'obtention d'un copolymère d'isoporphyrine radicalaire stable. Les propriétés électrochimiques et photoélectrochimiques de tels copolymères d'isoporphyrines radicalaires seront décrites dans ce chapitre.

En résumé, cette thèse rapporte une stratégie facile et aisée pour obtenir et synthétiser des copolymères du type poly(iso)porphyrine stables à partir du monomère de porphyrine **ZnT$_2$P** et de ligands dipyridyle ou diphosphine. Les propriétés électrochimiques, photoélectrochimiques et d'impédance mesurée par spectroscopie d'impédance électrochimique de ces poly-isoporphyrines et poly-porphyrines parentes ont été comparées et discutées.

Réferences

1. (a) J. Bhuyan, S. Sarker, *Chem. Eur. J.*, **2010**, 16, 10649-10652. (b) J. Bhuyan, *Dalton Trans.*, **2016**, 45, 2694-2699. (c) K. D. Borah, J. Bhuyan, *J. Coord. Chem*, **2019**, 72, 2251–2260.

2. D.-L. Long, R. Tsunashima, L. Cronin, *Angew. Chem. Int. Ed. Engl*. **2010**, 49, 1736–1758.

3. C. M. Drain, X. Chen in Encyclopedia of Nanoscience & Nanotechnology (Ed.: H.S. Nalwa), *American Scientific Press*, **2004**, 9, 593–616.

4. a) D. E. Katsoulis, *Chem. Rev.* **1998**, 98, 359-388. b) D. L. Long, E. Burkholder, L. Cronin, *Chem. Soc. Rev*. **2007**, 36, 105–121.

5. M. Piepenbrink, M. U. Triller, N. H. J. Gorman, B. Krebs, *Angew. Chemie - Int. Ed*. **2002**, 41, 2523–2525.

6. A. Yokoyama, T. Kojima, K. Ohkubo, M. Shiro, S. Fukuzumi, *J. Phys. Chem. A*, **2011**, 115, 986–997.

7. D. Schaming, C. Costa-Coquelard, I. Lampre, S. Sorgues, M. Erard, X. Liu, J. Liu, L. Sun, J. Canny, R. Thouvenot, L. Ruhlmann, *Inorganica Chim. Acta,* **2010**, 363, 2185–2192.

8. a) D. Schaming, C. Allain, R. Farha, M. Goldmann, S. Lobstein, A. Giraudeau, B. Hasenknopf, L. Ruhlmann, *Langmuir,* **2010**, 26, 5101–5109. b) Z. Huo, I. Azcarate, R. Farha, M. Goldmann, H. Xu, B. Hasenknopf, E. Lacôte, L. Ruhlmann, *J. Solid State Electrochem*, **2015**, 19, 2611–2621. c) C. Allain, D. Schaming, N. Karakostas, M. Erard, J. Gisselbrecht, S. Sorgues, I. Lampre, L. Ruhlmann, B. Hasenknopf, *Dalton Trans.*, **2013**, 42, 2745–2754.

9. L. Ruhlmann, A. Giraudeau, *Chem Commun*, **1996**, 17, 2007–2008.

10. L. Ruhlmann, A. Giraudeau, *Eur J Inorg Chem*, **2001**, 13, 659–668.

11. L. Ruhlmann, M. Gross, A. Giraudeau, *Chem Eur J*, **2003**, 9, 5085–5096.

Chapter I

Introduction and literature review

Chapter I: Introduction and literature review

1. Porphyrin and isoporphyrin

1.1. Structure and properties

1.1.1. Structure of porphyrin and isoporphyrin

The word porphyrin comes from porphura (an ancient Greek word), which means the color purple. The basic structure of porphyrin consists four methine bridges which linked four pyrrole rings, named porphine. Figure 1.1 (left part) showed the structure of porphine with IUPAC numbering of the ring system.[1]

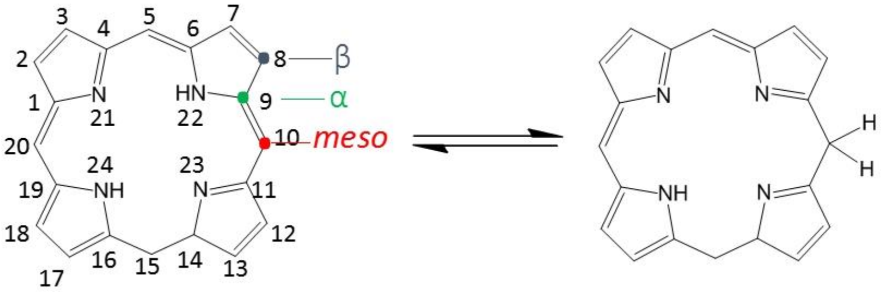

Figure 1.1. Structure of porphine and isoporphyrin.

The carbon atom of 5, 10, 15 and 20 are referred to as the *meso*-positions, carbons 2,3,7,8,11,12,17,18 as the β-position, 1,4,6,9,11,14,16,19 as the α-positions. Porphyrin contains 22 π electrons and 18 π electrons delocalized on the macrocycle.[2] The inner nitrogen atom 22, 24 could lose protons to form dianion species. Accordingly, metal could be coordinated with such dianion porphyrin, named metalloporphyrin. The incorporation of metal may give rise to the distortion of the planar macrocycle to adjust the binding strength towards the metal fragment.[3]

Natural porphyrins have colors and are distributed in living tissues[4] where they participate in vital biochemical processes (Fig. 1.2),[5] such as the oxygen transport (myoglobin and hem), the photosynthesis (chlorophylls), the electron transport (cytochromes b and c), and O_2 activation and utilization (cytochrome P450, cytochrome oxidase, and vitamin B12).[6] In addition, Iron (II) porphyrin derivatives are some of the most studied biological molecules in haemoglobin, cytochrome c and myoglobin which could transports oxygen from the lungs and the skin to muscle tissue.[7] Another Mg (II) porphyrin molecule in chlorophyll convert and collect solar energy in order to transform CO_2 and H_2O to glucose and O_2 in the second step.[8]

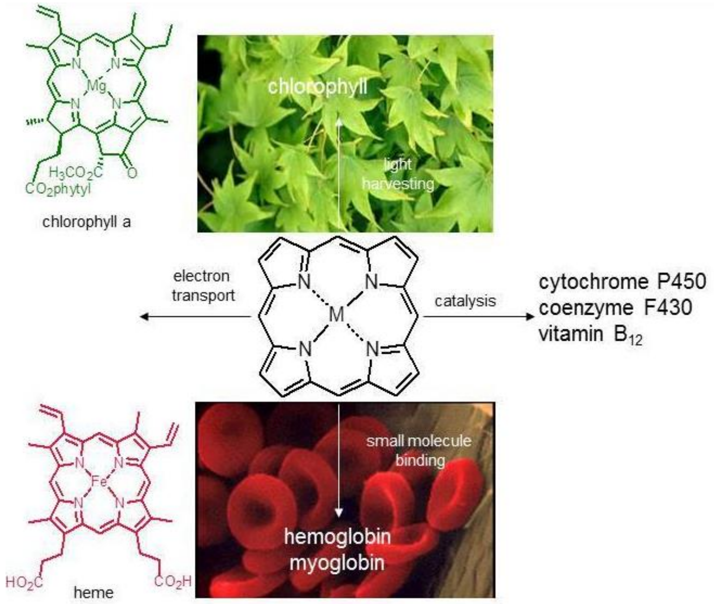

Figure 1.2. Diverse functions of metalloporphyrin in Nature.[5]

Isoporphyrin can be formed from free base porphyrin (without central metal) with one proton of NH group moved to *meso* carbon position with destroyed ring current (Fig. 1.1 right part).[9-10] However, this kind of isoporphyrin is not stable and easy re-established the aromatic system. Isoporphyrin have been reported as intermediates of heme oxidation and biosynthesis of chlorophyll molecules.[11-13] The first metallo-isoporphyrin was synthesized in 1970 by Dolphin and co-workers using electrochemical oxidation of zinc *meso*-tetraphenylporphyrin (ZnTPP) in methanol solution (Fig. 1.3).[14] Various metallo-isoporphyrins were synthesized during the past years, either by chemical oxidation,[15-18] electrochemical oxidation,[19-21] and photooxidation[22-25] of metalloporphyrins in the presence of various type of nucleophiles.

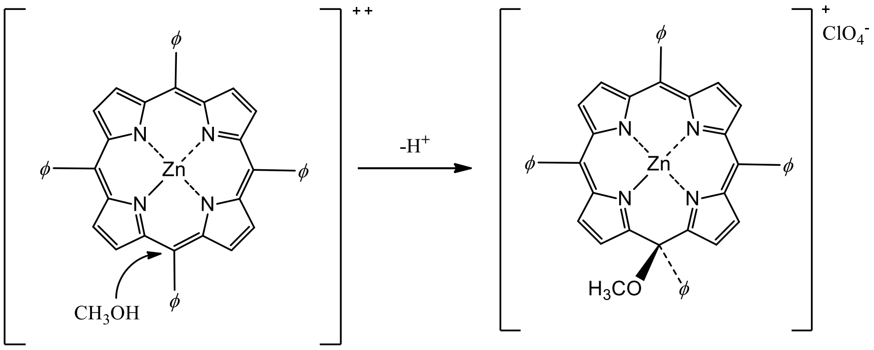

Figure 1.3. Mechanism of formation of isoporphyrin from porphyrin.[26]

1.1.2. Spectral properties

1.1.2.1. UV-vis absorption spectroscopy

Because of the extensive electron delocalization on the macrocycle, porphyrins have very intense absorption bands in the visible region which give them their characteristic bright colors. A strong absorption band shows around 420 nm in the case of TPP porphyrin, known as the Soret absorption, as well as weak absorption Q bands between 600 nm and 800 nm (Fig. 1.4).[27] The transition from the ground state to the second excited state (S_0-S_2) corresponds to the Soret or B band. The Q bands are due to a transition from the ground state to the first excited state (S_0-S_1).[28] The lower energy band (higher wavelength) Q (0,0) is due to the excitation to the first state, the higher energy band (lower wavelength) Q (1,0) is referred to a vibronic overtone with vibrational transitions interacting with the electronic transitions of the macrocycles.[28]

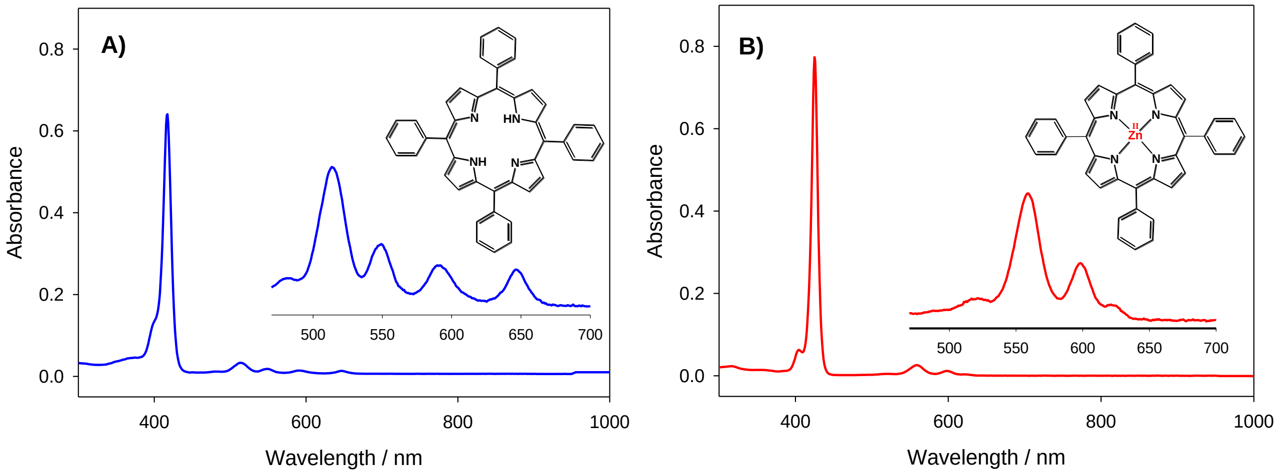

Figure 1.4. UV-visible absorption spectra of A) free base tetraphenylporphyrin and B) zinc tetraphenylporphyrin in DMF (c = 1.5×10^{-6} mol L^{-1}).

Compared with metalloporphyrin, the symmetry of free base porphyrins macrocycles is lowered from D_{4h} to D_{2h}, due to the non-equivalent HN-NH and N-N axis. Thus, the degenerate Q(0,0) is replaced by transitions polarized along to $Q_x(0,0)$ and $Q_y(0,0)$, and also the vibronic overtones $Q_x(1,0)$ and $Q_y(1,0)$ which results in four bands in the visible region for free base porphyrins (Fig.1.4). Metals with closed electron shells of the porphyrins have small effect on the absorption spectra of the chromophores, while metal orbitals of open shell metals mix much more strongly with the ring orbitals, thus having intense effect on the absorption spectra.[28]

Because of the presence of a saturated bridging *meso*-carbon which interrupts the macrocyclic conjugation, isoporphyrins have weak Soret band (around 400 nm) and intense Q bands between 750-900 nm. This bathochromic shift of the B bands as well as the Q band is shown in Fig.1.5. It is due to the presence of the partial conjugation which could be seen in chlorins and chlorophylls.[29]

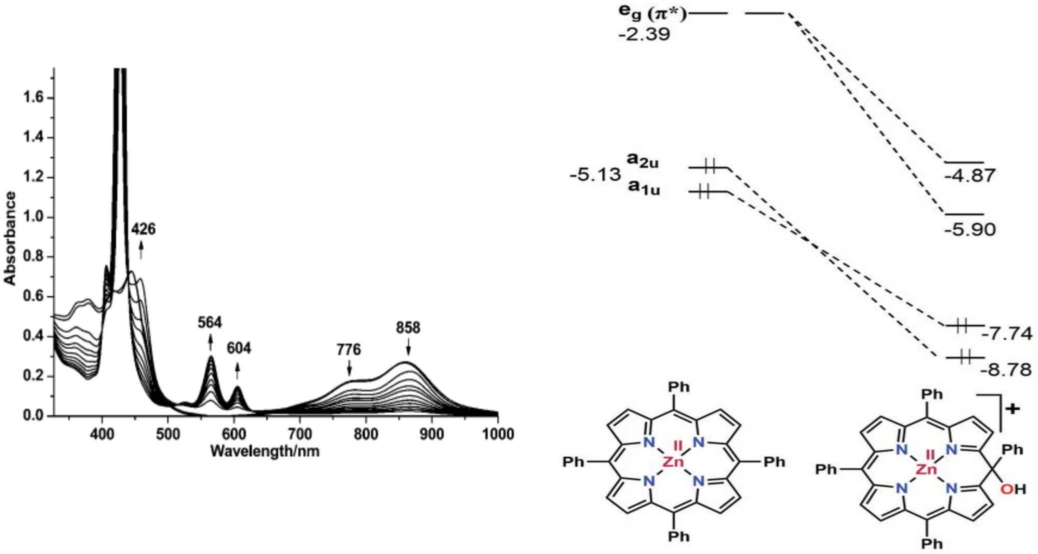

Figure 1.5. (Left) Reduction of isoporphyrin (zinc hydroxyisoporphyrin) to porphyrin (zinc meso-tetraphenylporphyrin) in dichloromethane.[30] (Right) Simplified Gouterman's MO level for ZnTPP and zinc hydroxyisoporphyrin.[31-33]

The absorption bands can be academically discussed and explained by Gouterman et al[34-36] in the 1960's who proposed "four orbital model" and further discussed by Anderson.[37] Figure 1.5 (right part) shows the four HOMOs and LUMOs of a typical metalloporphyrin ZnTPP. Because of the similar energy of a_{1u} (HOMO) and a_{2u} (HOMO-1) and the degeneracy of the pair of LUMOs (e_{gy} (LUMO) and e_{gx} (LUMO+1)) there is a strong interaction between the $a_1 \rightarrow e_g$ and the $a_{2u} \rightarrow e_g$ transitions.

Due to the sp^3 saturated *meso*-carbon atom, the asymmetric structure of isoporphyrin become asymmetry makes the orbital energy associated to the Q bands increase. The frontier molecular orbitals energy of ZnTPP and zinc hydroxyisoporphyrin are shown in Figure 1.5.[31] The energy gap between HOMO and LUMO orbitals for isoporphyrin is smaller than ZnTPP analogue, resulting the red (bathochromic) shift of the Q-bands. The hybridized *meso*-carbon atom of isoporphyrin unsettled the LUMO orbital, because abundant electron density is present at the *meso* position.[31] The crystallographic results proved that the complex is cationic and incorporates a saturated *meso* carbon, features characteristic of a metallo-isoporphyrin. The isoporphyrin displays distinctive bond distance values and bond angles comparing with porphyrin with the overall pattern of bond distances being consistent with the resonance forms of the interrupted π system as illustrated in Figure 1.6.

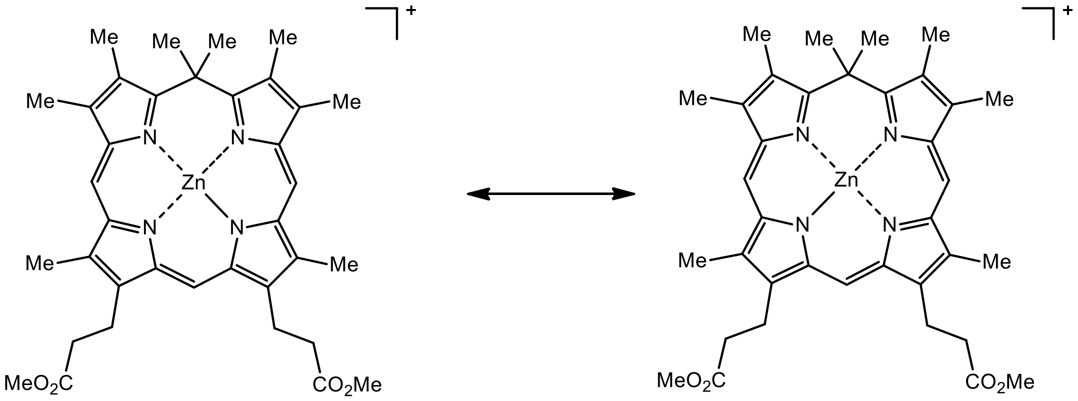

Figure 1.6. Resonance structures of the zinc isoporphyrin.[28]

1.1.2.2. Fluorescence emission spectroscopy

According to Kasha's rule, the emission is coming principaly from the lowest excited state S_1 after excitation from the ground state S_0.[38] From S_1 the molecule can directly go back to the ground state S_0 and emits fluorescence radiation, or converts to the lowest triplet state T_1 with intersystem crossing and then decay to the ground state S_0, with emitting phosphorescence radiation. There are two bands Q(0,0), and Q(0,1) of metalloporphyrins in fluorescence spectra which are mirror images of the absorption bands Q(0,0) and Q(1,0).

For isoporphyrin, the difference of energy between fluorescence and absorption is around 600 cm^{-1}. This Stokes shift is larger than the ~50 cm^{-1} observed for instance for zinc *β*-octaethylporphyrin (ZnOEP) porphyrin.[28] The Stokes shift is usually < 200 cm^{-1} for planar porphyrins, and in the range 850-1000 cm^{-1} for nonplanar porphyrins.[39] Thus, the Stokes shift observed for the isoporphyrin is closer to the nonplanar porphyrins. In addition, the zinc isoporphyrin exhibits an unusually short singlet excited state lifetime (130 ± 15 ps) compared with parent zinc porphyrin. Generally, similar perturbations of photophysical properties could be observed for the highly nonplanar macrocycles.[40]

1.1.2.3. ^{1}H NMR spectroscopy

For the zinc tetraphenylporphyrin (ZnTPP), because of the symmetry structure, the ring current is due to the eight equivalent *β* protons, which appear at 9.05 ppm. The sp^3 hybridized *meso*-carbon atom changes the symmetry structure and lose ring current in the case of the isoporphyrin. As the β protons of isoporphyrin are no longer equivalent and appear as four doublets instead of a singlet at higher field (Fig. 1.7). The similar shift was observed of the phenyl protons.[14] In the research of Bhuyan,[30] a similar ^{1}H NMR spectrum of the synthesized zinc isoporphyrins are obtained and the four doublets β-H peaks of pyrrole are observed. By the work of Gold,[41] the iron isoporphyrin (paramagnetic compound) shows four peaks of pyrrole in ^{1}H NMR spectrum. Comparable upfield shift of the β protons has been observed for zinc *meso*-tetraphenylphlorin in the absence of the macrocyclic ring current.[42]

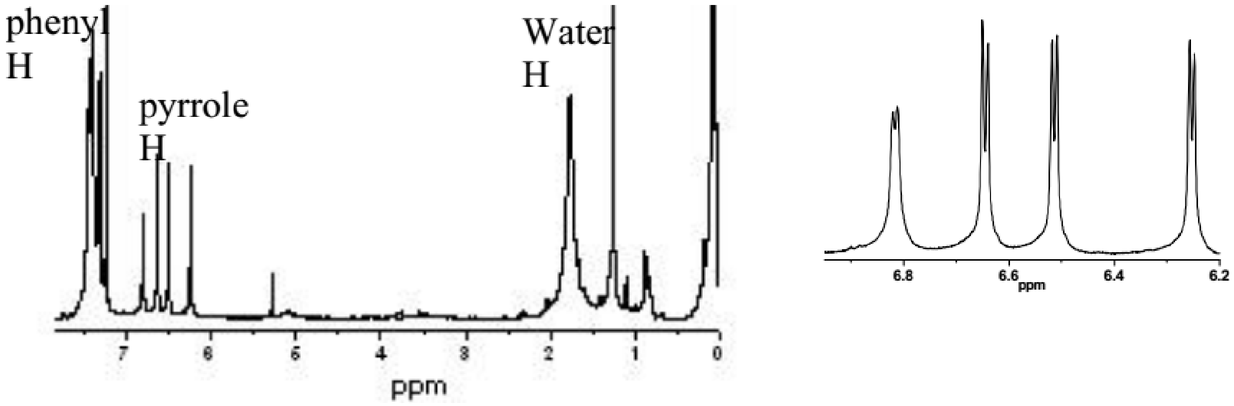

Figure 1.7. ^{1}H NMR spectrum of the zinc hydroxy-isoporphyrin (left) and splitting of pyrrole protons (right).[30a]

1.1.2.4. Infrared spectroscopy

Infrared spectroscopy is a useful tool for identifying porphyrin π-radical cations.[43] The porphyrin π-cation radical displays a peak at in the region of 1270-1295 cm^{-1} characteristic of the TPP$^{+\bullet}$, which is not present in parent porphyrin. Moreover, infrared spectrum could show the peak shift of nucleophile which has been covalently bound with porphyrin due to the different vibrational frequency. In the work of Hinman, the zinc nitrato-isoporphyrin showed a strong peak at 1659 cm^{-1} in infrared absorption spectrum due to the covalently bound nitrite anion to the *meso* carbon atom.[44]

1.1.3. Electrochemical properties

As published, during electrochemical oxidation process, the π ring in usually oxidized through two one-electron steps first the radical cation and then the dication. Similarly, in the cathodic domain, the radical anion and the dianion could be generated successively with two one electron steps.[45]

For isoporphyrin ring, the interruption of the conjugation has effect on the electron transfer. One stable kind of metallo-isoporphyrin could be formed by chemical synthesis.[46] Xie has compared the electrochemical behaviour of zinc isoporphyrin (ZnIP) and zinc octaethylporphyrin (ZnOEP).[47] The results showed different reduction potentials, and the stability of the species formed on transfer of an electron to or from one species is solvent dependent. The reduction form of ZnIP is stable in polar solvent DMSO. Oxidation gives stable dication form $ZnIP^{2+}$ in the case of weak polar solvent such as DCM. The difference between the oxidation and reduction potentials of Zinc isoporphyrin is 1.38 V compared with 2.25 V for ZnOEP. This value is close to the energy gap between HOMO and LUMO estimated from optical spectrum.

Metalloisoporphyrin could be obtained by electrochemical oxidation of metalloporphyrin in the presence of nucleophiles.[14] For instance, two successive reversible one-electron oxidation waves of ZnTPP (zinc meso-tetraphenylporphyrin) were observed due to the formation of the π cation radical and the dication porphyrin. The π cation radical is stable in nucleophilic solvents such as methanol but dication is only stable in the absence of nucleophiles or nucleophilic solvent. The methanol could be considered as nucleophile which could attack dication at a *meso* carbon atom giving the isoporphyrin. Thus, the oxidative process of ZnTPP in the presence of nitrogenous base ligands could be explained by Scheme 1.1.[20] $[(TPP)ZnL]^{+\bullet}$ (L is a substituted pyridine ligands) could be obtained from the coproportionate of (TPP)ZnL with the remaining dication. This cation radical is then further reduced back to (TPP)ZnL.

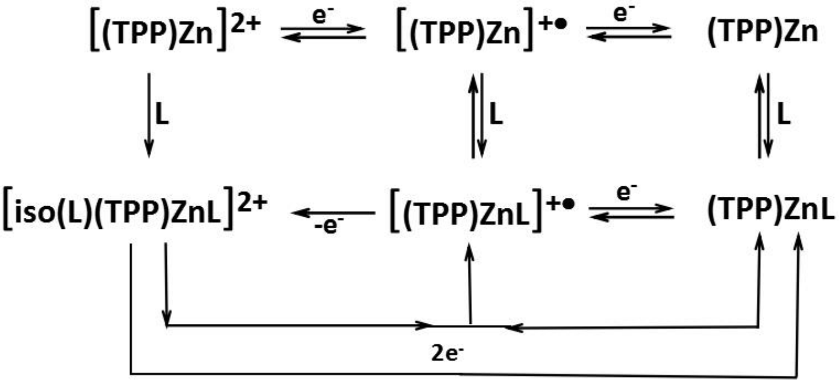

Scheme 1.1. The mechanism for the redox process of ZnTPP with nucleophile.[20]

Hinman and co-workers also studied the oxidation behaviour of ZnTPP.[44] The metalloisoporphyrin could be formed from dication with nucleophilic attack of nitrate (Fig. 1.8). Peaks 1 and 2 is the formation and reduction of π radical cation. The second oxidation peak 3 is irreversible, and a new reduction peak 7 appears on the subsequent cathodic scan. This new reduction peak corresponds to the reduction of the nitratoisoporphyrin cation formed after the nucleophilic attack on the porphyrin dication. The third oxidation peak 5 results from oxidation of the isoporphyrin cation to isoporphyrin dication.

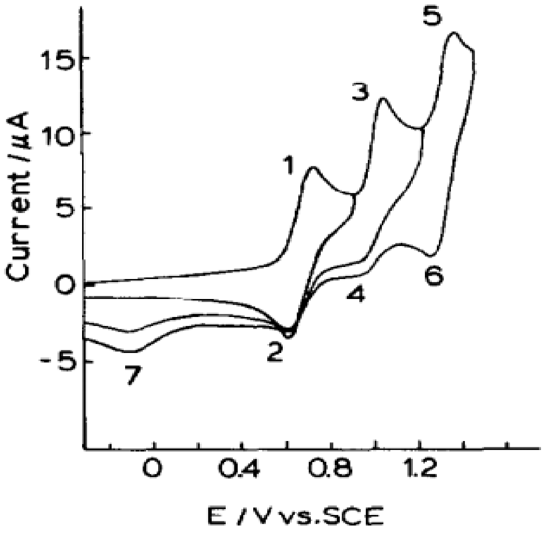

Figure 1.8. Cyclic voltammetry of 1.38 mM ZnTPP in $C_2H_4Cl_2$ + 0.2 M tetra-n-butylammonium perchlorate in the presence of 2 mmol L^{-1} tetrabutylammonium nitrate. Scan rate was 200 mV s^{-1}.

Bhuyan studied the electrochemistry of zinc hydroxy-isoporphyrin prepared from zinc porphyrin in the presence of nitrogen dioxide.[30] Compared with ZnTPP, zinc hydroxy-isoporphyrin exhibited higher potential for the formation of isoporphyrin dication (1.24 V) than the oxidation potentials of

ZnTPP to form π cation radical and dication (0.80 V and 1.11 V). Furthermore, an irreversible reduction peak around -0.11 V was observed for zinc hydroxy-isoporphyrin (Fig. 1.9).

Borah and Bhuyan have also prepared two methoxy-isoporphyrins of water-soluble porphyrins.[48] The isoporphyrins are formed due to nucleophilic attack of the methanol to the *meso* carbon position of zinc porphyrin dication. Ceric ammonium nitrate was used to oxidize zinc porphyrin and to form zinc porphyrin dication. The zinc isoporphyrins showed a typical irreversible reduction peak at lower potential. If the nucleophiles are added into the zinc isoporphyrins solution, isoporphyrins could convert to their parent porphyrins, which supports the electrochemical observations.

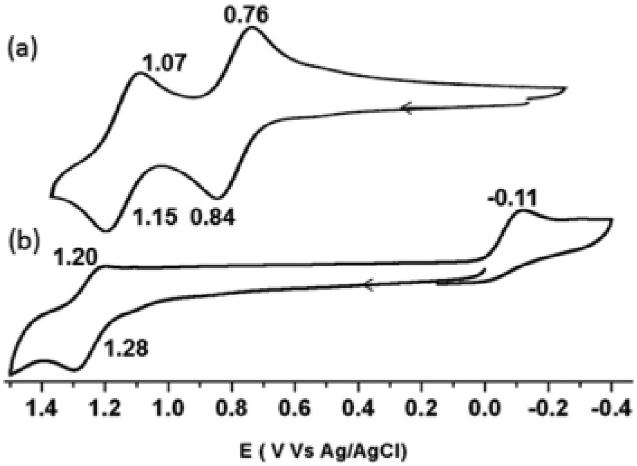

Figure 1.9. Comparison of cyclic voltammogram of (a) ZnTPP, (b) zinc hydroxy isoporphyrin in CH_2Cl_2 (294 K). Scan rate: 100 mV s^{-1}

1.2. Synthesis of isoporphyrin

1.2.1. Chemical synthesis

Smith and Xie successfully reported the total synthesis of the first thermodynamically stable zinc isoporphyrin (3).[46] The synthesis of zinc isoporphyrin was achieved according to the MacDonald[49] '2+2'method of porphyrin synthesis. The isoporphyrin was obtained from the condensation of dipyrromethane dicarboxylic acid (**1**) and diformyldipyrromethane (**2**) in the presence of zinc(II) acetate (Scheme 1.2). The isoporphyrins are stable in water and methanol, even at high temperature (100°C) but could decompose in trifluoroacetic acid within 30 minutes, and the yield is not so good (23% and 4%). Xie have synthesized additional isoporphyrins using the same methods.[15] The metal-free isoporphyrin could be obtained by demetalation of zinc isoporphyrin with TFA. Other metal salts (Cu, Ni, Fe) could not be obtained either by metalation during ring synthesis or by subsequent metalation of metal-free isoporphyrins. The zinc isoporphyrins can be stored in solid form at room temperature in daylight for months without decomposition, and they also survive high temperatures. The metal-free isoporphyrins are stable in dichloromethane and methanol but are not stable in the presence of bases (sodium bicarbonate). Correspondingly, the yields of these zinc isoporphyrins are very low.

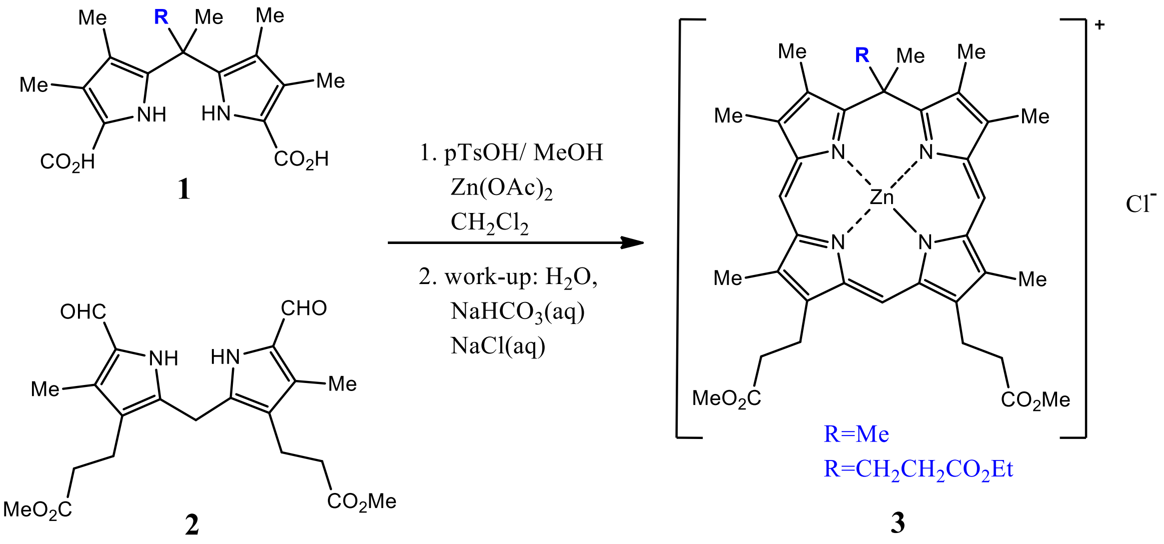

Scheme 1.2. Synthesis of stable isoporphyrin via MacDonald approach.

Smith developed a new method to synthesize metal-free isoporphyrin and metalloisoporphyrin by using ring opened tetrapyrrol, b-bilene salts.[16] The precursor b-bilene hydrochloride (**6**) was synthesized from the condensation of dipyrromethane-1-carboxylic acid (**4**) and 1-formyldipyrromethane (**5**) (Scheme 1.3). Then the 2,2- dimethoxypropane was used as the carbon linking unit for cyclization. The stable free base isoporphyrin **(7)** could convert to the zinc or copper isoporphyrin cation in the presence of metal salts of zinc, copper in dichloromethane. The yield is better than the previous metallo-isoporphyrin reported.[46, 15]

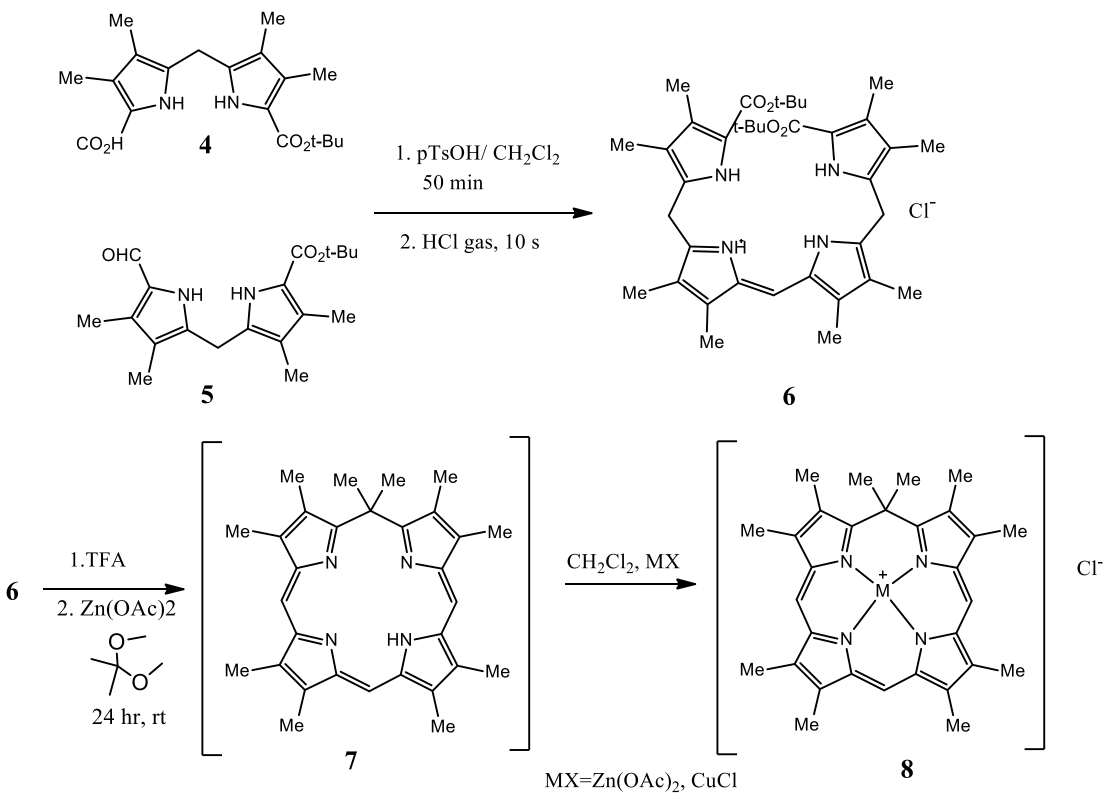

Scheme 1.3. Synthesis of stable isoporphyrin via b-biliene.

1.2.2. Electrosynthesis

Dolphin first reported the isoporphyrin obtained from the oxidized porphyrin dication in the presence of methanol which is fast and easy.[14] We have already had a short discussion of the electrochemical behaviours of porphyrin and isoporphyrin before. By the theoretical calculations, the *meso*-carbon atoms of the zinc porphyrin dication was found having higher electron density of 0.32 electron, which explained why the nucleophilic attack happened on the *meso*-carbon position. Hinman et al synthesized zinc(II) isoporphyrin from ZnTPP in the presence of nitrate, trifluoroacetate, or methanol. Manganese(III) isoporphyrin has also been obtained in dry dichloroethane. Isoporphyrin obtained from octaethylporphyrin (OEP) and natural porphyrins are not stable showing deprotonation and regeneration of the starting OEP porphyrin rapidly. In the case of a *meso*-substituted metalloporphyrin such as the tetraphenyl porphyrin with aryl group on *meso* carbon atom, the corresponding isoporphyrin is relatively more stable.[50-51]

Similar procedure was used to synthesize iron(III) isoporphyrin cation by nucleophilic attack on the *meso* carbon position of iron(III) porphyrin dication with tert-butyl hydroperoxide.[52] Sakuragi et al also propose that the formation of isoporphyrin can occur after the electron transfer observed from ZnTPP to dichloromethane at liquid helium temperature upon excitation at 425 nm (Soret band of ZnTPP).[53] According to this research, some isoporphyrins were synthesized by nucleophilic attack at the porphyrin dication.[54] One special isoporphyrin was also obtained under the passage of NO_2 gas through the solution of a μ-oxo-dimeric iron(III) porphyrin. Then, a nitratoiron(III) porphyrin complex is formed at the initial stage and on further passing of NO_2 this gets oxidized to a π-cation radical that finally converts to hydroxy-isoporphyrin in the presence of trace amount of water.

1.3. Light-harvesting systems based on porphyrin

The light energy is a renewable source to help alleviate climate change. Thus, the conversion of light energy into electrical energy has attracted a lot of attentions. Dye-sensitized solar cells (DSSCs) whichwere first introduced by Grätzel and O'Regan[55] led to a substantial improvement in photoelectric transformation efficiency (PCE)[56] due to the high flexible, low-weight, and low-cost. The device was shown in Figure 1.10. contains a dye-sensitized mesoporous nanocrystalline electrode (anode, TiO_2), a counter electrode (cathode, Pt-coated conductive glass substrate) and reducing species electrolyte (with iodine or cobalt-based redox couple) between two electrodes.[57] The mechanisms can be briefly summarized as: (1) photoexcitation of the dye as sensitizer, (2) electron injection from the excited dyes into the TiO_2 conduction band, (3) dye regeneration with the reducing species and (4) reduction of the oxidized redox species at the counter electrode complete the external circuit.

As researched, a good sensitizer always follows these requirements:[58]

a) Strong absorption in visible region and even the near-infrared part (NIR),

b) Anchoring groups like –COOH or –H_2PO_3 to bind the dye on the TiO_2 surface,

c) Excited state level energy higher than the conduction band of TiO_2 for efficient electron injection,

d) Oxidized state level lower than the redox mediator electrolyte for dye regeneration,

e) Suppression of aggregation on TiO_2 surface with coadsorption or cosensitization,

f) Good photochemical, electrochemical and thermal stability.

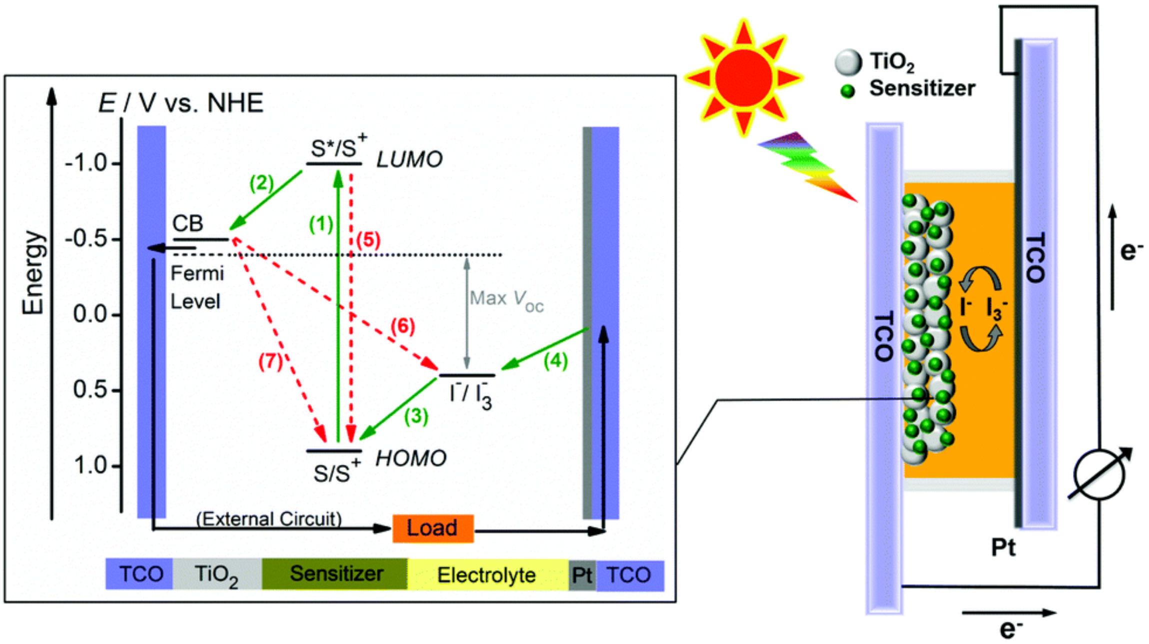

Figure 1.10. Construction and operating principle of a typical DSSC.[59]

The power conversion efficiency (PCE), η, are determined from the current-voltage (I-V) characteristics under illumination (eqn.1). I is the short-circuit current, V is the open-circuit potential, P_{in} is the power density of the incident light and FF is the fill factor. The maximum output power is found where the value $| I \times V |$ reaches maximum.

$$\eta = \frac{|IV|_{\max}}{P_{in}} = \frac{I_{sc}V_{oc}FF}{P_{in}} \qquad \text{(eqn.1)}$$

There are three representative sensitizers in DSSC researches. Sensitizers based on ruthenium complexes are used with an efficiency of 10% early by Grätzel,[59] and then ruthenium sensitizers took the lead position among the sensitizers of high efficiencies before 2010.[60–62] The restriction of the efficiency is due to structural modification and scarcity of materials. At the same time, metal-free organic sensitizers attracted attention due to the easy synthesis, low cost, and flexible functionalization. Some solar cells have been reported with over 10% efficiencies in recent years.[63–70] Except for two kinds of sensitizers, porphyrin based sensitizers have been studied a lot due to the nature structure like chlorophylls as the light-harvesting centers. In the recent years, the porphyrin based sensitizers have developed a lot, DSSCs based on porphyrin dyes have achieved PCE over 13% under standard (1.5) illumination.[71] In general, porphyrin based sensitizers have strong absorption in the visible region and flexible structural modification.[71–77]

Current research of porphyrin dyes generally focuses on the functionalization of its β position[78] or *meso* position[79] to generate dyes with appropriate energy levels and strong light-harvesting property. In general, these organic sensitizers have the donor-π-acceptor (D-π-A) configuration as strong intramolecular charge transfer properties are expected for these push-pull type structures (Fig. 1.11).

Figure 1.11. Typical structures of D-π-A push-pull sensitizer.

1.3.1. Modification of donor

The first examples of D–π–A push–pull porphyrin based sensitizer were reported by Diau, Yeh and coworkers as molecule coded YD1 (Fig. 1.12).[80] YD1 contains diphenylamine donor exhibited a higher power conversion efficiency (PCE) of 6.0% than 2.4% of YD0 having only 3,5-di-tert-butylphenyl pendant group. The results showed that the electron donating group in YD1 not only broadens its absorption region but also ‘‘pushes’’ the electrons to the acceptor facilitating electron injection.

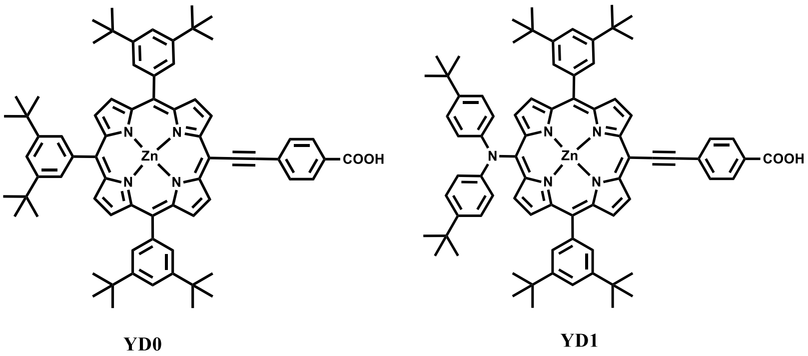

Figure 1.12. Structures of YD0 and YD1.

Since then, various donors connected with porphyrin were developed (Fig.1.13), a) diphenylamine,[80] b) triphenylamine,[81] c) pyrene,[82] d) N,N-dialkylaminophenyl,[83,84] e) fluorene,[85] f) carbazole,[86] g) indoline,[87] h) diphenylaminothiophene,[88] i) phenothiazine,[89] j) ullazine,[90] k) diphenylaminoanthryl,[91] l) bis(diphenylamino)-substituted diphenylamino-anthryl.[92]

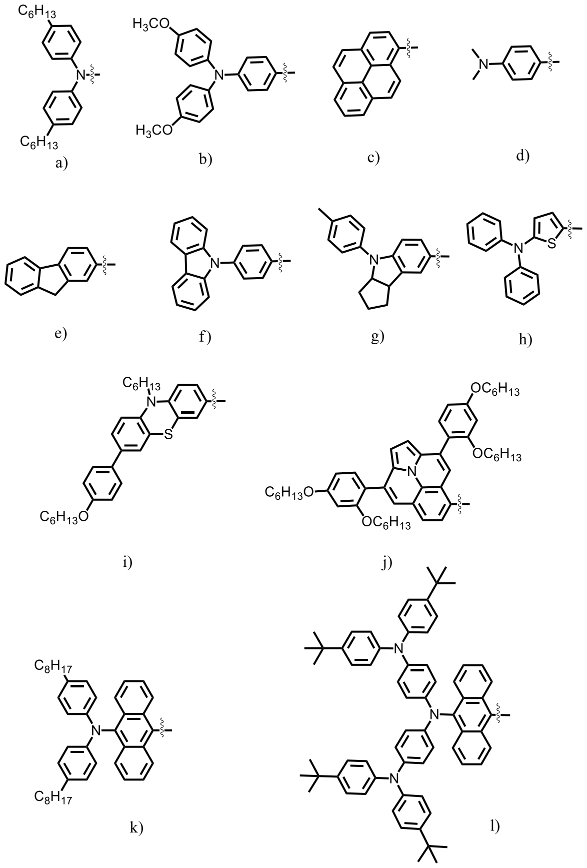

Figure 1.13. Various structures of donors which are connected to the porphyrin.

The shape and geometry of donor also affect the dye performance. The butterfly-shaped phenothiazine and triphenylamine are excellent examples of this class.

1.3.2. Modification of porphyrin ring

The sensitizers based on porphyrin most widely used are modified with long alkoxyl chains named ‘‘alkoxyl-wrapped’’ structure (Fig. 1.14): LD14,[83] LD16,[93] YD2-o-C8,[73] XW18-21.[94] The *ortho*-alkoxyl exhibits advantages over the *meta*- and *para* positions of porphyrin:[83,93] (I) The LUMO levels of the dyes increase facilitating electron injection;

(II) The alkoxyl chains increase the solubility and facilitate dye-uptake;

(III) The rigid porphyrin core surrounded by the *ortho*-chains with eight or more carbon atoms with suppress dye aggregation;

(IV) TiO_2 conduction band (CB) edge have an upward shift of the dye adsorption with improving the V_{oc};

(V) Insulating layers could be formed and slow down the charge recombination.

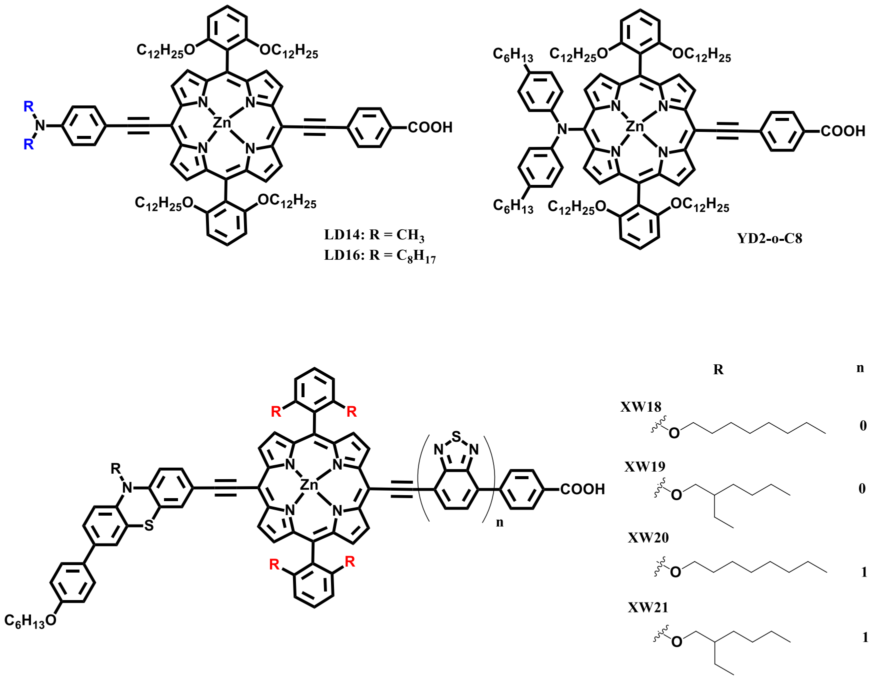

Figure 1.14. Structure of several porphyrins with ‘‘alkoxyl-wrapped’’.

1.3.3. Modification of acceptor

The electron acceptor effect as the anchoring group correlated with the adsorption geometry on TiO_2, the electron injection behavior and the adsorption strength.[95] Most types of acceptor/anchoring groups are the carboxylic acid and cyanoacrylic acid groups which could connect with TiO_2. By researching the literature, the cyanoacrylic acid is used a lot for metal-free organic dyes, and the carboxylic acid mainly for porphyrin dyes with better photovoltaic performance (Fig. 1.15). In recent years the incorporation of an auxiliary acceptor group has been proved to increase the absorption region, to facilitate the intramolecular charge transfer and to modulate the energy levels.[96] The results indicated that the ethynyl group induces more red-shifted in absorption spectrum than the cyanoacrylic group, the latter also induce large red-shift than the carboxyphenyl group.

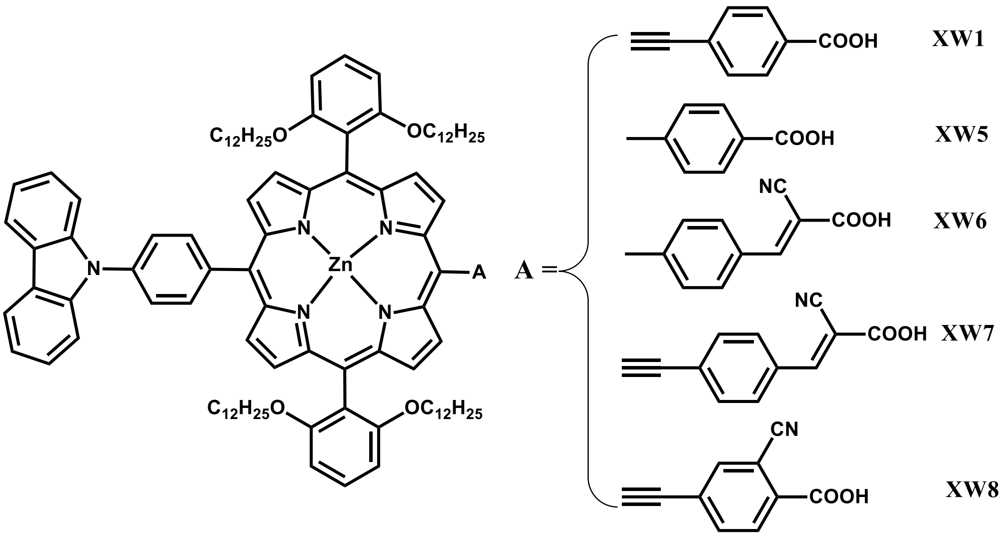

Figure 1.15. Structure of several Acceptor connected to the porphyrin.

1.4. Photodynamic therapy (PDT)

Photodynamic therapy (PDT) is a method which could be used against cancer in malignant and non-malignant tumors. PDT was first proposed in the 1980's and throughout the world, there are three key components: light source, a photosensitizer (could be activated by light), and tissue oxygen, to destroy cancer cells.[97,98] The lasers are widely used light sources in the range of approximately 620-850 nm where the maximum of skin permeability occurs.[99] For PDT, the photosensitizer (PS) plays an important role and could be excited under visible light of a wavelength irradiation in the presence of the bacterial sample. The excited singlet state is unstable and quickly turn to the ground state via emission of fluorescence or turn into triplet state then back to ground state with emission of phosphoresce. For the latter process, PS triplet state could transfer the energy to form an electron or proton which could react with oxygen and produce reactive oxygen species (ROS), as singlet oxygen, superoxide anion, hydroxyl radicals via two competing pathways in Figure 1.16. The singlet oxygen was considered as the mainly ROS for photodynamic action[100–102] and it has also been shown to inactivate the antioxidant enzymes such as superoxide dismutase, catalase, and peroxidase.[103,104]

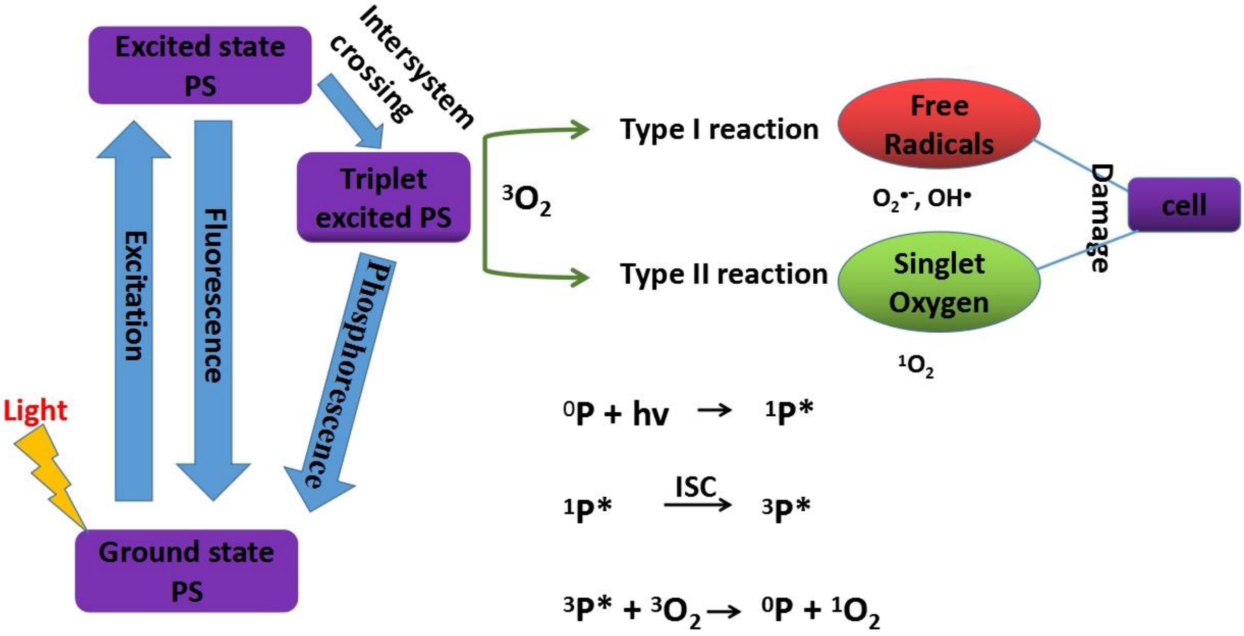

Figure 1.16. The photochemical processes of ROS such as $^1O_2$ produced during PDT.

Porphyrin-based compounds possess good photochemical, photophysical and biological properties: they have strong absorption in the visible region of the optical spectrum, are non-toxic in the dark, have high chemical stability, have affinity for serum proteins, have favorable pharmacokinetic properties.[105] Thus, several porphyrin-type photosensitizers are currently in various stages of preclinical or clinical development as phototherapeutic agents (*vide infra*).

The first-generation porphyrins are the primitive porphyrins known as hematoporphyrin derivatives (HpD) present in the first commercially available PDT drug, Photofrin. These disadvantages of porphyrins are limited by impurity, poor in depth light absorption, and photosensitivity.[106] The latter is an uncomfortable body reaction that occurs because of the activation of the photosensitizer remaining in the body by sunlight after PDT. The second-generation porphyrins like chlorin, bacteriochlorin, and phthalocyanine derivatives (Fig. 1.17) which are chemically pure, have high fluorescence detection and quantum yields, absorb at longer wavelengths, and induce significantly less skin photosensitivity, are being developed compared with the first-generation porphyrins.[107] Due to the work of Vicente,[105] some porphyrin-type photosensitizers include mono-L-aspartyl chlorines e_6,[108-112] benzoporphyrin derivative mono-carboxylic acid,[113-117] zinc(II) phthalocyanine [118-121] and texaphyrins [122-124] all absorbing strongly in the 650-750 nm spectral region.[125]

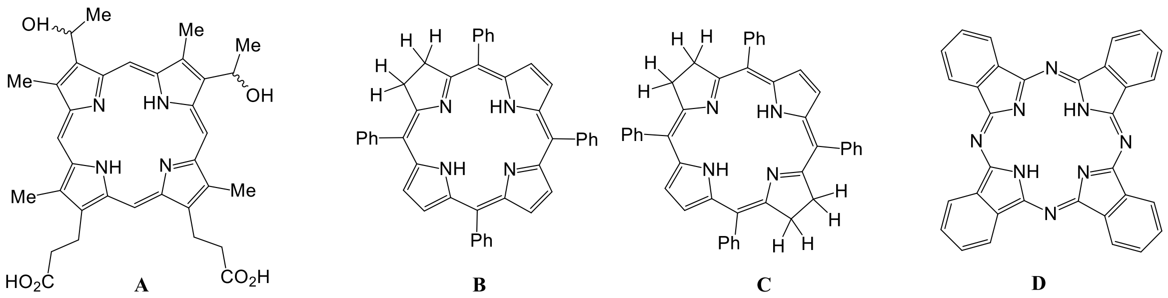

Figure 1.17. Structure of porphyrin derivatives: (A) Hematoporphyrin, (B) Chlorin, (C) Bacteriochlorin, and (D) Phthalocyanine.

Due to the research, an ideal photosensitizer has the characteristics bellow:[126] i) Chemically pure with a reproducible synthesis. ii) High quantum yield for singlet oxygen production. iii) Strong absorption with high extinction coefficient (ε) for the absorption peaks at NIR region. iv) High triplet state yields and long triplet state life times. v) Possess minimal dark toxicity and only be cytotoxic in presence of light. vi) Preferential retention by target tissue (tumor cells) vii) Rapidly excreted from the body, thus inducing a low systemic toxicity.

To improve the singlet oxygen generation efficiency, efforts have been made to modify the sensitizers based on porphyrin systems either by halogenation or metal ion incorporation. From the work of Ramaiah,[127] introducing of Zn^{2+} metal ions in the core as well as in the periphery regions improved the intersystem crossing efficiency, and more zinc metal ions exhibited good water solubility and higher quantum yields of the triplet excited state and higher singlet oxygen generation efficiency. Nifiatis[128] proved it in penetre the introduce of halogen atoms of the *meso*-phenyl groups could be able to manipulate the energy spacing and electron density distribution for the a_{1u} and a_{2u} orbitals, excited state quantum yields, and lifetimes, as well as the capability of porphyrin-based PSs to generate singlet oxygen. Tuncel[129] synthesized porphyrin-thiophene based compound, the results suggested that the sulfur atoms facilitates the intersystem crossing due to spin-orbit coupling which increases singlet oxygen generation efficiency. Similarly, the polymer showed higher efficiency than the oligomers and the monomers.

Because isoporphyrin has a strong absorption between 750-900 nm in NIR region (the phototherapeutic window is approximately 620-850 nm), it can be activated to penetrate deeper into the tissues which are prospective candidates as photosensitizing agents in photodynamic therapy.

2. Electrosynthesis of polyporphyrins using various spacers

2.1. Substituents attached to the porphyrin ring

Pyrrole and thiophene (also dithiophene and terthiophene) attached groups are the widely used units for porphyrin electropolymerization.[130-173] The surface coverage is limited by the number of pendant groups around porphyrin ring because of a cross-linking effect formed and the steric hindrance increased. Other pendant groups such as amino, hydroxy or methoxy, and vinyl also been used in porphyrin electropolymerization (Fig. 1.18).[174-194]

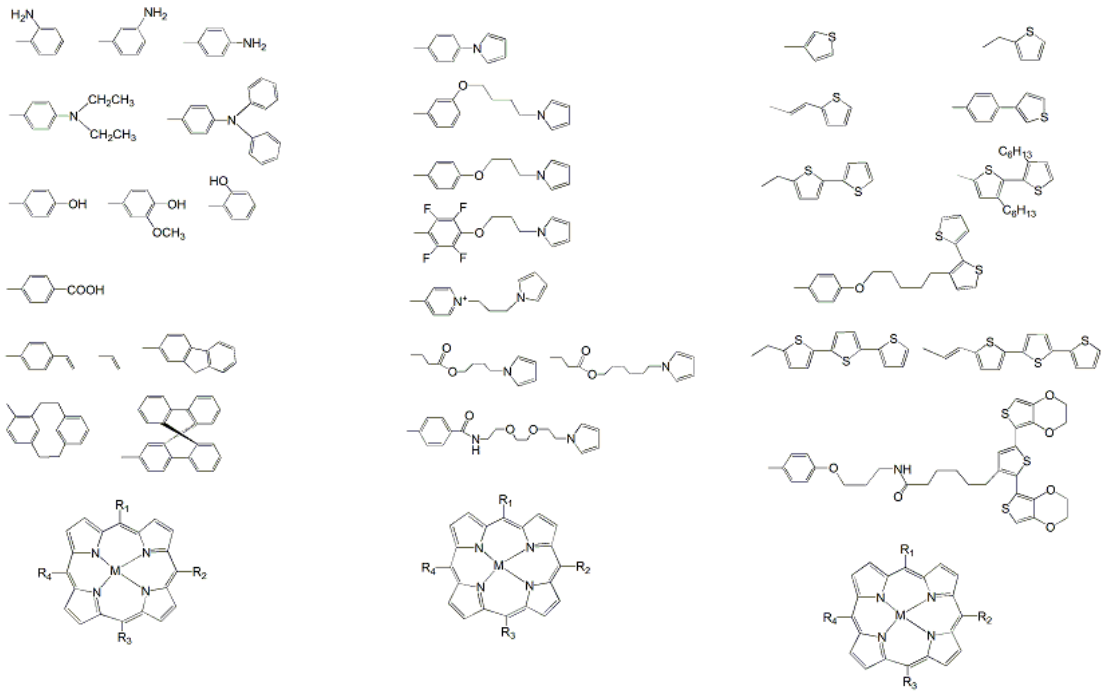

Figure 1.18. Examples of electropolymerizable pendant groups used for porphyrin polymerization.

From the work of Wamser, an aminophenyl derivative with -NH_2 groups at the *para* position of the phenyl substituents,[195] the oxidation of porphyrin derivatives produce a highly interconnected nanofibrous network and a linear porphyrin polymer. The mechanism was assumed to the aniline polymerization and the rule of electrophilic nitrogen first attacked the *meso* position of another porphyrin monomer. In the work of Toma and coworkers,[196-198] for the tetraruthenated porphyrin [H_2(4-TPyP) {Ru(5-Clphen)$_2$Cl}$_4$] with halogen-substituted aromatic compounds (Fig. 1.19), the reduction of 5-chloro-phenanthroline ligand induces the elimination of the phenanthroline’s chloro group as chloride with the formation of radical, which should then react with another radical forming.

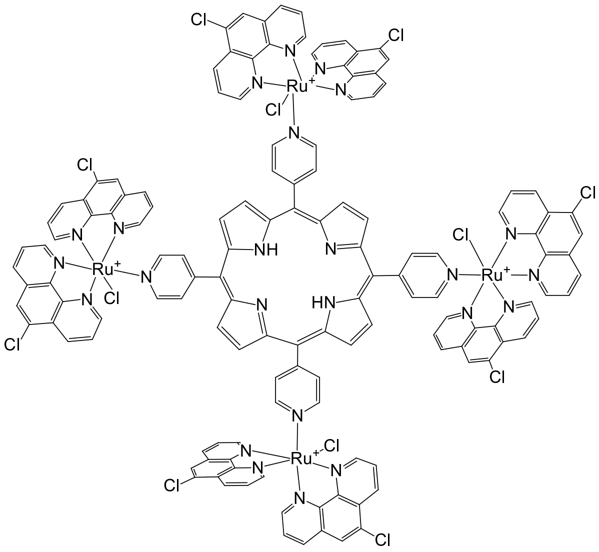

Figure 1.19. Structure of the $[H_2(4\text{-TPyP})\{Ru(5\text{-Clphen})_2Cl\}_4]^{4+}$ species.

Furthermore, porphyrin bearing two N-methyl-3-pyridylethynyl substituents could give polymer by reduction of the pyridinium groups (Fig. 1.20).[199] The mechanism contains two steps. The first step is the reduction of pyridinium groups, the electrons only stay at the pyridium ring because the chemical structure prevents the delocalization to the porphyrin macrocycle. Then in the second step, the pyridyl radicals could form dimer and further give the electropolymers. For 2-methylpyridinium and 4-methylpyridinium ligands, no polymers could be formed due to the delocalization of two extra electrons through the triple bond as well as the porphyrin.

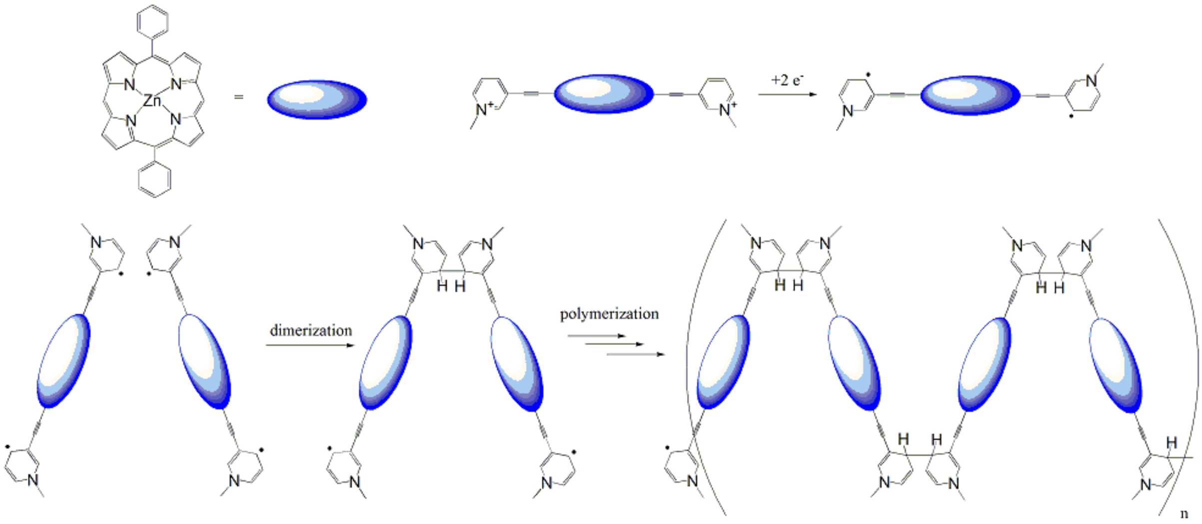

Figure 1.20. the mechanism of reductive electropolymerization of 10,20-bis-(Nmethyl-3-pyridylethynyl)-5,15-biphenylporphinato species.

2.2. Direct C-C couplings of porphyrins

Osuka and coworkers developed another strategy to prepare oligomers or polymers without spacers in between macrocycles, based on the direct coupling of porphyrin radical cations. The dimers and longer oligomers were obtained by electrolysis at a potential to form the π radical cation.[200] Under electrolyses, the metal center influence the link position *meso-meso* or *meso-β*. Magnesium and zinc 5,15-di-substituted porphyrin led to the corresponding *meso-meso* linked dimer, while for copper, palladium, nickel, and free base porphyrin, *meso-β* lined dimer could be formed.[201]

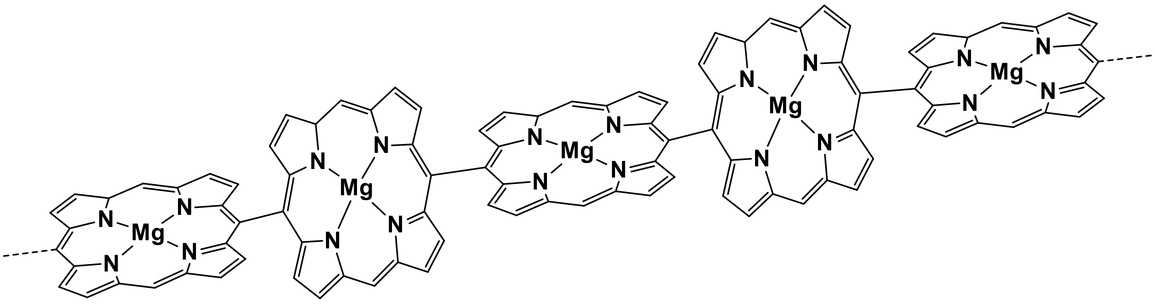

Figure 1.21. *meso-meso* linked polymer of magnesium porphin.

Lucas and coworkers tried to obtain such type of porphyrin polymers by using electrochemical method (Fig. 1.21).[202] The magnesium porphin was used as monomer to form long chains of porphin subunits through *meso-meso* bonds. The mechanism is the same than described by Osuka: porphyrin radical coupling at the applied potential corresponding to the first ring oxidation of porphyrin ring. UV-visible absorption spectra showed no shift of the initial porphin Soret band in solution, but decreases of the intensity of the band of the monomer was detected and was due to the deposition of porphin polymers at the electrode.

2.3. Using di-nucleophilic compounds as spacers

Instead of mono-nucleophilic compounds, some studies based on the compound with two accessible nucleophilic sites. After formation of one nucleophilic function to a porphyrin ring, the compounds can connect another macrocycle through the second site and form the dimers even oligomers.

An easy and well-designed strategy to obtain poly-porphyrins is based on the oxidation or reduction of electropolymerizable substituents attached to the porphyrin macrocycle. The porphyrin could be oxidized to π radical cation and dication, then oxidized porphyrin could react with nucleophilic groups or couple with each other. The deposition of the film of copolymer can be obtained by constant potential electrolysis, constant current electrolysis, or iterative cyclic voltammetry. The mechanism (Fig. 1.22) could be described as followed:[203, 204]

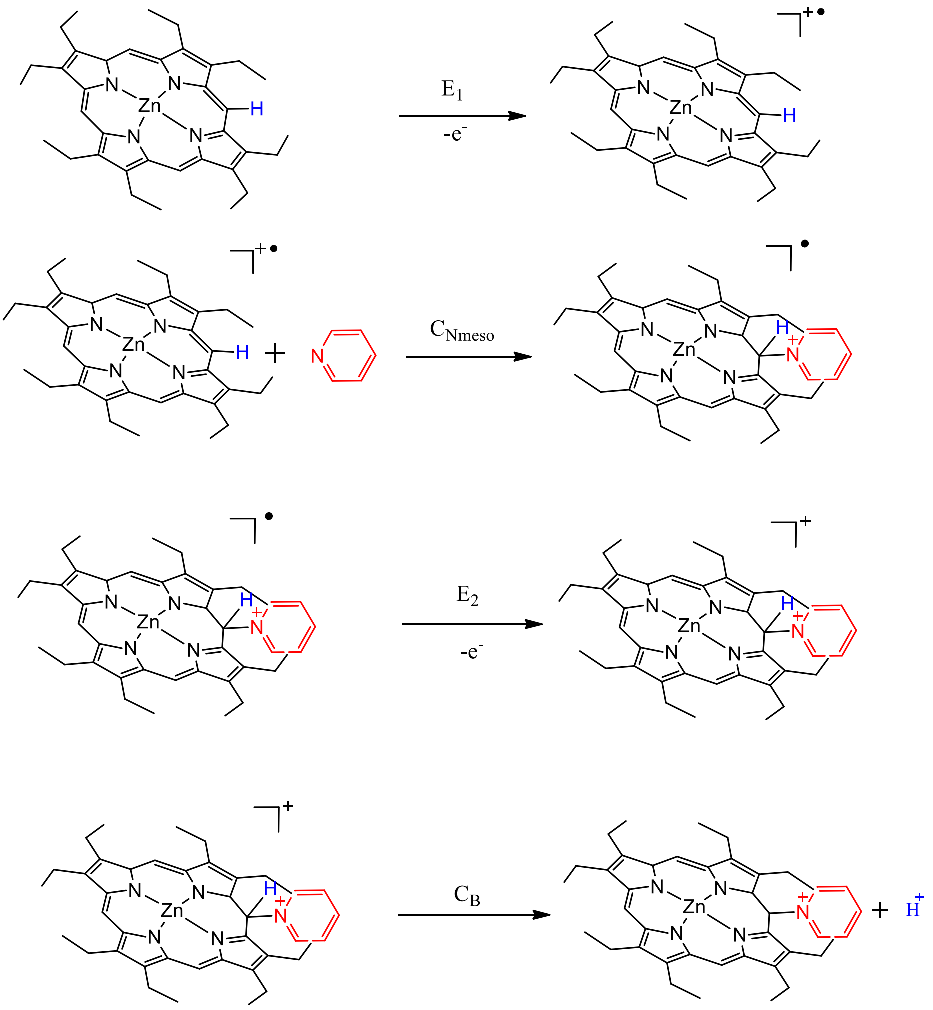

Figure 1.22. ECEC mechanism of pyridine nucleophilic attack to a *meso*-position of ring oxidized ZnOEP.

First, the electrogenerated porphyrin radical cation ($ZnOEP^{\bullet+}$, electrochemical step E_1) can be attacked by a nucleophile (abbreviated Nu) (chemical step C_{Nmeso}) at *meso*-carbon position to yield an isoporphyrin. The isoporphyrin is then oxidized (electrochemical step E_2) and the hydrogen atom present at that *meso*-carbon is removed as proton (chemical step C_B) to give the mono-substituted $ZnOEP(Nu)^+$ where Nu can be the pyridine.

2.3.1 Using mono-substituted porphyrins

Giraudeau has reported the possibility to obtain a polymer from the mono-substituted ZnOEP(bpy)$^+$ species under iterative scanning by cyclic voltammetry.[205] The potential needs to be enough high to form the porphyrin dication. During the electropolymerization, the current increased meaning the formation a conducting copolymer. The irreversible oxidation wave observed is due to the occurrence of a chemical reaction after the oxidation of the porphyrin ring. The two new reduction waves detected in the 0.00 to -0.65 V/SCE range is due to the reduction of viologen spacers formed in between the macrocycles (Fig. 1.23). As porphyrins have several free *meso*-carbons, the ‘zig-zag’ polymers could be formed and eventually hyper-branched polymers. To prepare linear polymers, ZnOEP with two protecting groups as chlorides or pyridinium at 5,15-positions could be used (Fig. 1.24).

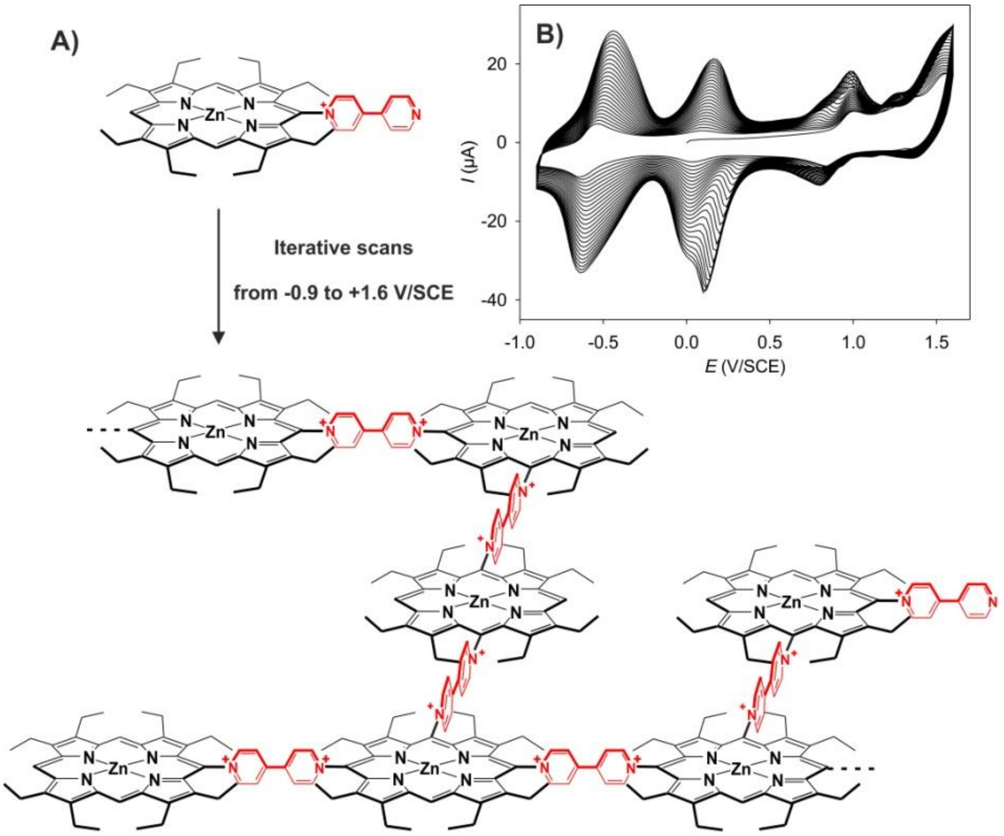

Figure 1.23. A) Electropolymerization process of the mono-substituted ZnOEP(bpy$^+$) macrocycle B) Cyclic voltammograms recorded during the iterative scans between –0.9 and +1.6 V/SCE from a solution of ZnOEP(bpy$^+$) in 1,2-$C_2H_4Cl_2$ (working electrode: ITO; scan rate: 200 mV s^{-1}).[205]

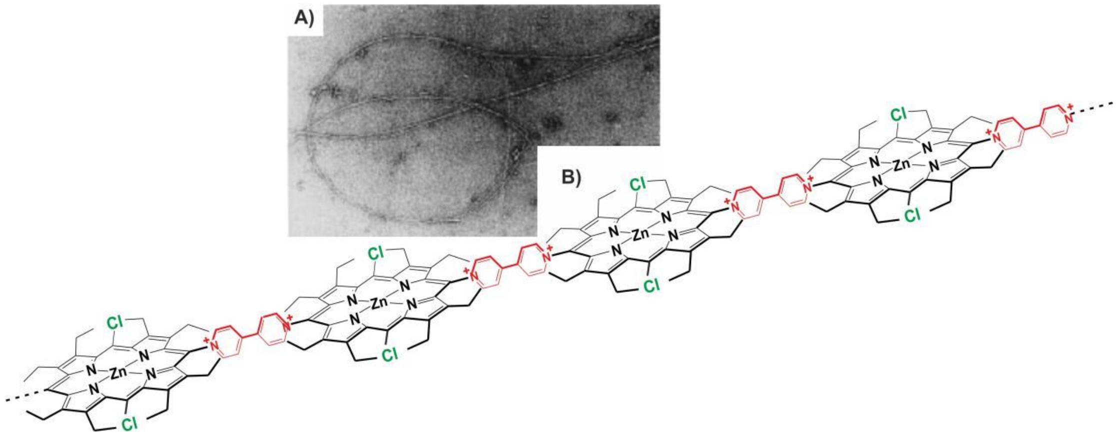

Figure 1.24. A) TEM image of a linear fiber obtained by electropolymerization of ZnOEP(Cl)$_2$(bpy$^+$), B) Scheme of a linear polymer obtained from ZnOEP(Cl)$_2$(bpy$^+$).[205]

In order to decrease the size of the spacers connecting the macrocycles and the distance between porphyrins, Ruhlmann et coworkers[200,206] prepared porphyrin oligomers by using di-, tri- or tetra-pyridyl porphyrins as Lewis bases giving after electrooxidation pyridinium spacers instead of viologen spacers. The pyridyl-substituted porphyrins can act as a nucleophile and then react with ZnOEP radical cation. The different numbers of pyridyl group of substituted porphyrin could form dimer, trimer and tetramers.

Gust and coworkers have obtained porphyrin copolymers by electropolymerization of porphyrin substituted by an aniline group (Fig. 1.25).[207] The proposed mechanism was a classical aniline polymerization with the radical on porphyrin macrocycle. Moreover, under the experimental conditions, the porphyrin macrocycle could also be oxidized during the iterative scans, with a similar reactivity described by Ruhlmann, Giraudeau and co-workers, which could be a nucleophilic substitution onto the oxidized porphyrin macrocycle.

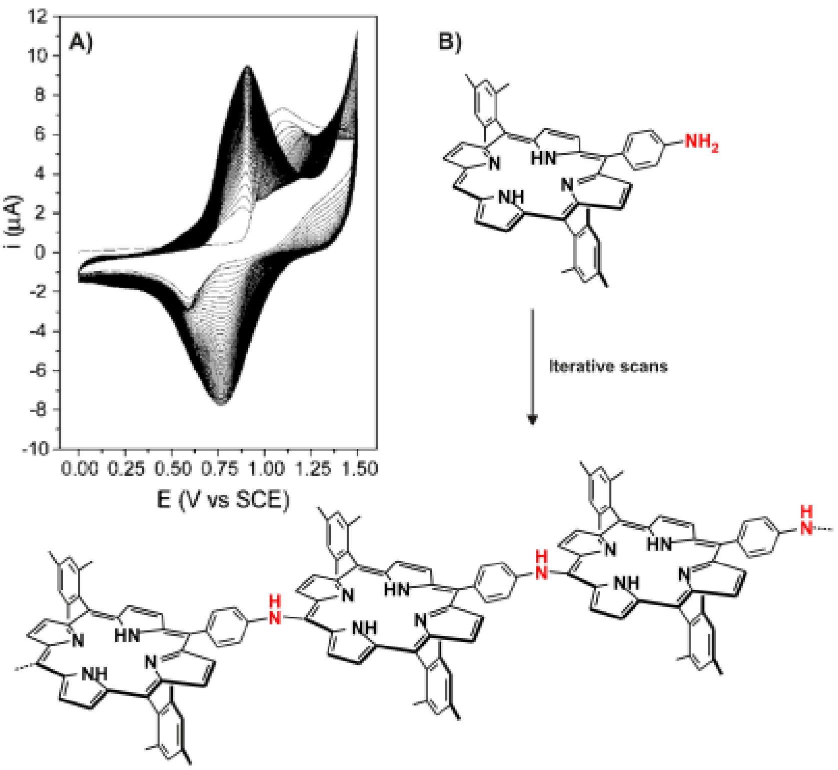

Figure 1.25. (**A**) Cyclic voltammograms recorded during the iterative scans between 0.0 and +1.5 V vs.SCE. Solution: 5-(4-aminophenyl)-10,20-bis(2,4,6-trimethylphenyl)porphyrin in acetonitrile. Working electrode: Pt. (**B**) Electropolymerization scheme of the corresponding polymer.[207]

2.3.2 Using non-functionalized porphyrins

Giraudeau, Ruhlmann and coworkers prepared porphyrin dimer, trimers, tetramer and pentamer in the presence of ZnOEP and 4,4'-dipyridine (bpy) as nucleophile under controlled potential with around 70% yield.[208-210] Ruhlmann and coworkers[211] proposed an easy polymerization of porphyrins process using ZnOEP and free 4,4'-bipyridine by iterative cyclic voltammetry scans. The free base porphyrin H_2OEP and metalloporphyrins MOEP (Zn(II), Co(II), Mg(II), Ni(II), Ru(II)(CO) all been successfully used. Furthermore, various type of nucleophile having two pendant pyridyl groups could be uses with success, such as 1,2-bis(4-pyridyl)ethane, trans-1,2-bis(4-pyridyl)ethylene, 4,4′-azopyridine, 3,6-bis(4-pyridyl)-s-tetrazine, and 1,1″- (1,3-propanediyl)bis-4,4′-bipyridinium.[211]

Since phosphanes could be used to perform electrochemical grafting, Giraudeau and Ruhlmann prepared porphyrin dimers and trimers with phosphonium bridges connected at the β-positions of the ZnTPP macrocycle (Fig. 1.26). Di- and triphosphanes such as bis(diphenylphosphino)acetylene, bis(diphenylphosphino)alkyl, and 1,2-bis(diphenylphosphino)benzene were used as spacers to form porphyrin dimers and trimers.[212-214]

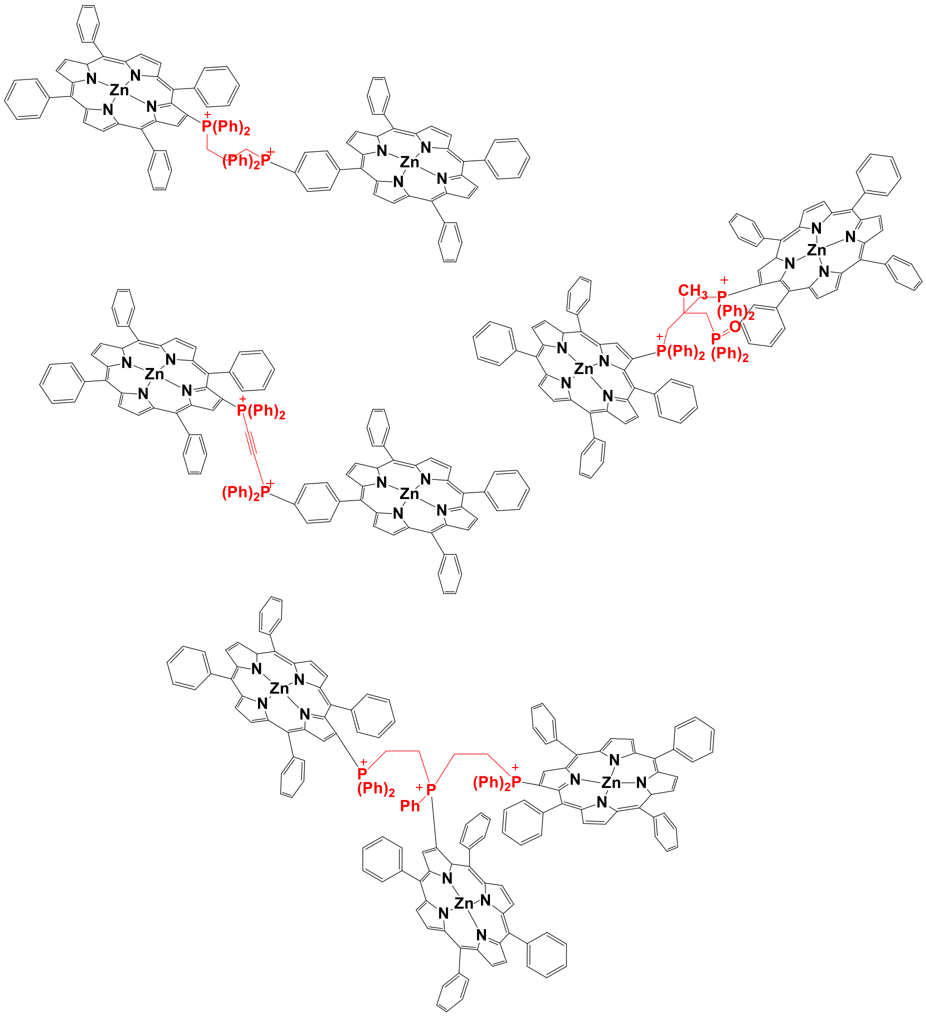

Figure 1.26. Example of porphyrin dimers and trimers with diphosphonium bridges.

3. Polyoxometalate

3.1. Structures and properties

3.1.1. Structure of polyoxometalates

Polyoxometalates (POM) are a large family of anionic polynuclear metal oxide molecular compounds containing arrays of corner- and edge-sharing pseudo-octahedrally coordinated [MO_6], and M is restricted to the group 5 and 6 metals with high-valence transition (e.g. Vanadium(V), Niobium(V), Tantalum(V), Molybdenum(VI), Tungsten(VI)). The POMs can be divided into two types: 1) isopolyanions (IPAs) involve only one type of metal atom, $[M_mO_y]^{q-}$, and 2) heteropolyanions (HPAs), involve the general formula $[X_rM_mO_y]^{q-}$, where X is the so-called heteroatom. Common structure include the Anderson, Lindqvist, Keggin, Wells-Dawson, Waugh, Silverton (Figure 1.27).[215]

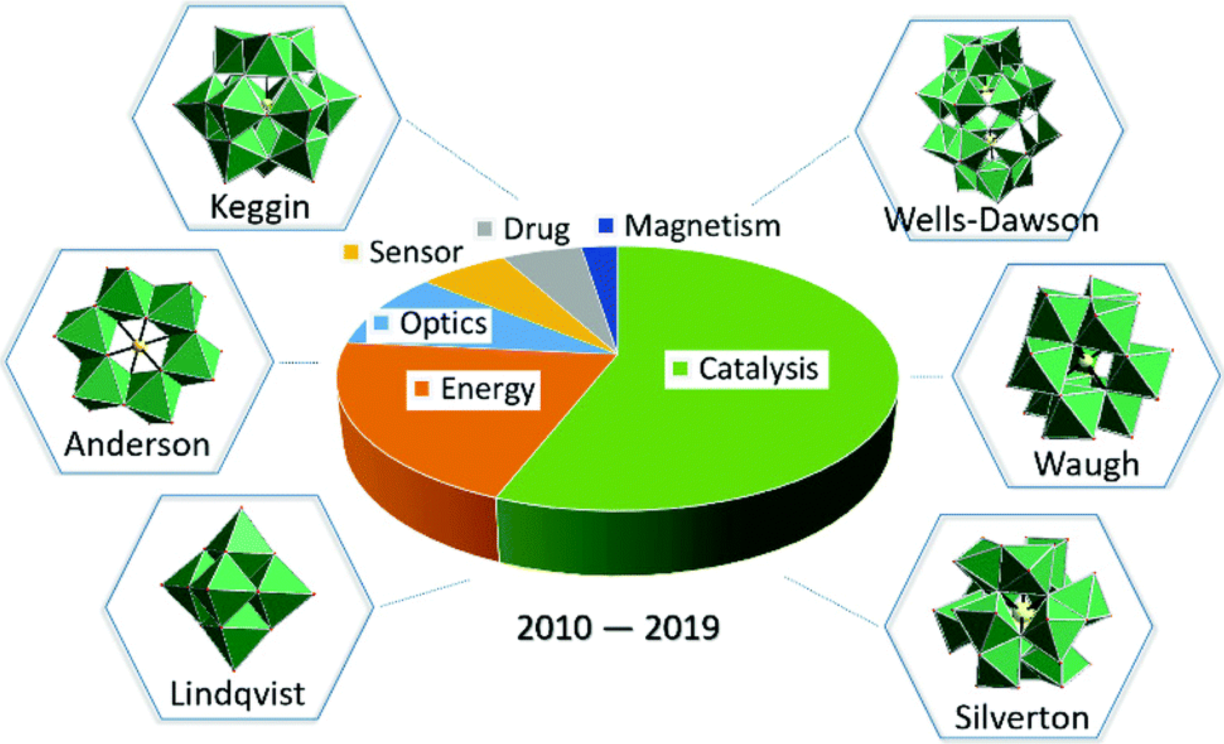

Figure 1.27. Typical structures of POMs and some reported applications in recent ten years.

POMs possess the great diversity of nuclearities, sizes and structures with properties of strong acidity, oxygen-riched surfaces, electron-accepting capability, chemical adjustability allowing multiple applications in several areas, such as catalysis,[216,217] bio- and nanotechnology,[218] medicine,[219,220] macromolecular crystallography,[221-223] electrochemistry,[224] material sciences[225] and molecular magnetism.[226]

3.1.2. Synthesis

The way to synthesis new POM clusters is often through a small number of steps, or even just one step (Fig. 1.28).[227] Upon acidification, for example, sodium molybdate solution would produce metal oxide fragments, and the nuclearity could increase with the decreased pH of the solution. So traditionally, the POM cluster will be formed in aqueous solution in the presence of simple metal cations; however, this approach can be extended to organic cations, and the solvent system can be extended to an aqueous/organic solvent mixture; for example, water/CH_3CN. The important parameters are exhibited below, in no particular order: 1) pH, 2) concentration/type of metal oxide anion, 3) ionic strength, 4) heteroatom type/concentration, 5) presence of additional ligands, 6) reducing agent, and 7) temperature of reaction and processing (e.g. microwave, hydrothermal, refluxing).

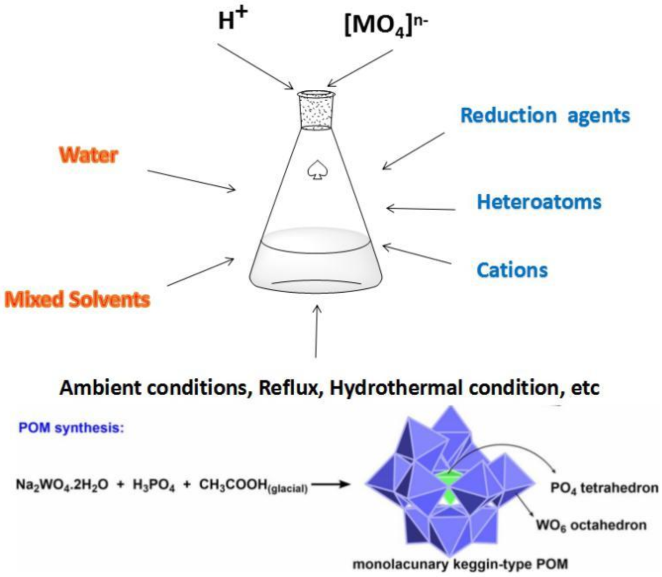

Figure 1.28. Parameters used in the one-pot synthesis/isolation of new POM clusters (up) and one example for synthesis of Keggin-type POM (below).[228]

3.1.3. Spectra of polyoxometalates

Polyoxometalates have characteristic absorption or vibration absorption between 190–400 nm for UV radiation due to M-O bonds[229] For Keggin type polyoxometalates, the UV spectrum presents intense absorption peaks corresponding to the ligand-to-metal charge-transfer (LMCT) between 185–195 nm corresponding to W = O_d bonds, 251–268 nm due to W-O-W bridge bonds, depending on heteroatom types (As, Sb, P, Co, etc.). The explanation of combination between Metal and Oxygen atom is shown in Figure 1.29.[230] The unsaturated cryptand ligand having Co^{2+} coordinated presents the most intense peak, due to the involvement of oxygen atoms from terminal W = O_d coordinative bonds with high electronic densities in coordination of W-O-Co bond. For the Keggin type polyoxometalate (POM) $H_3[PW_{12}O_{40}]$,[231,232] the ligand-to-metal charge-transfer (LMCT) transition band of PW is located around 260 nm. Similar observations for other Keggin type POM $[XM_{12}O_{40}]^{n-}$ have been reported.[228,233] Finally, in the case of the Wells–Dawson-type POM structure

$[X_2M_{18}O_{62}]^{n-}$, absorption bands are also due to ligand-to-metal charge-transfer (LMCT) transitions (O→W(VI) or O→V(V)).

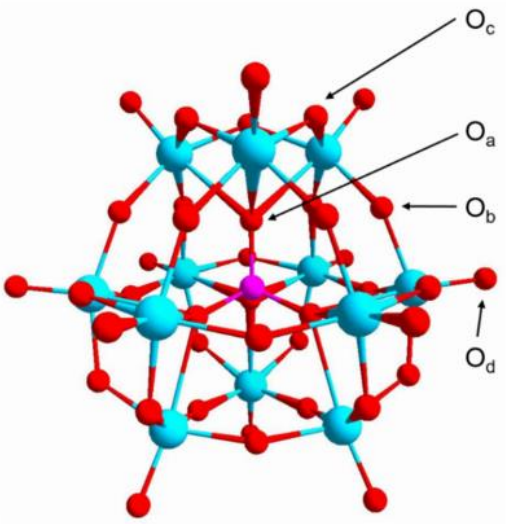

Figure 1.29. The structure of Keggin-type polyoxometalates (POMs), taking $PW_{12}O_{40}^{3-}$ as an example, identifying the four types of oxygen in the structure: the central oxygen atom (O_a); the bridging oxygen atom that bridges two tungsten atoms not sharing a central oxygen atom (corner-sharing, O_b); the bridging oxygen atom that bridges two tungsten atoms sharing a central oxygen atom (edge-sharing, O_c) and the terminal oxygen atom (O_d). P, pink ball; W, blue ball; O, red ball.

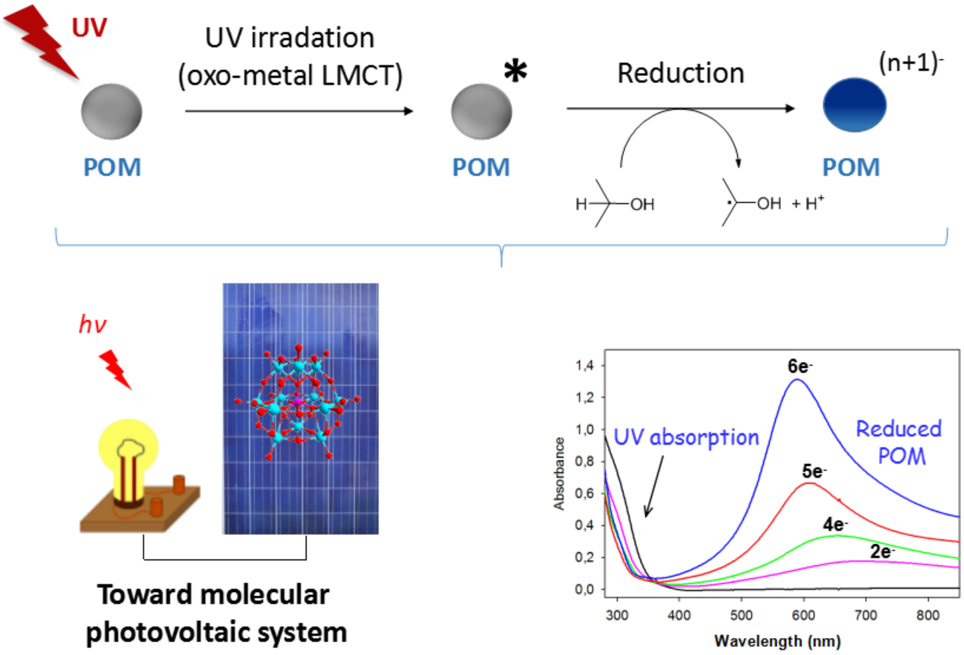

Figure 1.30. The redox processes for the excited POM and the optical spectrum of reduced Dawson POM ($[P_2W_{18}O_{62}]^{6-}$).

POM can be used for photocatalysis, which would be discussed in part 3.2. These redox processes are possible because POMs is primarily excited in the ultraviolet due to the ligand-to-metal charge-transfer (from oxygen to metal). The highly reactive excited state, is more reductive and oxidizing than the basic state. The excited state can be used to oxidize various organic substrates, such as alcohols, ethers, amides, aldehydes, ketones or carboxylic acids, as shown in Figure 1.30.[234] The reduction of the POM produce a new absorption band in the visible region (intervalence band due to the delocalization of the electron) which is the origin of the blue light characteristic of the reduced POMs. As shown in Figure 1.30, reduction of the Dawson type polyoxometalate ($[P_2W_{18}O_{62}]^{6-}$ (couples W(VI)W(V)) induced the UV-visible spectrum changed and the appearance of one additional absorption band near 600 nm (hypervalence band). The photoreduction can reduce six W(VI) to W(V) in the Dawson polyanion giving $[P_2W_{18}O_{62}]^{12-}$. The additional intervalence band is localized in the visible domain corresponding to the whole delocalization of the electron through the polyanion (O-W(VI)-O-W(V)-O ↔ -O-W(V)-O-W(VI)-O). Ruhlmann and coworker have shown that similar optical spectra was obtained by direct electrolysis and the exchange of 6 electrons. This characteristic enables them to be applied for the electronic storage.[235]

3.1.4. Redox behaviour of POM

Voltammetric studies of polyoxometalate polyanions present an extensive series of reduction processes.[236,237] For tetrabutylammonium salts of isostructural pairs of polyoxometalates ($[Bu_4N]_2[M_6O_{19}]$, $[Bu_4N]_4[R\text{-}SiM_{12}O_{40}]$, and $[Bu_4N]_4[R\text{-}S_2M_{18}O_{62}]$ (M) Mo or W)) in ionic liquids, the redox mechanisms have been described as below:[238]

$[M_6O_{19}]^{2-} + e^- \leftrightarrows [M_6O_{19}]^{3-}$ eq.1

$[M_6O_{19}]^{3-} + e^- \leftrightarrows [M_6O_{19}]^{4-}$ eq.2

$[\alpha\text{-}SiM_{12}O_{40}]^{4-} + e^- \leftrightarrows [\alpha\text{-}SiM_{12}O_{40}]^{5-}$ eq.3

$[\alpha\text{-}SiM_{12}O_{40}]^{5-} + e^- \leftrightarrows [\alpha\text{-}SiM_{12}O_{40}]^{6-}$ eq.4

The cyclic voltammogram of$[S_2M_{18}O_{62}]^{4-}$ with M= Mo or W showed several successive reductions. For instance, in the case of $[S_2W_{18}O_{62}]^{4-}$ six successive well-defined reversible one-electron-transfer processes were detected (eq.5-10) while $[S_2Mo_{18}O_{62}]^{4-}$ showed more complex electrochemical behavior of which the waves are not well-shaped after the second electron-transfer step.

$[S_2W_{18}O_{62}]^{4-} + e^- \rightleftharpoons [S_2W_{18}O_{62}]^{5-}$ eq.5

$[S_2W_{18}O_{62}]^{5-} + e^- \rightleftharpoons [S_2W_{18}O_{62}]^{6-}$ eq.6

$[S_2W_{18}O_{62}]^{6-} + e^- \rightleftharpoons [S_2W_{18}O_{62}]^{7-}$ eq.7

$[S_2W_{18}O_{62}]^{7-} + e^- \rightleftharpoons [S_2W_{18}O_{62}]^{8-}$ eq.8

$[S_2W_{18}O_{62}]^{8-} + e^- \rightleftharpoons [S_2W_{18}O_{62}]^{9-}$ eq.9

$[S_2W_{18}O_{62}]^{9-} + e^- \rightleftharpoons [S_2W_{18}O_{62}]^{10-}$ eq.10

Figure 1.31 shows the redox behaviour of Keggin and Dawson type POM measured in aqueous solution. As we can see, the Keggin type POM $[SiW_{12}O_{40}]^{4-}$ showed three well-shaped waves, the first two reversible single-electron processes a and b are due to eq.3 and eq. 4, the third two-electron step c depends on the pH ($[SiW_{12}O_{40}]^{6-} + 2e^- + 2H^+ \rightleftharpoons [H_2SiW_{12}O_{40}]^{6-}$).[239]

In the case of the Dawson type POM $[P_2W_{18}O_{62}]^{6-}$, four successive waves a, b, c, d have been observed and correspond to four successive reversible one-electron (similar to the eqs.7, 8, 9, and 10). Note that, in the presence case, all the processes are controlled-diffusion reaction because the peak currents *versus* the square root of the scan rate give always one linear representation. The nature of the solvent as well as the pH of the solution in the case of aqueous solution could influence the redox potentials measured.

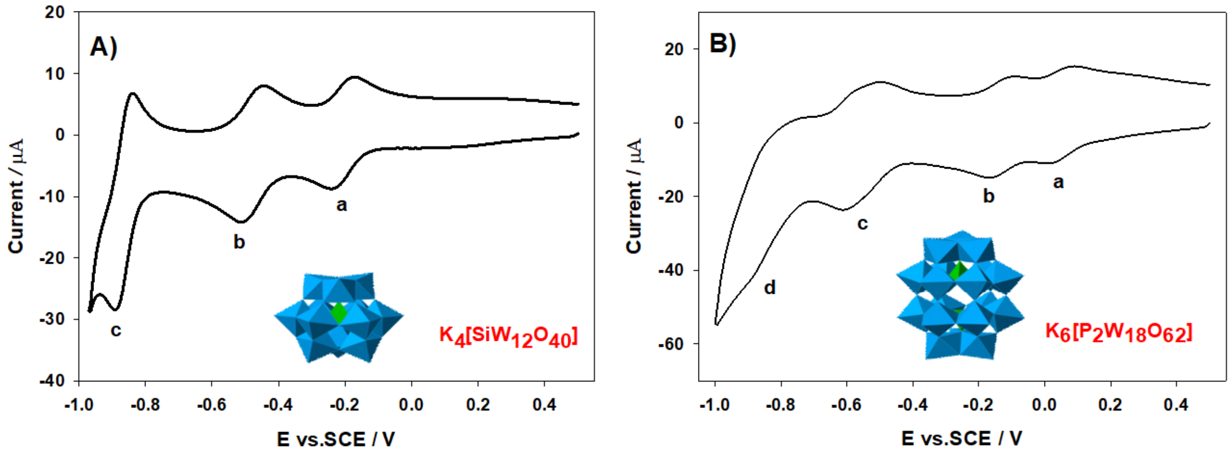

Figure 1.31. Cyclic voltammetry spectrum of A) 0.5 mM Keggin $K_4[SiW_{12}O_{40}]$ and B) 0.5 mM Dawson $K_6[P_2W_{18}O_{62}]$ in 0.5 M Na_2SO_4 (pH=3, adjusted with H_2SO_4) at scan rate 100 mV s^{-1}. *Note that the cyclic voltammetry have been measured during this thesis.*

For example, Keita et al found that the formal potential $E^{0'}$ for the reduction processes of α-$[SiW_{12}O_{40}]^{4-/5-}$ and α-$[P_2W_{18}O_{62}]^{6-/7-}$ depended strongly on the Lewis acidity of the solvent.[236a] The solvents with higher Lewis acidity make more positive potential due to solvent stabilization of the more highly charged reduced forms which are stronger Lewis bases than the corresponding oxidized form.[236c,237,240]

For the $[(P_2O_7)Mo_{18}O_{54}]^{4-}$ complex,[241] with the addition of a trace amount of H^+, one four-electron reduction wave was obtained in solvents of weaker basicity like acetone, acetonitrile and propylene carbonate (PC); the relative permittivity of the solvent did not affect the appearance of the four-electron wave. On the other hand, two two-electron waves were obtained in solvents of stronger basicity like *N*,*N*-dimethylformamide (DMF), *N*,*N*-dimethylacetamide (DMA), and *N*-methylpyrrolidinone (NMP).

3.2. Application

3.2.1. Photocatalysis

For excited POMs, the charge transfer from an oxygen atom to the transition metals will form a hole center and trapped electron center pair under light irradiation.[242] The band gaps between HOMO and LUMO orbitals of POM polyanion inhibit the recombination of electron and hole generated when the light energy is higher than or equal with the band gap energy. Thus, the photogenerated electrons and holes are capable of initiating the chemical reaction as electron donors and electron acceptors due to the strong photooxidative ability of the holes and photoreductive ability of the electrons.

The photooxidation properties are very useful for the degradation of various aqueous organic pollutants.[243-254] The resin-supported POM $[PW_{12}O_{40}]^{3-}$ thus obtained catalyzes the efficient degradation of rhodamine B in the presence of H_2O_2 under visible-light irradiation. Fluorescence lifetime measurements revealed the electron transfer from the visible-light-excited RB molecules to the POMs. The excited RB* promotes an electron to a higher energy level, and then the electron was transferred to the lowest unoccupied molecular orbital (LUMO) of the POM with reduced POM and $RB^{+\bullet}$ radical which could be proved from the redox potentials of the POMs which are more positive than that of the photoexcited RB. When H_2O_2 is used as an oxidant, it regenerates the resin-supported POMs more rapidly under acidic conditions forming the seven-coodinate W-O peroxo species via an inner-sphere mechanism. Moreover, the interaction between the active peroxo species •OOH and the $RB^{+\bullet}$ radicals causes the efficient degradation of the RB dye.

Furthermore, photocatalytic reactions cover the oxidation of alcohols,[255–257] of benzene,[258] and of phenol,[259] the oxidative bromination of arenes and alkenes,[260] the reduction of CO_2[261,262] in the presence of POMs. Li et al used, $H_3[PW_{12}O_{40}]$ as photocatalyst to reduce graphene oxide via a UV-irradiated photoreduction process. $[PW_{12}O_{40}]^{3-}$ can absorb on the reduced graphene oxide as anionic stabilizer which increase the water dispersible of graphene sheets.[263]

As the light absorption by POM anions generally only occurs in the region of 190−400 nm, some photosensitizers which could be triggered by visible light, can be covalently attached to POM anions.[264-274] Some cationic photosensitizers can be associated with POM anions via electrostatic interaction.[275-282] However, POM can be inserted covalently. Izzet and coworkers prepared Keggin and Dawson-type polyoxometalates (POMs) covalently grafted to heteroleptic cyclometalated iridium(III) complexes (POM–[Ir] dyads) under visible light irradiation for hydrogen evolution (Fig. 1.32).[266] Wu and coworkers designed a photoresponsive surfactant-encapsulated POM complexes with the surface of the POM electrostatically modified with cationic surfactants bearing azo groups at the hydrophobic ends.[276]

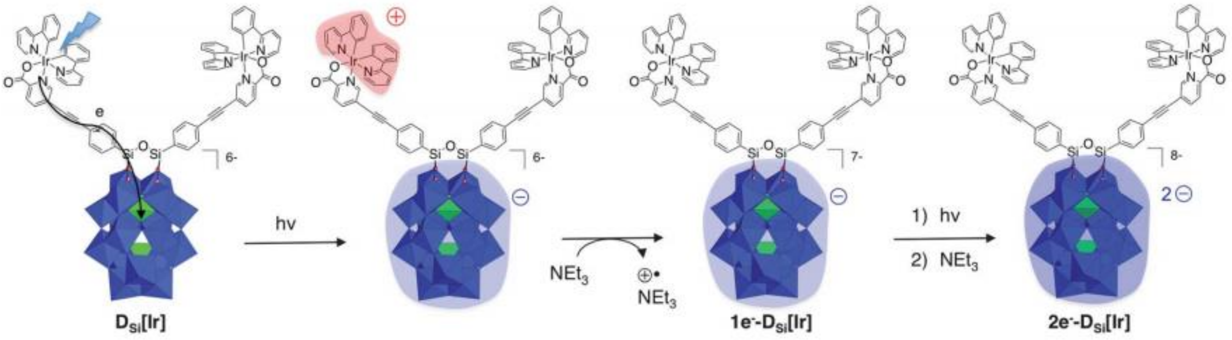

Figure 1.32. Charge photo-accumulation occurring in the DSi[Ir] dyad.

Parent POMs are usually supported on other materials for heterogeneous photocatalysts, such as TiO_2,[283–287] SiO_2,[288–292] ZrO_2,[293,294] etc. The substrate combined with POMs provides much larger specific surface areas increasing their catalytic activities by providing large contact areas between the catalysts and substrates for the surface-mediated electron-transfer reactions.

3.2.2. Electrocatalysis

Owing to the high oxidation states of M in peripheral metal−oxygen MO_x, POM anions have rapid one- and two-electron reversible reductions increasing the negative charge density at the POM anions and thus their basicity. In paragraph 3.1.4, we have discussed the influence of solvent, the reduction can be accompanied by protonation depending on the pK_a of the produced anions. In aqueous or organic solution, Keggin- and Dawson-type POMs/HPAs have been applied as reductive and oxidative electrocatalysts. The nickel substituted $(Ni_4[(P_8W_{48}O_{184})(WO_2)]^{28-}$, crown type polyoxometalate, was electrochemically polymerized with conducting polymer pyrrole for the electrocatalytic reduction of bromate in water. The immobilized films of different thickness were characterized by electrochemical and surface based techniques. The resulting films were found to be extremely stable towards redox switching between the various redox states associated with the incorporated POM.[295]

Moreover, POMs could be used for water oxidation electrocatalysis. Non-functionalized POMs are not suitable for water oxidation because the redox potential of the high-valent central metals (Mo(VI), W(VI), V(V)) is not sufficient for electron abstraction from water or oxo ligands. So functionalization of the cluster shell with suitable reaction sites,[296,297] mainly transition metals, such as Ruthenium,[298-301] Cobalt,[302,303] Nickel,[304] or Manganese,[305,306] are used.

POMs were also used as catalyst for the reduction of carbon dioxide,[307-309] nitrite,[310-313] bromate,[310,314] and hydrogen peroxide.[310,314] Ying and coworkers prepared a series of Keggin- and Wells-Dawson polyoxometalate-based compounds constructed from oxygen-functional imidazole derivatives, and all four compounds exhibited good electrocatalytic activities for the reduction of nitrite, bromate, and hydrogen peroxide (Fig. 1.33). With the addition of KNO_2, potassium bromate, or hydrogen peroxide, the current of the three reduction successive waves of POM increase remarkably with the decrease of corresponding oxidation peak currents.[314]

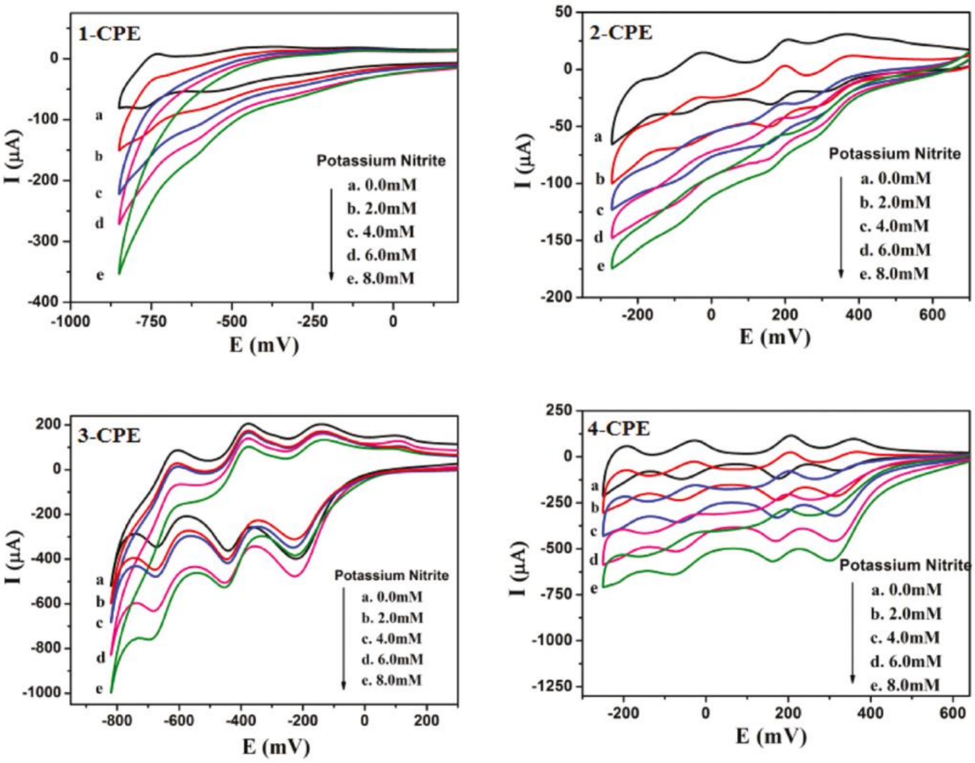

Figure 1.33. Cyclic voltammograms of reduction of nitrite by electrocatalysis with POM. The solution contains 0.1 M H_2SO_4 + 0.5 M Na_2SO_4. Scan rate: 60 mV s^{-1}.[314]

4. Polyoxometalate (POM)-photosensitizer hybrids

4.1. Different types of ligand

Photosensitizer can be covalently attached to POM anions giving robust hybrid systems. However, some cationic photosensitizers can be associated with POM anions via electrostatic interactions. A substantial amount of POM-based hybrids assembled from versatile organic ligands have been reported in recent years, such as pyridine derivatives,[315,316] imidazole derivatives,[317,318] triazole derivatives,[319,320] tetrazole derivatives,[321,322] pyridyl-tetrazole derivatives,[323] poly(carboxylic acid)s,[324,325] pyridine carboxylate derivatives,[326,327] imidazole carboxylate derivatives,[328,329] and so on, which could be used directly in the construction of the target POM-based hybrids.

Bond et coworkers published a series of $[Ru^{II}L_n]^{+/2+}$ cations [L_n = $(bpy)_3$, $(bpy)_2(Im)_2$, $(bpy)_2(dpq)$, $(bpy)_2(box)$ and $(biq)_2(box)$] which could be associated with Dawson POM anion α-$[S_2M_{18}O_{62}]^{4-}$ (M = Mo, W) via electrostatic interactions which increase the quantum yield for photo-reduction in the visible spectral region.[330] Du and coworkers published the cobalt tetraaminophthalocyanine

(CoTAPc) and Dawson-type POM (P_2M_{18} M=Mo or W) hybrid compound fabricated through the layer-by-layer (LbL) assembly relying on electrostatic absorption of oppositely charged species method.[331,332] Such non-covalent assembly between POMs and cation complexes have been developed and published recently.[333-339]

For covalently linked POM–photosensitizer, the tris-alkoxylation of POM precursors by triol-functionalized organic molecules has been used a lot.[340] For example, TRIS (TRIS: tris(hydroxymethyl)-aminomethane) or its derivates (diol-amide pendand group), can be used for the organo-functionalization of Anderson,[341,342] Lindqvist[343] or Dawson[344-346] type POMs (Fig. 1.34). For the TRIS-functionalized Anderson POMs, the [MO_6] unit is capped by two TRIS moieties located on opposite sides of the cluster, then the terminal amine can work as anchoring point for further linkage using Schiff base or amide chemistry.[341]

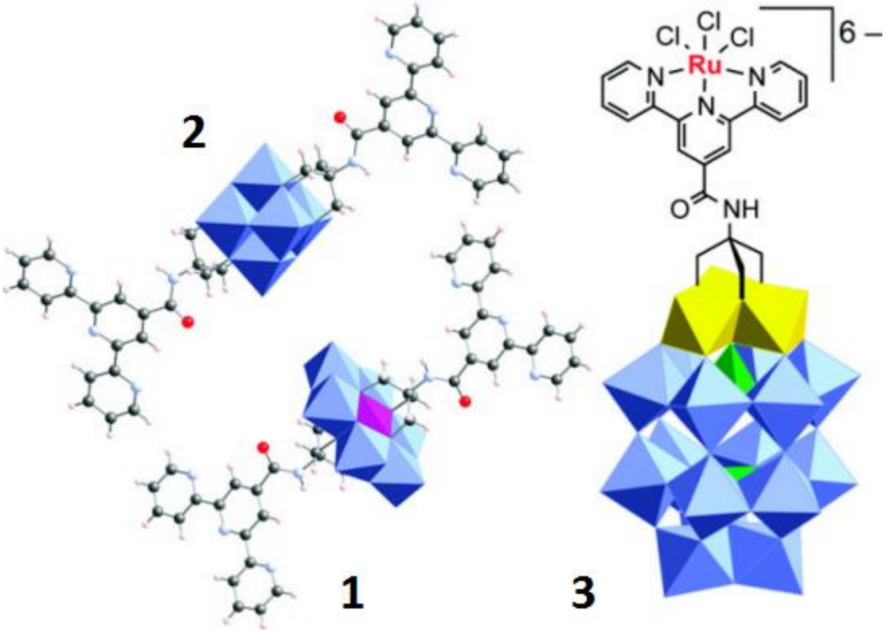

Figure 1.34. The trialkoxo polyoxometalates (Anderson (1), Lindqvist (2), Dawson (3)) grafted with remote terpyridine coordination.[346]

Covalent compounds have been prepared out by Proust and coworkers with Keggin and Dawson type polyoxotungstates functionalized by organosilane with ruthenium and iridium photosensitizers and demonstrated their improved charge separation and electron transfer (Fig. 1.35). These kinds of photosensitizers have been used a lot to form hybrid organic-inorganic compounds with POM.[271-275] Hanan and Hasenknopf introduced an alternative approach in which polypyridyl ligands equipped with a triol anchor group were used to synthesize POMs with pending ligands for transition metal ion complexation.[347] More recently, Hasenknopf, Lacôte, Thorimbert et al have developed new route to prepare bis-alkoxo-amide tripodal functionalization of a Dawson phosphovanadotungstate.[348]

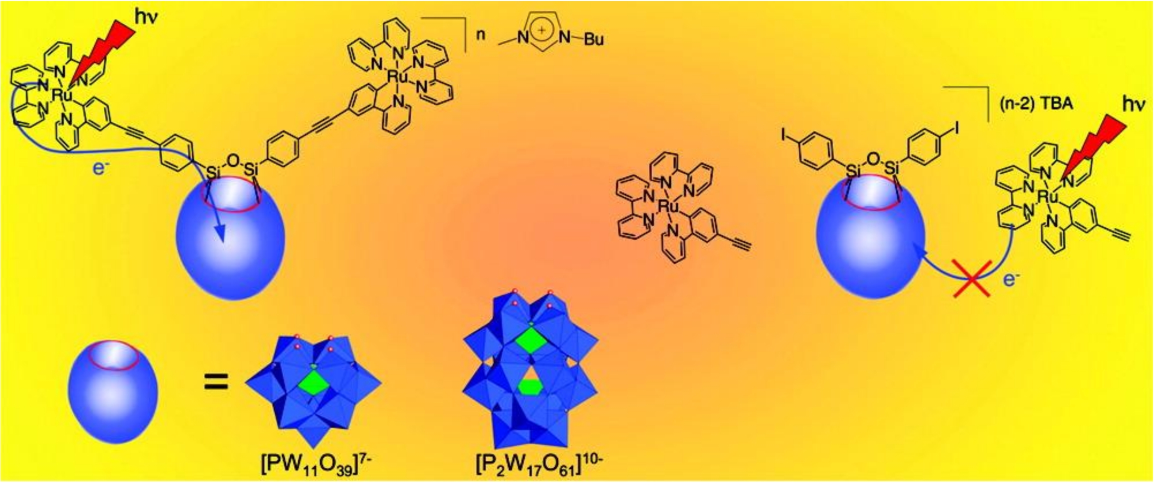

Figure 1.35. Silyl POM−ruthenium Hybrid and electron transfer process.

4.2. Hybrid Porphyrin – polyoxometalates systems

Porphyrins are attractive components due to their appealing chemical and photochemical properties. So porphyrin with intense visible absorption bands and long-lived excited states makes it as a good photosensitizer connected with POMs.

4.2.1. Electrostatic systems

The hybrid POM-porphyrin(s) complexes and films could be formed through electrostatic interactions for catalysis or electrocatalytic reductions.[349-360]

4.2.1.1. Electrostatic complexes

Ruhlmann, et al reported a series of porphyrin-POMs hybrid compounds via electrostatic interactions between a tetracationic porphyrin and an anionic Dawson type POM in aqueous solution. Illumination with only visible light induced the reduction of silver cations and the formation of stable silver nanoparticles.[352] A mixture of a cationic cobalt 5,10,15,20-tetrakis(1-methyl-4-pyridinio)porphyrin (CoPP) and an anionic metatungstate (POM) supported on graphite carbon was also developed for the oxygen reduction reaction (ORR) with high current density and low hydrogen peroxide production in a fuel cell.[356]

4.2.1.2. Electrostatic films

The layer-by-layer method has been also used to obtain POMs-chromophorses films, like POMs-phthalocyanines,[331,332] POMs-ruthenium complexes,[361,341] and POMs-porphyrins systems.[350,351,349,359,360] Ruhlmann and coworkers prepared multilayers films on ITO electrode. Films based on electrostatic interactions between tetracationic porphyrin and Dawson type polyoxometalate are formed by layer-by-layer method which showed significant photocurrent response. The absorption intensity increases with each deposition cycle on ITO substrate which means the film grows uniformly and homogeneously. For the photocurrent process, the POMs as a strong acceptor can accept one electron from the excited porphyrin, then the reduced form can transfer one electron to reduced I_3^-. POM assists to relay the electron via a downhill electrochemical cascade where the separated charges (oxidized π radical cation porphyrin and reduced POM) are far away which decrease the charge recombination and simultaneously enhance the photocurrent response (Fig. 1.36).[350]

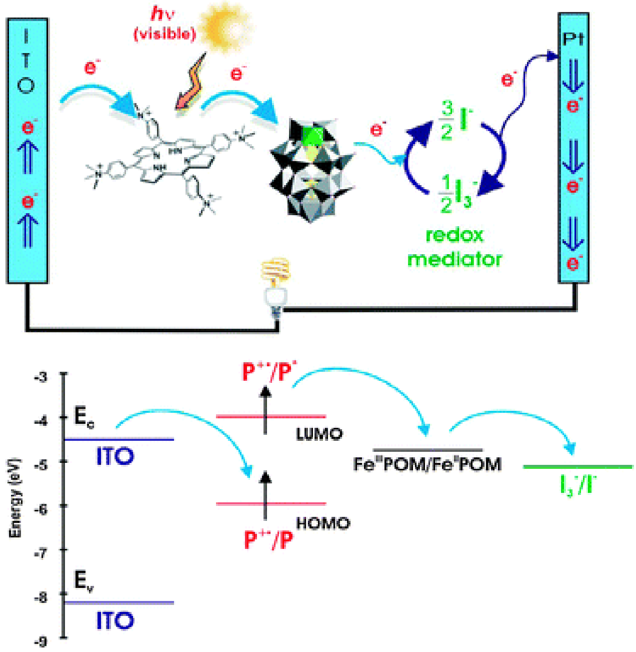

Figure 1.36. Schematic representation of the internal layer structure of [α_2-$Fe^{III}P_2W_{17}O_{61}^{7-}$ / $H_2TN(Me)_3PhP^{4+}$]$_n$ film on a ITO substrate in the photo-electrochemical cell and schematic diagram showing electron transfer processes.[350]

Using similar strategy, hybrid films composed of oppositely charged Keggin-type 12-molybdophosphoric acid $H_3[PMo_{12}O_{40}]$ (PMo_{12}) and water-soluble cationic *meso*-tetra (N-methyl-4-pyridyl) porphinetetratosylate (TMPyP) were prepared by Hao and coworkers onto silicon and ITO substrates, and the LbL films also displayed good electrocatalytic activities toward the reduction of BrO_3^- , IO_3^-, and $S_2O_8^{2-}$.[354]

4.2.2. Coordination systems

4.2.2.1. Coordination complexes

Coordination complexes can be tethered to POMs by grafting organic ligands onto the organometallic framework through a bridging μ-oxo ligand: the subclass of "decorated" POMs.[363] Kojima, Fukuzumi et al. have synthesized nanosized discrete hybrids combining POMs and metalloporphyrins as photoactive counterparts.[344,364] Two $[Mo(DPP)(O)]^+$ (H_2DPP = dodecaphenylporphyrin) units were coordinated to two terminal oxo groups of the Keggin-type POM (Fig. 1.37 left). This hybrid compound was obtained by mixing two precursors in organic media and vapour diffusion with hexanes. The hybrid $[Sn(TMPP(Ph)_8)(OMe)(\alpha\text{-}[PW_{12}O_{40}])]^{2-}$ was found by substitution of one sterically hindered and axial MeO^- ligand on the precursor $[Sn(TMPP(Ph)_8)(OMe)_2]$($TMPP(Ph)_8$=5,10,15,20-tetrakis(4-methoxyphenyl)-2,3,7,8,12,13,17,18-octaphenylporphyrinato) (Fig. 1.37 right).

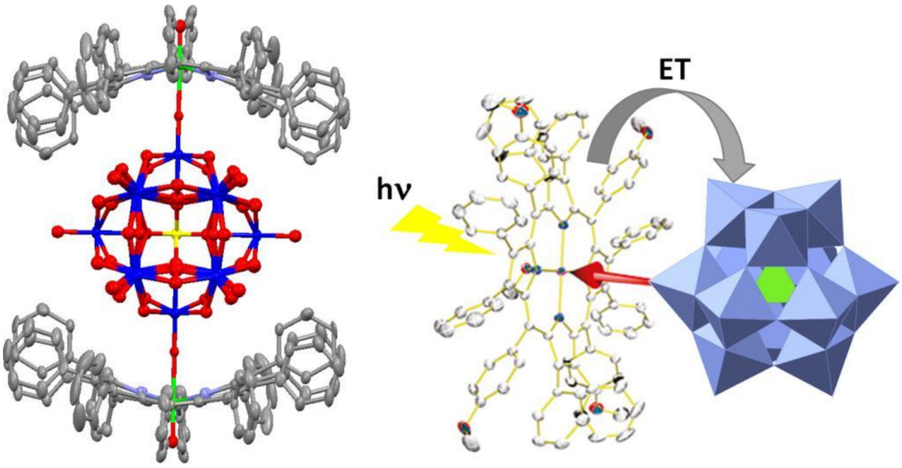

Figure 1.37. (Left) The "sandwich" hybrid $[\{Mo(DPP)(O)\}_2(H_2SiW_{12}O_{40})]$[364] (H atoms were omitted for clarity; O = red; C = grey; N = pale blue; W = blue; Mo = green; Si = yellow) (Right) a Charge-separated state in the Sn-phorphyrin-POM dyad[344] $[Sn(TMPP(Ph)_8)(OMe)(\alpha\text{-}[PW_{12}O_{40}])]^{2-}$ (H atoms were omitted for clarity, C = grey, N = blue, O = red, Sn = pink, W = pale blue, P = green)

Su and coworkers use this coordination strategy to form porphyrin–metal–polyoxometalate (por–metal–POM) sandwich structures $[(por)M(PW_{11}O_{39})]^{5-}$ (por = TPP, TPyP, $TPPF_{20}$, M = Hf; por =TPP, M = Zr) and $[(TPP)Hf(XW_{11}O_{36})]^{6-}$ (X = Si, Ge). The porphyrin ligand acts as an electron acceptor and the lacunary Keggin-type POM acts as an electron donor and these compounds possesses remarkably second-order nonlinear optical (NLO) properties.[366]

Hasenknopf and Ruhlmann prepared two Anderson-type polyoxometalates $[FeMo_6O_{18}\{(OCH_2)_3\text{-}CNHCO(4\text{-}C_5H_4N)\}_2]^{3-}$ and $[MnMo_6O_{18}\{(OCH_2)_3CNHCO(4\text{-}C_5H_4N)\}_2]^{3-}$ and two Lindqvist-type polyoxovanadates $[V_6O_{13}\{(OCH_2)_3CCH_2OC(O)(4\text{-}C_5H_4N)\}_2]^{2-}$ and $[V_6O_{13}\text{-}\{(OCH_2)_3CNHCO(4\text{-}C_5H_4N)\}_2]^{2-}$ with axial coordination to metalloporphyrins (ruthenium(II) and zinc(II) *meso*-tetraphenylporphyrins [Ru(CO)TPP] and [ZnTPP]) by pendant pyridyl groups (Fig. 1.38).[367]

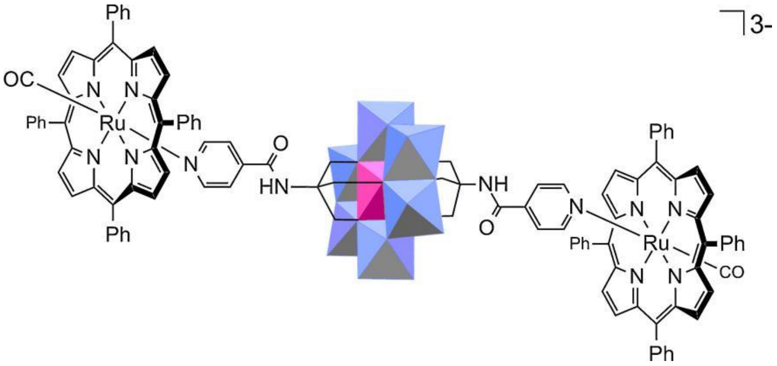

Figure 1.38. Structure of Anderson type POM and porphyrin coordinated by pendant pyridyl groups

4.2.3. Covalent systems

Covalent interaction between POMs and porphyrin as photosensitizer have been researched and published in recent years.[344,367-371] The anchor like silane, phosphonate, alkoxide, organotin and imine moieties have recently been reviewed.

4.2.3.1. Covalent complexes

Harriman et al proposed that the Dawson type POM functionalized with alkyne or azido groups could subsequent be attached to the porphyrin (Fig. 1.39). The connection has been made via a Huisgen reaction, which gives good yields in all cases, and modified to provide linkages that vary in their degree of internal flexibility.[367] The various anchorings ligands were chosen from flexible (phosphonic anchors) to semi-rigid (organosilyl anchors). The choice of anchoring group can affect the reduction potential of the POM by 0.5 V. Before reduction of the porphyrin occurs, two electrons can be added to the POM. For the rigid connection, the appended POM cannot be reduced by porphyrin π-radical anion and the reduced POM is a poor electron donor for the S_1 state localized on the porphyrin unit. For the flexible connection, the electron transfer was promoted from the reduced POM to the porphyrin S_1 for the flexibly linked system compared with rigid linkage.

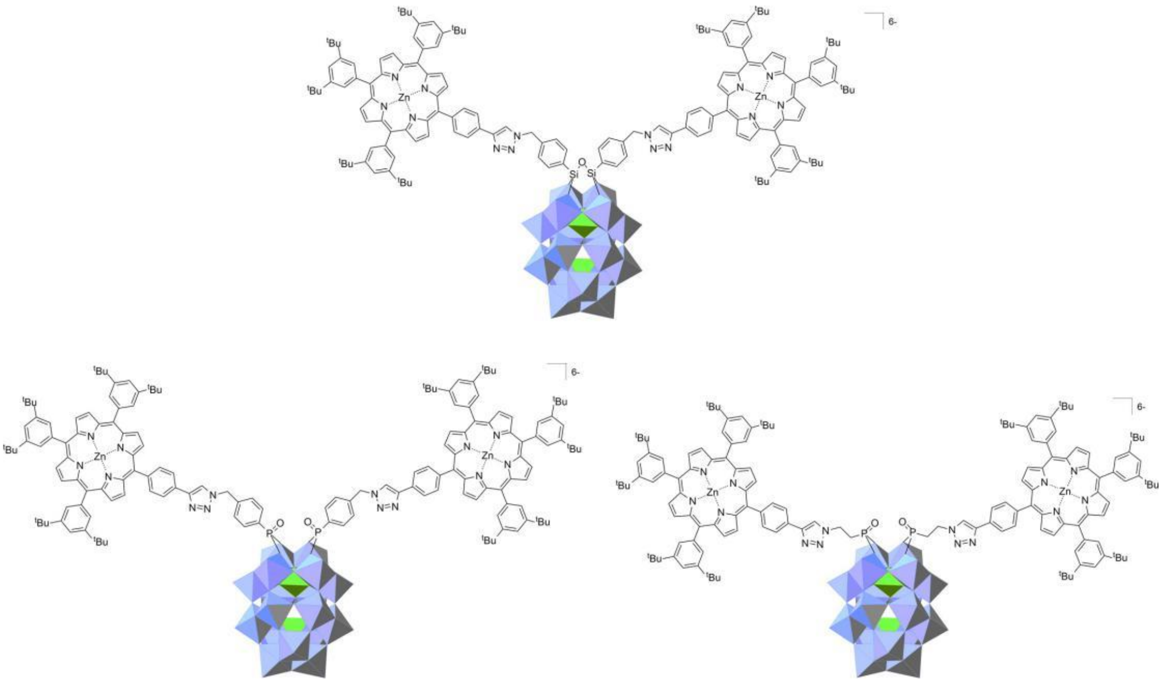

Figure 1.39. Formation of three porphyrin-POMs connected through Huisgen reaction.[367]

The same authors prepared a multi-porphyrin cluster covalently connected with POM.[368] The porphyrin cluster comprises three zinc(II) porphyrins (ZnP) covalently linked to a free-base porphyrin (FbP). The efficient energy transfer from the peripheral zinc porphyrins (ZnP) as photon collectors to the central free-base porphyrin (FbP) as energy reservoir. The porphyrin clusters were covalently attached POM with Huisgen reaction (Fig. 1.40). The charge recombination between ZnP and the POM could be inhibited by the oxidizing equivalent transferring from the FbP to the ZnP. POM can connect with two or even six zinc metalloporphyrins for charge accumulation at the POM (Figure.1.40). Efficient light collection is accompanied with photon migration to a redox-active site. Charge accumulation was detected under steady-state irradiation ($\lambda > 400$ nm) of Zn_3Fb in deoxygenated DMF containing water (20% v/v) and triethanolamine (TEOA) as a sacrificial electron donor. The reduced POM is accumulated in solution because TEOA reduces both FbP π-radical cation, and also ZnP π-radical cation, before the charge-recombination takes place.

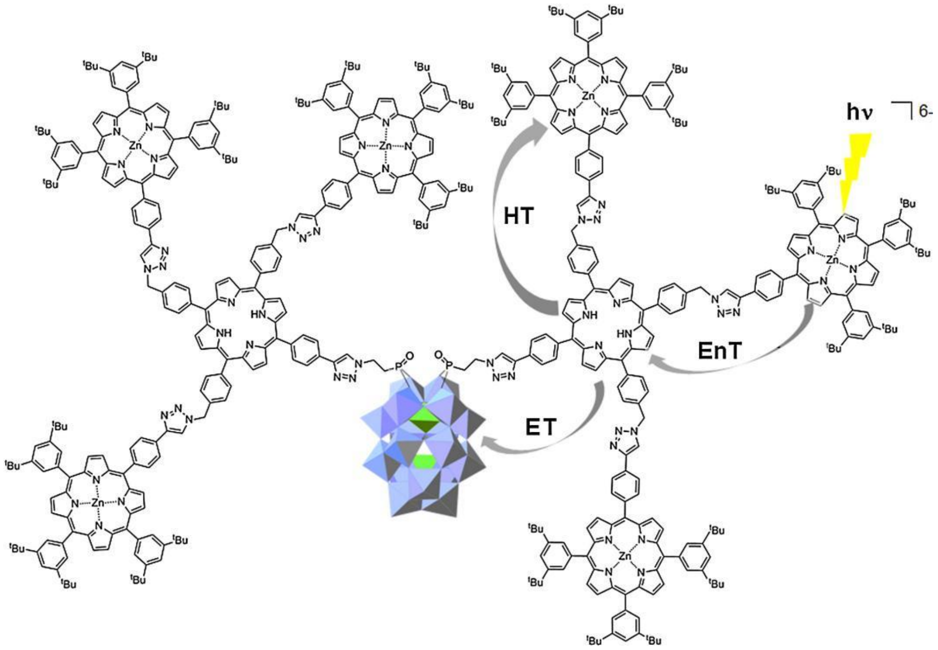

Figure 1.40. Schematic porphyrin-POM hybrid for photoaccumulation of charges. (EnT refers to energy transfer, ET to electron transfer and HT to hole transfer.)[368]

Ruhlmann, Hasenknopf et al prepared two covalently linked porphyrin–polyoxometalate hybrids: an Anderson-type hexamolybdate $[N(C_4H_9)_4]_3[MnMo_6O_{18}\{(OCH_2)_3CNHCO(ZnTPP)\}_2]$ with two pendant zinc(II)-tetraphenylporphyrins, and a Dawson-type vanadotungstate $[N(C_4H_9)_4]_5H[P_2V_3W_{15}O_{59}\{(OCH_2)_3CNHCO(ZnTPP)\}]$ with one porphyrin connected via a tris-alkoxo linker (Fig. 1.41). Photophysical results showed an electron transfer from the excited porphyrin to the Dawson polyoxometalate, but not to the Anderson polyoxometalate.[369]

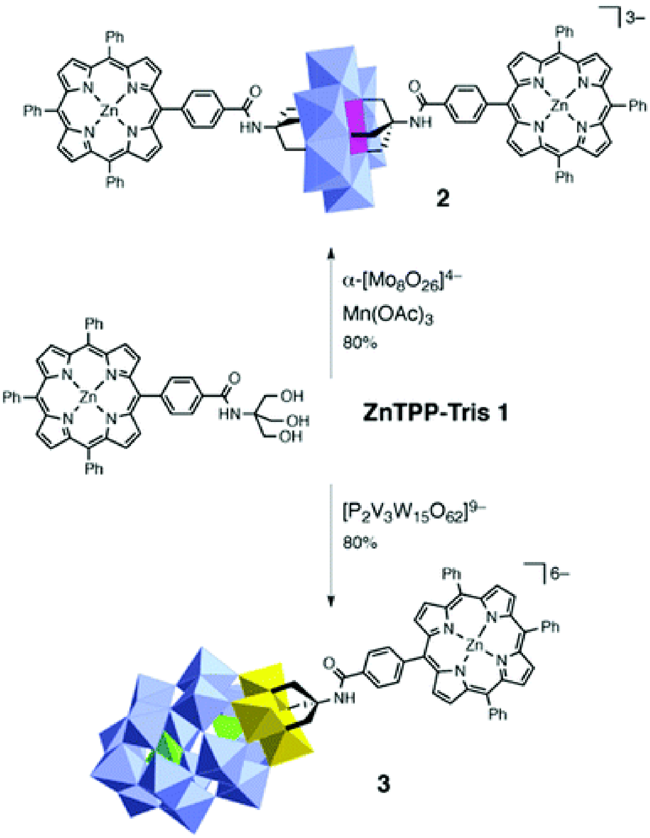

Figure 1.41. Synthesis of porphyrin-POMs hybrid compound via tris-alkoxo linker.[369]

4.2.3.2. Covalent copolymers

Porphyrin copolymers can be formed using electropolymerization method in the presence of nucleophiles such as dipyridyl ligand. Ruhlmann and Hasenknopf obtained hybrid polyoxometalate-porphyrin copolymeric films by the electro-oxidation of zinc octaethylporphyrin (ZnOEP) in the presence of a Dawson type polyoxometalate bearing two pyridyl groups ($POM(py)_2$) (Fig. 1.42).[344,372] A series of $POM(py)_2$ consisting of $[P_2W_{15}V_3O_{62}]^{9-}$ functionalized with diol-amide or triol moieties were synthesized, as well as the characterization of the copolymers were presented. The copolymer films relied on the electrocopolymerization of porphyrins with several bis-pyridine-capped phosphovanadotungstate $[P_2W_{15}V_3O_{62}]^{9-}$ on ITO electrode. The corresponding global reaction can be written as:

$(n+1)ZnOEP + (n+1)Py\text{-}R\text{-}Py \rightarrow ZnOEP\text{-}(Py^{+}\text{-}R\text{-}Py^{+}\text{-}ZnOEP)_n\text{-}Py^{+}\text{-}R\text{-}Py + (2n+1)H^{+} + (4n+2)e^{-}$ (R = spacer)

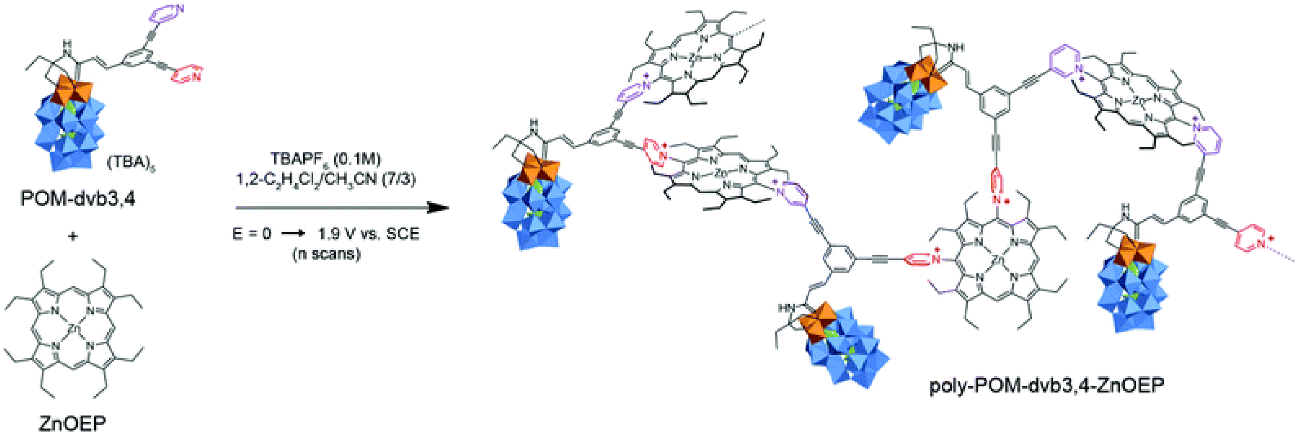

Figure 1.42. Copolymer obtained by iterative scans of POM-dvb3,4 and ZnOEP.

Ruhlmann et coworker also published the copolymer using lindqvist type POM (py-POM-py) with 5,15-ditolyl porphyrin (H_2T_2P) or zinc-β-octaethylporphyrin (ZnOEP) using the same method.[343] Other copolymers could be obtained by using Anderson-type polyoxometalate (POM) bearing two pyridyl groups (Py-POM-Py) with ZnOEP porphyrin. If ZnOEP was functionalized with two pyridinium protecting groups on 5,15 *meso* positions, named zinc 5,15-dipyridinium octaethylporphyrin ($5,15\text{-ZnOEP(py)}_2^{2+}$), the linear copolymer with (Py-POM-Py) were formed (Fig. 1.43).[342] Under ambient conditions, under visible illumination, $Ag^I_2SO_4$ was reduced at the interface between water and the copolymeric films deposited on quartz plates. First the photochemical excitation of the porphyrin units would lead to their oxidation and the simultaneous reduction of the POM units. Then, the reduced POM would be able, in turn, to transfer one electron to the Ag^+ cation to give Ag^0. The porphyrin would finally be reduced by propan-2-ol, used as a sacrificial electron donor.

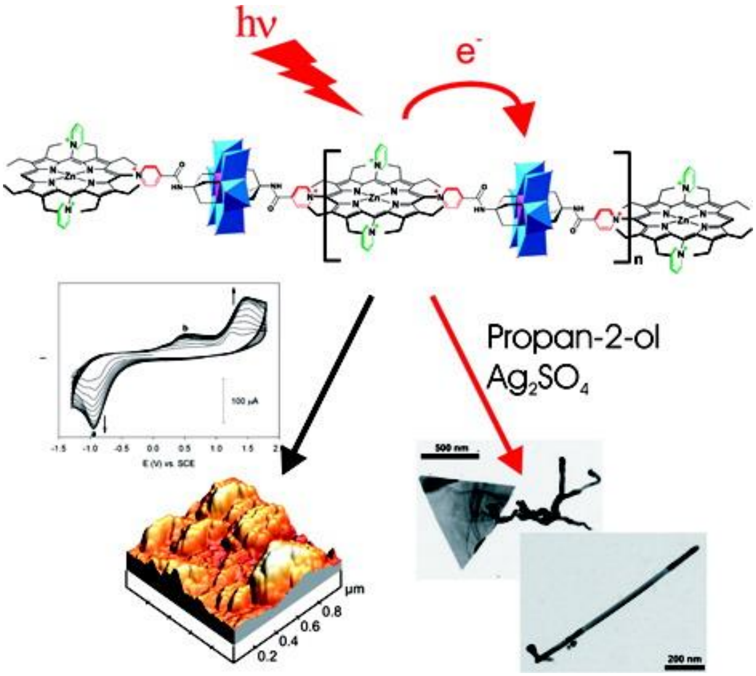

Figure 1.43. Cyclic voltammograms recorded during the electropolymerization of 5,15-ZnOEP(py)$_2^{2+}$ in the presence of Py-POM-Py in 1,2-$C_2H_4Cl_2$/CH_3CN (7:3) $(NBu_4)PF_6$ 0.1 mol L^{-1}. Below are shown the atomic force micrograph image, and TEM images of individual silver triangular nanosheets and individual silver nanowires.

The porphyrin possesses good electrochemical and photochemical properties. The porphyrin copolymers could be obtained by using ligands such as dipyridyl and compound modified with pyridyl groups to form the covalent connections. The ligands react as nucleophile which could attack the meso position of oxidized porphyrin to form dimer, trimer, oligomer and polymer by ECEC process. The work in next chapter focus on the formation of porphyrin/isoporphyrin copolymers with various dipyridyl ligands by electropolymerization under different upper potentials. The mechanism of redox processes has been discussed a lot and explained the difference observed in the optical spectrum and photocurrent measurements between porphyrin and isoporphyrin copolymers.

References

1. L. R. Milgrom, The Colors of Life. Oxford University Press: Oxford, **1997**.

2. R. Bonnett, In the porphyrins; D. Dolphin, Ed.; Academic Press: New York, **1978**; Vol. 1, p 1-27.

3. J. W. Buchler, In the porphyrins; D. Dolphin, Ed.; Academic Press: New York, **1978**; Vol. 1, p 389-483.

4. L. Milgrom, Oxford University Press: New York, NY, USA, **1997**, pp. 66–99, ISBN1 0198553803, ISBN2 9780198553809.

5. R. Geier, Available online: http://www.colgate.edu/facultysearch/facultydirectory/ggeier.

6. I. J. MacDonald, J. Dougherty, *J. Porphyrins. Phthalocyanines* **2001**, 5, 105–129.

7. M. Dixon, E. C. Webb, Enzymes; 3re ed.; Longman: London, **1979**.

8. L. Stryer, Biochemistry; 4th ed.; W.H. Freeman: New York, **1995**.

9. R. B. Woodward, *Pure Appl. Chem.* **1961**, 2, 383-404.

10. R. B. Woodward, *Ind. Chim. Belge*, **1962**, 27, 1293-1308.

11. W. R. Fawcett, M. Fedurco, K. M. Smith, H. Xie, *J. Electroanal. Chem*., **1993**, 354, 281-287.

12. K. M. Kadish, R. K. Rhodes, *Inorg. Chem*., **1981**, 20, 2961-2966.

13. K. M. Kadish, E. V, Caemelbecke, G. Royal, in The Porphyrin Handbook (Eds.: K. M. Kadish, K. M. Smith, R. Guilard), Elsevier, San Diego, CA, **2003**, 8, 1.

14. D. Dolphin, R. H. Felton, D. C. Borg, J. Fajer, *J. Am. Chem. Soc*., **1970**, 92, 743-745.

15. H. Xie, S. H. Leung, K. M. Smith, **2002**, 06, 607–616.

16. S. C. Mwakwari, H. Wang, T. J. Jensen, M. G. H. Vicente, K. M. Smith, *J. Porphyrins Phthalocyanines,* **2011**, 15, 918–929.

17. A. Ehudin, L. Senft, A. Franke, I. Ivanovic-Burmazovic, D. Karlin, *J. Am. Chem. Soc.* **2019**, 141, 10632−10643.

18. P. Schweyen, M. Hoffmann, J. Krumsieck, B. Wolfram, X. Xie, M. Bröring, *Angew.Chem.Int. Ed*. **2016**, 55, 10118–10121.

19. J. A. Guzinski, R. H. Felton, *J. Chem. Sot*., *Chem Commurr.* **1973**, 715–716.

20. K. M. Kadish, R. K. Rhodes, *Inorg. Chem.* **1981**, 20, 1274–1277.

21. A. S. Hinman, B. J. Pavelich, A. E. Kondo, *J. Electroanal.* Chem. **1987**, 234, 145–162.

22. A. Harriman, G. Porter, P. Walters, *J. Chem. Soc., Faraday Trans. 1,* **1983**, 79, 1335–1350.

23. S. Mosseri, J. C. Mialocq, B. Perly, P. Hambright. *J. Phys. Chem.* **1991**, 95, 2196–2203.

24. M. C. Richoux, P. Neta, P. A. Christensen, A. Harriman, *J. Chem. Soc., Faraday Trans. 2,* **1986**, 82, 235–249.

25. W. Szulbinski, J. W. Strojek. *J. Electroanal. Chem.* **1988**, 252, 323–334.

26. D. Dolphin, Z. Muljiani, K. Rousseau, D. C. Borg, J. Fajer. R. H. Felton, *Ann. N .Y.* Acad. *Sci.,* **1973**, 206, 177–200.

27. T. P. Wijesekera, D. Dolphin, Some Preparations and Properties of Porphyrins, Springer: Boston, MA, USA, **1985**, 229–266, ISBN 978-1-4612-9276-0.

28. M. Gouterman, In the Porphyrins; D. Dolphin, D., Ed.; Academic Press: New York, **1978**, 3, 1–165.

29．G. D. Dorough, F. M. Huennekens. *J. Am. Chem. Soc*. **1952**, 74, 3974–3976.

30．(a) J. Bhuyan, S. Sarker, *Chem. Eur. J.*, **2010**, 16, 10649–10652. (b) J. Bhuyan, *Dalton Trans*., **2016**, 45, 2694-2699. (c) K. D. Borah, J. Bhuyan, *J. Coord. Chem*, **2019**, 72, 2251–2260.

31．J. Bhuyan, *Dalton Trans*., **2015**, 44, 15742–15756.

32．M. Liao, S. Scheiner, *J. Chem. Phys*., **2002**, 117, 205–219.

33．A. Irfan, N. Hina, A. G. Al-Sehemi, A. M. Asiri, *J. Mol. Model*, **2012**,18, 4199–4207.

34．M. Gouterman, *J. Mol. Spectrosc*. **1961**, 6, 138–63.

35．M. Gouterman, G. Wagniere, L. C. Synder, *J. Mol. Spectrosc*. **1963**, 11, 108–27.

36．C. Weiss, H. Kobayashi, M. Gouterman, *J. Mol. Spectrosc*. **1965**, 16, 415–50.

37．G. D. Dorough, J. R. Miller, F. M. Huennekens, *J. Am. Chem. Soc*. **1951**, 73, 4315–20.

38．J. Michl, In Handbook of photochemistry; 3 rd ed.; Montalti, M., Credi, A., Prodi, L., Gandolfi, M. T., Eds.; CRC: Boca Raton, **2006**, 1–43.

39．S. Gentemann, C. J. Medforth, T. P. Forsyth, D. J. Nurco, K. M. Smith, J. Fajer, D. Holten, *J. Am. Chem. Soc*. **1994**, 116, 7363–7368.

40．S. Gentemann, N. Y. Nelson, L. Jaquinod, D. J. Nurco, S. H. Leung, C. J. Medforth, K. M. Smith, J. Fajer and D. Holten, *J. Phys. Chem. B*, **1997**, 101, 1247–1254.

41．A. Gold, **W.** Ivey, G. E. Toney, R. Sangaiah, *Inorg. Chem*. **1984**, 23, 2932–2935.

42．G. L. Closs and L. E. Closs, *J. Am. Chem. Soc*., **1963,** 85, 818–819.

43．T. Shimomura, M. A. Pbillipi, H. M. Goff, W. F. Scholz, C. A. Reed, *J. Am. Chem. Soc.*, **1981**, 103, 6778–6780.

44．A. S. Hinman, B. J. Pavelich, A. E. Kondo and S. Pones, *J. Electroanal. Chem.*, **1987**, 234, 145–162.

45．K. M. Kadish, K. M. Smith, R. Guilard, *The Porphyrin Handbook*, Academic Press, San Diego, **2000**.

46．H. Xie, M. S. Kevin *Tetrahedron Letters*, **1992**, 33, 1197–1200.

47．W. R. Fawcett, M. Fedurco, K. M. Smith, H. Xie, *J. Electroanal. Chem.*, **1993**, 354, 281–287.

48．K. D. Bboah, J. Bhuyan, *J. Coord. Chem*, **2019**, 72, 2251–2260.

49．G. P. Arsenault, E. Bullock, S. F. MacDonald, *J. Am. Chem. Soc*, **1960**, 82, 4384–4389.

50．E. C. Johnson, D. Dolphin, *Tetrahedron Lett.*, **1976**, 26, 2197–2200.

51．L. Gong, D. Dolphin, *Can. J. Chem*., **1985**, 63, 401–405.

52．A. Gold, W. Ivey, G. E. Toney and R. Sangaiah, *Inorg. Chem*., **1984**, 23, 2932–2935.

53．N. Kishii, K. Shirai, S. Tamura, J. Seto, K. Tokumaru, S. Takagi, T. Arai, H. Sakuragi, *J. Lumin*., **1995**, 64, 125–129.

54．a) M. A. Ehudin, L. Senft, A. Franke, I. Ivanovic-Burmazovic, K. D. Karlin, *J. Am. Chem. Soc.* **2019**, 141, 10632−10643. b) A. Harriman, G. Porter and P. J. Walters, *Chem. Soc., Faraday Trans*. 1, **1983**, 79, 1335–1350.

55．B. Oregan, M. Grätzel, *Nature*, **1991**, 353, 737–740.

56．a) M. Grätzel, *Acc. Chem. Res*., **2009**, 42, 1788–1798. b) M. E. Ragoussi, T. Torres, *Chem. Commun*., **2015**, 51, 3957–3972. c) A. Mishra, M. K. R. Fischer, P. Bauerle, *Angew. Chem., Int. Ed.*, **2009**, 48, 2474–2499.

57．H. Song, Q. Liu and Y. Xie, *Chem. Commun.*, **2018**, 54, 1811–1824.

58. A. Hagfeldt, G. Boschloo, L. Sun, L. Kloo and H. Pettersson, *Chem. Rev.*, **2010**, 110, 6595–6663.

59. M. K. Nazeeruddin, A. Kay, I. Rodicio, R. Humphry-Baker, E. Mueller, P. Liska, N. Vlachopoulos, M. Grätzel, *J. Am. Chem. Soc.*, **1993**, 115, 6382–6390.

60. Y. Chiba, A. Islam, Y. Watanabe, R. Komiya, N. Koide, L. Han, *Jpn. J. Appl. Phys.*, **2006**, 45, L638–L640.

61. M. K. Nazeeruddin, F. De Angelis, S. Fantacci, A. Selloni, G. Viscardi, P. Liska, S. Ito, B. Takeru, M. Grätzel, *J. Am. Chem. Soc.*, **2005**, 127, 16835–16847.

62. Q. Yu, Y. Wang, Z. Yi, N. Zu, J. Zhang, M. Zhang, P. Wang, *ACS Nano,* **2010**, 4, 6032–6038.

63. N. Zhou, K. Prabakaran, B. Lee, S. H. Chang, B. Harutyunyan, P. Guo, M. R. Butler, A. Timalsina, M. J. Bedzyk, M. A. Ratner, S. Vegiraju, S. Yau, C. G. Wu, R. P. H. Chang, A. Facchetti, M. C. Chen, T. J. Marks, *J. Am. Chem. Soc.*, **2015**, 137, 4414–4423.

64. J. Yang, P. Ganesan, J. Teuscher, T. Moehl, Y. J. Kim, C. Yi, P. Comte, K. Pei, T. W. Holcombe, M. K. Nazeeruddin, J. Hua, S. M. Zakeeruddin, H. Tian, M. Grätzel, *J. Am. Chem. Soc.*, **2014**, 136, 5722–5730.

65. Z. Yao, M. Zhang, R. Li, L. Yang, Y. Qiao, P. Wang, *Angew. Chem., Int. Ed*., **2015**, 54, 5994–5998.

66. Z. Yao, M. Zhang, H. Wu, L. Yang, R. Li, P. Wang, *J. Am. Chem. Soc*., **2015**, 137, 3799–3802.

67. Y. Ren, Y. Li, S. Chen, J. Liu, J. Zhang, P. Wang, *Energy Environ. Sci.,* **2016**, 9, 1390–1399.

68. K. Kakiage, Y. Aoyama, T. Yano, T. Otsuka, T. Kyomen, M. Unno, M. Hanaya, *Chem. Commun.*, **2014**, 50, 6379–6381.

69. K. Kakiage, Y. Aoyama, T. Yano, K. Oya, T. Kyomen, M. Hanaya, *Chem. Commun*., **2015**, 51, 6315–6317.

70. K. Kakiage, Y. Aoyama, T. Yano, K. Oya, J. I. Fujisawa, M. Hanaya, *Chem. Commun*., **2015**, 51, 15894–15897.

71. S. Mathew, A. Yella, P. Gao, R. Humphry-Baker, F. E. CurchodBasile, N. Ashari-Astani, I. Tavernelli, U. Rothlisberger, K. M. Nazeeruddin, M. Grätzel, *Nat. Chem*., **2014**, 6, 242–247.

72. T. Bessho, S. M. Zakeeruddin, C. Y. Yeh, E. W. G. Diau, M. Grätzel, *Angew. Chem., Int. Ed.*, **2010**, 49, 6646–6649.

73. A. Yella, H. W. Lee, H. N. Tsao, C. Yi, A. K. Chandiran, M. K. Nazeeruddin, E. W. G. Diau, C. Y. Yeh, S. M. Zakeeruddin, M. Grätzel, *Science*, **2011**, 334, 629–634.

74. J. W. Shiu, Y. C. Chang, C. Y. Chan, H. P. Wu, H. Y. Hsu, C. L. Wang, C. Y. Lin, E. W. G. Diau, *J. Mater. Chem. A*, **2015**, 3, 1417–1420.

75. J. Luo, M. Xu, R. Li, K. W. Huang, C. Jiang, Q. Qi, W. Zeng, J. Zhang, C. Chi, P. Wang, J. Wu, *J. Am. Chem. Soc*., **2014**, 136, 265–272.

76. T. Higashino, Y. Fujimori, K. Sugiura, Y. Tsuji, S. Ito, H. Imahori, *Angew. Chem., Int. Ed.*, **2015**, 54, 9052–9056.

77. S. H. Kang, M. J. Jeong, Y. K. Eom, I. T. Choi, S. M. Kwon, Y. Yoo, J. Kim, J. Kwon, J. H. Park, H. K. Kim, *Adv. Energy Mater.*, **2017**, 7, 1602117.

78. (a) A. Kay, M. Grätzel, *J. Phys. Chem.* **1993**, 97, 6272-6277. (b) M. K. Nazeeruddin, R. Humphry-Baker, D. L. Officer, W. M. Campbell, A. K. Burrell, M. Grätzel, *Langmuir,* **2004**, 20, 6514–6517. (c) Q. Wang, W. M. Carnpbell, E. E. Bonfantani, K. W. Jolley, D. L. Officer, P. J. Walsh, K. Gordon, R. HumphryBaker, M. K. Nazeeruddin, M. Grätzel, *J. Phys. Chem. B,* **2005**, 109, 15397–15409. (d) W. M. Campbell, K. W. Jolley, P. Wagner, K. Wagner, P. J. Walsh, K. C. Gordon, L. SchmidtMende, M. K. Nazeeruddin, Q. Wang, M. Grätzel, D. L. Officer, *J. Phys. Chem. C,* **2007**, 111, 11760–11762. (e) J. K. Park, H. R. Lee, J. P. Chen, H. Shinokubo, A. Osuka, D. Kim, *J. Phys. Chem. C,* **2008**, 112, 16691–16699. (f) M. Ishida, S. W. Park, D. Hwang, Y. B. Koo, J. L. Sessler, D. Y. Kim, D. Kim, *J. Phys. Chem. C*, **2011**, 115, 19343–19354.

79. (a) V. Lin, S. DiMagno, M. Therien, *Science*, **1994**, 264, 1105–1111. (b) S. Cherian, C. C. Wamser, *J. Phys. Chem. B*, **2000**, 104, 3624–3629. (c) T. E. O. Screen, K. B. Lawton, G. S. Wilson, N. Dolney, R. Ispasoiu, T. Goodson Iii, S. J. Martin, D. D. C. Bradley, H. L. Anderson, *J. Mater. Chem.*, **2001**, 11, 312–320. (d) J. Rochford, D. Chu, A. Hagfeldt, E. Galoppini, *J. Am. Chem. Soc.*, **2007**, 129, 4655–4665. (e) J. R. Stromberg, A. Marton, H. L. Kee, C. Kirmaier, J. R. Diers, C. Muthiah, M. Taniguchi, J. S. Lindsey, D. F. Bocian, G. J. Meyer, D. Holten, *J. Phys. Chem. C,* **2007**, 111, 15464–15478. (f) S. Eu, S. Hayashi, T. Umeyama, A. Oguro, M. Kawasaki, N. Kadota, Y. Matano, H. Imahori, *J. Phys. Chem. C*, **2007**, 111, 3528–3537. (g) H. P. Lu, C. Y. Tsai, W. N. Yen, C. P. Hsieh, C. W. Lee, C. Y. Yeh, E. W. G. Diau, *J. Phys. Chem. C,* **2009**, 113, 20990–20997.

80. C. W. Lee, H. P. Lu, C. M. Lan, Y. L. Huang, Y. R. Liang, W. N. Yen, Y. C. Liu, Y. S. Lin, E. W. G. Diau, C. Y. Yeh, *Chem. Eur. J.*, **2009**, 15, 1403–1412.

81. C. P. Hsieh, H. P. Lu, C. L. Chiu, C. W. Lee, S. H. Chuang, C. L. Mai, W. N. Yen, S. J. Hsu, E. W. G. Diau, C. Y. Yeh, *J. Mater. Chem.*, **2010**, 20, 1127–1134.

82. C. L. Wang, Y. C. Chang, C. M. Lan, C. F. Lo, E. Wei-Guang Diau, C. Y. Lin, *Energy Environ. Sci.,* **2011**, 4, 1788–1795.

83. Y. C. Chang, C. L. Wang, T. Y. Pan, S. H. Hong, C. M. Lan, H. H. Kuo, C. F. Lo, H. Y. Hsu, C. Y. Lin, E. W. G. Diau, *Chem. Commun*., **2011**, 47, 8910–8912.

84. S. Kotteswaran, V. Mohankumar, M. Senthil Pandian, P. Ramasamy, *Inorg Chem Acta,* **2017**, 467, 256–263.

85. C. H. Wu, T. Y. Pan, S. H. Hong, C. L. Wang, H. H. Kuo, Y. Y. Chu, E. W. G. Diau and C. Y. Lin, *Chem. Commun*., **2012**, 48, 4329–4331.

86. Y. Wang, B. Chen, W. Wu, X. Li, W. Zhu, H. Tian, Y. Xie, *Angew. Chem., Int. Ed*., **2014**, 53, 10779–10783.

87. L. Pellejà, C. V. Kumar, J. N. Clifford, E. Palomares, *J. Phys. Chem. C,* **2014**, 118, 16504–16509.

88. Y. Wang, L. Xu, X. Wei, X. Li, H. Ågren, W. Wu, Y. Xie, *New J. Chem*., **2014**, 38, 3227–3235.

89. Y. Xie, Y. Tang, W. Wu, Y. Wang, J. Liu, X. Li, H. Tian, W. H. Zhu, *J. Am. Chem. Soc.*, **2015**, 137, 14055–14058.

90. S. Mathew, N. A. Astani, B. F. E. Curchod, J. H. Delcamp, M. Marszalek, J. Frey, U. Rothlisberger, M. K. Nazeeruddin, M. Grätzel, *J. Mater. Chem. A*, **2016**, 4, 2332–2339.

91. C. L. Wang, M. Zhang, Y. H. Hsiao, C. K. Tseng, C. L. Liu, M. Xu, P. Wang, C. Y. Lin, *Energy Environ. Sci*., **2016**, 9, 200–206.

92. J. Pan, H. Song, C. Lian, H. Liu, Y. Xie, *Dyes Pigm*., **2017**, 140, 36–46.

93. C. L. Wang, C. M. Lan, S. H. Hong, Y. F. Wang, T. Y. Pan, C. W. Chang, H. H. Kuo, M. Y. Kuo, E. W. G. Diau, C. Y. Lin, *Energy Environ. Sci*., **2012**, 5, 6933–6940.

94. H. Song, X. Li, H. Ågren, Y. Xie, *Dyes Pigm*., **2017**, 137, 421–429.

95. Z. Ning, Y. Fu, H. Tian, *Energy Environ. Sci*., **2010**, 3, 1170–1181.

96. T. Wei, X. Sun, X. Li, H. Ågren, Y. Xie, *ACS Appl. Mater. Interfaces*, **2015**, 7, 21956–21965.

97. http://en.wikipedia.org/wiki/Photodynamic_therapy.

98. http://www.cancer.org/docroot/ETO/content/ETO_1_3X_Photodynamic_Therapy.asp.

99. K. Szacilowski, W. Macyk, A. Drzewiecka-Matuszek, M. Brindell, G. Stochel, *Chem. Rev.* **2005**, 105, 2647–2694.

100. M. Wainwright, K.B. Crossley, *Int. Biodeterior. Biodegrad.* **2004**, 53, 119–126.

101. M. Maclean, S.J. MacGregor, J.G. Anderson, G.A. Woolsey, *J. Photochem. Photobiol.* **2008**, 92, 180–184.

102. E. Alves, M.A.F. Faustino, M.G.P.M.S. Neves, A. Cunha, J.P.C. Tomé, A. Almeida, *Future Med. Chem.* **2014**, 6, 141–164.

103. S.Y. Kim, O.J. Kwon, J.W. Park, *Biochimie*, **2001**, 83, 437–444.

104. O. Planas, E. Boix-Garriga, B. Rodríguez-Amigo, J. Torra, R. Bresolí-Obach, C. Flors, C. Viappiani, M. Agut, R. Ruiz-González, S. Nonell, Chapter 9: Newest approaches to singlet oxygen photosensitisation in *Biological Media*. In *Photochemistry*; Fasani, E., Albini, A., Eds.; Royal Society of Chemistry: Cambridge, UK, **2015**; Volume 42, pp. 233–278, ISBN 978-1-84973-956-6.

105. M. G. H. Vicente, *Curr. Med. Chem. - Anti-Cancer Agents*, **2001**, 1, 175–194.

106. J. J. Schuitmaker, P. Baas, H. L. van Leengoed, F. W. van der Meulen, W. M. Star, N. *J.* van Zandwijk, *Photochem. Photobiol. B Biol.* **1996**, 34, 3–12.

107. J. R. Mccarthy, J. Bhaumik, N. Merbouh, R. Weissleder, *Org. Biomol. Chem.* **2009**, 7, 3430–3436.

108. D. *J.* Kessel, *Photochem. Photobiol. B: Biol.*, **1997**, 39, 81–83.

109. J. D. Spikes, J. C. Bommer, *J. Photochem. Photobiol. B: Biol.*, **1993**, 17, 135–143.

110. G. A. Peyman, A. A. Kazi, D. Moshfeghi, M. Unal, B. Khoobehi, S. Yoneya, K. Mori, I. Rivera, *Ophthal. Surg. Lasers*, **2000**, 31, 323–327.

111. S. W. Taber, V. H. Fingar, C. T. Coots, T. J. Wieman, *Clin. Cancer Res.*, **1998**, 4, 2741–2746.

112. K. Mori, S. Yoneya, M. Ohta, A. Sano, K. Anzai, G. A. Peyman, D. M. Moshfeghi, *Ophthalmol.*, **1999**, 106, 1384–1391.

113. A. Richter, E. Waterfield, A. K. Jain, A. J. Canaan, B. A. Allison, J. G. Levy, *Photochem. Photobiol.*, **1993**, 57, 1000–1006.

114. J. W. Miller, U. Schmidt-Erfurth, M. Sickenberg, C. J. Pournaras, H. Laqua, I. Barbazetto, L. Zografos, B. Piguet, G. Donati, A.-M. Lane, R. Birngruber, H. van den Berg, A. Strong, U. Manjuris, T. Gray, M. Fsadni, N. M. Bressler, E. S. Gragoudas, *Arch. Ophthalmol.*, **1999**, 117, 1161–1173.

115．B. A. Allison, M. T. Crespo, A. K. Jain, A. M. Richter, Y. N. Hsiang, J. G. Levy, *Photochem. Photobiol.*, **1997**, 65, 877–883.

116．D. Husain, J. W. Miller, A. G. Kenney, N. Michaud, T. J. Flotte, E. S. Gragoudas, *Ophthalmol.*, **1997**, 104, 1242–1250.

117．N. M. Bressler, S. B. Bressler, *Arch. Inv. Ophthalmol. Vis. Sci.*, **2000**, 41, 624–628.

118．H. L. L. M. van Leengoed, V. Cuomo, A. A. C. Versteeg, N. van Veen, G. Jori, W. M. Star, *Br. J. Cancer*, **1994**, 69, 840–845.

119．U. Isle, K. Schieweck, R. Kessler, P. van Hoogevest, H.-G. Caprano, *J. Pharm. Sci.*, **1995**, 84, 166–173.

120．W. G. Love, S. Duk, R. Biolo, G. Jori, P. W. Taylor, *Photochem. Photobiol.*, **1996**, 63, 656–661.

121．W.-S. Chan, N. Brasseur, C. La Madeleine, J. E. van Lier, *Eur. J. Cancer*, **1997**, 33, 1855–1859.

122．K. W. Woodburn, F. Qing, D. Kessel, Y. Luo, S. W. Young, *J. Inv. Dermat.*, **1998**, 110, 746–751.

123．M. S. Blumenkranz, K. W. Woodburn, F. Qing, S. Verdooner, D. Kessel, R. Miller, *Amer. J. Ophthal.*, **2000**, 129, 353–362.

124．T. D. Mody, J. L. Sessler, D. N. Reinhoudt, (Ed); Wiley, New York, **1999**, 245–294.

125．S. C. Mwakwari, *LSU Doctoral Dissertations*. **2007**, 1741.

126．S. K. Pushpan, S. Venkatraman, V. G. Anand, J. Sankar, D. Parmeswaran, S. Ganesan, T. K. Chandrashekar, *Curr. Med. Chem. - Anti-Cancer Agents* **2002**, 2, 187–207.

127．B. Marydasan, A.K. Nair, D. Ramaiah, *J. Phys. Chem. B*, **2013**, 117, 13515−13522.

128．F. Nifiatis, J. C. Athas, K. D. D. Gunaratne, Y. Gurung, K. Mae Monette, P. Joseph Shivokevich, *The Open Spectroscopy Journal*, **2011**, 5, 1–12.

129．R. Khan, M. Idris, D. Tuncel, *Org. Biomol. Chem.*, **2015**, 13, 10496–10504.

130．S. Griveau, F. Bedioui, Chapter 55 in the porphyrin handbook, **2011**, vol 12.

131．A. Deronzier, J. M. Latour, *J Electroanal Chem* **1987**, 224, 295–301.

132．A. Bettelheim, B. A. White, S. A. Raybuck, R. W. Murray, *Inorg Chem*, **1987**, 26, 1009–1017.

133．F. Bedioui, A. Merino, J. Devynck, C. E. Mestres, C. Bied Charreton, *J Electroanal Chem* **1988**, 239, 433–439.

134．C. Armengaud, P. Moisy, F. Bedioui, J. Devynck, C. Bied Charreton, *J Electroanal Chem*, **1990**, 277, 197–211.

135．F. Bedioui, M. Voisin, J. Devynck, C. Bied Charreton, *J. Electroanal Chem*, **1991**, 297, 257–269.

136．G. Ramachandraiah, F. Bedioui, J. Devynck, M. Serrar, C. Bied Charreton, *J. Electroanal Chem*, **1991**, 324, 325–337.

137．A. Deronzier, R. Devaux, D. Limosin, JM. Latour, *J. Electroanal Chem*, **1992**, 324, 325–337.

138．A. Deronzier, *J. Chim Phys Phys Chim Biol*, **1996**, 93, 611–619.

139．F. Bedioui, J. Devynck, C. Bied Charreton, *J Mol Catal A*, **1996**, 113, 3–11.

140．M. A. C. De Medeiros, S. Cosnier, A. Deronzier, J. C. Moutet, *Inorg Chem*, **1996**, 35, 2659–2664.

141．S. Cosnier, C. Gondran, R. Wessel, F. P. Montforts, M. Wedel, *J Electroanal Chem*, **2000**, 488, 83–91.

142．S. Cosnier, C. Gondran, R. Wessel, F-P. Montforts, M. Wedel, *Sensors*, **2003**, 3, 213–222.

143．N. Diab, W. Schuhmann, *Electrochim Acta*, **2001**, 47, 265–273.

144．M. Wedel, A. Walter, F. P. Monforts, *Eur J Org Chem*, **2001**, 9, 1681–1687.

145．S. Cosnier, C. Gondran, K. Gorgy, R. Wessel, F. P. Montforts, M. Wedel, *Electrochem Commun*, **2002**, 4, 426–430.

146．T. Shimidzu, *Pure Appl Chem*, **1995**, 67, 2039–2046.

147．T. Shimidzu, T. Iyoda, H. Segawa, *Macromol Symp*, **1996**, 101, 127–135.

148．T. Shimidzu, *Macromol Symp*, **1996**, 104, 127–135.

149．T. Shimidzu, *Polym Adv Technol*, **1997**, 8, 275–280.

150．M. Schaferling, P. Bauerle, *Synth Met*, **1999**, 101, 38–39.

151．M. Schaferling, P. Bauerle, *Synth Met*, **2001**, 119, 289–290.

152．C. O. Too, G. G. Wallace, A. K. Burrell, G. E. Collis, D. L. Officer, E. W. Boge, S. G. Brodie, E. Evans, *J Synth Met*, **2001**, 123, 53–60.

153．K. Yamashita, M. Ikeda, M. Takeuchi, S. Shinkai, *Chem Lett*, **2003**, 32, 264–265.

154．M. A. C. De Medeiros, K. Gorgy, A. Deronzier, S. Cosnier, *Mater Sci Eng C Biomim Supramol Syst* **2008,** 21, 731–738.

155．S. Cosnier, A. Deronzier, J. Roland, *J Electroanal Chem*, **1990**, 285, 133–147.

156．M. Yuasa, K. Oyaizu, A. Yamaguchi, M. Ishikawa, K. Eguchi, T. Kobayashi, Y. Toyoda, S. Tsutsui, *Polym Adv Technol*, **2005**, 16, 287–292.

157．C. L. Lin, M. Y. Fang, S. H. Cheng, *J Electroanal Chem*, **2002**, 531, 155–162.

158．R. Buttemeyer, A.W. Philipp, J.W. Mall, B. X. Ge, F.W. Scheller, *Lisdat F*, **2002**, 22, 108–113.

159．K.V., Gobi, F. Mizutani, *J. Electroanal Chem*, **2000**, 484, 172–181.

160．F. Lisdat, B. Ge, E. Ehrentreich-Forster, R. Reszka, F. W. Scheller, *Anal Chem*, **1999**, 71, 1359–1365.

161．K. Tammeveski, T.T. Tenno, A.A. Mashirin, E.W. Hillhouse, P. Manning, C. McNeil, *J Free Rad Biol Med*, **1998**, 25, 973–978.

162．L. Campanella, L. Persi, M. Tomassetti, *Sens Actuators, B*, **2000**, 68, 351–359.

163．W. Scheller, W. Jin, E. Ehrentreich-Forster, B. Ge, F. Lisdat, R. Buttemeier, U. Wollenberger, F. W. Scheller, *Electroanalysis*, **1999**, 11, 703–706.

164．P. Manning, C. J. McNeil, J. M. Cooper, E. W. Hillhouse, *Free Rad Biol Med*, **1998**, 24, 1304–1309.

165．C. J. McNeil, D. Athey, W.O. Ho, *Biosens Bioelec*, **1995**, 10, 75–83.

166．J. M. Cooper, K. R. Greenough, C. J. McNeil, *J. Electroanal Chem*, **1993**, 347, 267–275.

167．C. J. McNeil, K. R. Greenough, P. A. Weeks, C. H. Self, J. M. Cooper, *Free Rad Res Commun*, **1992**, 17, 399–406.

168. L. Jiang, A. Glidle, A. Griffith, C. J. McNeil, J. M. Cooper, *Bioelec Bionerg*, **1997**, 42, 15–23.

169. Y. Sato, F. Mizutani, *J. ElectroanalChem*. **1997**, 438, 99–104.

170. Y. Sato, F. Mizutani, *Electrochim Acta*, **2000**, 45, 2869–2875.

171. K. V. Gobi, Y. Sato, F. Mizutani, *Electroanalysis*, **2001**, 13, 397–403.

172. M. K. Beissenhirtz, R. C. H. Kwan, K. M, Ko, R, Renneberg, F.W, Scheller, F. Lisdat, *Phyt Res*, **2004**, 18, 149–153.

173. M. A. C. Medeiros, S. Cosnier, A. Deronzier, J-C. Moutet, *Inorg Chem*, **1996**, 34, 2659–2664.

174. B. A. White, R. W. Murray, *J. Electroanal Chem*, **1985**, 89, 345–352.

175. K. A. Macor, Y. O. Su, L. A. Miller, T. G. Spiro, *Inorg Chem*, **1987**, 26, 2594–2598.

176. B. A. White, R. W. Murray, *J Am Chem Soc*, **1987**, 109, 2576–2581.

177. S. Daunert, S. Wallace, A. Florido, L. G. Bachas, *Anal Chem*, **1991**, 63, 1676–1679.

178. D. M. Kliza, M. E. Meyerhoff, *Electroanalysis*, **1992**, 4, 841–849.

179. J. Hayon, A. Raveh, A. Bettelheim, *J Electroanal Chem*, **1993**, 359, 209–221.

180. F. Armijo, M. C. Goya, Y. Gimeno, M. C. Arévalo, M. J. Aguirre, A. H. Creus, *Electrochem Commun*, **2006**, 8, 779–784.

181. M. C. Goya, M. Lucero, A.G. Orive, A. Marín, Y. Gimeno, A.H. Creus, M.J. Aguirr, Arévalo M.C, F. Armijo, *Int J Electrochem Sci*, **2011**, 6, 4984–4998.

182. A. Bettelheim, L. Soifer, E. Korin, *J Electroanal Chem*, **2004**, 571, 265–272.

183. N. K. Subbaiyan, I. Obraztsov, CA. Wijesinghe, K. Tran, W. Kutner, F. D'Souza, *J Phys Chem C*, **2009**, 13, 8982–8989.

184. T. L. Blair, J. R. Allen, S. Daunert, L. G. Bachas, *Anal Chem*, **1993**, 65, 2155–2158.

185. T. J. Savenije, R. B. M. Koehorst, T. J. Schaafsma, *J Phys Chem B*, **1997**, 101, 720–725.

186. T. Malinski, A. Ciszewski, J. Bennett, J. R. Fish, L. Czuchajowski, *J Electrochem Soc*, **1991**, 138, 2008–2015.

187. T. Malinski, A. Ciszewski, J. Fish, E. Kubaszewski, L. Czuchajowski, *Adv Mater*, **1992**, 4, 354–357.

188. J. R. Fish, E. Kubaszewski, A. Peat, T. Malinski, J. Kaczor, P. Kus, L. Czuchajowski, *Chem Mater*, **1992**, 4, 795–803.

189. K. A. Macor, T. G. Spiro, *J Am Chem Soc*, **1983**, 105, 5601–5607.

190. K. A. Macor, T. G. Spiro, *J Electroanal Chem*, **1984**, 163, 223–236.

191. J. Basu, K. K. Rohatgimukherjee, *Photochem Photobiol*, **1988**, 48, 417–422.

192. J. Basu, K. K. Rohatgimukherjee, *Sol Energy Mater*, **1991**, 21, 317–325.

193. J. N. Younathan, K. S. Wood, T. Meyer, *Inorg Chem*, **1992**, 31, 3280–3285.

194. S. M. Chen, Y. L. Chen, *J Electroanal Chem*, **2004**, 573, 277–287.

195. M. G. Walter, C. C. Wamser, *J Phys Chem C*, **2010**, 114, 7563–7574.

196. H. Winnischofer, S. S. Lima, K. Araki, H. E. Toma, *Anal Chim Acta*, **2003**, 480, 97–107.

197. H. E. Toma, *J Braz Chem Soc*, **2003**, 14, 845–869.

198. H. Winnischofer, A. L. B. Formiga, M. Nakamura, H. E. Toma, K. Araki, A. F. Nogueira, *Photochem. Photobiol. Sci.*, **2005**, 4, 359–366.

199. S-C. Huang, C-Y. Li, *Chem Commun*, **2015**, 51, 519–521.

200. T. Ogawa, Y. Nishimoto, N. Yoshida, N. Ono, A. Osuka, *Chem Commun*, **1998**, 3, 337–338.

201. T. Ogawa, Y. Nishimoto, N. Yoshida, N. Ono , A. Osuka, *Angew Chem Int Ed*, **1999**, 38, 176–179.

202. C. H. Devillers, D. Lucas, A. K. D. Dime, Y. Rousselin, Y. Mugnier, *Dalton Trans*, **2012**, 39, 2404-2411.

203. A. Giraudeau, L. Ruhlmann, L. El-Kahef, M. Gross, *J Am Chem Soc*, **1996**, 118, 2969–2979.

204. D. Schaming, S. Marggi-Poullain, I. Ahmed, R. Farha, M. Goldmann, J-P. Gisselbrecht, L. Ruhlmann, *New J Chem*, **2011**, 35, 2534–2543.

205. L. Ruhlmann, A. Schulz, A. Giraudeau, C. Messerschmidt, J-H. Fuhrhop, *J Am Chem Soc*, **1999**, 121, 6664–6667.

206. D. Schaming, Y. Xia, R. Thouvenot, L. Ruhlmann, *Chem Eur J*, **2013**, 19, 1712–1719.

207. P. A. Liddell, M. Gervaldo, J. W. Bridgewater, A. E. Keirstead, S. Lin, T. A. Moore, A. L. Moore, D. Gust, *Chem. Mater.* **2008**, 20, 135–142.

208. A. Giraudeau, S. Lobestein, L. Ruhlmann, D. Melamed, K. M. Barkigia, J. Fajer, *J. Porphyrins Phthalocyanines*, **2001**, 5, 793–797.

209. D. Schaming, A. Giraudeau, L. Ruhlmann, In: Kaibara A, Matsumara G (eds) Handbook of porphyrins: chemistry, properties and applications. *Nova Publishers, USA*, **2012.**

210. L. Ruhlmann, S. Lobstein, M. Gross, A. Giraudeau, *A J Org Chem*, **1999**, 64, 1352–1355.

211. A. Giraudeau, D. Schaming, J. Hao, R. Farha, M. Goldmann, L. Ruhlmann, *J Electroanal Chem*, **2010**, 638, 70–75.

212. L. Ruhlmann, A. Giraudeau, *Chem Commun*, **1996**, 17, 2007–2008.

213. L. Ruhlmann, A. Giraudeau, *Eur J Inorg Chem*, **2001**, 13, 659–668.

214. L. Ruhlmann, M. Gross, A. Giraudeau, *Chem Eur J*, **2003**, 9, 5085–5096.

215. D. Wang, L. Liu, J. Jiang, L. Chen, J. Zhao, *Nanoscale*, **2020**, 12, 5705-5718.

216. S. S. Wang, G. Y. Yang, *Chem. Rev.* **2015**, 115, 4893–4962.

217. H. Lv, Y. V. Geletii, C. Zhao, J. W. Vickers, G. Zhu, Z. Luo, J. Song, T. Lian, D. G. Musaev, C. L. Hill, *Chem. Soc. Rev.* **2012**, 41, 7572–89.

218. T. Yamase, M. T. Pope, in *Polyoxometalate chemistry for nano-composite design*; (Kluwer, Dordrecht, **2002**).

219. S. G. Sarafianos, U. Kortz, M. T. Pope, M. J. Modak, *Reactions*, **1996**, 626, 619–626.

220. J. T. Rhule, C. L. Hill, D. Judd, R. F. Schinazi, *Chem. Rev.* **1998**, 98, 327–358.

221. A. Bijelic, A. Rompel, *Coord. Chem. Rev.* **2015**, 299, 22–38.

222. A. Bijelic, A. Rompel, *Acc. Chem. Res*. **2017**, 50, 1441–1448.

223. C. Molitor, A. Bijelic, and A. Rompel, *IUCrJ,* **2017**, 4, 734–740.

224. M. Sadakane, E. Steckhan, *Chem. Rev.* **1998**, 98, 219–238.

225. A. Proust, R. Thouvenot, P. Gouzerh, *Chem. Commun.,* **2008**, 16, 1837–1852.

226. J. M. Clemente-Juan, E. Coronado, A. Gaita-Ariño, *Chem. Soc. Rev.* **2012**, 41, 7464–7478.

227. D. L. Long, R. Tsunashima, L. Cronin, *Angew. Chem. Int. Ed*. **2010**, 49, 1736–1758.

228. M. Guzel, Y. Torlak, E. Karatas, M. Ak, *J. The Electrochemical Society*, **2019**, 166, H313-H319.

229．G. Lavinia, B. F, G. Florea AS, C. A, M. D.-Lucia, *Acta Medica Marisiensis*, **2014**, 60, 84-88.
230．M. J. Janik, K. A. Campbell, B. B. Bardin, R. J. Davis, M. Neurock, *Appl. Catal. A* **2003**, 256, 51–68.
231．H. Li, S. Pang, S. Wu, X. Feng, K. Mullen, C. Bubeck, *J. Am. Chem. Soc*. **2011**, 133, 9423–9429.
232．A. Pearson, S.K. Bhargava, V. Bansal, *Langmuir* **2011**, 27, 9245–9252.
233．H. Bao, X. Wang, Guo-qiang Yang, H. Li, F. Zhang, W. Feng, *Colloid Polym Sci*, **2014**, 292, 2883–2889.
234．J. Zhang, A. M. Bond, D. R. Macfarlane, S. A. Forsyth, J. M. Pringle, A. W. A. Mariotti, A. F. Glowinski, A. G. Wedd, *Inorg. Chem*. **2005**, 44, 5123–5132.
235．D. Schaming. Assemblages hybrides porphyrines-polyoxométallates : étude électrochimique, photochimique et photocatalytique. Catalyse. Université Paris Sud - Paris XI, **2010**. Français. fftel00714499f.
236．(a) B. Keita, D. Bouaziz, L. Nadjo, *J. Electrochem. Soc.* **1988**, 135, 87–91. (b) Keita, B.; Nadjo, L. *J. Electroanal. Chem.* **1987**, 230, 267–271. (c) B. Keita, L. Nadjo, *J. Electroanal. Chem.* **1987**, *227*, 77-98. (d) B. Keita, L. Nadjo, *J. Electroanal. Chem.* **1987**, 219, 355-363. (e) B. Keita, L. Nadjo, *J. Electroanal. Chem.* **1987**, 217, 287–304. (f) B. Keita, L. Nadjo, *J. Electroanal. Chem.* **1986**, 208, 343–356. (g) M. T. Pope, E. Papaconstantinou, *Inorg. Chem.* **1967**, 6, 1147–1152.
237．T. Ueda, *ChemElectroChem* **2018**, 5, 823–838.
238．J. Zhang, A. M. Bond, D. R. Macfarlane, S. A. Forsyth, J. M. Pringle, A. W. A. Mariotti, A. F. Glowinski, A. G. Wedd, *Inorg. Chem*. **2005**, 44, 5123–5132.
239．N. Vilà, P. Oliveira, A. Walcarius, I. M. Mbomekallé, *Electrochim. Acta*, **2019**, 309, 209-218.
240．J. Zhang, A. M. Bond, *Inorg. Chem.* **2004**, 43, 8263−8271.
241．S. Himeno, M. Takamoto, *J. Electroanal. Chem*. **2000**, 492, 63–69.
242．Y. H. Guo, C. W. Hu, *J. Mol. Catal. A: Chem*. **2007**, 262, 136–148.
243．R. R. Ozer, J. L. Ferry, *J. Phys. Chem. B*, **2002**, 106, 4336–4342.
244．S. Y. Gao, R. Cao, J. Lu, G. L. Li, Y. F. Li, H. X. Yang, *J. Mater. Chem*. **2009**, 19, 4157–4163.
245．Z. Y. Fu, Y. Zeng, X. L. Liu, D. S. Song, S. J. Liao, J. C. Dai, *Chem. Commun.* **2012**, 48, 6154–6156.
246．Y. H. Guo, Y. H. Wang, C. W. Hu, Y. H. Wang, E. B. Wang, Y. C. Zhou, S. H. Feng, *Chem. Mater*. **2000**, 12, 3501–3508.
247．H. X. Yang, T. F. Liu, M. N. Cao, H. F. Li, S. Y. Gao, R. Cao, *Chem. Commun*. **2010**, 46, 2429–2431.
248．R. N. Biboum, F. Doungmene, B. Keita, P. de Oliveira, L. Nadjo, B. Lepoittevin, P. Roger, F. Brisset, P. Mialane, A. Dolbecq, I. M. Mbomekalle, C. Pichon, P. C. Yin, T. B. Liu, R. Contant, *J. Mater. Chem.* **2012**, 22, 319–323.
249．P. X. Lei, C. C. Chen, J. Yang, W. H. Ma, J. C. Zhao, L. Zang, *Environ. Sci. Technol.* **2005**, 39, 8466–8474.

250. B. Yue, Y. Zhou, J. Y. Xu, Z. Z. Wu, X. A. Zhang, Y. F. Zou, S. L. Jin, *Environ. Sci. Technol.* **2002**, 36, 1325–1329.

251. A. Dolbecq, P. Mialane, B. Keita, L. Nadjo, *J. Mater. Chem*. **2012**, 22, 24509–24521.

252. J. Tucher, Y. L. Wu, L. C. Nye, I. Ivanovic-Burmazovic, M. M. Khusniyarov, C. Streb, *Dalton Trans.* **2012**, 41, 9938–9943.

253. J. A. Rengifo-Herrera, M. N. Blanco, L. R. Pizzio, *Appl. Catal., B: Environ*. **2011**, 110, 126–132.

254. A. X. Tian, Y. L. Ning, H. P. Ni, X. Hou, R. Xiao, J. Ying, *Z. Naturforsch.* **2016**, 71, 1125–1133.

255. M. Bonchio, M. Carraro, G. Scorrano, E. Fontananova, E. Drioli, *Adv. Synth. Catal*. **2003**, 345, 1119–1126.

256. S. Farhadi, M. Afshari, M. Maleki, Z. Babazadeh, *Tetrahedron Lett*. **2005**, 46, 8483–8486.

257. A. Troupis, A. Hiskia, E. Papaconstantinou, *Angew. Chem., Int. Ed*. **2002**, 41, 1911–4.

258. M. Schulz, C. Paulik, G. Knor, *J. Mol. Catal. A: Chem*. **2011**, 347, 60–64.

259. M. Bonchio, M. Carraro, G. Scorrano, A. Bagno, *Adv. Synth. Catal.* **2004**, 346, 648–654.

260. A. Molinari, G. Varani, E. Polo, S. Vaccari, A. Maldotti, *J. Mol. Catal. A: Chem.* **2007**, 262, 156–163.

261. A. M. Khenkin, I. Efremenko, L. Weiner, J. M. L. Martin, R. Neumann, *Chem.—Eur. J.* **2010**, 16, 1356–1364.

262. J. Ettedgui, Y. Diskin-Posner, L. Weiner, R. Neumann, *J. Am. Chem. Soc*. **2011**, 133, 188–190.

263. H. Li, S. Pang, X. Feng, K. Mullen, C. Bubeck, *Chem. Commun*., **2010**, 46, 6243–6245.

264. Streb, C. *Dalton Trans*. **2012**, 41, 1651–1659.

265. A. Winter, P. Endres, E. Schröter, M. Jäger, H. Görls, C. Neumann, A. Turchanin, U. S. Schubert, *Molecules,* **2019**, 24, 4446.

266. B. Matt, J. Fize, J. Moussa, H. Amouri, A. Pereira, V. Artero, G. Izzet, A. Proust, *Energy Environ. Sci.* **2013**, 6, 1504–1508.

267. M.-P. Santoni, G.S. Hanan, B. Hasenknopf, *Coord. Chem. Rev.* **2014**, 281, 64–85.

268. S. Schönweiz, M. Heiland, M. Anjass, T. Jacob, S. Rau, C. Streb, *Chem. Eur. J.* **2017**, 23, 15370–15376.

269. S. Herrmann, C. Ritchie, C. Streb, *Dalton Trans.* **2015**, 44, 7092–7104.

270. Y. Ji, L. Huang, J. Hu, C. Streb, Y.-F. Song, *Energy Environ. Sci.* **2015**, 8, 776–789.

271. B. Matt, C. Coudret, C. Viala, D. Jouvenot, F. Loiseau, G. Izzet, A. Proust, *Inorg. Chem.* **2011**, 50, 7761–7768.

272. B. Matt, S. Renaudineau, L.M. Chamoreau, C. Afonso, G. Izzet, A. Proust, *J. Org. Chem.* **2011**, 76, 3107–3112.

273. B. Matt, J. Moussa, L.-M. Chamoreau, C. Afonso, A. Proust, H. Amouri, G. Izzet, *Organometallics,* **2012**, 31, 35–38.

274. B. Matt, X. Xiang, A.L. Kaledin, N. Han, J. Moussa, H. Amouri, S. Alves, C.L. Hill, T. Lian, D.G. Musaev, G. Izzet, A. Proust, *Chem. Sci.* **2013**, 4, 1737–1745.

275．F. Puntoriero, G. La Ganga, A. Sartorel, M. Carraro, G. Scorrano, M. Bonchio, S. Campagna, *Chem. Commun.*, **2010**, 46, 4725–4727.

276．S. Zoladek, I. A. Rutkowska, M. Blicharska, K. Skorupska, P. J. Kulesza, *J Solid State Electrochem*, **2016**, 20, 1199–1208.

277．I. Bazzan, P. Bolle, O. Oms, H. Salmi, N. Aubry-Barroca, A. Dolbecq, H. Serier-Brault, R. Dessapt, P. Roger, P. Mialane, *J. Mater. Chem. C*, **2017**, 5, 6343–6351.

278．Z. Huo, A. Bonnefont, Y. Liang, R. Farha, M. Goldmann, E. Saint-Aman, H. Xu, C. Bucher, L. Ruhlmann, *Electrochim. Acta*, **2018**, 274, 177–191.

279．Y. Wang, H. Li, W. Qi, Y. Yang, Y. Yan, B. Li, L. Wu, *J. Mater. Chem.*, **2012**, 22, 9181–9188.

280．C. Jahier, M. Coustou, M. Cantuel, N. D. McClenaghan, T. Buffeteau, D. Cavagnat, M. Carraro, S. Nlate, *Eur. J. Inorg. Chem.* **2011**, 727–738.

281．Y. Yang, B. Zhang, Y. Wang, L. Yue, W. Li,, L. Wu, *J. Am. Chem. Soc.* **2013**, 135, 14500−14503.

282．K. X. Li, X. Yang, Y. N. Guo, F. Y. Ma, H. C. Li, L. Chen, Y. H. Guo, *Appl. Catal., B: Environ.* **2010**, 99, 364–375.

283．D. F. Li, Y. H. Guo, C. W. Hu, C. J. Jiang, E. B. Wang, *J. Mol. Catal. A: Chem*. **2004**, 207, 183–193.

284．Y. Yang, Q. Y. Wu, Y. H. Guo, C. W. Hu, E. Wang, *J. Mol. Catal. A: Chem*. **2005**, 225, 203–212.

285．S. Q. Zhang, L. Chen, H. B. Liu, W. Guo, Y. X. Yang, Y. H. Guo, M. X. Huo, *Chem. Eng. J.* **2012**, 200, 300–309.

286．L. Li, Q. Y. Wu, Y. H. Guo, C. W. Hu, *Microporous Mesoporous*, *Mater.* **2005**, 87, 1–9.

287．D. F. Li, Y. H. Guo, C. W. Hu, L. Mao, E. Wang, *Appl. Catal.,A: Gen*. **2002**, 235, 11–20.

288．Y. H. Guo, C. W. Hu, S. C. Jiang, C. X. Guo, Y. Yang, E. Wang, *Appl. Catal*., *B: Environ*. **2002**, 36, 9–17.

289．Y. H. Guo, C. W. Hu, X. L. Wang, Y. H. Wang, E. B. Wang, Y. C. Zou, H. Ding, S. H. Feng, *Chem. Mater*. **2001**, 13, 4058–4064.

290．Y. H. Guo, C. W. Hu, C. J. Jiang, Y. Yang, S. C. Jiang, X. L. Li, E. B. Wang, *J. Catal*. **2003**, 217, 141–151.

291．Y. H. Guo, Y. Yang, C. W. Hu, C. X. Guo, E. B. Wang, Y. C. Zou, S. H. Feng, *J. Mater. Chem*. **2002**, 12, 3046–3052.

292．S. Farhadi, M. Zaidi, *Appl. Catal., A: Gen*. **2009**, 354, 119–126.

293．X. S. Qu, Y. H. Guo, C. W. Hu, *J. Mol. Catal. A: Chem*. **2007**, 262, 128–135.

294．B. Ali, F. Laffir, L.Kailas, G. Armstrong, L.Kailas, R. O'Connell,, T. McCormac, A. Sartorel, M. Carraro, F.M. Toma, M. Prato, M. Bonchio, *Energy Environ. Sci.* **2012**, 5, 5592–5603.

295．H. Lv, Y.V. Geletii, C. Zhao, J.W. Vickers, G. Zhu, Z. Luo, J. Song, T. Lian, D.G. Musaev, C.L. Hill, *Chem. Soc. Rev.* **2012**, 41, 7572–7589.

296．J. Li, R. Güttinger, R. Moré, F. Song, W. Wan, G.R. Patzke, *Chem. Soc. Rev.* **2017**, 46, 6124–6147.

297．S.W. Gersten, G.J. Samuels, T.J. Meyer, *J. Am. Chem. Soc.* **1982**, 104, 4029–4030.

298．A. R. Howells, A. Sankarraj, C. Shannon, *J. Am. Chem. Soc.* **2004**, 126, 12258–12259.

299．A. Sartorel, M. Carraro, G. Scorrano, R. De Zorzi, S. Geremia, N. D. McDaniel, S. Bernhard, M. Bonchio, *J. Am. Chem. Soc.* **2008**, 130, 5006–5007.

300．Y. V. Geletii, B. Botar, P. Kögerler, D. A. Hillesheim, D. G. Musaev, C. L. Hill, *Angew. Chem.* **2008**, 120, 3960–3963.

301．S. Goberna-Ferrón, L. Vigara, J. Soriano-López, J. R. Galán-Mascarós, *Inorg. Chem.* **2012**, 51, 11707–11715.

302．Q. Yin, J. M. Tan, C. Besson, Y. V. Geletii, D. G. Musaev, A. E. Kuznetsov, Z. Luo, K. I. Hardcastle, C. L. Hill, *Science* **2010**, 328, 342–345.

303．L. Yu, Y. Ding, M. Zheng, H. Chen, J. Zhao, *Chem. Commun.* **2016**, 52, 14494–14497.

304．J. Kern, R. Chatterjee, I. D. Young, F. D. Fuller, L. Lassalle, M. Ibrahim, S. Gul, T. Fransson, A. S. Brewster, *Nature* **2018**, 563, 421–425.

305．B. Schwarz, J. Forster, M. K. Goetz, D. Yücel, C. Berger, T. Jacob, C. Streb, *Angew. Chem. Int. Ed.* **2016**, 55, 6329–6333.

306．S.-X. Guo, F. W. Li, L. Chen, D. R. MacFarlane, J. Zhang, *ACS Appl. Mater. Interfaces*, **2018**, 10, 12690–12697.

307．Y.-R. Wang, Q. Huang, C.-T. He, Y. F. Chen, J. Liu, F.-C. Shen, Y.-Q. Lan, *Nat. Commun.*, **2018**, 9, 4466.

308．G. L. Cao, J. Xiong, Q. Xue, S. T. Min, H. M. Hu, G. L. Xue, *Electrochim. Acta*, **2013**, 106, 465–471.

309．J. Du, Z. Lang, Y. Ma, H. Tan, B. Liu, Y. Wang, Z. Kang, Y. Li, *Chem. Sci.*, **2020**, 11, 3007–3015.

310．R. Wan, H. F. Li, X. Y. Ma, Z. Liu, V. Singh, P. T. Ma, C. Zhang, J. Y. Niu, J. P. Wang, *Dalton Trans.*, **2019**, 48, 10327–10336.

311．S. Imar, M. Yaqub, C. Maccato, C. Dickinson, F. Laffir, M. Vagin, T. McCormac, *Electrochim. Acta*, **2015**, 184, 323–330.

312．O. Oms, S. Yang, W. Salomon, J. Marrot, A. Dolbecq, E. Riviere, A. Bonnefont, L. Ruhlmann, P. Mialane, *Inorg. Chem.*, **2016**, 55, 1551–1561.

313．X. L. Wang, J. J. Sun, H. Y. Lin, Z. H. Chang, G. C. Liu, X. Wang, *CrystEngComm*, **2017**, 19, 3167–3177.

314．J. Ying, H. Mou, J. Liu, G. Liu, X. Ji, T. Li, A. Tian, *Z. Naturforsch*. **2019**; 74(2)b: 159–169.

315．X. L. Wang, Y. F. Bi, B. K. Chen, H. Y. Lin, G. C. Liu, *Inorg. Chem*. **2008**, 47, 2442−2448.

316．S. B. Li, H. Y. Ma, H. J. Pang, L. Zhang, *Cryst. Growth Des*. **2014**, 14, 4450−4460.

317．Y. Y. Liu, J. F. Ma, J. Yang, Z. M. Su, *Inorg. Chem*. **2007**, 46, 3027−3037.

318．S. Taleghani, M. Mirzaei, H. Eshtiagh-Hosseini, A. Frontera, *Coord. Chem. Rev.*, **2016**, 309, 84−106.

319．A. X. Tian, J. Ying, J. Peng, J. Q. Sha, H. J. Pang, P. P. Zhang, Y. Chen, M. Zhu, Z. M. Su, *Inorg. Chem*. **2009**, 48, 100−110.

320．X. L. Wang, H. L. Hu, G. C. Liu, H. Y. Lin, A. Tian, X. *Chem. Commun*. **2010**, 46, 6485−6487.

321．X. L. Wang, H. L. Hu, A. X. Tian, H. Y. Lin, *Inorg. Chem*. **2010**, 49, 10299−10306.

322．X. L. Wang, N. Li, A. X. Tian, J. Ying, T. J. Li, X. L. Lin, J. Luan, Y. Yang, *Inorg. Chem*. **2014**, 53, 7118−7129.

323．S. T. Zheng, J. Zhang, X. X. Li, W. H. Fang, G. Y. Yang, *J. Am. Chem. Soc*. **2010**, 132, 15102−15103.

324．F. J. Ma, S. X. Liu, C. Y. Sun, D. D. Liang, G. J. Ren, F. Wei, Y. G. Chen, Z. M. Su, *J. Am. Chem. Soc*. **2011**, 133, 4178−4181.

325．K. Wang, D. D. Zhang, J. C. Ma, P. T. Ma, J. Y. Niu, J. P. Wang, *CrystEngComm*, **2012**, 14, 3205−3212.

326．D. C. Zhao, Y. Y. Hu, H. Ding, H. Y. Guo, X. B. Cui, X. Zhang, Q. S. Huo, J. Q. Xu, *Dalton Trans*. **2015**, 44, 8971−8983.

327．B. Artetxe, S. Reinoso, L. San Felices, P. Vitoria, A. Pache, J. Martín-Caballero, J. M. Gutierrez-Zorrilla, *Inorg. Chem*. **2015**, 54, 241−252.

328．G. G. Gao, C. Y. Song, X. M. Zong, D. F. Chai, H. Liu, Y. L. Zou, J. X. Liu, Y. F. Qiu, *CrystEngComm*, **2014**, 16, 5150−5158.

329．Y. Luo, M. Wächtler, K. Barthelmes, A. Winter, U. S. Schubert, B. Dietzek, *Chem. Commun*., **2018**, 54, 2970–2973.

330．N. Fay, V. M. Hultgren, A. G. Wedd, T. E. Keyes, R. J. Forster, D. Leane, A. M. Bond, *Dalton Trans.*, **2006**, 4218–4227.

331．Y. Yang, L. Xu, B. Xu, X. Du, W. Guo, *Mater. Lett.* **2009**, 63, 608–610.

332．Y. Yang, L. Xu, F. Li, X. Du, Z. Sun, *J. Mat. Chem.*, **2010**, 20, 10835–10840.

333．X.-L. He, Y.-P. Liu, K.-N. Gong, Z.-G. Han, X.-L. Zhai, *Inorg. Chem*., **2015**, 54, 1215–1217.

334．S. Farhadi, M. M. Amini, M. Dusek, M. Kucerakova, *J. Mol. Struct*., **2017**, 1130, 592–602.

335．M. A. Moussawi, N. Leclerc-Laronze, S. Floquet, P. A. Abramov, M. N. Sokolov, S. Cordier, A. Ponchel, E. Monflier, H. Bricout, D. Landy, M. Haouas, J. Marrot, E. Cadot, *J. Am. Chem. Soc.*, **2017**, 139, 12793–12803.

336．L.-X. Cai, S.-C. Li, D.-N. Yan, L.-P. Zhou, F. Guo, Q.-F. Sun, *J. Am. Chem. Soc*., **2018**, 140, 4869–4876.

337．P. Bolle, H. Serier-Brault, R. G´ enois, E. Faulques, A. Boulmier, O. Oms, M. Lepeltier, J. Marrot, A. Dolbecq, P. Mialane, R. Dessapt, *J. Mater. Chem. C*, **2016**, 4, 11392–11395.

338．M. Stuckart, K. Yu. Monakhov, *Chem. Sci.*, **2019**, 10, 4364–4376.

339．J. Zhang, Y. Huang, G. Li, Y. Wei, *Coord. Chem. Rev.* **2019**, 378, 395–414.

340．S. Schönweiz, S.A. Rommel, J. Kübel, M. Micheel, B. Dietzek, S. Rau, C. Streb, *Chem. Eur. J.* **2016**, 22, 12002–12005.

341．C. Allain, S. Favette, L. Chamoreau, J. Vaissermann, L. Ruhlmann, B. Hasenknopf, *Eur. J. Inorg. Chem.* **2008**, 3433–3441.

342．D. Schaming, C. Allain, R. Farha, M. Goldmann, S. Lobstein, A. Giraudeau, B. Hasenknopf, L. Ruhlmann, *Langmuir*, **2010**, 26, 5101–5109.

343．Z. Huo, D. Zang, S. Yang, R. Farha, M. Goldmann, B. Hasenknopf, H. Xu, L. Ruhlmann, *Electrochim. Acta*, **2015**, 179, 326–335.

344．I. Azcarate, I. Ahmed, R. Farha, M. Goldmann, X. Wang, H. Xu, B. Hasenknopf, E. Lacôte, L. Ruhlmann, *Dalton Trans*., **2013**, 42, 12688–12698.

345. M.-P. Santoni, A.K. Pal, G.S. Hanan, M.-C. Tang, A. Furtos, B. Hasenknopf, *Dalton Trans.* **2014**, 43, 6990–6993.

346. M.-P. Santoni, A.K. Pal, G.S. Hanan, A. Proust, B. Hasenknopf, *Inorg. Chem.* **2011**, 50, 6737–6745.

347. T. Auvray, M.-P. Santoni, B. Hasenknopf, G.S. Hanan, *Dalton Trans.* **2017**, 46, 10029–10036.

348. J. Li, I. Huth, L.M. Chamoreau, B. Hasenknopf, E. Lacôte, S. Thorimbert, M. Malacria, *Angew. Chem. Int. Ed.* **2009**, 48, 2035–2038.

349. D. Schaming, C. Costa-Coquelard, S. Sorgues, L. Ruhlmann, I. Lampre, *Appl. Catal. A,* **2010**, 373, 160–167.

350. I. Ahmed, R. Farha, M. Goldmann, L. Ruhlmann, *Chem. Commun.*, **2013**, 49, 496–498.

351. I. Ahmed, X. Wang, N. Boualili, H. Xu, R. Farha, M. Goldmann, L. Ruhlmann, *Appl. Catal. A: Gen,* **2012,** 447–448, 89–99.

352. C. Costa-Coquelard, S. Sorgues, L. Ruhlmann, *J. Phys. Chem. A,* **2010**, 114, 6394–6400.

353. D. Schaming, R. Farha, Xu, M. Goldmann, L. Ruhlmann, *Langmuir,* **2011**, 27, 132–143.

354. D. Fan, G. Li, J. Hao, *J. Colloid Interf. Sci.*, **2010**, 351, 151–155.

355. S. Liu, J. Xu, H. Sun, D. Li, *Inorg. Chim. Acta*, **2000**, 306, 87–93.

356. M. Nagai, H. Sanpei, M. Shirakura, *J. Mater. Chem.*, **2012**, 22, 9222–9229.

357. I. C. M. S. Santos, S. L. H. Rebelo, M. S. S. Balula, R. R. L. Martins, M. M. M. S. Pereira, M. M. Q. Simoes, M. G. P. M. S. Neves, J. A. S. Cavaleiro, A. M. V. Cavaleiro, *J. Mol. Catal. A* **2005**, 231, 35–45.

358. C. Zou, Z. Zhang, X. Xu, Q. Gong, J. Li, C Wu, *J. Am. Chem.Soc.* **2012**, 134, 87−90.

359. Y. Shen, J. Liu, J. Jiang, B. Liu, S. Dong, *Electroanal.* **2002**, 14, 22–28.

360. Y. Shen, J. Liu, J. Jiang, B. Liu, S. Dong, *J. Phys. Chem. B,* **2003**, 107, 9744–9748.

361. J. Zhu, Q. Zeng, S. O'Carroll, A. Bond, T. E. Keyes, R. J. Forster, *Electrochem. Commun*, **2011**, 13, 899–902.

362. J. Zhu, J. J. Walsh, A. M. Bond, T. E. Keyes, R. J. Forster, *Langmuir* **2012**, 28, 13536−13541.

363. (a) H. K. Chae, W .G. Klemperer, V. W. Day, *Inorg. Chem.* **1989**, 28, 1424–1431, (b) J.Q. Sha, J. W. Sun, C. Wang, G. M. Li, P. F. Yan, M.T. Li, *Cryst. Growth Des.* **2012**, 12, 2242–2250; (c) L.N. Xiao, Y. Peng, Y. Wang, J.N. Xu, Z.M. Gao, Y.B. Liu, D.F. Zheng, X.B. Cui, J.Q. Xu, *Eur. J. Inorg. Chem.* **2011**, 12, 1997–2005; (d) X. Lu, X. Shi, Y. Bi, C. Yu, Y. Chen, Z. Chi, *Eur. J. Inorg. Chem.* **2009**, 34, 5267–5276; (e) M. Yuan, Y. Li, E. Wang, C. Tian, L. Wang, C. Hu, N. Hu, H. Jia, *Inorg. Chem.* **2003**, 42, 3670–3676; (f) M. Mirzael, H. Eshtiagh-Hosseini, M. Alipour, A. Fontera, *Coord. Chem. Rev.* **2014**, 275, 1–18. (g) T. Zhang, N. Ma, L. Yan, S. Wen, T. Ma, Z. Su, *J. Mol. Graph. Model,* **2013**, 46, 59–64.

364. A. Yokoyama, T. Kojima, K. Ohkubo, S. Fukuzumi, *Chem. Commun.* **2007**, 3997–3999.

365. A. Yokoyama, T. Kojima, K. Ohkubo, M. Shiro, S. Fukuzumi, *J. Phys. Chem. A,* **2011**, 115, 986–997.

366. C. Yao, L. Yan, W. Guan, C. Liu, P. Song, Z. Su, *Dalton Trans.*, **2010**, 39, 7645–7649.

367. A. Harriman, K. J. Elliott, M. A. H. Alamiry, L. Le Pleux, M. Severac, Y. Pellegrin, E. Blart, C. Fosse, C. Cannizzo,.C. dric R. Mayer, F. Odobel, *J. Phys. Chem. C,* **2009,** 113, 5834–5842.

368．K. J. Elliott, A. Harriman, L. Le Pleux, Y. Pellegrin, E. Blart, C. R. Mayerc, F. Odobel, *Phys. Chem. Chem. Phys.*, **2009**, 11, 8767–8773.

369．C. Allain, D. Schaming, N. Karakostas, M. Erard, J. Gisselbrecht, S. Sorgues, Is. Lampre, L. Ruhlmann, B. Hasenknopf, *Dalton Trans*., **2013**, 42, 2745–2754.

370．I. Ahmed, R. Farha, Z. Huo, C. Allain, X. Wang, H. Xu, M. Goldmann, B. Hasenknopf, L. Ruhlmann, *Electrochim. Acta*, **2013**, 110, 726–734.

371．M. Araghi, V. Mirkhani, M. Moghadam, S. Tangestaninejad, I. Mohammdpoor-Baltork, *Dalton Trans*., **2012**, 41, 3087–3094.

372．Z. Huo, I. Azcarate, R. Farha, M. Goldmann, H. Xu, B. Hasenknopf, E. Lacôte, L. Ruhlmann, *J. Solid State Electrochem*., **2015**, 19, 2611–2621.

Chapter II

Stable porphyrin/isoporphyrin copolymers prepared with various dipyridinium spacers

Chapter II: Stable porphyrin/isoporphyrin copolymers prepared with various dipyridinium spacers

In the former work of our group, porphyrin copolymer can be obtained by electropolymerization through the oxidation of the zinc-*β*-octaethylporphyrin (**ZnOEP**) in the presence of 4,4'-bipyridine or $bpy^{+}–CH_2–CH_2–CH_2–^{+}bpy·2PF_6^{-1}$.[1] The isoporphyrin was the intermediate during the electropolymerization process. The results proved the dipyridyl ligands can be used as good nucleophiles connected with the *meso* carbon of porphyrin. However, if oxidizing the 5,15-bis(3,5-di-tert-butylphenyl) porphyrin alone, it showed spontaneous radical–radical coupling of two the π-radical-cation porphyrin. The homo-radical coupling gave the formation of a mixture of *meso*-*meso* and *meso*-*β* linked dimers.[2-4]

In this chapter, a new strategy to obtain stable isoporphyrin intermediate integrated in the copolymers is presented. These new copolymers containing stable isoporphyrins are described and compared with the “classical” porphyrin copolymer prepared using the strategy developed in our group.

Electrogenerated radical cation as well as dication porphyrin using porphyrin such as zinc-5,15-ditolyl-porphyrin (ZnT_2P) are powerful electrophiles which can rapidly react with nucleophiles such as dipyridyl ligand (py-R-py) to form copolymers containing isoporphyrin radical (poly-$ZnT_2isoP^{\bullet}$) or porphyrin (**poly-ZnT_2P**) depending of the upper potential limit (1.0 V *versus* 1.6 V) of the iterative potential cycles. The 1,1"-(1,3-propanediyl)bis-4,4'-bipyridinium hexafluorophosphate salt ($bpy^{+}–(CH_2)_3–^{+}bpy·2PF_6^{-}$) and 4,4’-dipyridine was used for this study.

The formation of these copolymers on ITO electrode has been monitored *in-situ* by Electrochemical Quartz Microbalance (EQCM). The two copolymers were also characterized by UV-Vis-NIR spectroscopy, X-ray Photoelectron Spectroscopy (XPS), electrochemistry, Electron Spin Resonance (ESR), Atomic Force Microscopy (AFM) and Electrochemical Impedance Spectroscopy (EIS). The photocurrent generation has been investigated under visible light illumination and the performances of **poly-$ZnT_2isoP^{\bullet}$** and **poly-ZnT_2P** copolymer thin films have been compared.

1. Introduction

Isoporphyrin can be defined as a porphyrin species with two substituents bonds at a same *meso*-carbon atom which break the ring aromaticity. Isoporphyrins have been reported as the intermediates of heme oxidation as well as biosynthesis of chlorophyll.[5]

The ^{1}H NMR spectra proved the presence of metallo-isoporphyrins by the interruption in the macrocyclic conjugation.[6] The typical optical properties of isoporphyrins is the absorption between 750 nm and 950 nm.[7] In addition isoporphyrins can act as photosensitizer for photodynamic therapy.[8]

Most of the isoporphyrins reported until now show a high tendency to decompose either by ring opening or by rearomatization to regenerate the initial porphyrin. In the case of *β*-octaethyl porphyrins, the formed isoporphyrins are not stable, due to the loss of a proton from the saturated *meso*-carbon atom while isoporphyrin is reasonably more stable in the case of tetraphenylporphyrin (**TPP**) where the *meso*-carbon atoms are bound to a phenyl group. The oxidized porphyrin (π-radical cation and dication) species are known to be powerful electrophiles which can rapidly react with nucleophiles having one or two pyridyl pendant groups.

Electrogenerated radical cation as well as dication porphyrin using porphyrin such as zinc-5,15-ditolyl-porphyrin (**ZnT$_2$P**) are powerful electrophiles which can rapidly react with nucleophiles such as dipyridyl ligand (py-R-py) to form copolymers containing isoporphyrin radical (**poly-ZnT$_2$isoP$^\bullet$**) or porphyrin (**poly-ZnT$_2$P**) depending of the upper potential limit.

2. Formation and characterization

2.1. Reagents and synthesis of ZnT$_2$P and ZnAT$_2$P.

All solvents were of reagent grade quality and used without further purification. Zinc-*β*-octaethylporphyrin (**ZnOEP**) was purchased from Sigma-Aldrich and used without further purification. The 1,1''-(1,3-propanediyl)bis-4,4'-bipyridinium hexafluorophosphate salt (bpy^+–$(CH_2)_3$–$^+bpy{\cdot}2PF_6^-$) and 4,4'-bipyridine were synthesized according to procedures described in literature.[9]

The free base 5,15-bis(p-tolyl)porphyrin (**H_2T_2P**)[10] was synthetized according to published procedures from 2,2'-dipyrromethane and *p*-tolualdehyde.[11] The free base was then metallated with $Zn(OAc)_2$ in THF to give zinc-5,15-bis(p-tolyl)porphyrin (**ZnT_2P**). Free-base porphyrin 5-(4-methoxyphenyl)-10,20-di-*p*-tolylporphyrin[12] was prepared by literature procedures and subsequently metallated (288 mg, 0.48 mmol, 1 eq) in THF using zinc acetate $Zn(OAc)_2$ (1059 mg, 4.8 mmol, 10 eq). The solution was refluxed for 1h. The crude product was purified by silica gel column chromatography with dichloromethane/cyclohexane (3/7) to afford 5-(4-methoxyphenyl)-10,20-di-p-tolylporphyrin zinc **$ZnAT_2P$** (294 mg, 0.45 mmol, 93%) as purple solid.

2.2. Electropolymerization of porphyrin/isoporphyrin copolymers

Electrochemical measurements were carried outby using a PARSTAT 2273 potentiostat with glassy carbon or single-side coated indium-tin-oxide (ITO, SOLEMS, 25-35 Ω/cm^{-2}) plates, with a surface of about 1 cm^{-2} as working electrodes. A platinum wire has been used as auxiliary electrode. The reference electrode was a Saturated Calomel Electrode (SCE). The syntheses of the copolymers were achieved via the electropolymerization method under an argon atmosphere in a 0.1 $mol.L^{-1}$ NBu_4PF_6 $CH_3CN/1,2\text{-}C_2H_4Cl_2$ (3/7) solution containing 2.5×10^{-4} $mol.L^{-1}$ of **ZnOEP** (Fig. 2.1A) or **ZnT_2P** (Fig. 2.1B) or 2.5×10^{-4} $mol.L^{-1}$ of **$ZnAT_2P$** and 2.5×10^{-4} $mol.L^{-1}$ $bpy^+–(CH_2)_3–bpy^+\cdot 2PF_6^-$ (Fig. 2.1D) or 4,4'-bipyridine (4,4'-bpy; Fig. 2.1E). ITO electrodes, with a surface of 1 cm^2, were used as working electrodes.

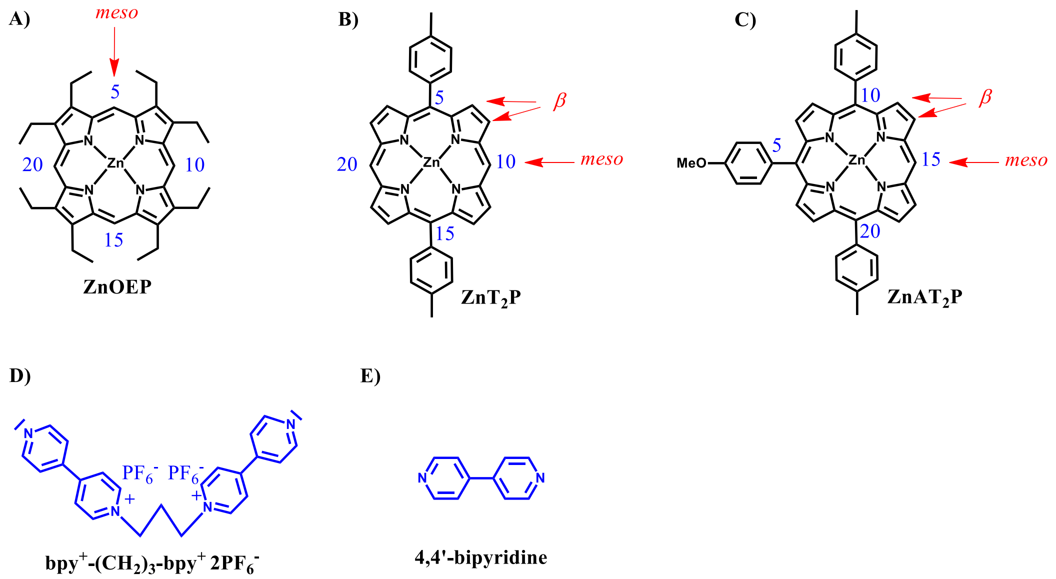

Figure 2.1. Representation of A) **ZnOEP**, B) **ZnT_2P**, C) **$ZnAT_2P$** D) $bpy^+\text{-}(CH_2)_3\text{-}bpy^+\cdot 2PF_6^-$, E) 4,4'-bipyridine.

The syntheses of the copolymers rely on the addition of dipyridyl ligands to an electro-generated π-radical cation or dication porphyrin produced by iterative voltammetric scans (Fig. 2.2).[13-16] The reactivity of oxidized porphyrins can be beneficially exploited to generate a wide range of poly-porphyrin materials as long as a bifunctional nucleophiles,[14,17] such as the bpy^{+}-$(CH_2)_3$-$^{+}bpy \cdot 2PF_6^{-}$, are used.

2.2.1. ZnOEP electropolymerization

According to our former research, the oxidation of **ZnOEP** was carried out at a sufficiently high positive potential value to produce doubly oxidized porphyrins (dication) which are readily reacting with dipyridyl nucleophile to produce copolymers. An $E(EC_{N\ meso}EC_B)_nE$ mechanism has been previously proposed in the case of **ZnOEP** to account for the electropolymerization process where $C_{N\ meso}$ relates to the nucleophilic attack at the *meso* position of the porphyrin to yield an isoporphyrin intermediate.[18] This latter compound is then oxidized (electrochemical step) and the hydrogen atom initially located on the *meso*-carbon is released (chemical step C_B). The corresponding global reaction is written in Eq. 1 assuming that only the disubstitution on the porphyrin occurs at *meso* positions (Schemes 1-2):

$(n+1)\ ZnP + (n+1)\ Py\text{-}R\text{-}Py \rightarrow ZnP\text{-}(Py^{+}\text{-}R\text{-}Py^{+}\text{-}ZnP)_n\text{-}Py^{+}\text{-}R\text{-}Py + (2n+1)H^{+} + (4n+2)e^{-}$ (Equation 1)

(where -R- = py^{+}-$(CH_2)_3$-py^{+} and ZnP = zinc porphyrin)

The nucleophiles used are 4,4'-bpy and bpy^{+}–$(CH_2)_3$–$bpy^{+} \cdot 2PF_6^{-}$ and the copolymer is obtained in the presence of **ZnOEP** only after generation of the porphyrin dications **ZnOEP**$^{2+}$ by iterative scans (between -1.3 V and 2.0 V) or by potentiostatic electrolysis at sufficiently high potential.[19] For this work, when the anodic potential limit is only above the potential at which the radical cation **ZnOEP**$^{+\bullet}$ is generated (i.e. 0.8 V), no film is deposited on the ITO electrode proving that the polymerization doesn't occur in this case (Fig. 2.2). Moreover, the oxidation wave of the macrocycle remains rather-irreversible showing that the electrogenerated radical cation does not react further. It should be noticed that the reduction wave detected at -0.7 V corresponds to the redox couple bpy^{+}–$(CH_2)_3$–^{+}bpy/ $bpy^{\bullet}$–$(CH_2)_3$–$^{\bullet}bpy$.

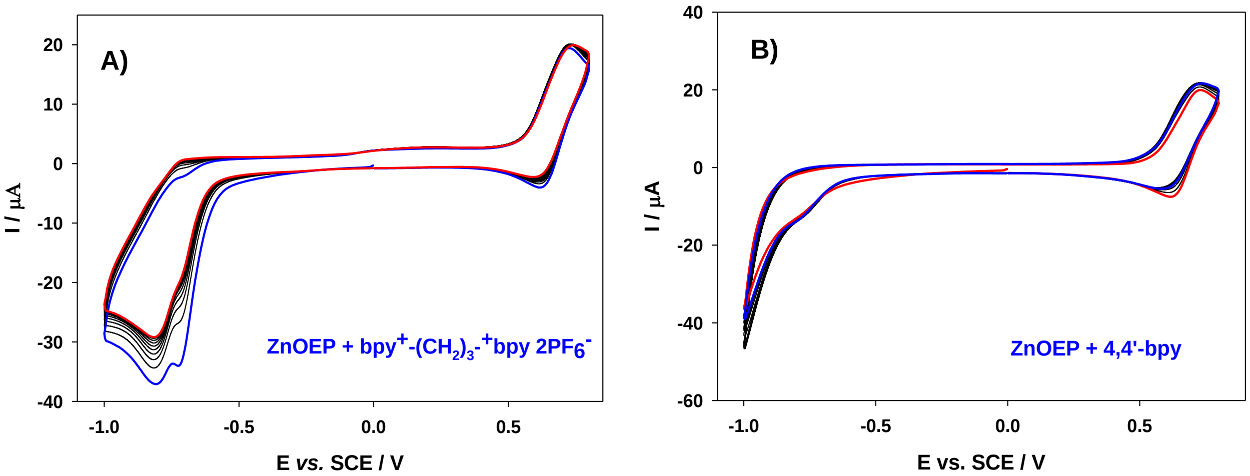

Figure 2.2. Cyclic voltammograms recorded during 25 iterative scans conducted between −1.0 V and +0.8 V *vs.* SCE in a 1,2-$C_2H_4Cl_2/CH_3CN$ (7/3) solution and NBu_4PF_6 (0.1 mol.L^{-1}) of **ZnOEP** (0.25 mmol L^{-1}) in the presence of A) $bpy^+–(CH_2)_3–^+bpy\ 2PF_6^-$ (0.25 mmol L^{-1}) and B) 4,4'-bpy (0.25 mmol L^{-1}). WE: ITO. S = 1 cm^2. v = 100 mV s^{-1}. Blue curve: first scan (n=1). Red curve: final scan (n = 25).

In our former work, we concluded that, while the formation of radical cation is enough to obtain monosubstituted porphyrins[17,20] *via* electrosynthesis (but necessitating much longer time than the duration time during the measurements of the cyclic voltammetry), the formation of dication is requested to perform the electropolymerization of **ZnOEP** *via* iterative cyclic voltammetry. First, a kinetic restraint can explain this difference. Indeed, the nucleophilic attack is faster onto the dication than onto the radical cation. As a result, if the iterative scans are stopped at a potential allowing only the formation of the radical cation, the characteristic time of the cyclic voltammetry at 100 mV.s^{-1} might be too short for the nucleophilic attack to occur. The presence in this case of the ethyl groups decreases drastically the kinetics of the nucleophilic attack at the *meso* position C5, C10, C15 or C20 respectively. The other point which can explain the need to apply a higher potential for electropolymerization is related to the degree of substitution of macrocycles. Indeed, the porphyrins in the copolymers are at least substituted twice by positively charged groups. Moreover, when the chain of copolymer grows, the quantity of positively charged groups increases. Consequently, porphyrins are more and more difficult to oxidize resulting in an increase of potential at which the polymerization occurs. This explanation is also supported by the fact that a higher applied potential has always been required to perform electrosynthesis of multi-substituted porphyrins through electrolysis.[21,22]

As a matter of fact, it can also be noted that higher anodic potential limit should lead to longer copolymers chains. Otherwise, if the upper potential is too low, but still higher than that of the first monomer oxidation, only small oligomers should be obtained which may dissolve.

2.2.2. Reactivity of zinc-*meso*-5,15-ditolyl-porphyrin ZnT$_2$P

In this study, we have decided to use the zinc-*meso*-5,15-ditolyl-porphyrin (**ZnT$_2$P**) which presents only two *meso* positions occupied by one substitutable proton at positions C10 and C20. Additionally, all the β positions of **ZnT$_2$P** are occupied only by protons. Such porphyrin will provide better accessibility for the nucleophilic attack of the pyridyl groups of bpy$^+$–(CH$_2$)$_3$–$^+$bpy·2PF$_6^-$ or of 4,4'-bpy in comparison to **ZnOEP**.

From the literature, the nucleophilic substitution with pyridine or triphenylphosphine nucleophiles only attack the *meso*-positions of magnesium porphyrin even if the β-positions are only occupied by protons.[23] Electrosynthesis of Zn and Mg *meso*-triaryltriphenylphosphonium porphyrin were also reported from Zn or Mg triarylporphyrin showing a nucleophilic substitution mainly at the *meso* and not the β position.[24] Furthermore, the electrochemical oxidation of pyridin-2-ylthio-meso substituted Ni(II) porphyrins afforded oxidative C-N fusion of pyridinyl-substituted porphyrins again at the *meso* position giving cationic and dicationic pyridinium-based products.[25]

Lastly, in order to demonstrate that the copolymer can be obtained using only **ZnT$_2$P** which presents two *meso* positions bearing H (*i.e.* position 10 and 20, methine bridges), Raphaël Lamare one PhD of our group has synthetized the zinc-5-(4-methoxyphenyl)-10,20-di-p-tolylporphyrin, **ZnAT$_2$P** in which one *meso* position (C5) is occupied by a metoxyphenyl group. The experimental protocol for the synthesis of **ZnAT$_2$P** is described in the ESI. In the presence of bpy$^+$–(CH$_2$)$_3$–$^+$bpy·2PF$_6^-$ or 4,4'-bpy and **ZnAT$_2$P** no copolymer was obtained even after a large number of iterative scans between -1.0 V and 1.0 V (v = 100 mV s^{-1}, Fig. 2.3) showing that two *meso* positions bearing H are required to form the copolymer. Additionally, for zinc 5,15-ditolyl porphyrin (**ZnT$_2$P**), the nucleophilic attack appears to be allowed only at the 10 as well as the 20 *meso* positions of the porphyrin.

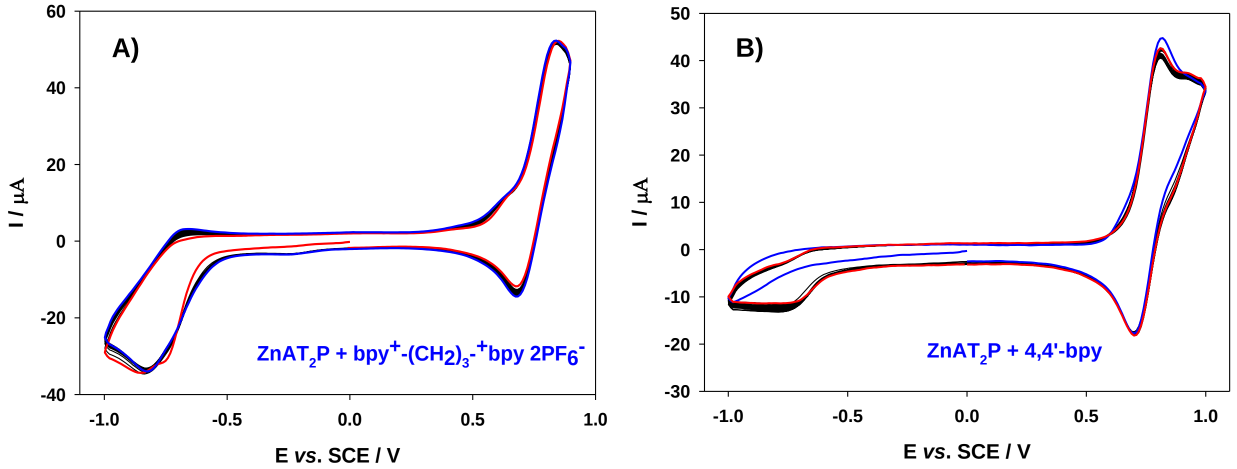

Figure 2.3. Cyclic voltammograms recorded during 25 iterative scans conducted between −1.0 V and +0.8 V *vs.* SCE in a 1,2-$C_2H_4Cl_2/CH_3CN$ (7/3) solution and NBu_4PF_6 (0.1 mol.L^{-1}) of **ZnAT$_2$P** (0.25 mmol L^{-1}) in the presence of A) (bpy$^+$-CH_2-CH_2-CH_2-$^+$bpy).2PF_6^- (0.25 mmol L^{-1}) and B) 4,4'-bpy (0.25 mmol L^{-1}). WE: ITO. S = 1 cm^2. v = 100 mV s^{-1}. Blue curve: first scan (n=1). Red curve: final scan (n = 25).

It must be noted that in the absence of nucleophile, the electrogenerated radical **ZnT$_2$P$^{+\bullet}$** may undergo a radical coupling reaction and the formation of one dimer with C-C bond formation through *meso–meso*, *meso–β* or *β–β* link between two macrocycles. Indeed, previous works in the literature using the 5,15-bis(3,5-di-tert-butylphenyl) porphyrin showed only the formation of a mixture of *meso–meso* and *meso–β* linked dimers. These dimers presented a splitting of the Soret band of the optical spectra. These resulting dimers are also easier to be oxidized.[26-28]

However, when potential iterative scans are performed between -1.0 V and +1.0 V or +1.6 V using **ZnT$_2$P** alone (in the absence of nucleophile) no film deposition onto the ITO electrode is observed suggesting that the kinetic of radical coupling reaction is relatively slow. The formation of dimer and eventually small oligomer which are soluble cannot be completely excluded.

Additionally, in the presence of 4,4'-bpy nucleophile during the oxidation of **ZnT$_2$P**, poly-porphyrin or oligomer of porphyrin **(ZnT$_2$P)$_n$** obtained by π-radical-cation porphyrin homo-radical coupling is still not detected during the iterative scans in solution or at the surface of the ITO electrode, copolymers being obtained only with viologen or double viologen spacers. The UV-vis-NIR spectra of the copolymer deposited onto ITO electrode also confirm the absence of dimer **(ZnT$_2$P)$_2$** trap in the film or oligomer **(ZnT$_2$P)$_n$** through radical coupling in the solid state respectively. The control of the solution after the electropolymerization has been checked by UV-vis-NIR spectroscopy (Fig. 2.4). Only the starting **ZnT$_2$P** monomer could be detected in the solution, even after a large number of iterative scans, showing the absence of significant quantity of dimer obtained by radical coupling under these conditions. UV-vis-NIR spectroscopy also confirms the absence of demetallation of the starting **ZnT_2P** porphyrin in solution even after deposition of a large number of films. It demonstrates that the Zn metal ion remains in the porphyrin ring during electropolymerization and that there is no **$(ZnT_2P)_2$** dimer or oligomer (formed through radical coupling) in detectable amount.

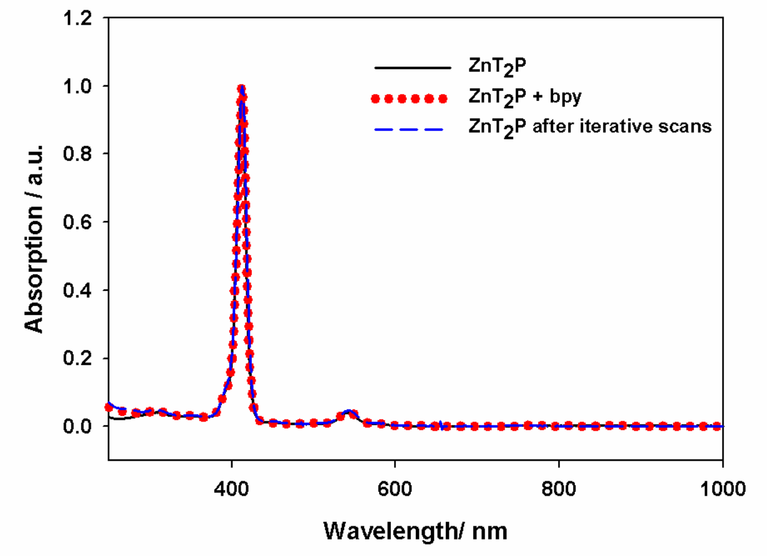

Figure 2.4. The UV-vis-NIR spectrum of **ZnT_2P** porphyrin solution (black solid line), **ZnT_2P** with 4,4’-bpy solution (red dotted line) and porphyrin with 4,4’-bpy solution after a large number of iterative scans (blue dash line).

The general electropolymerization procedure used to deposit the porphyrin-based polymers onto ITO electrode surfaces is described below. This process depends on the polarization of the working electrode during the potential scan that is either at the first oxidation potential to produce **$ZnT_2P^{+\bullet}$** (iteration between -1.0 V and +1.0 V) (Fig. 2.5) or at the second oxidation potential to produce **ZnT_2P^{2+}** (iteration between -1.0 V and +1.6 V) (Fig. 2.S1). It involves a series of intermolecular cascade reactions leading to formation of physisorbed oligomers and copolymers (Scheme 2.1).

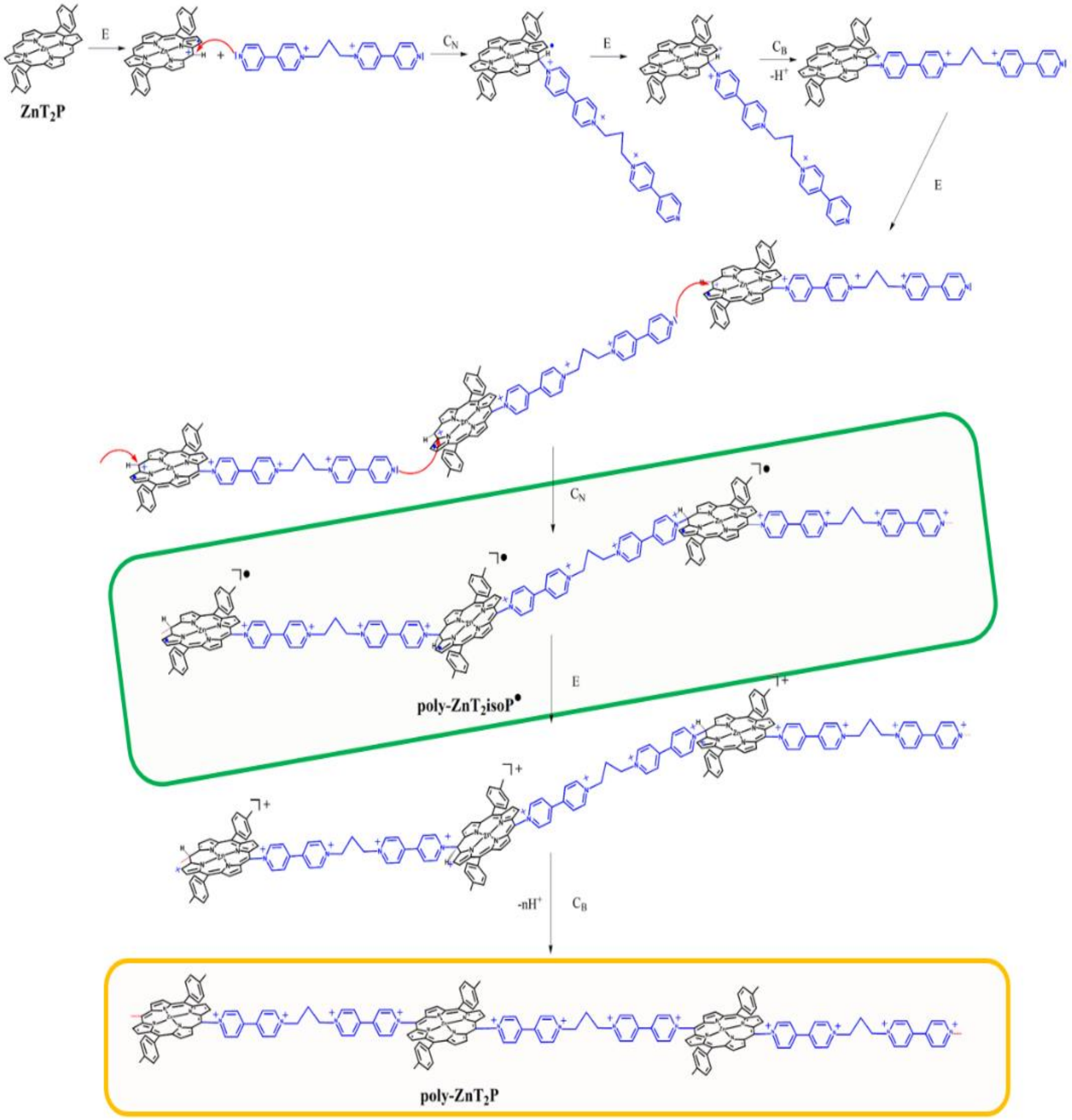

Scheme 2.1. Proposed $(E_1C_{N\mathit{meso}}E_2C_B)_n$ mechanism of the formation of the intermediate **poly-ZnT$_2$isoP1$^\bullet$** (green box) and the final **poly-ZnT$_2$P1** (yellow box) copolymer explaining the reactivity of a bpy$^+$–$(CH_2)_3$–$^+$bpy·2PF$_6^-$ during the oxidation of **ZnT$_2$P. Poly-ZnT$_2$isoP1$^\bullet$** is obtained using iterative scan between -1.0 V and 1.0 V and **poly-ZnT$_2$P1** is obtained in the case of iterative scan between -1.0 V and 1.6 V.

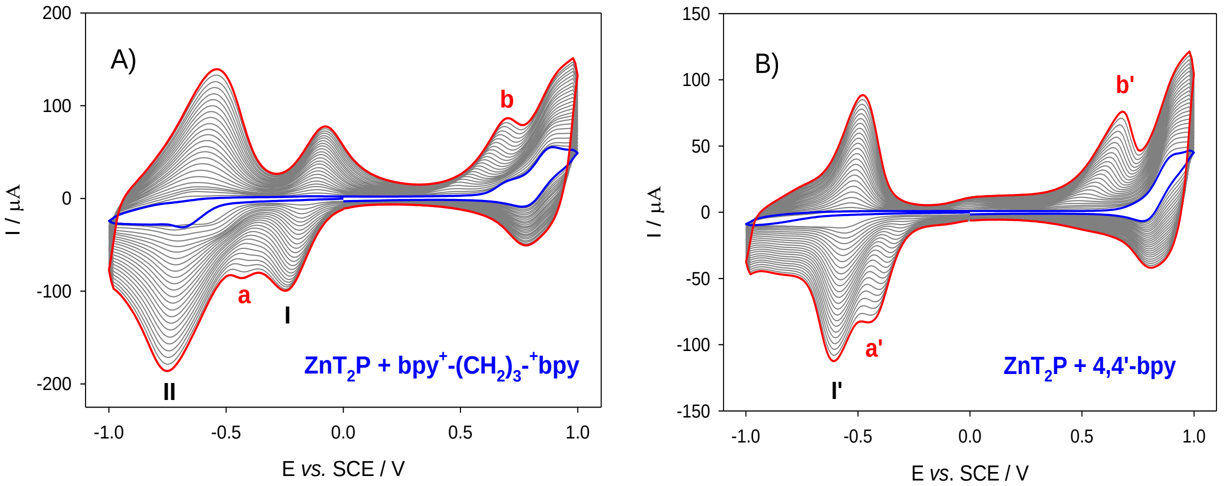

Figure 2.5. Cyclic voltammograms recorded during 25 iterative scans conducted between −1.0 V and +1.0 V *vs.* SCE in a 1,2-$C_2H_4Cl_2/CH_3CN$ (7/3) solution and NBu_4PF_6 (0.1 mol.L^{-1}) of **ZnT$_2$P** (0.25 mmol L^{-1}) in the presence of A) bpy$^+$–(CH$_2$)$_3$–$^+$bpy·2PF$_6^-$ (0.25 mmol L^{-1}) and B) 4,4'-bpy (0.25 mmol L^{-1}). WE: ITO. S = 1 cm^2. v = 100 mV s^{-1}. Blue curve: first scan (n=1). Red curve: final scan (n = 25).

During the electropolymerization of **ZnT$_2$P** in the presence of dipyridyl, when the anodic potential limit is +1.0 V, after the first porphyrin-based oxidation potential, the π-radical cation **ZnT$_2$P$^{+\bullet}$** is produced. As a consequence, we observed significant changes during the electropolymerization process (Fig. 2.5). In the anodic part, the intensity of the oxidation peak near +0.79 V corresponding to the first oxidation of **ZnT$_2$P**, continuously increases with no shift during the electropolymerization proving the formation of a new copolymer **poly-ZnT$_2$isoP$^\bullet$** in this potential range.

In the cathodic range, it must be noted that peak a (or a' in the second copolymer) is irreversible. Additional irreversible peak in oxidation (peak b or b') is observed around +0.5 V for **poly-ZnT$_2$isoP$^\bullet$**. More detailed discussion about peak a and peak b as well as waves I, II (peaks a, b, and waves I', II' for the second copolymer) will be done in part 2.5. These results point out to the formation of a poly-isoporphyrin radical copolymer **poly-ZnT$_2$isoP$^\bullet$** with different behavior than polyporphyrin **poly-ZnT$_2$P**. We present below a detailed characterization of the two copolymers, i.e. **poly-ZnT$_2$isoP$^\bullet$** and **poly-ZnT$_2$P**. A comparison between their different properties is made when appropriate. We named the **poly-ZnT$_2$isoP1$^\bullet$** (obtained from **ZnT$_2$P** and bpy$^+$–(CH$_2$)$_3$–$^+$bpy·2PF$_6^-$) and **poly-ZnT$_2$isoP2$^\bullet$** (obtained from **ZnT$_2$P** and 4,4'-bpy).

2.3. EQCM for the copolymer deposition

The electrosynthesis of **poly-ZnT$_2$isoP$^\bullet$** by electropolymerization with iterative scans between -1.0 and +1.0 V of (Fig. 2.6) has been monitored *in-situ* by EQCM. The variation of the quartz resonance frequency (Δf) decreases when the number of potential cycle increases, which is related to the increase of the amount of polymer deposited (Δm), calculated using Sauerbrey's equation.

Besides, the trace of the first scan in Figure 2.6 AB shows a significant decrease of the resonance frequency and thus an increase of the deposited mass at the first oxidation of the porphyrin; i.e. electropolymerization occurs upon the formation of the radical cation porphyrin **ZnT$_2$P$^{+\bullet}$** in the presence of bpy$^+$–(CH$_2$)$_3$–$^+$bpy·2PF$_6^-$ and 4,4'-bpy. The mass of the copolymer film increases with the number of potential cycle n (Fig. 2.6 CD). Note that a change of slope can be observed for n > 10 which might be related to a transition in the "porous" 3D architecture of the copolymer film and the incorporation of supporting electrolyte as well as solvent molecules.

After 25 iterative scans, 28.01 µg/cm^2 and 9.42 µg/cm^2 of **poly-ZnT$_2$isoP$^\bullet$** in the presence of bpy$^+$–(CH$_2$)$_3$–$^+$bpy·2PF$_6^-$ and 4,4'-bpy are deposited. The calculated surface coverage Γ in mole of repeat unit (ZnT$_2$P-bpy^{2+}–(CH$_2$)$_3$–$^{2+}$bpy·4PF$_6^-$) and (ZnT$_2$P-bpy^{2+}·2PF$_6^-$) for the polymer is 18.8×10^{-9} mol.cm^{-2} and 9.4×10^{-9} mol.cm^{-2}. Similar behavior was observed for the electropolymerization of **poly-ZnT$_2$P** using iterative scans between -1.0 and +1.6 V (Fig. 2.S2). Coverages after 25 iterative scans were about 35.4 µg/cm^2 and 29.1 µg/cm^2. The calculated surface coverage Γ in mole of repeat unit was 23.8 × 10^{-9} mol/cm^2 and 29.1× 10^{-9} mol/cm^2.

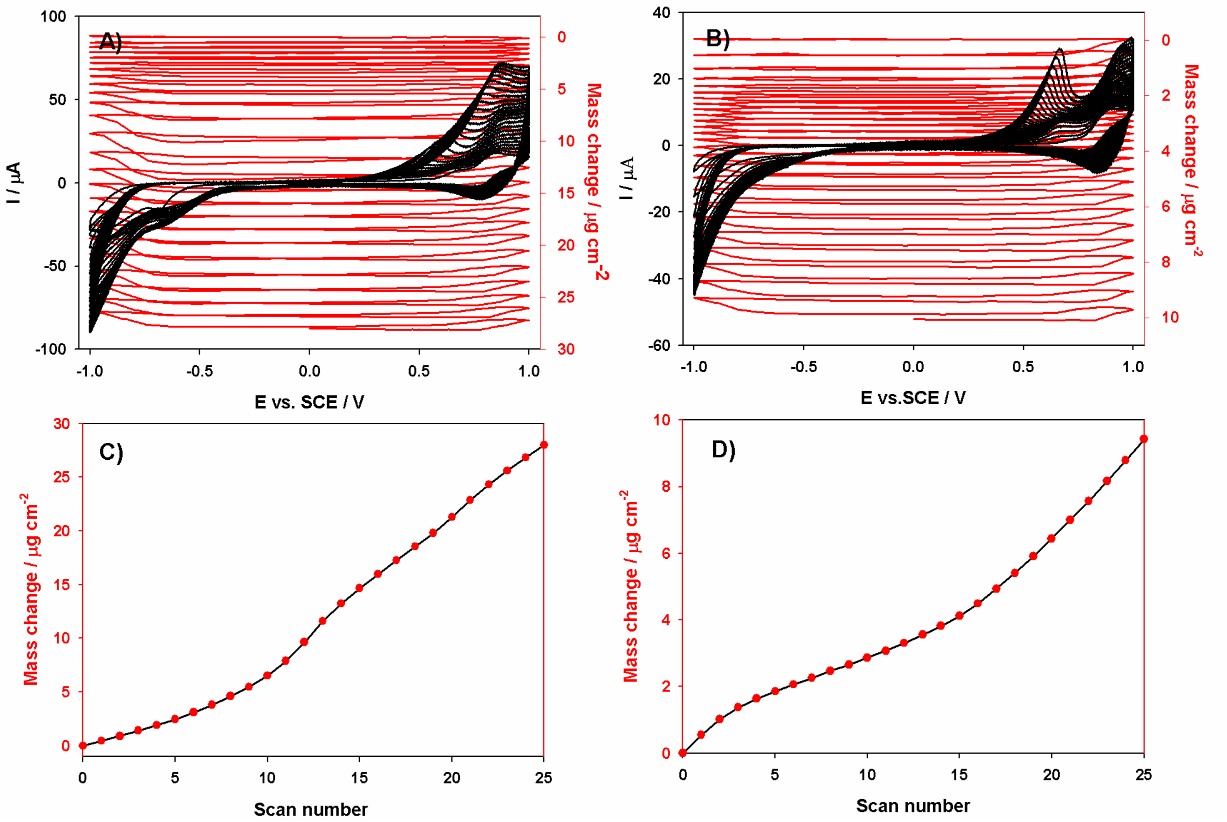

Figure 2.6. Consecutive cyclic voltammograms (first 25 scans) between -1.0 V and +1.0 V and electrochemical quartz crystal microbalance measurements (*Δm*) during the formation of A) **poly-ZnT$_2$isoP1$^{\bullet}$** obtained by the electropolymerization of 0.25 mmol L^{-1} **ZnT$_2$P** with 0.25 mmol L^{-1} bpy^{+}–(CH$_2$)$_3$–$^{+}$bpy·2PF$_6^-$ and B) **poly-ZnT$_2$isoP2$^{\bullet}$** obtained from ZnT$_2$P with 0.25 mmol L^{-1} 4,4'-bpy in 1,2-C$_2$H$_4$Cl$_2$–CH$_3$CN (7/3) in the presence of 0.1 mol L^{-1} NBu$_4$PF$_6$. Working electrode: ITO (A = 0.2 cm^2) deposited on a 9.08 MHz AT-cut quartz crystal. *v* = 100 mV s^{-1}. Mass change (*Δm*) of the first 25 scans calculated from Sauerbrey's equation *versus* the number of scan n of **poly-ZnT$_2$isoP$^{\bullet}$** with 0.25 mmol L^{-1} C) bpy^{+}–(CH$_2$)$_3$–$^{+}$bpy·2PF$_6^-$ and D) 4,4'-bpy.

2.4. UV–Vis-NIR spectroscopy

UV-visible-NIR spectra on ITO electrodes coated with the copolymer **poly-ZnT$_2$isoP$^{\bullet}$** and **poly-ZnT$_2$P** have been measured at various thickness and compared (Fig. 2.7 and Fig. 2.S3 respectively). The absorption intensity of the chromophores increases linearly with iterative scan number (Fig. 2.8). These results have been confirmed by AFM experiments (Figs. 2.14-2.15 for **poly-ZnT$_2$isoP1$^{\bullet}$**) where the thickness was found to increase also linearly *versus* the number of iterative scans.

For **poly-ZnT$_2$isoP1$^{\bullet}$**, the Soret bands were red-shifted by 17 and 58 nm respectively compared to the **ZnT$_2$P** monomer (Table 1 and Fig. 2.9A). The visible bands (Q bands) are also red-shifted by

25 and 51 nm compared to **ZnT$_2$P** and an additional band at 831 nm in the NIR region is also detected. A typical UV-visible-NIR spectrum of **poly-ZnT$_2$isoP2$^\bullet$** obtained after electropolymerization between -1.0 and +1.0 V exhibited a broad split Soret absorption band at λ = 433 nm and λ = 486 nm. The bands were red-shifted by 18 and 71 nm respectively compared to the **ZnT$_2$P** monomer (Table 1 and Fig. 2.9B). The visible bands (Q bands), observed at 573 and 650 nm, are also red-shifted by 27 and 66 nm compared to **ZnT$_2$P** and an additional band at 832 nm in the NIR region is also detected (Fig. 2.7).

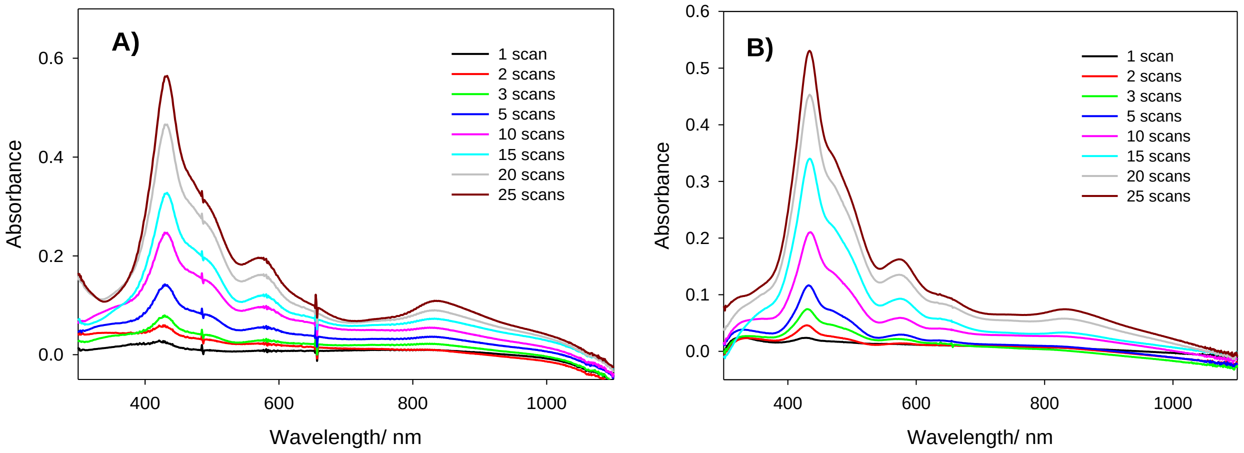

Figure 2.7. UV-visible-NIR absorption spectra of A) **poly-ZnT$_2$isoP1$^\bullet$** and B) **poly-ZnT$_2$isoP2$^\bullet$** onto ITO with different numbers of iterative scans between -1.0 and +1.0 V *vs.* SCE (v = 100 mV s^{-1}). Only one side is covered by ITO.

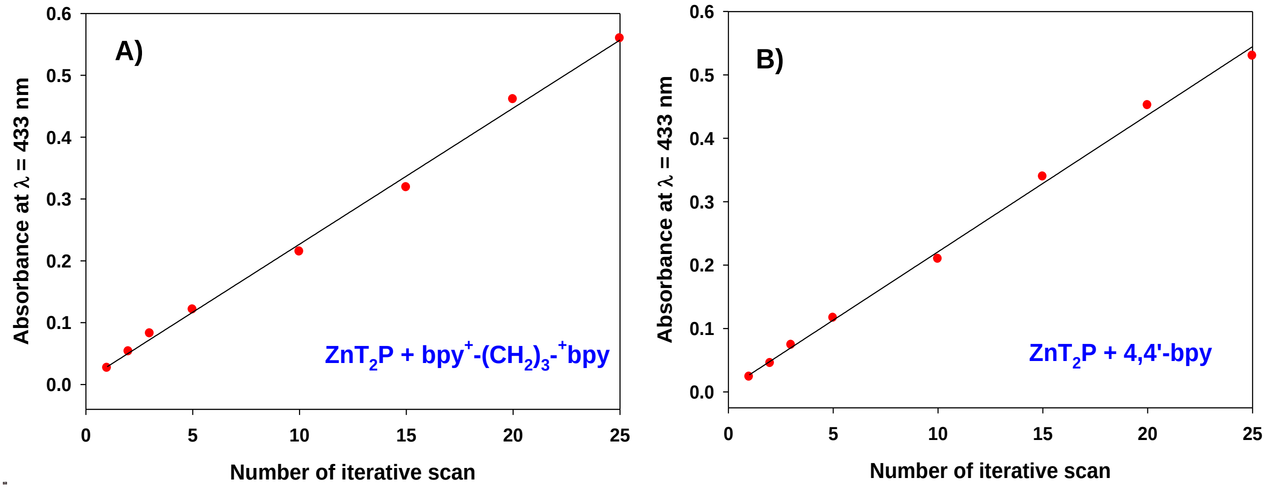

Figure 2.8. Plot of the absorbance measured of A) **poly-ZnT$_2$isoP1$^\bullet$** and B) **poly-ZnT$_2$isoP2$^\bullet$** at λ = 433 nm *versus* n the numbers of iterative scans.

These electropolymerized films have been found to be fully soluble in DMF. Analysis of **poly-ZnT$_2$isoP$^\bullet$** in solution by UV-Vis-NIR absorption spectroscopy revealed comparable spectra than the ones recorded on the solid film (Fig. 2.9).

The superposition of the UV-visible-NIR absorption spectra of **ZnT$_2$P** in solution and of the copolymer **poly-ZnT$_2$isoP$^\bullet$** deposited on ITO are shown for comparison in Figure 2.9. It reveals that the Soret band, attributed to the main porphyrin-based π-π* electronic transition, is much broader, is split and more red-shifted for **poly-ZnT$_2$isoP$^\bullet$** onto ITO electrodes than for **ZnT$_2$P** (Table 2.1). The UV-visible-NIR absorption spectra of ZnT$_2$P showed in Figure 2.S4.

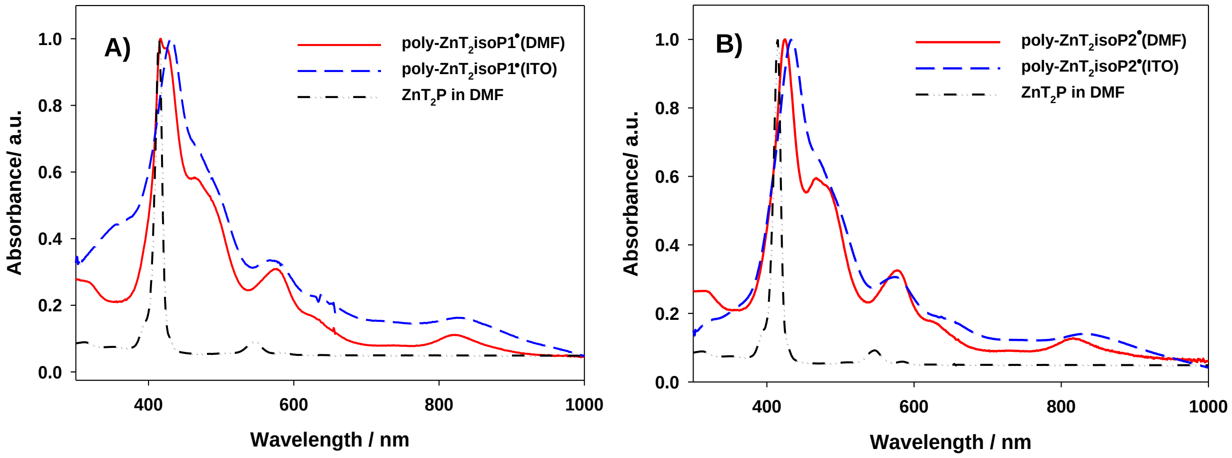

Figure 2.9. Normalized UV-Vis-NIR spectra with A) **poly-ZnT$_2$isoP1$^\bullet$**, and with B) **poly-ZnT$_2$isoP2$^\bullet$** obtained with 10 iterative scans between -1.0 and +1.0 V *versus* SCE at v = 100 mV s^{-1} in DMF solution (red solid line), and on the ITO electrode (blue dash line) and **ZnT$_2$P** (dark dash-dotted line) in DMF solution.

The red shift of the Soret (B) and the Q bands might result from the presence of the electron-withdrawing pyridinium groups as well as from the nonplanar saddle conformation of the macrocycle. Optical red shifts induced by the non-planarity of porphyrins are well documented[29-32] and have been rationalized by a larger destabilization of the highest occupied molecular orbitals (HOMOs) relative to the lowest unoccupied molecular orbitals (LUMOs) resulting in smaller HOMO to LUMO gaps.[33-36] Such changes can be also understood upon considering the presence of intra- and intermolecular exciton-coupling between the porphyrin macrocycle within the copolymer.[37]

Table 2.1. UV–visible spectral data for **ZnT_2P**, bpy$^+$–$(CH_2)_3$–bpy$^+$ $2PF_6^-$ and 4,4’-bpy in CH_3Cl_2, **poly-ZnT_2isoP1$^•$** and **poly-ZnT_2isoP2$^•$** on optical transparent ITO electrodes. Under bracket: molar extinction coefficient (ε /10^3 L.M.cm^{-1}).

Compound	Soret band/nm	Q bands/nm	π-π*Band/nm
ZnT_2P[a]	415 (405.4)	546 (18.9), 584 (4.9)	
bpy$^+$–$(CH_2)_3$–bpy$^+$ $2PF_6^-$[a]			266 (40.8)
4,4’-bpy[a]			238 (12.3)
poly-ZnT_2isoP1[b]	432, 473 (shoulder)	571, 635, 831	
poly-ZnT_2isoP1[c]	415,[f] 423 (shoulder) 463 (shoulder)	573, 631, 824	
poly-ZnT_2P1[d]	429	573, 614, 811	
poly-ZnT_2P1[e]	415,[f] 429	573, 614, 811	
poly-ZnT_2isoP2[b]	434, 486 (shoulder)	573, 650, 832	
poly-ZnT_2isoP2[c]	425, 464 (shoulder)	573, 644, 822	
poly-ZnT_2P2[d]	429	559, 621, 911	
poly-ZnT_2P2[e]	419	552, 608, 831	

[a] In CH_3Cl.
[b] Copolymers obtained by iterative scan between -1.0 V and +1.0 V *vs.* SCE onto ITO.
[c] Copolymers obtained by iterative scan between -1.0 V and +1.0 V *vs.* SCE in DMF.
[d] Copolymers obtained by iterative scan between -1.0 V and +1.6 V *vs.* SCE onto ITO.
[e] Copolymers obtained by iterative scan between -1.0 V and +1.6 V *vs.* SCE in DMF.
[f] Soret band of the **ZnT_2P** monomer which was encapsulated in the film during the electropolymerization and liberated during dissolution of **poly-ZnT_2isoP$^•$**.

The additional bands around 460-480 nm and 800-900 nm may be attributed to the isoporphyrin structure present in the copolymer. Similar absorption bands have been already observed in the case of stable isoporphyrin monomer.[38] Interestingly, the broadening and the splitting of the Soret band as well as the presence of one additional band in the NIR between 750 nm and 1000 nm are expected to be advantageous to photovoltaic applications by extending the domain of solar light absorption.

Poly-ZnT$_2$isoP$^\bullet$ isoporphyrin radical film was found to be highly stable in the presence of oxygen (still stable even after one year). The isoporphyrin radical **Poly-ZnT$_2$isoP$^\bullet$** is also stable in DMF solution.

We have also investigated these poly-porphyrin copolymers (Fig. 2.S3 and Scheme 2.S1) coated films, prepared by changing the number of iterative scans n used for electropolymerization (between -1.0 V and +1.6 V). They exhibited only one large Soret absorption band at λ = 429 nm with a red shift of 14 nm compared to the **ZnT$_2$P** monomer (Fig. 2.S4). Again, a plot of the absorbance recorded at λ = 429 nm (Soret band of the porphyrin) as a function of the number of iterative scans n (Fig. 2.S3) shows a quasi-linear increase of the intensity of the chromophore.

However, the additional band around 470 nm was nearly no detected. It suggested that at higher applied potential, isoporphyrin radical copolymer intermediate could be consumed giving the final poly-porphyrin copolymers with viologen or double viologen as spacers. But the consummation is not quantitative in the case of **poly-ZnT$_2$isoP1$^\bullet$** with double viologen as spacers, as seen in Figs. 2.S3-S4 (not complet deappearance of the NIR band characteristic of the poly-isoporphyrin radical copolymer **poly-ZnT$_2$isoP1$^\bullet$** in the NIR region). It is probably due to *i*) the important thickness of the film and *ii*) to the difficulty to fully oxidize the film if using scan rate of 100 mV s^{-1}.

2.5. Cyclic voltammetric investigations of the copolymeric films.

2.5.1. Cyclic voltammetric investigations of the poly-isoporphyrin poly-ZnT$_2$isoP$^\bullet$ film.

Electroactive polymers deposited by cyclic voltammetry (n iterative scans) on ITO surfaces have been characterized by electrochemical methods. The CV curves shown in Figure 2.10 have been recorded with a copolymer grown on the electrode surface for various potential scans (n = 2, 3, 5, 10, 15, 20 cycles) between -1.0 V and +1.0 V. The electrode was then removed from the electrochemical cell, washed with CH$_3$CN and used as working electrode in a clean electrolytic solution containing only the solvent and the supporting electrolyte.

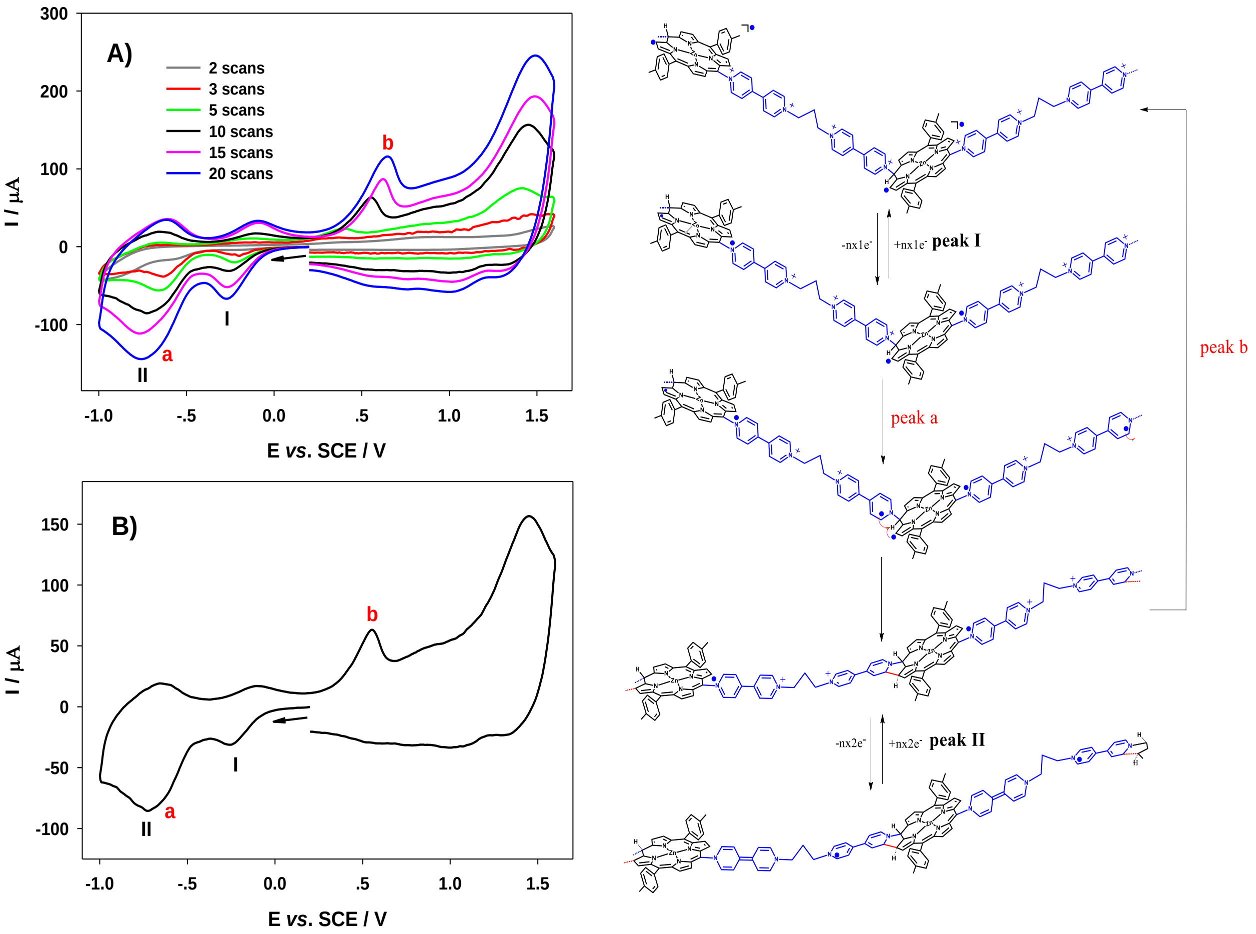

Figure 2.10. Left: cyclic voltammograms of **poly-ZnT$_2$isoP1$^\bullet$** obtained with bpy$^+$–(CH$_2$)$_3$–$^+$bpy·2PF$_6^-$ and **ZnT$_2$P** after A) n = 2, 3, 5, 10, 15 and 20 scans and B) after 10 scans between -1.0 V and +1.0 V in CH$_3$CN/1,2-C$_2$H$_4$Cl$_2$ (3/7) with 0.1 M NBu$_4$PF$_6$. WE: ITO. S = 1 cm^2, v = 100 mV s^{-1}. Irreversible peaks not labelled in anodic part correspond to the oxidation of the π-ring of the macrocycle. Right: proposed reaction mechanism. For more clarity, only intramolecular radical coupling is presented leading to the formation of one additional cycle connected to the porphyrin.

Three successive waves are observed for **poly-ZnT$_2$isoP$^\bullet$** during the cathodic scan (Table 2.2 and Fig. 2.10AB), the first and the last being reversible. The first well defined, bell-shaped, reduction wave observed at –0.18 V vs. SCE (peak I) is attributed to the formation of viologen radical cations in the copolymer (**-ZnT$_2$isoP-$^\bullet$py-py$^+$–(CH$_2$)$_3$–$^+$py-py$^+$-ZnT$_2$isoP-**). The second wave (peak a) detected at -0.62 V is irreversible and very close to the last process (peak II). This wave (peak a) corresponds probably to the reduction of the pyridinium connected to the isoporphyrin (**ZnT$_2$isoP-$^\bullet$py-py$^+$–(CH$_2$)$_3$–$^+$py-py$^\bullet$-ZnT$_2$isoP-**) while the last wave reversible well defined, bell-shaped, reduction wave observed (peak II) is attributed to the second viologen-centered electron transfer (two-electron transfer *per* spacer giving **ZnT$_2$isoP-py-py–(CH$_2$)$_3$–py-py-ZnT$_2$isoP-**).

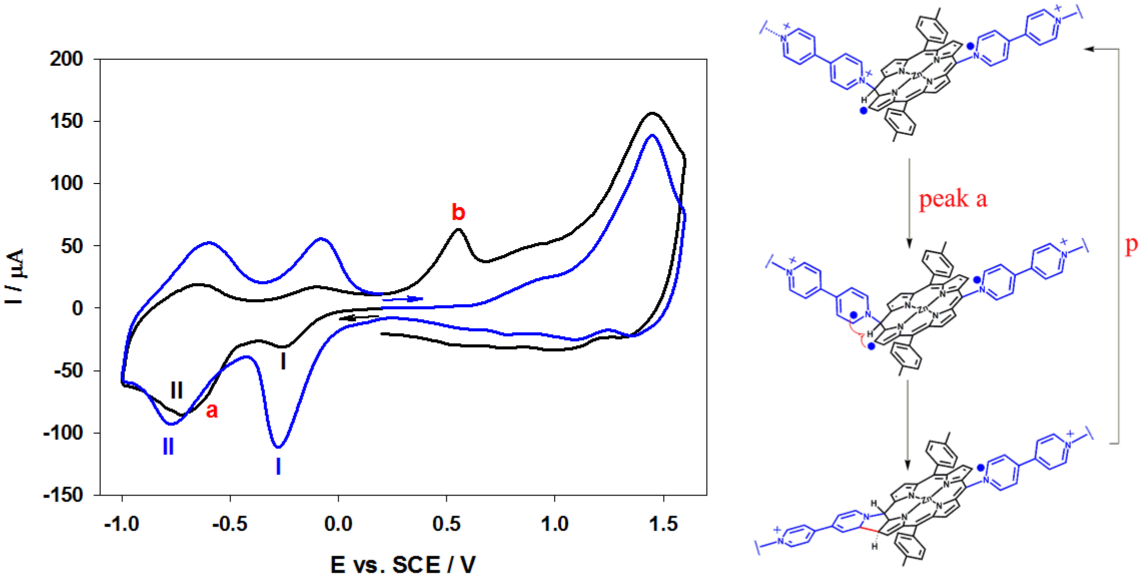

Figure 2.11. Left: cyclic voltammograms of **poly-ZnT$_2$isoP1$^\bullet$** obtained with bpy$^+$–(CH$_2$)$_3$–$^+$bpy·2PF$_6^-$ and **ZnT$_2$P** after n = 10 scans, using iterative scan between -1.0 V and +1.0 V in CH$_3$CN/1,2-C$_2$H$_4$Cl$_2$ (3/7) with 0.1 M TBAPF$_6$. WE: ITO. S = 1 cm^2. v = 100 mV s^{-1}. Blue curve: the direction of the potential scan is reversed (in comparison to the black curve) using new electrode. Right: proposed mechanism explaining the conversion of **poly-ZnT$_2$isoP1$^\bullet$** to **poly-ZnT$_2$P1** during oxidation (blue curve). Peaks I and II correspond to the formation of the bis-radical cation viologen (couple V^{2+}–(CH$_2$)$_3$–V^{2+}/V$^{+\bullet}$–(CH$_2$)$_3$–V$^{+\bullet}$, peak I) and the second reduction of two bis-radical cation viologen units of the spacers yielding V^0–(CH$_2$)$_3$–V^0 (couple V$^{+\bullet}$–(CH$_2$)$_3$–V$^{+\bullet}$/ V^0–(CH$_2$)$_3$–V^0, peak II). V = py-py.

It must be noted, that peak a is associated to the anodic peak b. The irreversibility of peak a may be explained by the radical coupling (intra- or inter-molecular) between two radical pyridyl electrogenerated forming a dipyridine as already observed in the case of the reduction of the pyridinium for ZnOEP-*meso*-py$^+$.[39] Peak b corresponds to the breaking of the C-C bound formed at peak a. Another explanation can be an intramolecular radical coupling between the radical pyridyl and the radical porphyrin and the formation of the C-C bound between the radical pyridyl and the porphyrin giving one additional cycle with five carbons (see in Figure 2.10 and Scheme 2.S1 for the proposed mechanism). The cyclic voltammetry of **poly-ZnT$_2$isoP2$^\bullet$** was showed in Figure 2.S5.

Additionally, **poly-ZnT$_2$isoP1$^\bullet$** films electropolymerized between by -1.0 V and 1.0 V, can be further oxidized up to 1.6 V (Fig. 2.11). Oxidation of the isoporphyrin radical units which give oxidized isoporphyrin is then possible. At this stage, the hydrogen atom located on the *meso*-carbon can be released giving copolymer with similar redox properties than **poly-ZnT$_2$P1**. Thus, it is feasible to oxidize the radical isoporphyrin **poly-ZnT$_2$isoP1$^{\bullet}$** copolymer and then remove the hydrogen atom located on the *meso*-carbon giving the formation of **poly-ZnT$_2$P1** with a double viologen spacer.

Table 2.2. Electrochemical data for **ZnOEP**, **ZnT$_2$P**, bpy$^+$–(CH$_2$)$_3$–$^+$bpy 2PF$_6^-$, **poly-ZnT$_2$P1**, **poly-ZnT$_2$isoP1$^{\bullet}$**, **poly-ZnT$_2$P2, poly-ZnT$_2$isoP2$^{\bullet}$**.

Compounds	Ring oxidation			Reduction of spacer			Ring reduction	
			peak b	peak I or I’	peak a (or peak c)	peak II or II’		
ZnOEP^a	1.08 (130)	0.71 (128)					-1.66	
ZnT$_2$P^b	1.08 (150)	0.79 (90)					-1.41 (160)	-1.84 (170)
bpy$^+$–(CH$_2$)$_3$– $^+$bpy·2PF$_6^-$					-0.68^{irr}			
poly-ZnT$_2$isoP1$^{\bullet}$□	$+1.45^{irr}$	$+0.89^{irr}$	$+0.55^{irr}$	-0.18 (140)	-0.62^{irr}	-0.70 (70)		
poly-ZnT$_2$P1	$+1.35^{irr}$	+1.09 (130)		-0.13 (170)	($+0.08^{irr}$)	-0.63 (120)		
poly-ZnT$_2$isoP2$^{\bullet}$	1.28^{irr}	$+0.97^{irr}$	$+0.48^{irr}$		-0.44^{irr}	-0.60 (124)		
poly-ZnT$_2$P2	1.45^{irr}			-0.09 (174)	($+0.12^{irr}$)	-0.61 (200)		

[a] Potentials in V *vs.* SCE were obtained from cyclic voltammetry in 1,2-C$_2$H$_4$Cl$_2$ with 0.1 mol L^{-1}TBAPF$_6$. Scan rate = 100 mV s^{-1}. Working electrode: ITO, S=1 cm^2.

[b] Potentials in V *vs.* SCE were obtained from cyclic voltammetry in CH$_3$CN/1,2-C$_2$H$_4$Cl$_2$ (3/7) with 0.1 mol L^{-1} TBAPF$_6$. Scan rate = 100 mV s^{-1}.

The given half-wave potentials are equal to $E_{1/2} = (E_{pa} + E_{pc})/2$. Under bracket: $\triangle E_p = |E_{pa} - E_{pc}|$.

2.5.2. Cyclic voltammetric investigations of the poly-porphyrin poly-ZnT$_2$P film.

Electropolymerization using iterative scan between -1.0 V and 1.6 V *vs.* SCE in the presence of **ZnT$_2$P** and bpy$^+$–(CH$_2$)$_3$–$^+$bpy·2PF$_6^-$, was also performed to obtain **poly-ZnT$_2$P1** film with double viologen spacers (Scheme 2.S1). **Poly-ZnT$_2$P1** copolymers were studied in the electrolyte used for electropolymerization that is CH_3CN/1,2-$C_2H_4Cl_2$ (3/7) solution with 0.1 M NBu_4PF_6.

In contrast with **poly-ZnT$_2$isoP1$^\bullet$**, no irreversible wave was detected in the cathodic part and only two successive reversible reductions (peaks I and II) were measured for the poly-poprhyrin **poly-ZnT$_2$P1**.

The two reduction peaks centered at ca. -0.13 V (peak I) and -0.63 V (peak II) correspond to the formation of the bis-radical cation viologen (couple V^{2+}–(CH$_2$)$_3$–V^{2+}/$V^{+\bullet}$–(CH$_2$)$_3$–$V^{+\bullet}$, V = py-py, peak I) and the second reduction of two bis-radical cation viologen units of the spacers yielding V^0-(CH$_2$)$_3$-V^0 (couple $V^{+\bullet}$–(CH$_2$)$_3$–$V^{+\bullet}$/ V^0–(CH$_2$)$_3$–V^0, peak II) (Table 2, Fig. 2.12). peak I' and II' is corresponding to the radical cation viologen (py$^+$-py$^+$/py$^\bullet$-py$^+$) and (py$^\bullet$-py$^+$/py-py).

It must be noted that under the measurement conditions, the splitting of the second reduction wave of the viologen, observed with the **ZnOEP** porphyrin[18] was not detected in the case of **ZnT$_2$P** porphyrin.

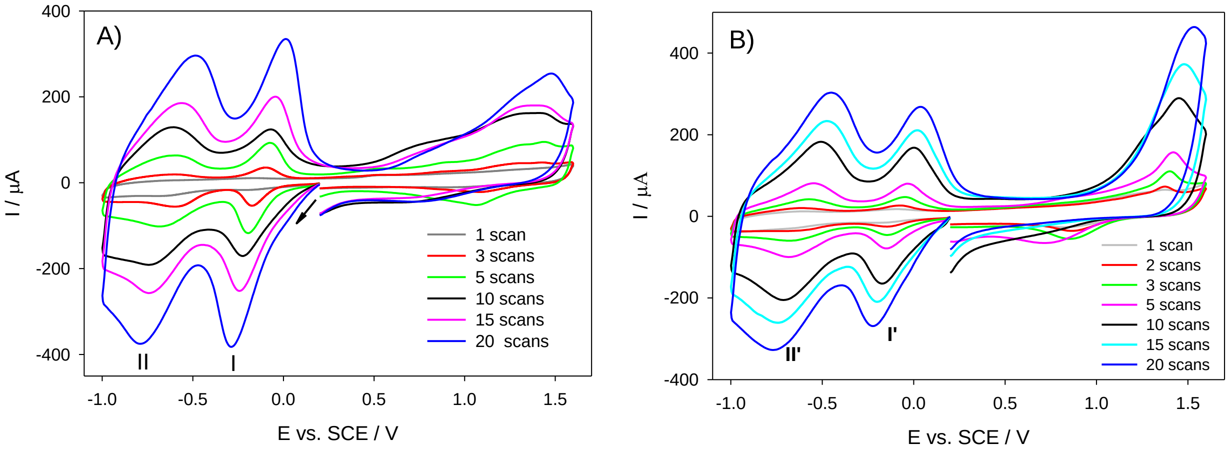

Figure 2.12. Cyclic voltammograms of A) **poly-ZnT$_2$P1** obtained with **ZnT$_2$P** and bpy$^+$–(CH$_2$)$_3$–$^+$bpy·2PF$_6^-$, B) **poly-ZnT$_2$P2** obtained with **ZnT$_2$P** and 4,4'-bpy after n = 1, 2, 3, 5, 10, 15 and 20 scans, between -1.0 V and +1.6 V in CH_3CN/1,2-$C_2H_4Cl_2$ (3/7) with 0.1 M NBu_4PF_6. WE: ITO. S = 1 cm^2. v = 100 mV s^{-1}.

2.6. Electron spin resonance (ESR) spectroscopy

Copolymer **poly-ZnT$_2$PisoP1$^\bullet$** onto ITO glass prepared after 50 iterative scans was inserted directly to the ESR cavity and the spectrum recorded at room temperature shows spectral contributions from two paramagnetic species. The dominant feature shows a broad signal of six lines and comes from an impurity in the ITO glass. A less intense line is observed in the middle of the spectrum and probably arises from an organic radical.

To confirm the presence of the organic radical, **poly-ZnT$_2$isoP1$^\bullet$** films onto ITO were prepared with the same conditions (25 iterative scans between -1.0 V and 1.0 V, v = 100 mV.s^{-1}).

Poly-ZnT$_2$isoP1$^\bullet$ was then removed from ITO using DMF. The operation was repeated three times. The obtained solutions were degassed and transferred to a capillary. The ESR spectrum shown in Fig. 2.13 reveals probably the presence of the radical centered on the isoporphyrin (g=2.0026, linewidth=6 G).[40] Increasing the concentration of the deposited copolymer on the ITO glass leads to an enhancement of the ESR intensity.

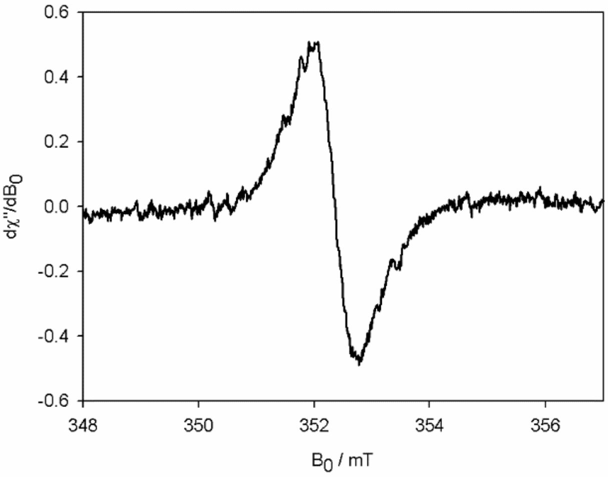

Figure 2.13. X-Band EPR spectrum in DMF of **poly-ZnT$_2$isoP1$^\bullet$** at room temperature. The solution of **poly-ZnT$_2$isoP1$^\bullet$** was prepared by washing with 160 µL of DMF the covered ITO obtained using 25 scans between -1.0 V and 1.0 V, v = 100 mV.s^{-1}. In order to have enough solution, the operation was repeated three times.

Usually, isoporphyrin or radical cations porphyrins are reactive and undergo facile degradation. In this study, **poly-ZnT$_2$isoP$^\bullet$** isoporphyrin radical film is remarkably stable for one year at the solid state (in air). This stability may be due to the *i*) electron-withdrawing groups which significantly facilitate the reduction and stabilize the radical cation, *ii*) the delocalization of the radical through the porphyrin as well as intermolecular π-π stacking and π-dimerization between macrocycles.

2.7. Film Morphology (Atomic Force Microscopy)

2.7.1. Film Morphology (Atomic Force Microscopy) of poly-ZnT$_2$isoP$^{\bullet}$ copolymer.

The films obtained by iterative scan between -1.0 V and +1.0 V were studied by scanning atomic force microscopy (AFM) (Figs 2.14-15). In a characteristic picture for **poly-ZnT$_2$isoP1$^{\bullet}$**, copolymer appears on the surface as tightly packed coils with an average diameter of ca. 60-70 nm, the height being around 8.0 nm for the film obtained after 3 iterative scans between -1.0 V and +1.0 V (Fig. 2.14). The rms surface roughness of the two films have been estimated at 2.0 nm for **poly-ZnT$_2$isoP1$^{\bullet}$**, (calculated from an area of 1.0 µm^2 for Figure 2.14). The **poly-ZnT$_2$isoP1$^{\bullet}$** copolymer obtained after higher iterative scan number exhibited comparable morphology but showed in several positions some aggregation of the coils accompanied by a larger value of the rms surface roughness (8.8 nm for n = 10). The formation of coil aggregates might be related to the change of slope of the deposited mass, observed from EQCM measurements in Figure 2.6.

The **poly-ZnT$_2$P1** films were also studied by AFM (Fig. 2.S6). The **poly-ZnT$_2$P1** copolymer appears on the surface yet again as tightly packed coils with an average diameter of ca. 120-150 nm, the height being around 25-30.0 nm for the film obtained after 20 iterative scans (n = 20). The rms surface roughness of the films has been estimated at 3.0 nm.

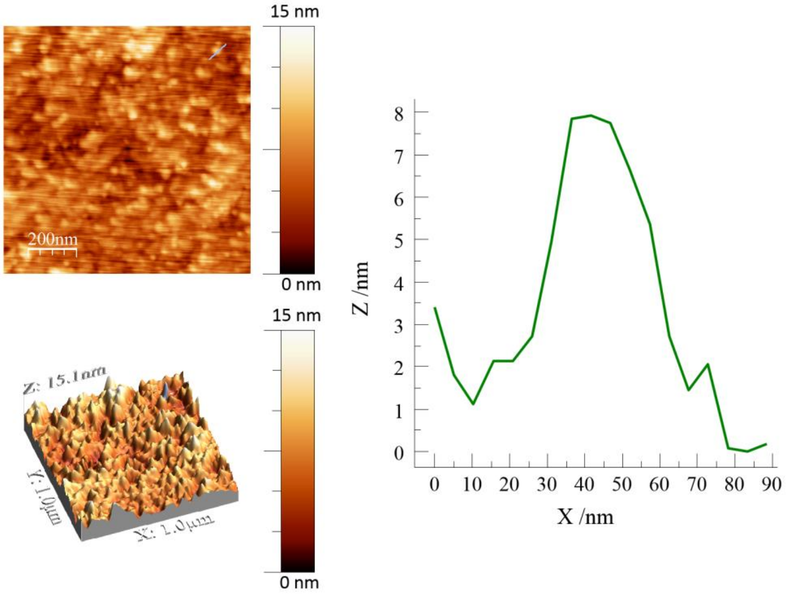

Figure 2.14. Left: Tapping mode AFM topography of **poly-ZnT$_2$isoP1$^{\bullet}$** (deposition between -1.0 V and +1.0 V vs. SCE on ITO, n = 3). Right: section analysis of the aggregate marked by a blue line.

2.7.2. Thickness measurement of copolymeric films

The thickness of the **poly-ZnT$_2$isoP1$^\bullet$** copolymer (Fig. 2.15) have been estimated upon scratching the film with a metallic tip and measuring the relative heights on each side of the scratch (Fig. 2.15AB). The thickness measured by AFM was found to increase with the deposition time to reach an upper limit value for all the films studied. This trend is in line with the data recorded by UV-Vis-NIR absorption spectroscopy. The thickness measured after ten iterative scans (scan rate 100 mV s^{-1}) was estimated to 30 nm for **poly-ZnT$_2$isoP1$^\bullet$** (Fig. 2.15CD, dark cyan triangle up).

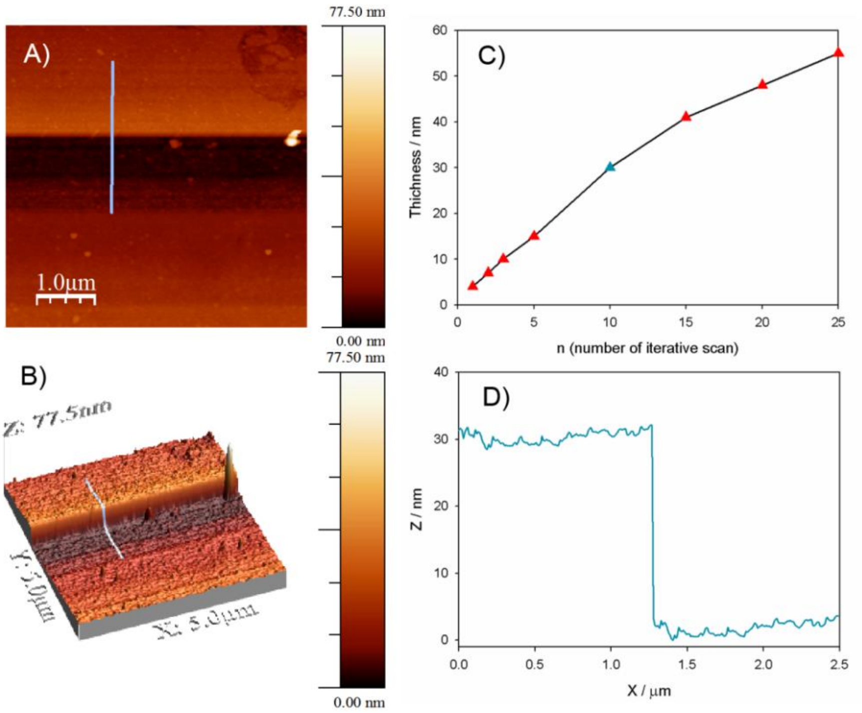

Figure 2.15. A) Tapping mode AFM topography (AFM, surface plot, 2D top view) image of the modified ITO electrode with **poly-ZnT$_2$isoP1$^\bullet$** obtained after 10 iterative scans. B) AFM 3D image and section analysis. C) Thickness measured from AFM versus different numbers of iterative scans (between -1.0 and 1.0 V vs. SCE). The dark cyan triangle up corresponds to the measurement obtained from B) and D). D) section analysis.

2.8. X-ray photoelectron spectra (XPS) of copolymers

The copolymer films were also investigated by X-Ray photoelectron spectroscopy. The analysis of the survey spectra of **poly-ZnT$_2$isoP1$^\bullet$** (Fig. 2.16) confirms the presence of the isoporphyrin and of the–V^{2+}–$(CH_2)_3$–V^{2+}– spacer (Zn 2p3 at 1021.7 eV, Nb1s, and C 1s peaks), while the signals for F 1s (686.6 eV), and P 2p (136.7 eV) electrons stem from the incorporated counterion PF_6^- to equilibrate the pyridiniums charges. The C1s peaks are composed of two signals at 284.8 and 286.5 eV attributed to homo and hetero (connected to nitrogen) carbon atoms respectively. The N1s peaks reveal the presence of three chemically different nitrogens. The contributions at 398.6 eV and 400.3 eV are attributed to the iminic nitrogen and to the reduced bis-viologen respectively. The peaks at ca. 402.3 eV might result from the two viologen groups and the presence of tetrabutylammonium in the film. The O 1s signal comes from H_2O adsorbed on the copolymer surface. Similar behavior is observed for **poly-ZnT$_2$P1, poly-ZnT$_2$isoP2$^\bullet$** and **poly-ZnT$_2$P2** film. (Figs. 2S7-9).

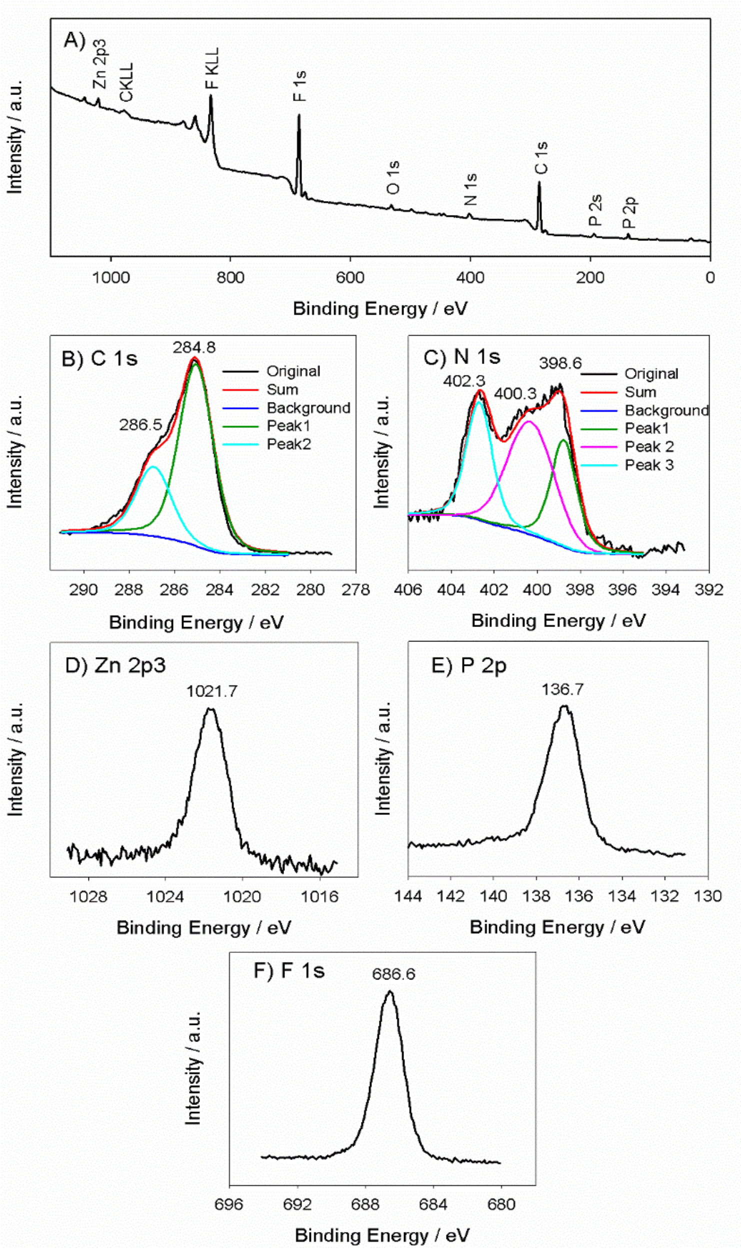

Figure 2.16. XPS spectra of the modified ITO electrodes **poly-ZnT$_2$isoP1$^\bullet$** on ITO (achieved from ZnT$_2$P and bpy$^+$-(CH$_2$)$_3$-$^+$bpy 2PF$_6^-$ obtained after 25 iterative scans between -1.00 and 1.00 V *versus* SCE. XPS spectra (A), C 1s (B), N 1s (C), Zn 2p3 (D), P 2p3 (E), F 1s (F).

3. Photoelectrochemical properties

3.1. Effect of film thickness

Figure 2.17A shows the typical current-potential curves of **poly-ZnT$_2$isoP1$^\bullet$** and **poly-ZnT$_2$P1** thin films on ITO electrodes obtained in 5 mM I_2 / 0.5 M I^- aqueous solution.

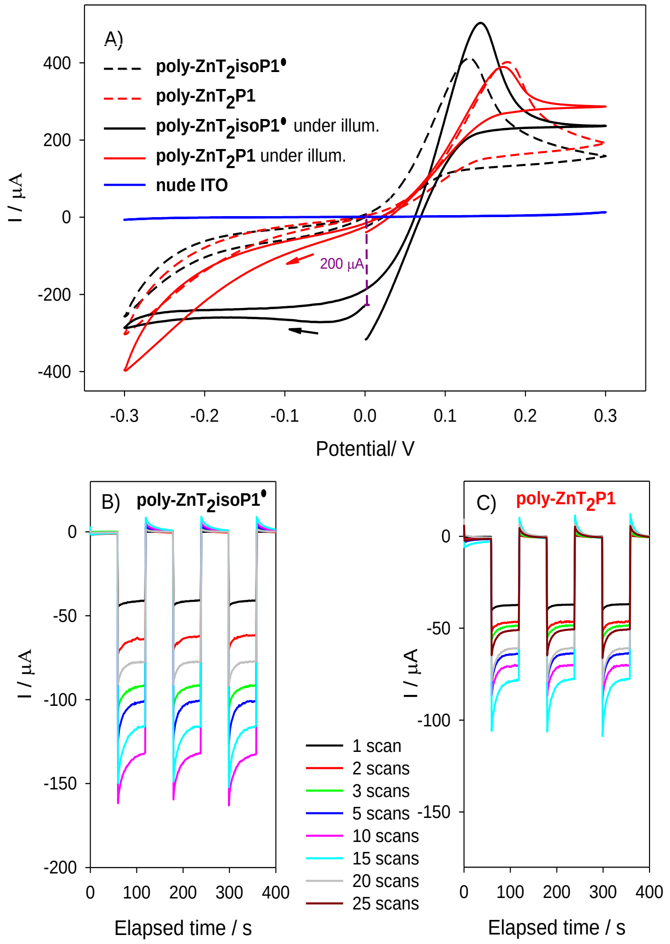

Figure 2.17. A) Current-potential curves of **poly-ZnT$_2$isoP1$^\bullet$** (obtained with n = 10 iterative scans between -1.0 V and +1.0 V) and **poly-ZnT$_2$P1** (obtained with n = 10 iterative scans between -1.0 V and +1.6 V) thin films on ITO electrodes obtained in 0.5 M I^- / 5 mM I_2 aqueous solution in the dark or under visible illumination. B) and C) Photoelectrochemical response of **poly-ZnT$_2$isoP1$^\bullet$** and **poly-ZnT$_2$P1** films obtained with n = 1, 2, 3, 5, 10, 15, 20 or 25 iterative scans. Measurements has been done under on-off light illumination from a 300 W Xe arc lamp (with $\lambda > 385$ nm long pass filter) in I_3^- 5 mmol L^{-1} and I^- 0.5 mol L^{-1} aqueous solution. BIAS potential: 0.00 V *vs.* OCP.

The equilibrium potential of I_3^-/I^- redox couple in solution is taken as reference potential at 0 V in the cyclic voltammograms. For ten electropolymerization cycles, the amount of deposited copolymer on ITO substrate is approximately the same (ca. 6 µg/cm^2) for both **poly-ZnT$_2$isoP1$^\bullet$**

and **poly-ZnT$_2$P1** samples, thus enabling the comparison of their (photo)electrochemical properties. First, we analyse the curves obtained in the absence of illumination (plotted with dashed lines in Figure 2.17A).

For bare ITO electrode (blue curve), almost no faradic current is observed between -0.3 and 0.3 V, revealing the slow I^- oxidation and I_3^- reduction kinetics on ITO. However, the I^- oxidation and I_3^- reduction currents are significantly enhanced on the ITO modified by the copolymers (black and red curves in Figure 2.17A).

For the I^- oxidation, anodic current peaks at ca. 0.1 V for **poly-ZnT$_2$isoP1$^\bullet$** and at ca. 0.2 V for **poly-ZnT$_2$P1** are observed. At this stage, the reasons why the I^- oxidation current goes through a maximum are unclear. Considering the high I^- concentration in solution (0.5 mol L^{-1}), the current limitation cannot be attributed to the I^- mass transport in solution. One possible explanation is that the current peak arises from the low solubility of the I_2 produced in the vicinity of the electrode surface, the undissolved I_2 blocking the access of I^- to the electrode surface and then its oxidation. Interestingly, the anodic peak potential is negatively shifted by ca. 0.1 V on **poly-ZnT$_2$isoP1$^\bullet$** compared to **poly-ZnT$_2$P1** suggesting that the I^- oxidation kinetics is significantly faster on the **poly-ZnT$_2$isoP1$^\bullet$** modified electrode. In contrast, the I_3^- reduction current is slightly lower on **poly-ZnT$_2$isoP1$^\bullet$** than on **poly-ZnT$_2$P1** showing that the **poly-ZnT$_2$P1** copolymer is a better catalyst for the I_3^- reduction than **poly-ZnT$_2$isoP1$^\bullet$**.

The current-potential curves measured under visible light illumination and potentiodynamic conditions are also plotted in Figure 2.17A (full line) for the **poly-ZnT$_2$isoP1$^\bullet$** and **poly-ZnT$_2$P1** copolymers respectively. The photocurrent response in the potentiostatic mode at 0 V under on-off light illumination cycles is shown in Figure 2.17BC. Under visible light, the open circuit potential increases of ca. 80 and 30 mV for the **poly-ZnT$_2$isoP1$^\bullet$** and **poly-ZnT$_2$P1** copolymers respectively. Above this potential, the I^- oxidation current becomes predominant due to the high I^- concentration in solution, impeding thus further increase of the photovoltage. For potentials below the OCP, a negative photocurrent is observed for both copolymers, the photocurrent at 0 V of the **poly-ZnT$_2$isoP1$^\bullet$** copolymer thin film reaching ca. -140 µA cm^{-2} (potentiostatic experiment) or -200 µA cm^{-2} (measured from the CV) while it is only of -70 µA cm^{-2} (potentiostatic experiment) or -30 µA cm^{-2} (in the CV) on **poly-ZnT$_2$P1** for approximately the same amount of electrodeposited copolymer. The photocurrent at 0 V of the poly-isoporphyrin radical copolymer thin film **poly-**

$ZnT_2isoP2^{\bullet}$ reaching ca. -185 µA cm^{-2} while it is only of -147 µA cm^{-2} (potentiostatic experiment) for the corresponding poly-porphyrin **poly-ZnT_2P2** (Fig. 2S10).

The better performances of isoporphyrin radical copolymer can be tentatively attributed to the broad Soret absorption band improving the light harvesting efficiency in the visible range and then the photocurrent. It should be mentioned that the presence of an additional absorption band at 850 nm in the optical spectra of the isoporphyrin copolymer may also be beneficial for the photocurrent. For all the copolymers, the photocurrent level remains stable after several hours of on-off illumination cycles at 0 V (not shown) indicating that the copolymers are stable under photocurrent generation.

The magnitude of the photocurrent strongly depends on the number of potential scans n and then of the amount of copolymer film deposited as displayed in Figure 2.17BC and in Figure 2.19A. For both copolymers, the photocurrent goes through an optimum as a function of n, the best performances being obtained for n=10 or 15 electropolymerization cycles. It is confirmed that higher photocurrents are obtained with the isoporphyrin copolymer **poly-$ZnT_2isoP1^{\bullet}$** than **poly-ZnT_2P1**.

Further insights into the photoelectrochemical behaviour of the copolymer films as a function of n could be gained by electrochemical impedance spectroscopy, which is widely used in the investigation of dye sensitized solar cell. The Nyquist and Bode plots of a typical impedance spectra measured for (**poly-$ZnT_2isoP1^{\bullet}$**) at 0 V in 5 mM I_3^- / 0.5 M I^- aqueous solution are plotted in Figure 2.18 for n=10. All the impedance spectra of the copolymer films (**poly-$ZnT_2isoP^{\bullet}$** and **poly-ZnT_2P)** obtained for various number of potential scans, n=1, 2, 3, 5, 10, 15 and 20 are given in supplementary information (Figs. 2. S11-S14). For low n values (i.e. 1 or 2 scans), the Nyquist diagrams exhibit only one semi-circle, which can be modelled by the charge transfer resistance R_{ct} of the I^-/I_3^- species at the ITO/solution interface in parallel with the interfacial capacitance C_i. Interestingly, two semicircles are clearly observed in the Nyquist plots when the thickness of the copolymer film increases, i.e. for n >2 for (**poly-$ZnT_2isoP1^{\bullet}$**) and n>10 for (**poly-ZnT_2P1**). The emergence of the second impedance loop is attributed to the charge transport processes within the copolymer film. In this case, the impedance spectra can be modelled with the equivalent circuit displayed in Figure 2.18 where R_{ct_film} is a charge transfer resistance in the film, C_f the chemical capacitance of the film and Z_w the Warburg impedance.

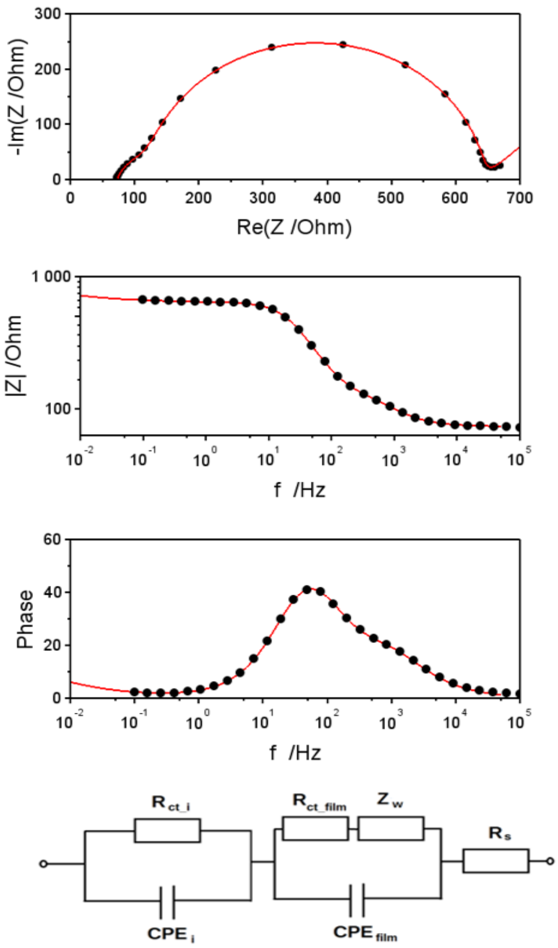

Figure 2.18. Electrochemical impedance spectroscopy (EIS) Nyquist and Bode plots (phase *vs.* frequency (f) and ∣ Z ∣ *vs.* f) of **poly-ZnT$_2$isoP1$^\bullet$** (n = 10). Measurements has been done in H_2O containing I_3^- 5 mmol L^{-1} and I^- 0.5 mol L^{-1}. BIAS potential: 0.0 V *vs.* OCP. Bottom: equivalent circuit use for fit of experimental data.

The evolution of R_{ct} and R_{ct_film} values as a function of n can be estimated from the fit of the experimental impedance spectra and is displayed in Figure 2.19B for the **poly-ZnT$_2$isoP1$^\bullet$** and **poly-ZnT$_2$P1** copolymers thin films. Overall, the charge transfer resistance R_{ct} at the ITO/copolymer interface decreases when n increases while the charge transfer resistance R_{ct_film} increases with the amount of copolymer deposited. For the **poly-ZnT$_2$isoP1$^\bullet$** copolymer, R_{ct} ITO/copolymer decreases from ca. 20 kΩ for n=1 to ca. R_{ct} ~ 500 Ω for n=10, confirming the enhancement of the I^-/I_3^- charge transfer kinetics when the copolymer is present on the ITO. For n>10, R_{ct} reaches a plateau suggesting that the ITO surface is fully covered by the copolymer.

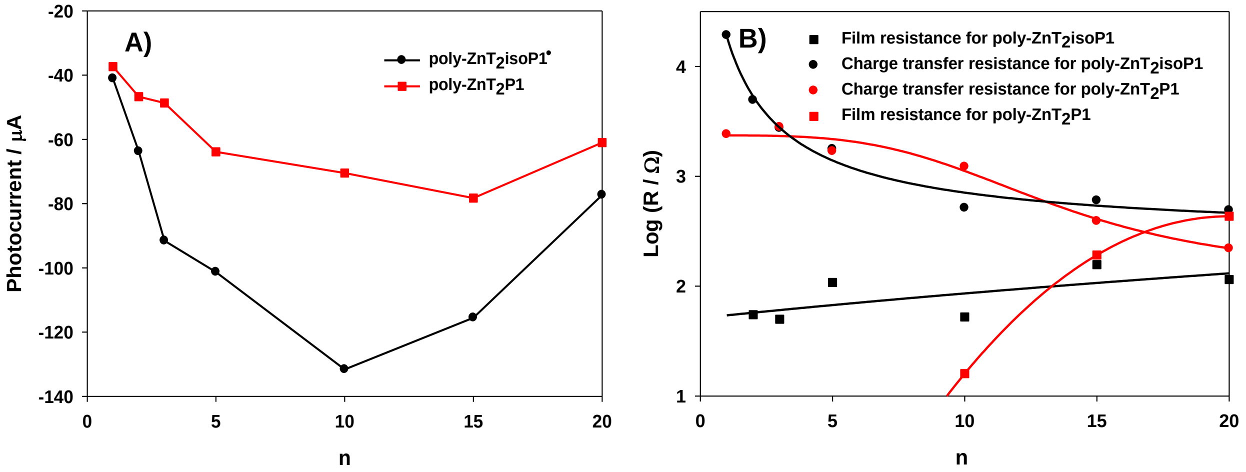

Figure 2.19. A) Photoelectrochemical response of **poly-ZnT$_2$isoP1$^\bullet$** (black line) and **poly-ZnT$_2$P1** (red line) obtained with bpy$^+$–(CH$_2$)$_3$–$^+$bpy 2PF$_6^-$ and **ZnT$_2$P** obtained with n = 1, 2, 3, 5, 10, 15 and 20 iterative scans. B) Plot of the Log(R) versus n (number of iterative scan, v = 100 mV s^{-1}, between -1.0 V and +1.0 V for **poly-ZnT$_2$isoP1$^\bullet$** and between -1.0 V and +1.6 V for **poly-ZnT$_2$P1**. Measurements has been done in H$_2$O under one off light illumination from a 300W Xe arc lamp (with λ > 385 nm long pass filter) containing I$_3^-$ 5 mmol L^{-1} and I$^-$ 0.5 mol L^{-1}. BIAS potential: 0.00 V *vs.* OCP.

Thus the enhancement of the photocurrent generation with the amount of deposited copolymer that is observed for n<10 might be attributed to the improvement kinetics interfacial charge transfer kinetics and to the increase of the light harvesting efficiency of the film (Fig. 2.19A). For n>10, the charge transfer resistance within the film R$_{ct\_film}$ start to increase reaching 100 Ω and 500 Ω at n=20 for the **poly-ZnT$_2$isoP1$^\bullet$** and **poly-ZnT$_2$P1** copolymers, respectively. The decrease of the photocurrent for n>10 stems from the slow kinetics of the charge transfer within the polymer films. Similar conclusion could be obtained for **poly-ZnT$_2$isoP2$^\bullet$** and **poly-ZnT$_2$P2** (Fig. 2S15)**.**

3.2. Effect of radicals of isoporphyrin

To prove the effect of NIR absorption band for photocurrent generation, the light was controlled by using filter which could absorb the visible light and the results showed in Figure 2.20. The typical current-potential curves were shown in Figure 2.S16. It demonstrated that under NIR light illumination, the photocurrent at 0 V of the **poly-ZnT$_2$isoP2$^\bullet$** copolymer thin film reaching ca. -35 µA cm^{-2} while it is -199 µA cm^{-2} of **poly-ZnT$_2$isoP2$^\bullet$** under visible-NIR light illumination. Also for **poly-ZnT$_2$isoP1$^\bullet$**, photocurrent can reach -33 µA cm^{-2} under NIR light and -127 µA cm^{-2} under visible-NIR light illumination. From the results, the NIR absorption band of **poly-ZnT$_2$isoP2$^\bullet$** can make 17.5% contribution of photocurrent generation under visible-NIR illumination. For **poly-ZnT$_2$isoP1$^\bullet$**, the ratio is 26.0%. It means the NIR absorption band of isoporphyrin radical copolymer prepared with double viologen spacers (**poly-ZnT$_2$isoP1$^\bullet$**) can make a better photocurrent generation than single viologen spacers (**poly-ZnT$_2$isoP2$^\bullet$**).

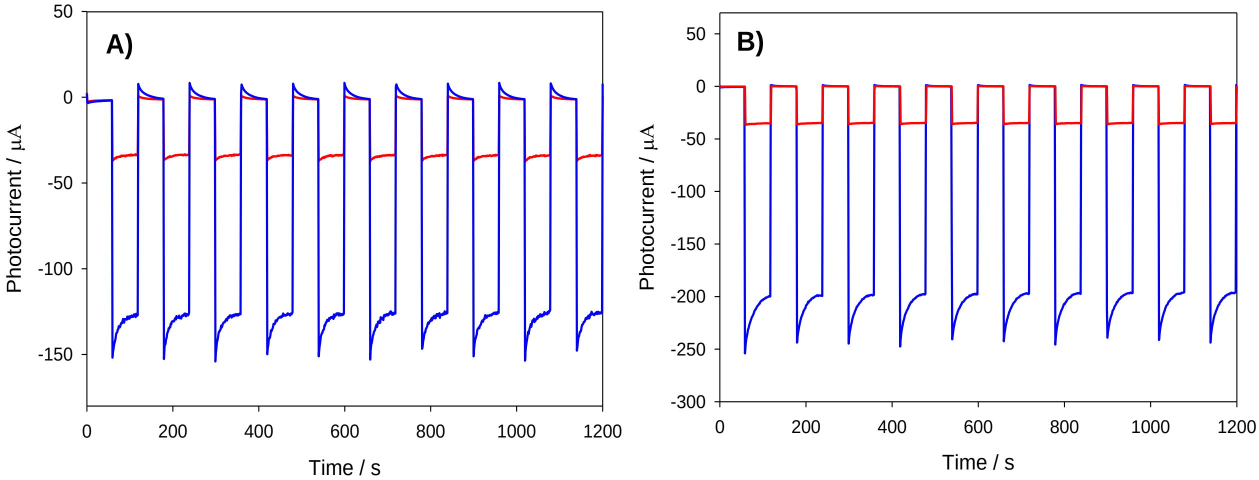

Figure 2.20. Photoelectrochemical response of **poly-ZnT$_2$isoP1$^\bullet$** and **poly-ZnT$_2$isoP2$^\bullet$** films obtained at 10 scans under on-off light under NIR light (red line) or visible-NIR light illumination (blue line) in I_3^- 5 mmol L^{-1} and I^- 0.5 mol L^{-1} aqueous solution. BIAS potential: 0.00 V *vs.* OCP.

3.3. Energy diagram of the electron transfer process

Figure 2.21. represents the energy diagram corresponding to the photoreduction of I_3^- on the copolymer **poly-ZnT$_2$isoP1$^\bullet$**. The explanation suits also for **poly-ZnT$_2$P1**, **poly-ZnT$_2$isoP2$^\bullet$**, and **poly-ZnT$_2$P2$^\bullet$**.

The HOMO level energies of the **poly-ZnT$_2$isoP$^\bullet$** and **poly-ZnT$_2$P** species have been estimated from the first oxidation potential observed in the CV, while the energy level of the dipyridinium species is given by the potential of the first reduction peak (Table 2.2). The LUMO levels of the excited **poly-ZnT$_2$isoP$^\bullet$** and **poly-ZnT$_2$P** species can be roughly estimated by subtracting the excitation energy of the Soret or Q bands from the HOMO level energies. The energy Level corresponding to the band in the NIR region has also been indicated in the energy diagram. Under illumination at 0 V, the photon absorption by the (iso)porphyrin entities generates an electron hole pair in the copolymer. The electron is transferred from the excited (iso)porphyrins to the I_3^- which is reduced into I^-, the double viologen spacer eventually acting as a relay for the electron transfer. The oxidized (iso)porphyrins are regenerated by an electron transfer from the ITO substrate. The I_3^-

reduction is in competition with the recombination of the photogenerated electron-hole pair. Thus, fast electron transfer kinetics between the ITO and the oxidized (iso)porphyrins and/or between the excited (iso)porphyrins and the I_3^- are crucial for the efficient photocurrent generation. In principle, the photoelectrons may also be transferred from the excited (iso)porphyrins to the ITO electrode which would result in a positive I^- oxidation photocurrent. Such photoelectrochemical oxidation of I^- on electropolymerized porphyrin thin films was observed when I^- and I_3^- are in acetonitrile solution.[1] However, only negative photocurrents are observed when the copolymer is in aqueous solution suggesting that the photooxidation of I^- is not favoured in such case.

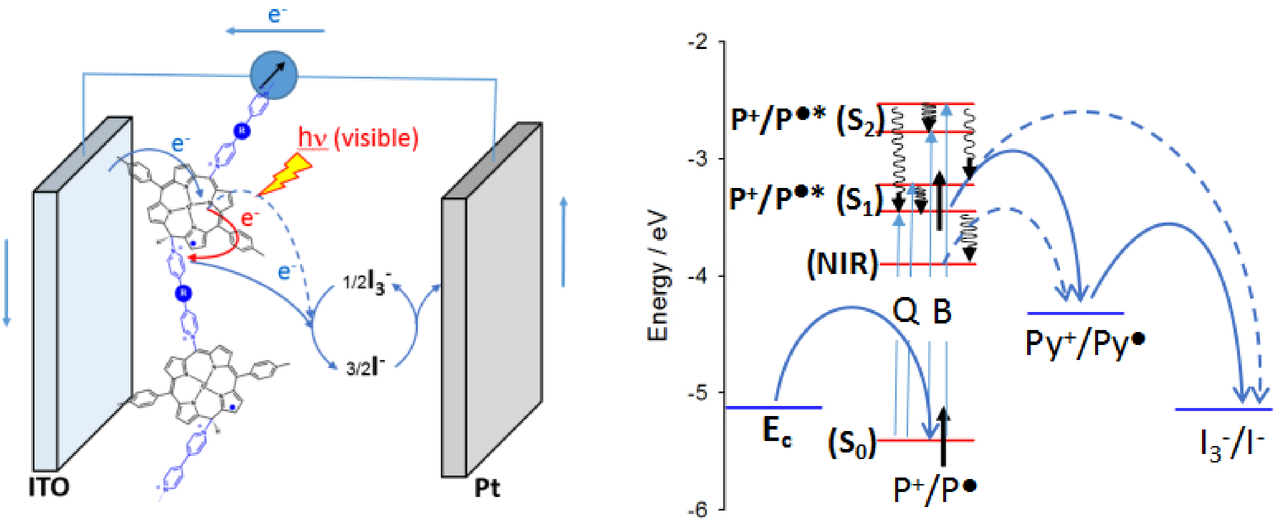

Figure 2.21. Schematic illustration of the energy level diagram for **poly-ZnT$_2$isoP1$^\bullet$** showing electron transfer processes in H_2O containing I_3^- 5 mmol L^{-1} and I^- 0.5 mol L^{-1} (Py^+ = pyridinium, P = porphyrin).

3.4. Singlet oxygen generation

During photodynamic therapy processes, the singlet oxygen has been considered as the main reactive oxygen species (ROS) which could cause cell death. Firstly, the photosensitizer (PS) could be excited to singlet state under visible light irradiation. The singlet state is unstable and can turn to the excited triplet state to produce a therapeutic. The triplet state PS could transfer energy to triplet oxygen ($^3O_2$) to obtain the singlet oxygen ($^1O_2$) (Scheme 2.2). There are two methods to quantify the singlet oxygen efficiency.[41] One is the direct method to detect the luminescence of singlet oxygen at 1273 nm. The other is to evaluate by monitoring the photooxidation of 1,3-diphenylisobenzofuran (DPBF). The processes are shown in Scheme 2.2. Because DPBF is a convenient acceptor which can rapidly scavenges singlet oxygen to give colorless products, it have been already reported. [42-44]

Some porphyrin derivatives have been used as photosensitizer in PDT.[45] Since the maximum skin permeability is in the 650-850 nm spectral range, photosensitizers with high singlet oxygen efficiency produced in this range are considered as the best choice for PDT. For porphyrin, it possesses intense Soret band located around 400 nm and weak Q bands usually located between 600 nm and 800 nm. The singlet oxygen is always generated under visible light irradiation with porphyrin.[42-44,46] For isoporphyrin, the intense Q bands could reach 800 nm and even further makes isoporphyrin as prospective candidates. Stable isoporphyrin radical copolymers have been obtained by electropolymerization as described bellow. The isoporphyrin sample was prepared by using DMF to wash the copolymers out from the ITO electrode and repeat six times then gathered together. Tetraphenylporphrin is chosen as standard for comparation with the literature.[42,46]

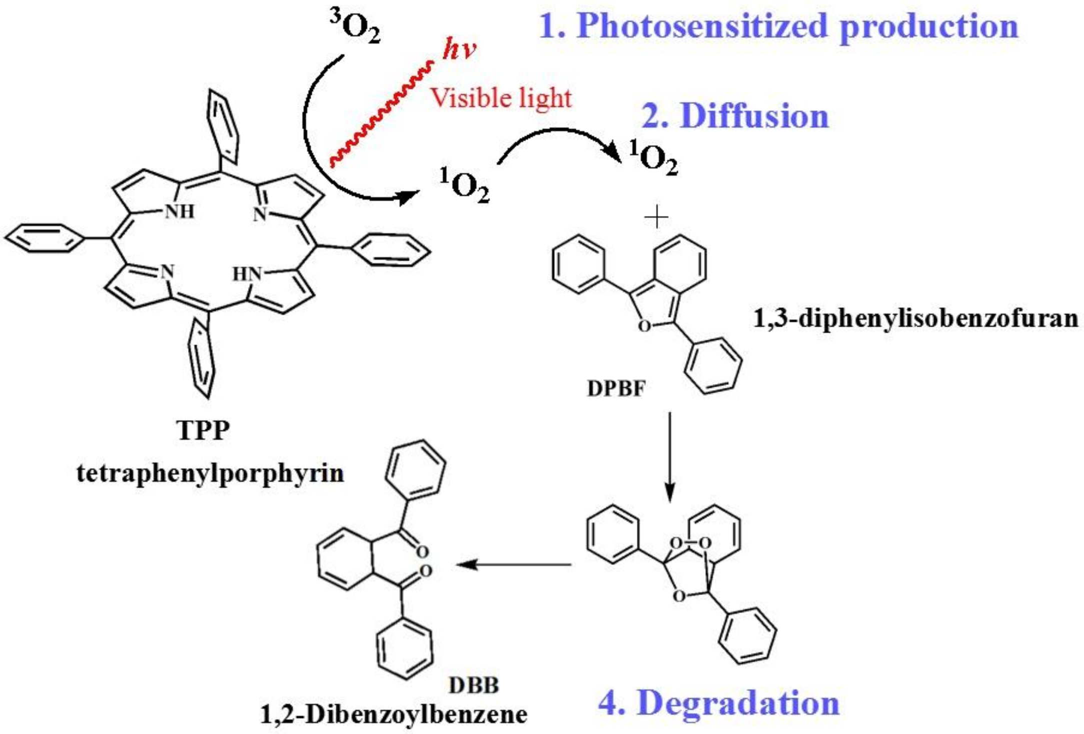

Scheme 2.2. Indirect method to quantify the singlet oxygen efficiency

The whole experiment has been conducted under NIR light illumination by using one black filter to prove the effect of NIR absorption band. According to the literature,[42] the relative ϕ_Δ $^1O_2$ generation efficiency was detected by monitoring the reduced loss of absorbance of DPBF (at 415 nm in DMF) in comparison with tetraphenylporphyrin (H_2TPP) with the increasing irradiation time. The results are shown in Figure 2.22.

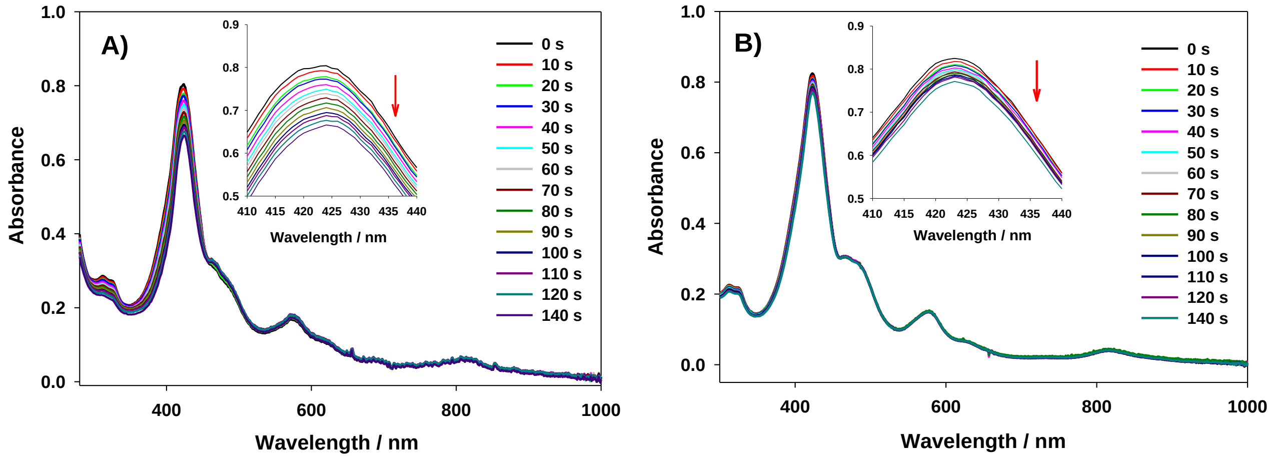

Figure 2.22. Normalized absorption spectra of A) **poly-ZnT$_2$isoP1$^{\bullet}$** with DPBF and B) **poly-ZnT$_2$isoP2$^{\bullet}$** with DPBF in DMF. The inset of the figure shows the focused version of the Soret band.

The following equation 2 was used to calculate the singlet oxygen quantum yield of **poly-ZnT$_2$isoP1$^{\bullet}$** and **poly-ZnT$_2$isoP2$^{\bullet}$**:

$$\Phi\ (^1O_2) = \Phi\ (^1O_2)^{H_2TPP}\, m^{isoPor} / m^{H_2TPP} \times F^{H_2TPP} / F^{isoPor} \qquad \text{Equation 2}$$

where the superscripts 'isoPor' and 'TPP' means **poly-ZnT$_2$isoP1$^{\bullet}$** or **poly-ZnT$_2$isoP2$^{\bullet}$** and tetraphenylporphyrin (H_2TPP), respectively; Φ ($^1O_2$) is the singlet oxygen quantum yield, m is the slope of a plot of difference in change in absorbance of DPBF (at 414 nm) with the irradiation time (Fig. 2.23) and F is the absorption correction factor, which is given by $F = 1–10^{-OD}$ (OD was the value of absorption intensity at the irradiation wavelength 823 nm). (Φ (H_2TPP) = 0.60 in DMF)[42] (Table 2.3). As the concentration of porphyrin in the copolymer is unknown, so the absorbance of poly-isoporphyrin was controlled to obtain similar absorbance with H_2TPP. The value Φ ($^1O_2$) is shown in Table 2.3. Because of H_2TPP has no absorption band around 800 nm, so the results can be treated as a reference.

The **Poly-ZnT$_2$isoP1$^{\bullet}$** shows good Φ_Δ in comparison with H_2TPP, H_2TPP works only with visible light and the copolymer of isopoporphyrin use NIR as well as visible light. The **poly-ZnT$_2$isoP1$^{\bullet}$** showed a more efficient singlet oxygen generation than **poly-ZnT$_2$isoP2$^{\bullet}$**. That is may due to the weak NIR band of **poly-ZnT$_2$isoP2$^{\bullet}$**. During NIR illumination, singlet oxygen can be generated. It opens one new application of such material, namely the use of such copolymer with isoporphyrin radical as photosensitizer in PDT where the light can be the NIR light. The NIR light is more penetration light and less dangerous for the body.

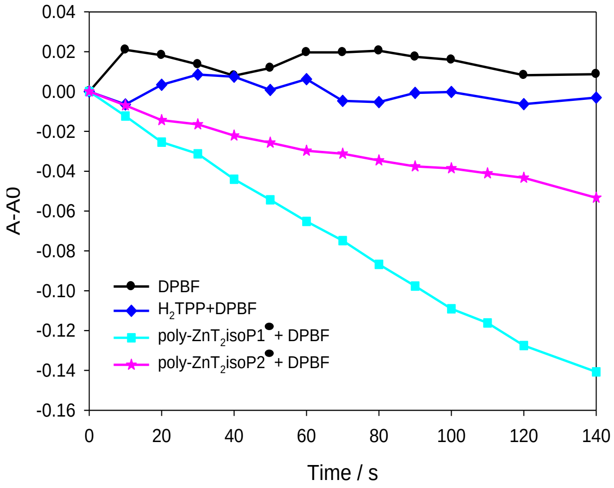

Figure 2.23. Time-dependent decrease of absorbance at 418 nm by oxidation of DPBF (20 µM) with porphyrin sensitizers (1.5 µM) in DMF against free base tetraphenylporphyrin (H_2TPP). A0 is the absorbance density of mixture solution in the beginning.

Table 2.3 Singlet oxygen quantum yield ($\phi\Delta$) in DMF with respect to tetraphenylporphyrin (H_2TPP).

Sample	**H_2TPP**[42]	**Poly-$ZnT_2isoP1^{\bullet}$**	**Poly-$ZnT_2isoP2^{\bullet}$**
Φ_Δ	0.60	0.95	0.69

4. Investigation of other isoporphyrin copolymers

Three different bipyridyl ligands with similar structures have been researched (1,2-di(pyridin-4-yl)ethyne, 1,4-di(pyridin-4-yl)benzene, 4,4'-di(pyridin-4-yl)-1,1'-biphenyl) as shown in Scheme 2.3. Exhaustive studies of such new copolymers need to be done with additional measurments: EQCM, AFM, and impedance. These additional studies are under work.

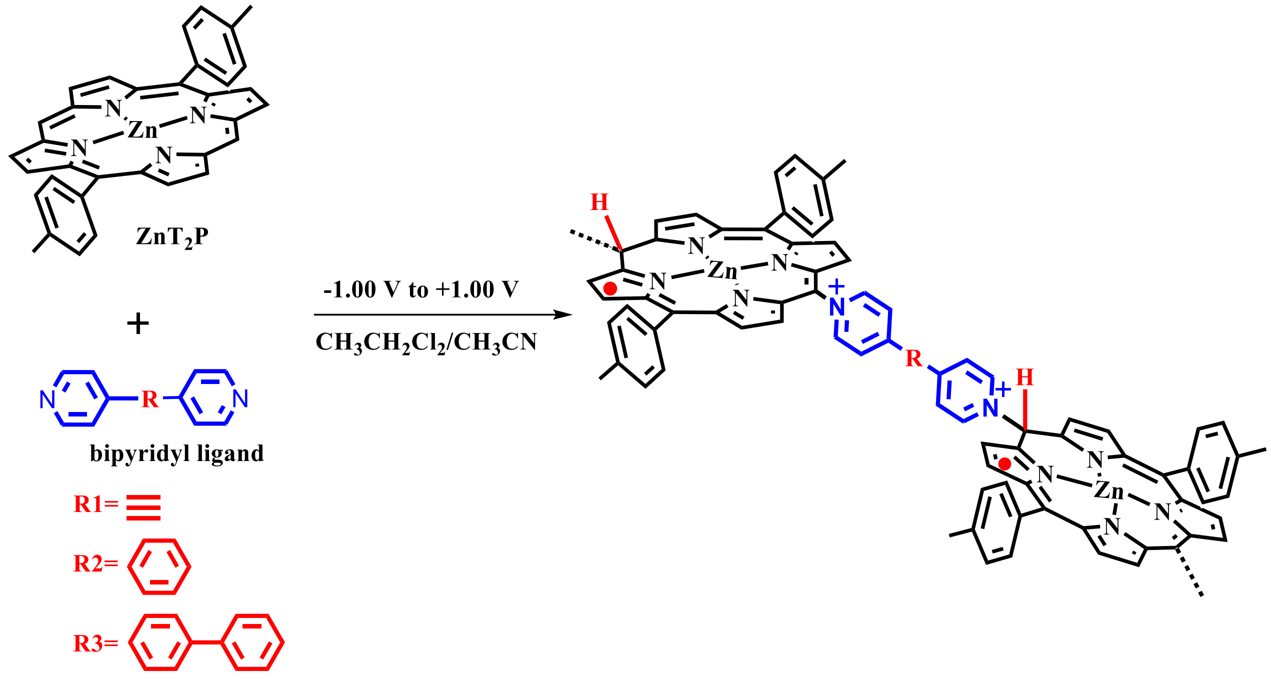

Scheme 2.3. The preparation of poly-isoporphyrin copolymers with three different bipyridyl ligands.

The general electropolymerization procedure used to deposit the isoporphyrin-based polymers or porphyrin-based polymers onto ITO electrode surfaces is the same as described before. This process depends on the polarization of the working electrode during the potential scan that is either at the first oxidation potential to produce **ZnT$_2$P$^{+\bullet}$** (iteration between -1.0 V and +1.0 V) or at the second oxidation potential to produce **ZnT$_2$P**$^{2+}$ (iteration between -1.0 V and +1.6 V). The CV curves measured during the iterative scans for the three bipyridyl ligands are shown in Figure 2.24. Compared with 4,4'-bpy and bpy$^+$–(CH$_2$)$_3$–$^+$bpy·2PF$_6^-$, the reduction processes are also due to the dipyridinum spacers reduction but they showed different redox behavior as compared to the copolymers described before with single or double viologen spacer (4,4'-bpy^{2+} and –bpy^{2+}–(CH$_2$)$_3$–$^{2+}$bpy-·). The differences are assumed to be explained by the delocalization and the reactivity of the radical pyridyl after the pyridinium reduction.

In the case of copolymer of isoprphyrin **poly-ZnT$_2$isoP3$^\bullet$** obtained with **ZnT$_2$P** and py-C≡C-py, the reduction of the dipyridium linker is less reversible than for the viologen or double viologen spacers described in the beginning of this chapter. It may be due to the reactivity of the radical pyridyl (py$^\bullet$). In contrast, **poly-ZnT$_2$isoP4$^\bullet$** or **poly-ZnT$_2$isoP5$^\bullet$** obtained from **ZnT$_2$P** and py-Ph-py or py-Ph-Ph-py show more reversible reductions of the dipyridinium spacers. It indicates probably a better delocalisation of the radical generated after the reduction of the dipyrinium spacers.

In addition, as shown in Figure 2.24, the oxidation waves kept increasing with scan numbers indicating the formation of the conducting copolymer based on isoporphyrin radical.

In summary, these results means that the isoporphyrin copolymers could be obtained in the presence of **ZnT$_2$P** and various type of dipyridyl ligands.

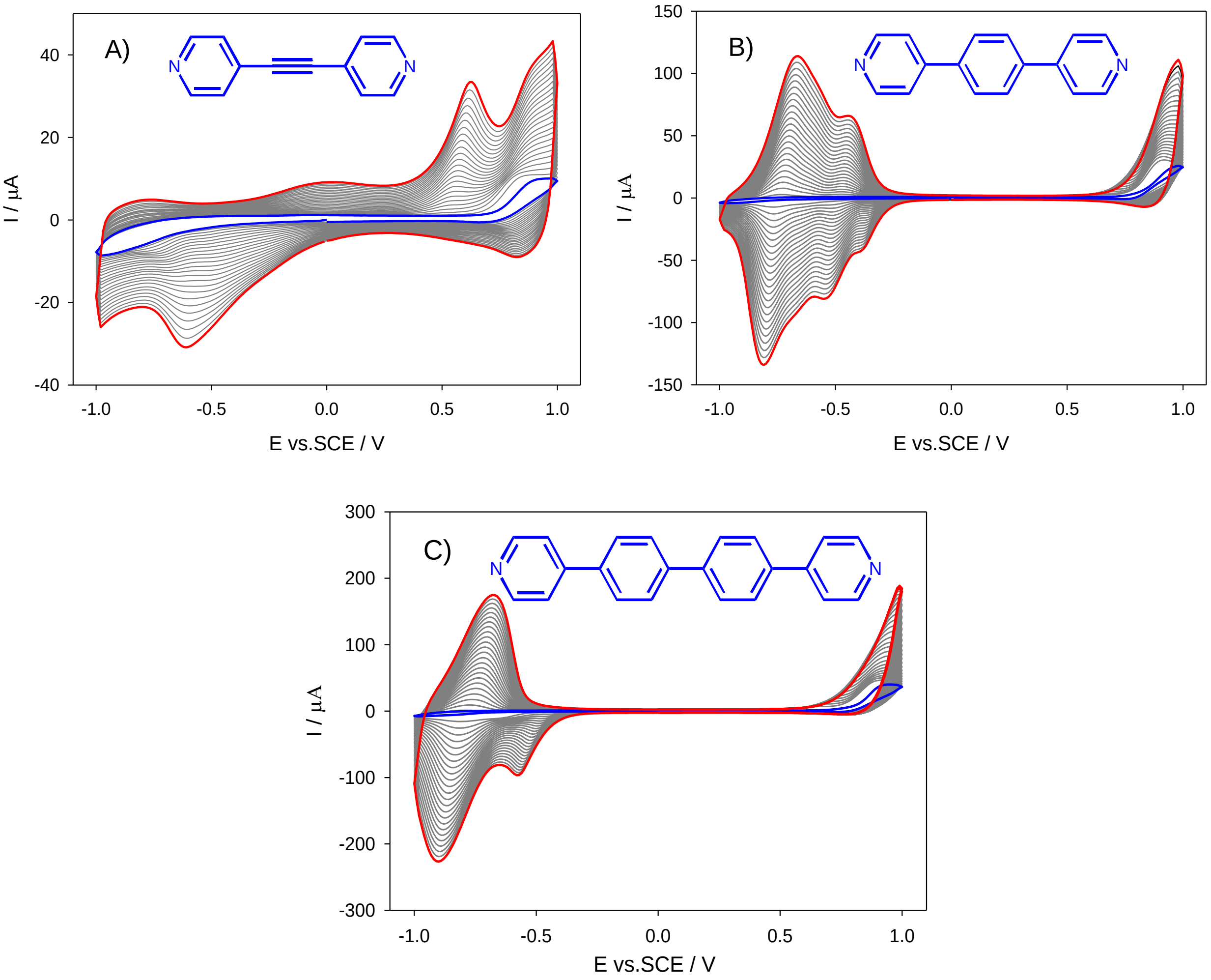

Figure 2.24. Cyclic voltammograms recorded during 25 iterative scans conducted between −1.0 V and +1.0 V *vs.* SCE in a 1,2-$C_2H_4Cl_2$/CH_3CN (7/3) solution and NBu_4PF_6 (0.1 mol L^{-1}) of **ZnT$_2$P** (0.25 mmol L^{-1}) in the presence of (A) py–C≡C-py (0.25 mmol L^{-1}) (B) py–Ph-py (0.25 mmol L^{-1}) and (C) py-Ph-Ph-py (0.25 mmol L^{-1}). WE: ITO. S = 1 cm^2. v = 100 mV s^{-1}. Blue curve: first scan (n=1). Red curve: final scan (n = 25).

The CVs during the formation of the polyporphyrin between -1.0 V and 1.6 V are also shown in Figure 2.25. In the case of poly-porphyrin copolymers, one irreversible wave near -0.1 V (with a slow process) is observed for **poly-ZnT$_2$P3** (Fig. 2.25A). The irreversible waves are also detected near -0.4 V and near -0.6 V for **poly-ZnT$_2$P4** and **poly-ZnT$_2$P5** respectively before one reversible reduction (Fig. 2.25BC). From the cyclic voltammograms recorded at 5 scans of **ZnT$_2$P** in the presence of py-C≡C-py, py–Ph-py or py-Ph-Ph-py during electropolymerization (Fig. 2.26A), we can observe one irreversible reduction wave (marked star, ∗) which is due to reduction of isoporphyrin intermediate produced during the polymerization process. After this irreversible peak (peak ∗), reversible wave(s) is (are) observed and correspond(s) to the reduction of pyridinum spacers.

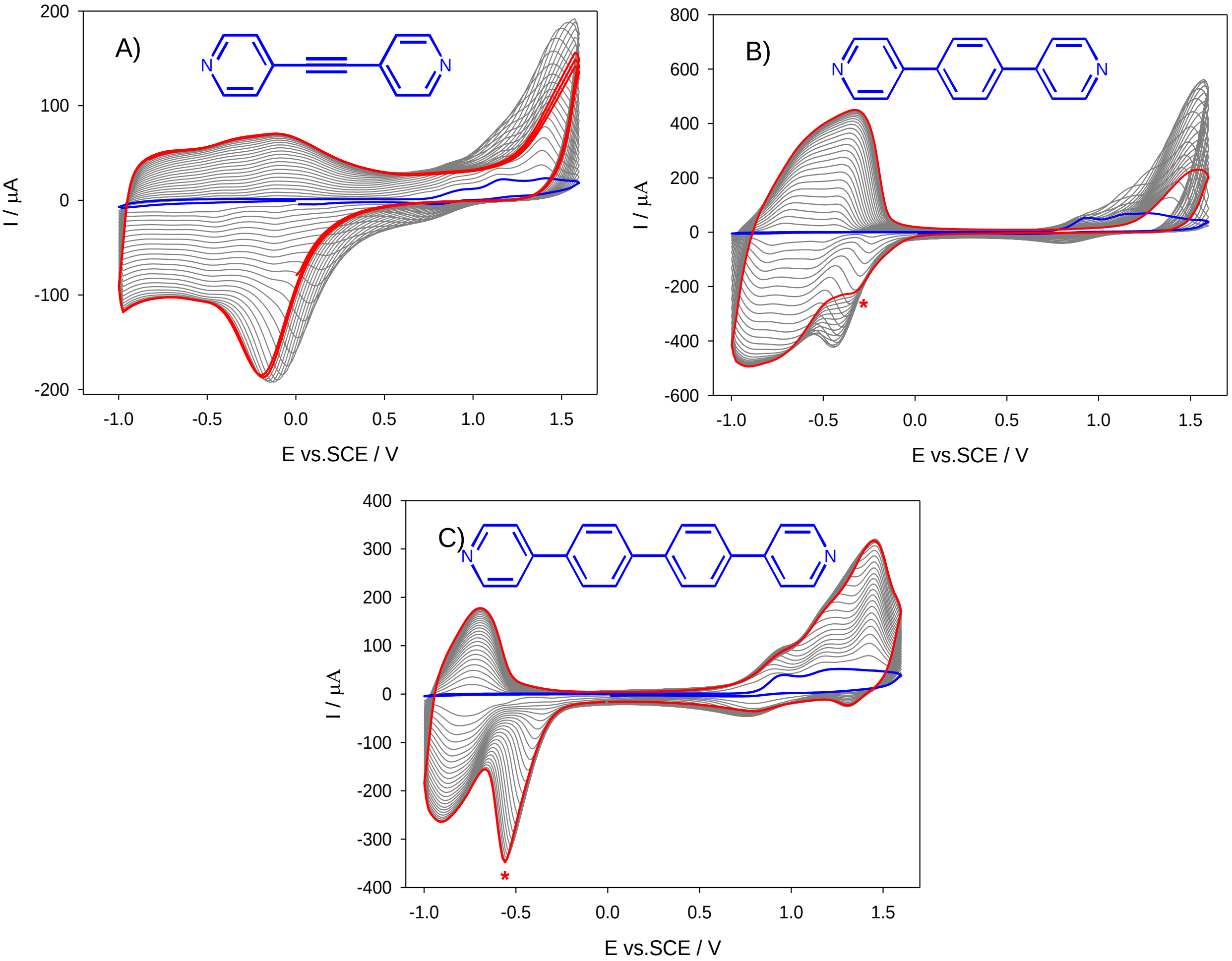

Figure 2.25. Cyclic voltammograms recorded during 25 iterative scans conducted between −1.0 V and +1.6 V *vs.* SCE in a 1,2-$C_2H_4Cl_2/CH_3CN$ (7/3) solution and NBu_4PF_6 (0.1 mol.L^{-1}) of **ZnT$_2$P** (0.25 mmol L^{-1}) in the presence of (A) py-C≡C-py (0.25 mmol L^{-1}) (B) py–Ph-py (0.25 mmol L^{-1}) and (C) py-Ph-Ph-py (0.25 mmol L^{-1}). WE: ITO. S = 1 cm^2. v = 100 mV s^{-1}. Blue curve: first scan (n=1). Red curve: final scan (n = 25).

In the case of the use py–Ph-Ph-py ligand giving **poly-ZnT$_2$P5** copolymer, we can detect only one two-electron reversible wave near -0.80 V corresponding to the reduction of the two pyridinium at nearly the same potential (Fig. 2.26). It shows not interaction between the two pyridinium groups because of the simultaneously reduction of the pyridinium groups.

In the case of py–ph-py ligand which leads to the formation of **poly-ZnT$_2$P4**, the reduction of the pyridinium groups splits into two one-electron reversible waves at ca. -0.74 V and -0.53 V. **poly-ZnT$_2$P4** showing now interactions between the 2 pydinium centers. Furthermore, the pyridinium groups are also easier to be reduced in comparison with **poly-ZnT$_2$P5** copolymer obtained from py–ph-ph-py. It indicates the presence of the delocalization of the radical which stabilized the radical cation obtained after the first reduction (ZnT$_2$P-py$^+$–Ph–py$^+$-ZnT$_2$P- / ZnT$_2$P-py$^+$–Ph–py$^\bullet$-ZnT$_2$P-). Thus, if the distance between two pyridinium is shortened with only one Ph group, a splitting of the reduction process into two one-electron steps is observed with easier reduction potential.

In the case of py-C≡C-py ligand forming **poly-ZnT$_2$P3**, only one reversible wave is observed.

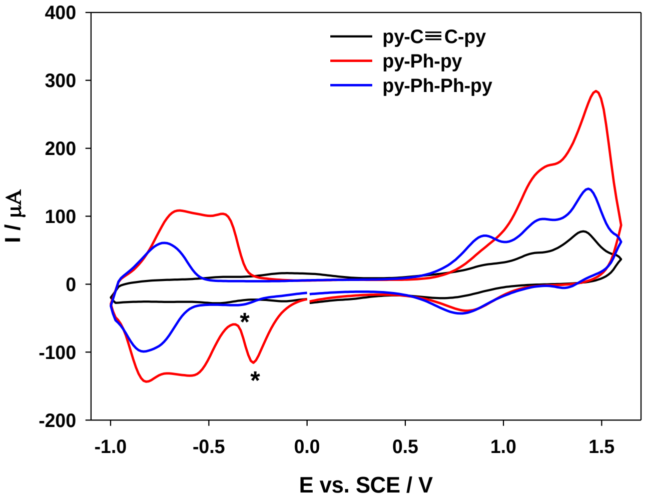

Figure 2.26. Cyclic voltammograms recorded of 5 cycles conducted between −1.0 V and +1.6 V *vs.* SCE in a 1,2-$C_2H_4Cl_2$/CH_3CN (7/3) solution and NBu_4PF_6 (0.1 mol.L^{-1}) of **ZnT$_2$P** (0.25 mmol L^{-1}) in the presence of py-C≡C-py (0.25 mmol L^{-1}, black line), py–Ph-py (0.25 mmol L^{-1}, red line) and py-Ph-Ph-py (0.25 mmol L^{-1}, blue line). WE: ITO. S = 1 cm^2. v = 100 mV s^{-1}.

A typical UV-visible-NIR spectrum of the copolymer **poly-ZnT$_2$isoP3$^\bullet$**, **poly-ZnT$_2$isoP4$^\bullet$ and poly-ZnT$_2$isoP5$^\bullet$** obtained after electropolymerization between -1.0 and +1.0 V of **ZnT$_2$P** in the presence of dipyridyl ligands: py–C≡C-py, py–Ph-py and py-Ph-Ph-py, exhibited a broad split Soret absorption band (Fig. 2.27). The bands were red-shifted respectively as compared to the **ZnT$_2$P** monomer (Table 2.4). The visible bands (Q bands), are also red-shifted compared to **ZnT$_2$P** and an additional band in the NIR region is also detected (Fig. 2.27). The copolymer **poly-ZnT$_2$isoP5$^\bullet$**

with $^{+}$py-Ph-Ph-py^{+} bridges showed highest absorption density than the other copolymer obtained with py–C≡C-py or py-Ph-Ph-py, which means that the mass deposited in the case of the use of py-ph-ph-py ($^{+}$py-Ph-Ph-py^{+} linkers) on the ITO electrode is more important using the same conditions compared to the two other dipyridyl ligands. The UV-visible-NIR spectrum of the copolymer **poly-ZnT$_2$P3**, **poly-ZnT$_2$P4**, **poly-ZnT$_2$P5** are shown in Figure 2.S17. Typical soret band and Q bands of porphyrin were observed.

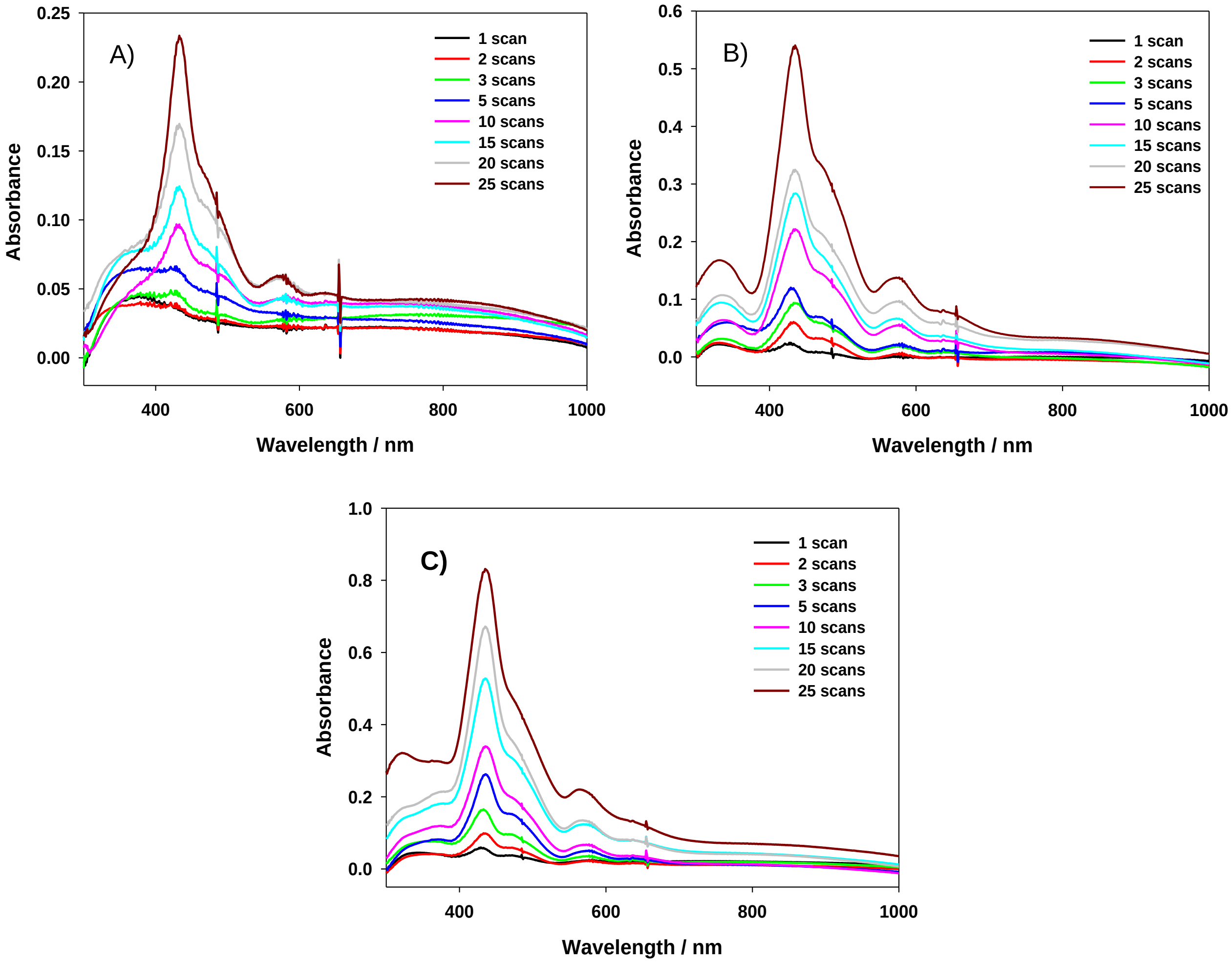

Figure 2.27. UV-visible-NIR absorption spectra of copolymer **poly-ZnT$_2$isoP3$^{\bullet}$, poly-ZnT$_2$isoP4$^{\bullet}$** and **poly-ZnT$_2$isoP5$^{\bullet}$** prepared between -1.00 V and 1.00V in the presence of **ZnT$_2$P** (0.25 mmol L^{-1}) and (A) py–C≡C-py (0.25 mmol L^{-1}) (B) py–Ph-py (0.25 mmol L^{-1}) and (C) py-Ph-Ph-py (0.25 mmol L^{-1}) respectively onto ITO with different numbers of iterative scans. Only one side is covered by ITO.

Table 2.4. UV–visible spectral data of **py–Ph–py, py-Ph-Ph-py** and **py-C≡C-py** in 7/3 $EtCl_2/CH_3CN$, and of **poly-ZnT$_2$isoP3$^\bullet$, poly-ZnT$_2$isoP4$^\bullet$** and **poly-ZnT$_2$isoP5$^\bullet$** deposited on optical transparent ITO electrodes. Under bracket: molar extinction coefficient (ε /10^3 $L.M.cm^{-1}$)

Compound	**Soret band/nm**	**Q bands/nm**	**π-π^*Band/nm**
py-C≡C-py			212 (9.7) 275 (17.2) 291(12.7)
py-Ph-py			213 (15.8) 302 (18.7)
py-Ph-Ph-py			212 (39.0) 280 (52.4)
poly-ZnT$_2$isoP3$^{\bullet a}$	433, 484 (shoulder)	569, 640, 793	
poly-ZnT$_2$isoP4$^{\bullet b}$	433, 486 (shoulder)	578, 656, 816	
poly-ZnT$_2$isoP5$^{\bullet c}$	435, 489 (shoulder)	565, 640, 816	
poly-ZnT$_2$P3	434	555, 627	
poly-ZnT$_2$P4	436	567, 618	
poly-ZnT$_2$P5	433	562, 620	

[a] **poly-ZnT$_2$isoP3$^\bullet$** obtained with **ZnT$_2$P** and py–C≡C-py between -1.0 V and 1.0 V.
[b] **poly-ZnT$_2$isoP4$^\bullet$** obtained with **ZnT$_2$P** and py–Ph-py between -1.0 V and 1.0 V.
[c] **poly-ZnT$_2$isoP5$^\bullet$** obtained with **ZnT$_2$P** and py-Ph-Ph-py between -1.0 V and 1.0 V.

The magnitude of the photocurrent strongly depends on the number of potential scans n and then of the amount of copolymer film deposited as displayed in Figure 2.28 as well as the nature of the dipyridyl ligand. For these three copolymers, the photocurrent goes through an optimum as a function of n, the best performances being obtained for n=10 or 15 electropolymerization cycles. Higher photocurrents are obtained for the copolymer **poly-ZnT$_2$isoP4$^\bullet$** formed from **ZnT$_2$P** and py-Ph-py. This result can be explained by the geometry of the spacers: linear with closer distance between the two pyridinium as of porphyrin macrocycles. Also higher delocalization of the pyridyl radical generated via the illumination through the porphyrin macrocycle as well as through the dipyridinum -py$^+$-Ph-py$^+$- spacer can be proposed.

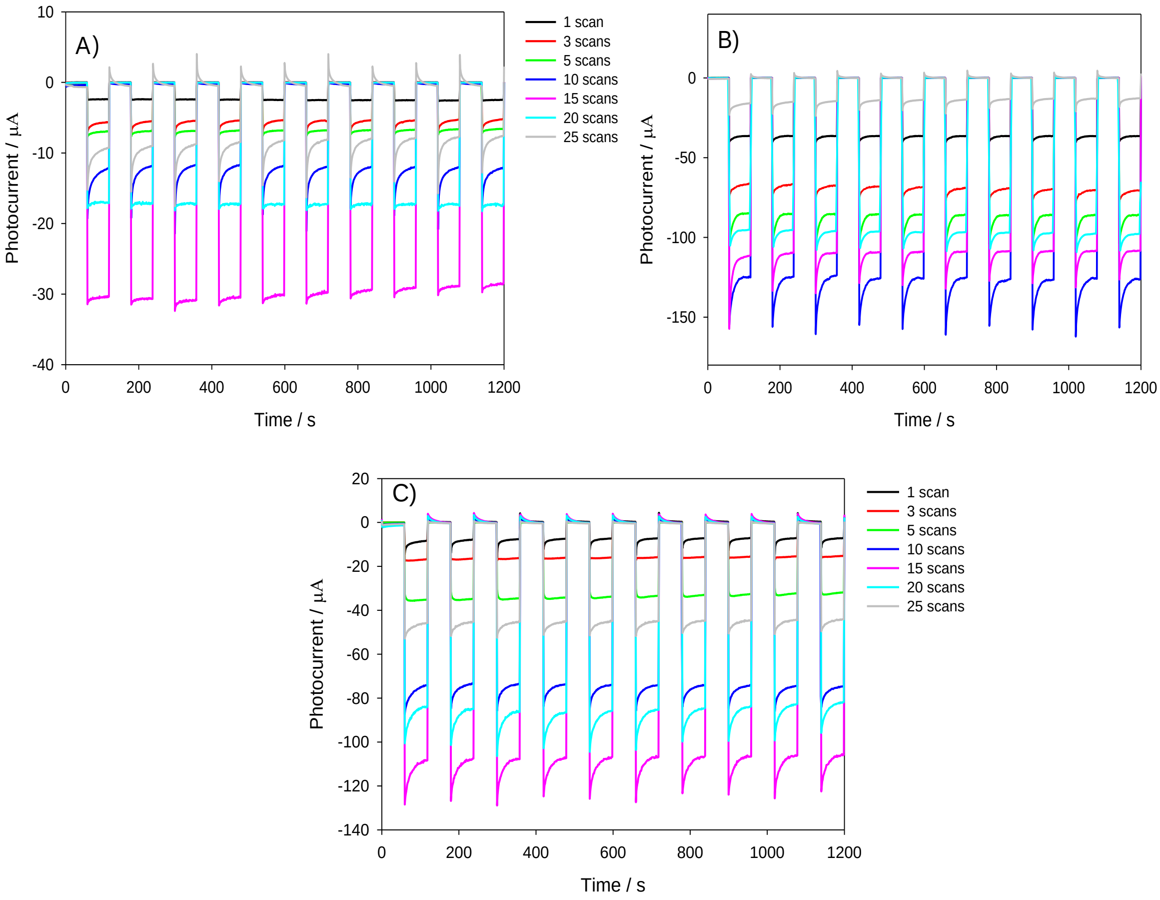

Figure 2.28. Photoelectrochemical response of **poly-ZnT$_2$isoP3$^\bullet$**, **poly-ZnT$_2$isoP4$^\bullet$** and **poly-ZnT$_2$isoP5$^\bullet$** films prepared with ZnT$_2$P in the presence of (A) py–C≡C-py (0.25 mmol L^{-1}) (B) py–Ph-py (0.25 mmol L^{-1}) and (C) py-Ph-Ph-py (0.25 mmol L^{-1}) respectively with n = 1, 2, 3, 5, 10, 15, 20 or 25 iterative scans. Measurements have been done under on-off light illumination from a 300 W Xe arc lamp (with $\lambda > 385$ nm long pass filter) in I_3^- 5 mmol L^{-1} and I^- 0.5 mol L^{-1} aqueous solution. BIAS potential: 0.00 V *vs.* OCP.

5. Conclusions

In summary, two porphyrin copolymer films, with single or double viologen spacers, have been prepared by the electro-oxidation of 5,15-ditolylporphyrin (**ZnT$_2$P**) in the presence of dipyridyl ligand (4,4'-bpy and bpy$^+$–(CH$_2$)$_3$–$^+$bpy·2PF$_6^-$). Further oxidation of **poly-ZnT$_2$isoP$^\bullet$** at higher applied potential induces the removal of the hydrogen and the formation of the porphyrin in the copolymer (**poly-ZnT$_2$P**). The electropolymerization process was scrutinized by EQCM. Electrogenerated radical cation porphyrin is a powerful electrophile which can rapidly react to form copolymer containing stable isoporphyrins (**poly-ZnT$_2$isoP$^\bullet$**). The existence of the π-cation radical of the isoporphyrin subunit of the copolymer was proved by electron spin resonance spectroscopy. The photocurrent measurements under visible-NIR light irradiation show that **poly-ZnT$_2$isoP$^\bullet$** thin films exhibit significantly enhanced performance in comparison to **poly-ZnT$_2$P**. However, the photovoltaic performances reach an optimum depending on the number of iterative scan n. The best performances are obtained for n =10 or 15, n being the number of iterative scan during the electropolymerization. From electrochemical impedance spectroscopy measurements, it is observed that the charge transfer resistance of the film increases for films obtained with more than 10 iteratives scans, thus explaining the decrease of photocurrent for films with n > 10. Therefore, the control of the thickness of the copolymer films is of great importance to optimize the generation of photocurrent under visible illumination. In addition, the NIR absorption band in UV-vis-NIR spectrum has made a contribution to the photocurrent. Otherwise, it is observed that the isoporphyrin radical copolymer could generate singlet oxygen under only NIR illumination which opens a new route for the use of such material for the photodynamic therapy.

Mechanisms of electrochemical routes to these two types of electroactive copolymers have been discussed as well as the description of the unusual redox properties of copolymers containing stable isoporphyrin radicals.

Finally, numerous type of copolymers containing stable isoporphyrin radicals can be generated using various type of dipyridinium spacer showing that this study opens a new route of formation of promising materials containing stable isoporphyrin.

References

1. Z. Huo, A. Bonnefont, Y. Liang, R. Farha, M. Goldmann, E. Saint-Aman, H. Xu, C. Bucher, L. Ruhlmann., *Electrochimica Acta*, **2018**, 274, 177–191.

2. T. Ogawa, Y. Nishimoto, N. Yoshida, N. Ono, A. Osukua, *Chem. Commun.* **1998**, 337–338.

3. T. Ogawa, Y. Nishimoto, N. Yoshida, N. Ono, A. Osukua, *Angew. Chem. Int. Ed*, **1999**, 38, 176–179.

4. A.K.D. Dime, C.H. Devillers, H. Cattey, B. Habermeyer, D. Lucas, *Dalton Trans.* **2012**, 41, 929–936.

5. J. P. Evans, F. Niemevz, G. Buldain, P. Ortiz de Montellano, *J. Bio. Chem*, **2008**, 283, 19530–19539.

6. H. Xie, S. H. Leung and K. M. Smith, *J. Porphyrins Phthalocyanines,* **2002**, 6, 607–616.

7. W. R. Fawcett, M. Fedurco, K. M. Smith, H. Xie, *J. Electroanal. Chem.*, **1993**, 354, 281–287.

8. S. C. Mwakwari, H. Wang, T. J. Jensen, M. G. H. Vicente.and K. M. Smith, *J. Porphyrins Phthalocyanines,* **2011**, 15, 918–929.

9. a) R. Kannappan, C. Bucher, E. Saint-Aman, J.-C. Moutet, A. Milet, M. Oltean, E. Métay, S. Pellet-Rosaing, M. Lemaire, C. Chaix, *New J. Chem*., **2010**, 34, 1373–1386. b) A. Iordache, M. Retegan, F. Thomas, G. Royal, E. Saint-Aman, C. Bucher, *Chem. Eur. J.* **2012**, 18, 7648–7653.

10. a) J. S. Manka, D. S. Lawrence, High yield synthesis of 5, 15-diarylporphyrins, *Tetrahedron Lett*. **1989**, 30, 6989–6992; b) T. Takanami, M. Hayashi, H. Chijimatsu, W. Inoue, K. Suda, *Org. Lett.* **2005**, 7, 3937–3940; c) B. Habermeyer, A. Takai, C. P. Gros, M. El Ojaimi, J.-M. Barbe, S. Fukuzumi, *Chem. Eur. J.* **2011**, 17, 10670–10681.

11. C. Brückner, J. J. Posakony, C. K. Johnson, R. W. Boyle, B. R. James, D. Dolphin, *J. Porphyrins Phthalocyanines*. **1998**, 2, 455–465.

12. M. O. Senge, Y. M. Shaker, M. Pintea, C. Ryppa, S. S. Hatscher, A. Ryan, Y. Sergeeva, *Eur. J. Org. Chem.* **2010**, 2, 237–258.

13. C. H. Devillers, A. K. D. Dime, H. Cattey, D. Lucas, *Chem. Commun*. **2011**, 47, 1893–1895.

14. L. Ruhlmann, A. Schulz, A. Giraudeau, C. Messerschmidt, J.-H. Fuhrhop, *J. Am. Chem. Soc*., **1999**, 121, 6664–6667.

15. I. Azcarate, I. Ahmed, R. Farha, M. Goldmann, X. Wang, H. Xu, *Dalton Trans*. **2013**, 42, 12688–12698.

16. A. Giraudeau, D. Schaming, J. Hao, R. Farha, M. Goldmann, L. Ruhlmann, *J. Electroanal. Chem*. **2010**, 638, 70–75.

17. L. Ruhlmann, J. Hao, Z. Ping, A. Giraudeau, *J. Electroanal. Chem*. **2008**, 621, 22–30.

18. D. Schaming, I. Ahmed, J. Hao, V. Alain-Rizzo, R. Farha, M. Goldmann, H. Xu, A. Giraudeau, P. Audebert, L. Ruhlmann, *Electrochim. Acta*, **2011**, 26, 10454–10463.

19. D. Schaming, S. M. Poullain, I. Ahmed, R. Farha, M. Goldmann, J. P. Gisselbrecht, L. Ruhlmann, *New J .Chem*. **2011**, 35, 2534–2543.

20. A. Giraudeau, L. Ruhlmann, L. El-Kahef, M. Gross, *J. Am. Chem. Soc*. **1996**, 118, 2969–2979.

21. D. Schaming, L. Ruhlmann, Publisher Nova, Editors: L. Ruhlmann and D. Schaming, **2015**, 237-264. b) D. Schaming, L. Ruhlmann, chapter in the book Electrochemistry of MN4 Macrocyclic Complexes, Springer, J. H. Zagal, , F. Bedioui, J. P. Dodelet (Eds.). **2016**, 2, 395–432.

22. A. Giraudeau, S. Lobstein, L. Ruhlmann, D. Melamed, K.M. Barkigia, J. Fajer, *J. Porphyrins Phthalocyanines,* **2001**, 5, 793–797.

23. C. H. Devillers, A.K.D. Dime, H. Cattey, D. Lucas, *Chem. Comm*. **2011**, 47, 1893–1895.

24. A. K. D. Dime, H. Cattey, D. Lucas, C. H. Devillers, *Eur. J. Inorg. Chem*. **2018**, 44, 4834–4841.

25. M. Berthelot, G. Hoffmann, A. Bousfiha, J. Echaubard, J. Roger, H. Cattey, A. Romieu, D. Lucas, P. Fleurat-Lessard, C. H. Devillers, *Chem. Comm*. **2018**, 54, 5414–5417.

26. T. Ogawa, Y. Nishimoto, N. Yoshida, N. Ono, A. Osukua, *Chem. Commun*. **1998**, 337–338.

27. T. Ogawa, Y. Nishimoto, N. Yoshida, N. Ono, A. Osukua, *Angew. Chem. Int. Ed*., **1999**, 38, 176–179.

28. A. K. D. Dime, C. H. Devillers, H. Cattey, B. Habermeyer, D. Lucas, *Dalton Trans*. **2012**, 41, 929–936.

29. J. Fajer, *J. Porphyrins Phthalocyanines,* **2000**, 4, 382–390.

30. J. A. Shelnutt, X. Song J. G. Ma, S. L. Jia, W. Jentzen, C. J. Medforth, *Chem. Soc. Rev.* **1998**, 27, 31–42.

31. K. M. Barkigia, M. D. Berber, J. Fajer, C. J. Medforth, M. W. Renner, K. M. Smith, *J. Am. Chem. Soc.* **1990**, 112, 8851–8857.

32. L. D. Sparks, C. J. Medforth, M. S. Park, J. R. Chamberlain, M. R. Ondrias, M. O. Senge, K. M. Smith, J. A. Shelnutt, *J. Am. Chem. Soc*, **1993**, 115, 581–592.

33. M. O. Senge, M. W. Renner, W. W. Kalisch, J. Fajer, *J Chem Soc Dalton Trans*. **2000**, 381–385.

34. F. D’Souza, M.E. Zandler, P. Tagliatesta, Z. Ou, J. Shao, C. E. Van Caemelbecke, K. M. Kadish, *Inorg. Chem.* **1998**, 37, 4567–4572.

35. M. E. Anderson, A. G. M. Barrett, B. M. Hoffman, *Inorg. Chem*. **1999**, 38, 6143–6151.

36. C. Bernard, J.-P. Gisselbrecht, M. Gross, E. Vogel, M. Lausmann, *Inorg Chem*. **1994**, 33, 2393–2401.

37. a) M. Kasha, *Rev. Mod. Phys.* **1959**, 31, 162–169; b) J. L. Sessler, M. R. Johnson, S. E. Creager, J. C. Fettinger, J.A. Ibers, *J. Am. Chem. Soc.* **1990**, 112, 9310–9329.

38. a) G. J. Abhilash, J. Bhuyan, P. Singh, S. Maji, K. Pal, S. Sarkar, *Inorg. Chem.* **2009**, 48, 1790–1792; b) J. Bhuyan, S. Sarkar, *Chem. Eur. J.* **2010**, 16, 10649–10652; c) P. Schweyen, M. Hoffmann, J. Krumsieck, B. Wolfram, X. Xie, M. Brçring, *Angew. Chem. Int. Ed.* **2016**, 55, 10118–10121.

39. D. Schaming, Y. Xia, R. Thouvenot, L. Ruhlmann, *Chem. Eur. J.* **2013**, 19, 1712–1719.

40. C. Inisan, J. Y. Saillard, R. Guilard, A. Tabard, Y. Le Mest, *New J. Chem.* **1998**, 823–830.

41. Betsy Marydasan, Akhil K. Nair, and Danaboyina Ramaiah, *J. Phys. Chem. B*, **2013**, 117, 13515–13522.

42. R. Khan, M. Idris and D. Tuncel, *Org. Biomol. Chem.*, **2015**, 13, 10496–10504.

43. N. Adarsh, R. R. Avirah, D. Ramaiah, *Org. Lett.*, **2010**, 12, 5720–5723.

44. B. Marydasen, A. K. Nair, D. Ramaiah, *J. Phys. Chem. B*, **2013**, 117, 13515–13522.
45. B. M. Amos-Tautua, S. P. Songca, O. S. Oluwafemi, *Molecules*, **2019**, 24, 2456.
46. F. Nifiatis, J. C. Athas, K. D. Gunaratne, Y. Gurung, K. M. Monette, P. J. Shivokevich, *The open Spectroscopy Journal,* **2011**, 5, 1–12.

Chapter III

Stable porphyrin/isoporphyrin copolymers prepared with bipyridyl ligands

Chapter III: Stable porphyrin/isoporphyrin copolymers prepared with bipyridyl ligands

In chapter II, we have prepared and studied porphyrin/isoporphyrin copolymers based on the nucleophilic attack of various type of bipyridyl groups.[1,2] In this chapter, we propose to vary the nature of the dipyridyl ligand use for the electropolymerization in order to favor the formation of face-to-face copolymer using ligand such as 3-(2-(3-(2-(pyridin-3-yl)ethynyl)phenyl)ethynyl)pyridine. The idea is to be able in the second turn to encapsulate polyoxometalate between the porphyrin subunits via electrostatic as well as coordination interactions (if using Sn, Mo, Zr or Hf porphyrin). Indeed, coordination complexes can be tethered to POMs by grafting metalloporphyrin (M = Mo, Sn) onto the organometallic framework through a bridging μ-oxo ligand: the subclass of "decorated" POMs as already described by Kojima, Fukuzumi et al.[3-5]

We can also use this coordination strategy to form porphyrin–metal–polyoxometalate sandwich structures between metalloporphyrin (M = Hf, Zr) and lacunary Keggin-type POM like $[PW_{11}O_{39}]^{5-}$. The porphyrin ligand acts as an electron acceptor and the lacunary Keggin-type POM acts as an electron donor.

All the copolymers obtained and described in this chapter have been characterized by electrochemical quartz crystal measurement (EQCM), UV-vis spectroscopy, X-ray photoelectron spectroscopy (XPS), atomic force microscopy (AFM), electrochemical impedance spectroscopy (EIS) and electrochemistry. Photocurrent transient measurements have been used to evaluate the photochemical active performances of copolymers.

1. Introduction

Many studies on the synthesis and reactivity of cofacial bisporphyrins are reported in the literature.[6-14] Different bridging groups have been used, such as biphenylethyl, 9,9-dimethylanthenyl, anthracenyl, dibenzofuranyl. The cofacial bisporphyrin has shown good catalytical application, such as for the reduction of CO_2 to CO.[15] The distance and angle between two porphyrin moieties can be adjusted by changing the size as well as the topology of bridge groups. For some researches,[16-18] an adjustable face to face cyclic dimer of porphyrin was prepared with inclusion of C_{60} inside.

In our group, one cyclic porphyrin copolymer was already obtained from **ZnOEP** and bipyridyl ligand (methyl 4-methyl-3,5-bis(2-(pyridin-3-yl)ethynyl)benzoate).[19] Four *meso* positions of **ZnOEP** could be attacked by nucleophilic ligands to form a cage type copolymers.

In this work, **ZnOEP** was replaced by **ZnT$_2$P** showing only two *meso* positions occupied by tolyl groups were used. The structure is shown in Scheme 3.1. Considering the space between porphyrin macrocycles, different type of POM have a possibility to be included to form organic-inorganic complex (Scheme 3.1). As we have discussed in chapter I, the POM could be inserted due to the electrostatic interactions between POM anion and porphyrin cation. Besides, POM could be fixed into the core of cofacial porphyrin due to the coordination between POM and metalloporphyrin. The zinc which is not good for such coordination will be replaced by other metals to give a stronger binding between POM and metalloporphyrin (Scheme 3.1).

Because of the covid-19 pandemic, the studies of the incorporation of various type of POM have not yet been conducted.

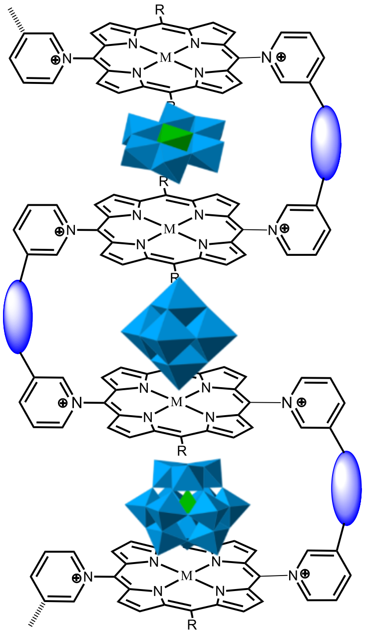

Scheme 3.1. Inclusion of Anderson, Linqvist or Dawson type POM into the cyclic cofacial porphyrin copolymers.

Let's remember that an easy strategy to obtain polyporphyrins is based on the oxidation or reduction of electropolymerizable substituents attached to the porphyrin ring. The porphyrins could be oxidized to the very reactive π-radical cations and dications, and then react with various type of dinucleophilic groups giving isoporphyrin or porphyrin oligomers or copolymers respectively.

In this chapter, we have used 3-(2-(3-(2-(pyridin-3-yl)ethynyl)phenyl)ethynyl)pyridine nucleophile abbreviated py–C≡C–Ph–C≡C-py (Scheme 3.2).

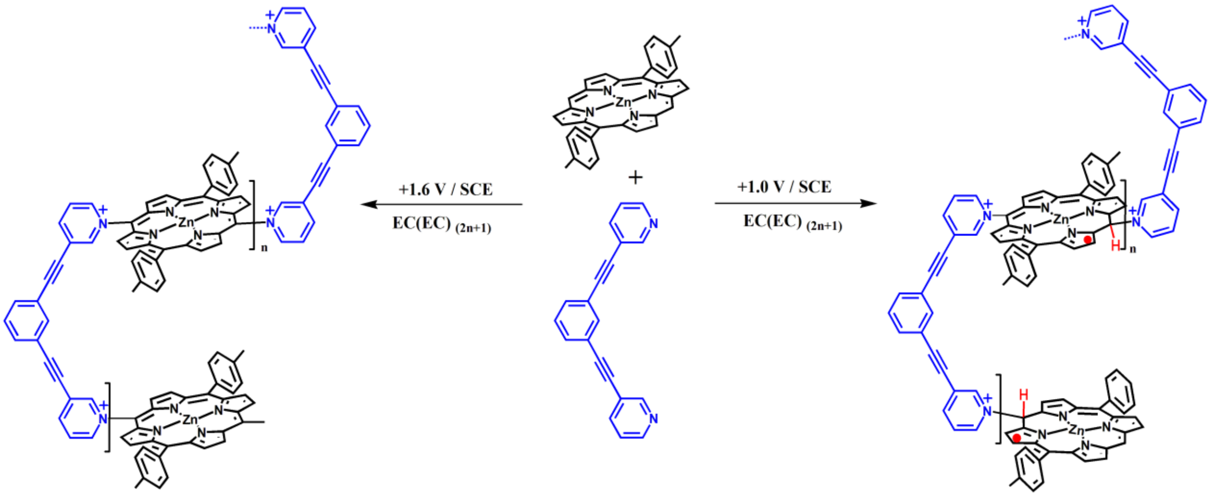

Scheme 3.2. Formation of poly-(iso)porphyrin with **ZnT$_2$P** and 3-(2-(3-(2-(pyridin-3-yl)ethynyl)phenyl)ethynyl)pyridine (py–C≡C–Ph–C≡C-py).

2. Formation and characterization

2.1. Electropolymerization of porphyrin

2.1.1. Ratio between porphyrin and bipyridyl ligand for the electropolymerization

The general electropolymerization procedure depends on the polarization of the working electrode during the iterative scans between -1.1 V and 1.6 V at the second oxidation potential to produce **ZnT$_2$P**$^{2+}$ (iteration between -1.0 V and +1.6 V). The mechanism is similar as before. To detect the influence of ratio between porphyrin and bipyridyl ligand, the concentration of **ZnT$_2$P** was fixed at 0.25 mmol L^{-1} and the concentration of bipyridyl was changed. The cyclic voltammetry behaviour is shown in Figure 3.1. The films formed on ITO are shown in Figure 3.S1. With the increase of amount of bipyridyl, the films shows higher quantity deposited. From the CV voltammograms, the reduction peak I (or I') corresponding to the reduction of the pyridium groups becomes obvious and keep increasing with ratio 1:3 between porphyrin and bipyridyl ligand. Moreover, from the optical spectrum Figure 3.S2, by changing the ratio porphyrin:ligand, namely 1:3, 1:1 or 3:1, the better quantity of the film deposited (with higher absorbance) were for ratio 1:3 and 1:1 which is in agreement with higher intensity of the current of peak I or I'.

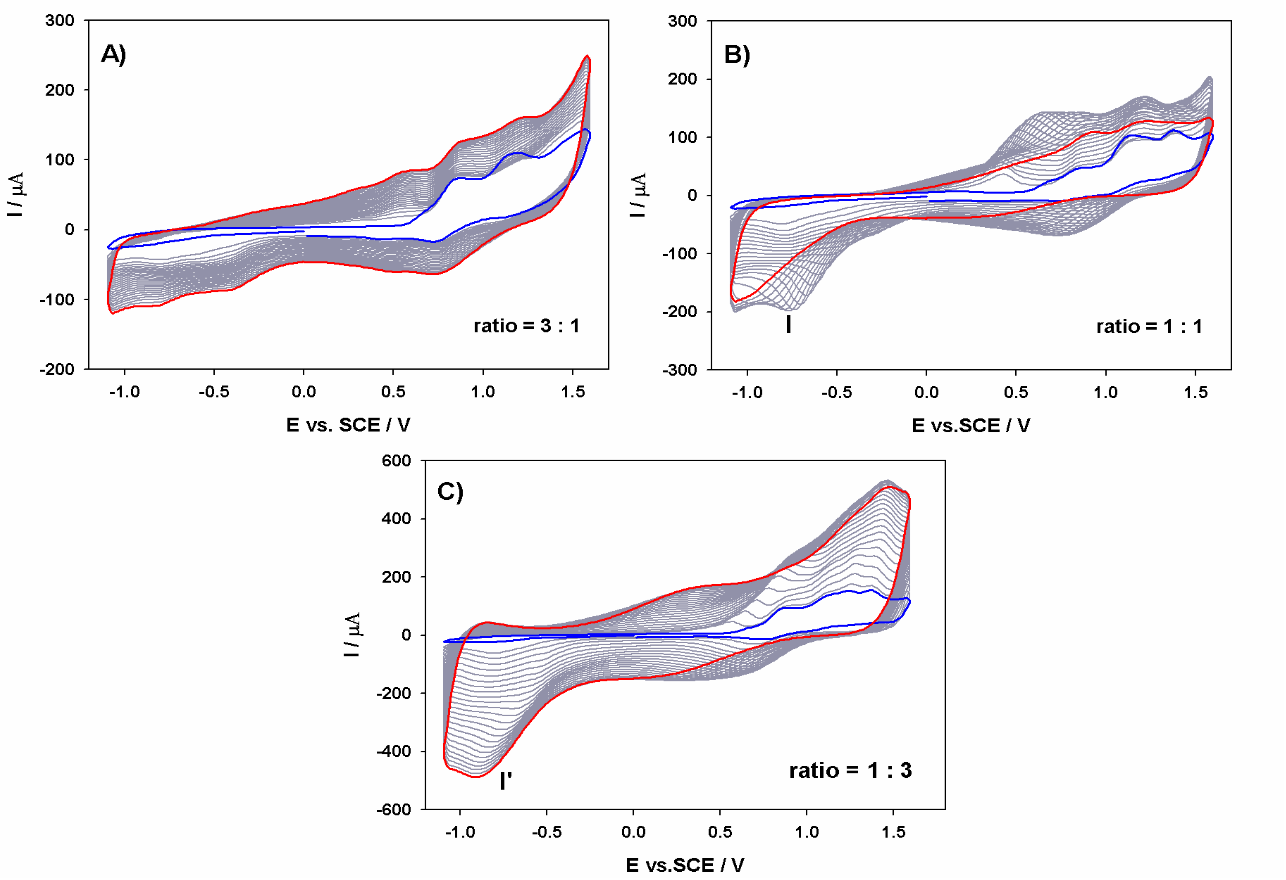

Figure 3.1. Cyclic voltammograms recorded during 25 iterative scans conducted between −1.1 V and +1.6 V *vs.* SCE in a 1,2-$C_2H_4Cl_2$/CH_3CN (7/3) solution and NBu_4PF_6 (0.1 mol.L^{-1}) of **ZnT$_2$P** (0.25 mmol L^{-1}) in the presence of py–C≡C–Ph–C≡C-py with different concentration A) 0.08 mmol L^{-1} , B) 0.25 mmol L^{-1} ,C) 0.75 mmol L^{-1}. WE: ITO. S = 1 cm^2. v = 100 mV s^{-1}. Blue curve: first scan (n=1). Red curve: final scan (n = 25).

2.1.2. Use of higher concentration of ZnT$_2$P

To obtain a better quality of the films, the higher concentration of **ZnT$_2$P**, i.e. 0.75 mmol L^{-1}, was tested for the electropolymerization. Different ratio between **ZnT$_2$P** and py-C≡C-Ph-C≡C-py was again used: 3:1, 1:1 and 1:1 (porphyrin:py-C≡C-Ph-C≡C-py). As shown in Figure 3.2A, in the case of the ration 1:3 and concentration of **ZnT$_2$P** equal to 0.75 mmol L^{-1} (py-C≡C-Ph-C≡C-py: c = 2.25 mmol L^{-1}), we can notice from the cyclic voltammetry that the reduction of pyridinum (peak I'') keeps increasing during the iterative scan indicating the formation of the porphyrin copolymer films **poly-ZnT$_2$P6** on to the ITO electrode with dipyridinium spacers. From Figure 3.2, in the anodic domain, we detect at least 3 peaks of oxidation corresponding to the first and second oxidation of the porphyrin as well as the oxidation of the isoporphyrin.

The optical spectrum of the deposited copolymer shows higher absorption intensity and better shapes of the bands associated to the porphyrin as compared to the copolymers obtained using lower concentration of **ZnT$_2$P** (i.e. 0.25 mmol L^{-1}). Additional, the optical spectra of copolymer **poly-ZnT$_2$P6** obtained using the ratio 3:1 (**[ZnT$_2$P**] = 0.75 mmol L^{-1}; [py-C≡C-Ph-C≡C-py] = 0.25 mmol L^{-1}) and 1:1 (**[ZnT$_2$P**] = 0.75 mmol L^{-1}; [py-C≡C-Ph-C≡C-py] = 0.75 mmol L^{-1}) are also shown in Figure 3.S3. But lower intensity of the Soret band and Q bands was detected

In resume, for **ZnT$_2$P** with higher concentration, i.e. 0.75 mmol L^{-1} in the presence of py–C≡C–Ph–C≡C-py (2.25 mmol L^{-1} corresponding to the ratio 1:3 more quantity of copolymer was deposited on ITO electrode. Consequently, the ratio 1:3 with the corresponding concentration 0.75 mmol L^{-1} **ZnT$_2$P** and 2.25 mmol L^{-1} py-C≡C-Ph-C≡C-py seems to be the best condition to have good quality but also quantity of the film using the same conditions of electropolymerization (identical scan rate, solvent, potential range, etc.). This ratio was chosen to form the films which will be fully studied in the last part of the chapter.

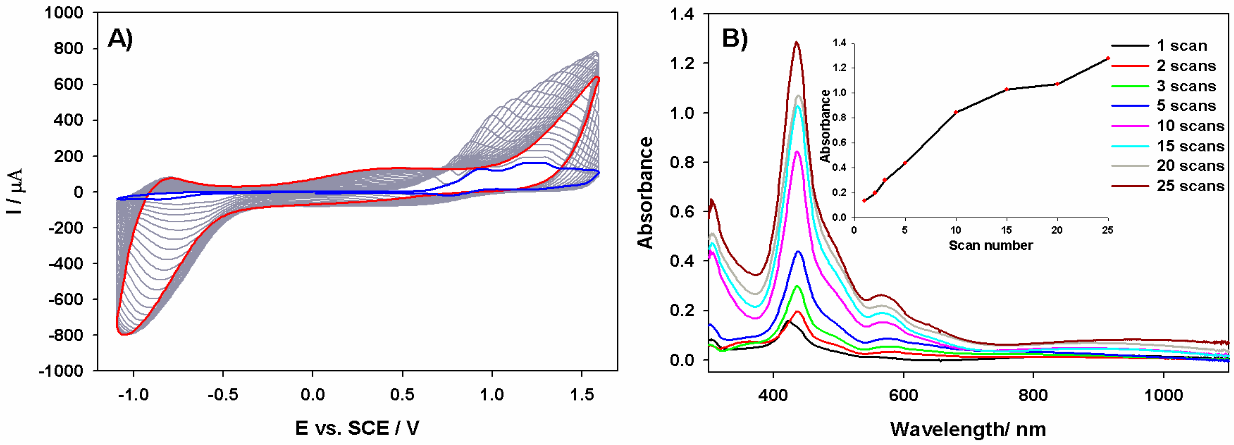

Figure 3.2. A) Cyclic voltammograms recorded during 25 iterative scans conducted between −1.1 V and +1.6 V *vs.* SCE in a 1,2-$C_2H_4Cl_2$/CH_3CN (7/3) solution and NBu_4PF_6 (0.1 mol.L^{-1}) of **ZnT$_2$P** (0.75 mmol.L^{-1}) in the presence of py–C≡C–Ph–C≡C-py (2.25 mmol L^{-1}) corresponding to the ration 1:3. Blue curve: first scan (n=1). Red curve: final scan (n = 25). B) UV-vis-NIR spectrum of porphyrin copolymers films, **poly-ZnT$_2$P6**, obtained with different scan numbers between −1.1 V and +1.6 V. Inset: plot of the absorbance measured at λ = 435 nm *versus* n the numbers of iterative scans.

In the case of the polyporphyrin **poly-ZnT$_2$P6**, a characteristic UV-visible-NIR spectrum is obtained after electropolymerization between -1.0 and +1.6 V exhibiting also a broad split Soret absorption band accompagnied by the red-shift at λ = 435 nm and λ = 491 nm. The visible bands (Q bands) are also red-shifted and are observed at 568 and 651 nm while a broad and large additional band at 884 nm in the NIR region is still a little observed suggesting that the film is not completely converted to the poly-porphyrin copolymer form and that one part of the copolymer is still the isoporphyrin intermediate (Table 3.1 and Fig. 3.2B).

2.1.3. Formation of isoporphyrin copolymer

Isoporphyrin was also obtained by iterative scans between -1.1 V and 1.0 V using the method developed and described in Chapter II. The oxidation wave of first cycle corresponds to the formation of the π-radical cation porphyrin **$ZnT_2P^{+\bullet}$**. Then, nucleophilic attack of the pyridyl group at the position of the positive charge (mainly at the *meso* position) occurs leading to the formation of the isoporphyrin which is in turn oxidized, followed by the removal of the hydrogen and the rearromatization of the porphyrin which gives one monosubstituted porphyrin **ZnT_2P-*meso*-py^+-C≡C-Ph–C≡C-py**. The oxidation of this monosubstituted compound leads to the formation of **$ZnT_2P^{+\bullet}$-*meso*-py^+–C≡C–Ph–C≡C-py**, which gives in turn to the formation of the copolymer of isoporphyrin **[iso$ZnT_2P^{\bullet}$(H)-*meso*-py^+–C≡C–Ph–C≡C-py^+-(H)iso$ZnT_2P^{\bullet}$]$_n$ 2nPF_6^-** namely **poly-ZnT_2iso$P6^{\bullet}$**.

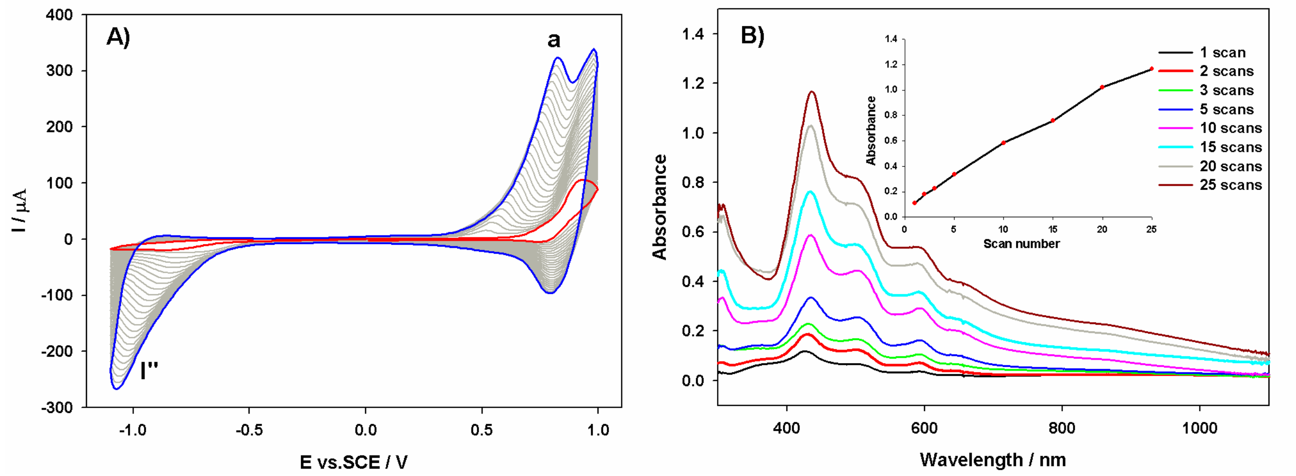

Figure 3.3. A) Cyclic voltammograms recorded during 25 iterative scans conducted between −1.1 V and +1.0 V *vs.* SCE in a 1,2-$C_2H_4Cl_2$/CH_3CN (7/3) solution and NBu_4PF_6 (0.1 mol.L^{-1}) of **ZnT_2P** (0.75 mmol L^{-1}) in the presence of py–C≡C–Ph–C≡C-py (2.25 mmol L^{-1}) corresponded to the ratio 1:3. Blue curve: first scan (n=1). Red curve: final scan (n = 25). B) UV-vis-NIR spectrum of porphyrin copolymers films obtained with different scan numbers between −1.1 V and +1.0 V. Inset: plot of the absorbance measured at λ = 435 nm *versus* n the numbers of iterative scans.

Additional irreversible peak in oxidation (peak a) was observed between +0.50 and 0.75 V (depending of the thickness of the film) during electropolymerization as shown in Figure 3.3A. Peak I'' which is irreversible is due to the reduction of the pyridinum spacers. Compared with the corresponding copolymer of porphyrin, **poly-ZnT$_2$P6**, the UV-vis-NIR spectrum of the copolymer of radical isopophyrin **poly-ZnT$_2$isoP6$^\bullet$** showed clear splitting of the Soret band as well as the presence of one additional broad band in the NIR between 800 nm and 1000 nm but with smaller intensity (Fig. 3.3B).

In the case of the optical spectra, the relationship between absorption density of the film and the number of iterative scan used for the electropolymerization (scan number n) for **poly-ZnT$_2$P6** and **poly-ZnT$_2$isoP6$^\bullet$** were showed in the insets of Figure 3.2 and Figure 3.3. The absorption density increased linearly at least for $n < 10$ with scan number n for both **poly-ZnT$_2$P6** and **poly-ZnT$_2$isoP6$^\bullet$** showing good electrodeposition of the film.

In the case of **poly-ZnT$_2$isoP6$^\bullet$**, the Soret bands were red-shifted by 20 and 85 nm respectively compared to the **ZnT$_2$P** monomer (Table 3.1). The visible bands (Q bands) are also red-shifted by 45 and 85 nm compared to **ZnT$_2$P** monomer. Finaly, an additional band at 861 nm in the NIR region, typical of the isoporphyrin, is also detected for **poly-ZnT$_2$isoP6$^\bullet$**.

Table. 3.1. UV–visible spectral data for **ZnT$_2$P**, py-C≡C-Ph-C≡C-py in CH_3Cl_2, **poly-ZnT$_2$P6** and **poly-ZnT$_2$isoP6$^\bullet$** on optical transparent ITO electrodes. Under bracket: molar extinction coefficient (ε /10^3 L.M.cm^{-1})

Compound	**Soret band/nm**	**Q bands/nm**	**π-π^* band/nm**
ZnT$_2$P^a	415 (405.4)	546 (18.9), 584 (4.9)	
py–C≡C-Ph–C≡C-py^b			284 (46.2) 294 (41.1) 303 (42.3)
poly-ZnT$_2$P6^c	435, 491 (shoulder)	568, 651, 884	
poly-ZnT$_2$isoP6$^{\bullet d}$	435, 500 (shoulder)	591, 669, 861	

[a] In CH_3Cl.

[b] In 1,2-$EtCl_2$/CH_3CN (7/3).(see Fig.3S4).

[c] Copolymers obtained by iterative scan between -1.1 V and +1.6 V *vs.* SCE onto ITO.

[d] Copolymers obtained by iterative scan between -1.1 V and +1.0 V *vs.* SCE onto ITO.

2.2. EQCM for the copolymer deposition

The formation of **poly-ZnT_2P6** and **poly-$ZnT_2isoP6^\bullet$** by electropolymerization with iterative scans between -1.1 and +1.6 V and -1.1 V and 0.9 V (Fig. 3.4) has been monitored *in-situ* by EQCM. The variation of the quartz resonance frequency (Δf) decreases when the number of potential cycle increases, which is related to the increase of the amount of polymer deposited (Δm), calculated using Sauerbrey's equation.

Besides, the trace of the first scan in Figure 3.4 shows a significant decrease of the resonance frequency and thus an increase of the deposited mass at the first oxidation of the porphyrin; i.e. electropolymerization occurs upon the formation of the radical cation porphyrin **$ZnT_2P^{+\bullet}$** in the presence of py-C≡C-Ph–C≡C-py. The mass of the copolymer film increases with the scan number of potential cycle n (Fig. 3.4CD). For **poly-$ZnT_2isoP6^\bullet$**, the mass increases linearly with iterative scan number, which indicated the copolymer keep deposited on the ITO electrode with 25 scans. For **poly-ZnT_2P6**, the mass increased quasi-linearly for n < 10 and much slowly after 15 scans. It can be explained that at first, the first slope corresponds to the formation of the stable isoporphyrin copolymer. Then the slow kinetic of the oxidation of this intermediate copolymer is present in order to obtain the copolymer of poly-porphyrin. The conversion of the **poly-$ZnT_2isoP6^\bullet$** to **poly-ZnT_2P6** induces in fact less change of the mass (release of the H atoms followed by rearomatization of the porphyrin followed by the oxidation of the porphyrin). Other explanation can be given: *i)* during the formation of poly-pophyrin, the thickness of the film is important and induce the decrease of the conductivity of the film (and the increase of the resistance of the charge transfer, which decrease the kinetic of the formation of the poly-porphyrin). *ii)* Meanwhile, at this stage, 2D to 3D copolymers was formed with incorportation of ligand, electrolyte salt as well solvent.

After 25 iterative scans, 52.8 µg/cm^2 and 39.1 µg/cm^2 of **poly-ZnT_2P6** and **poly-$ZnT_2isoP6^\bullet$** are deposited respetively. The calculated surface coverage Γ in mole of repeat unit (ZnT_2P-$^+$py–C≡C–Ph–C≡C-py$^+\cdot 2PF_6^-$) for the copolymers is 47.1×10^{-9} mol.cm^{-2} and 34.8×10^{-9} mol.cm^{-2} respectively.

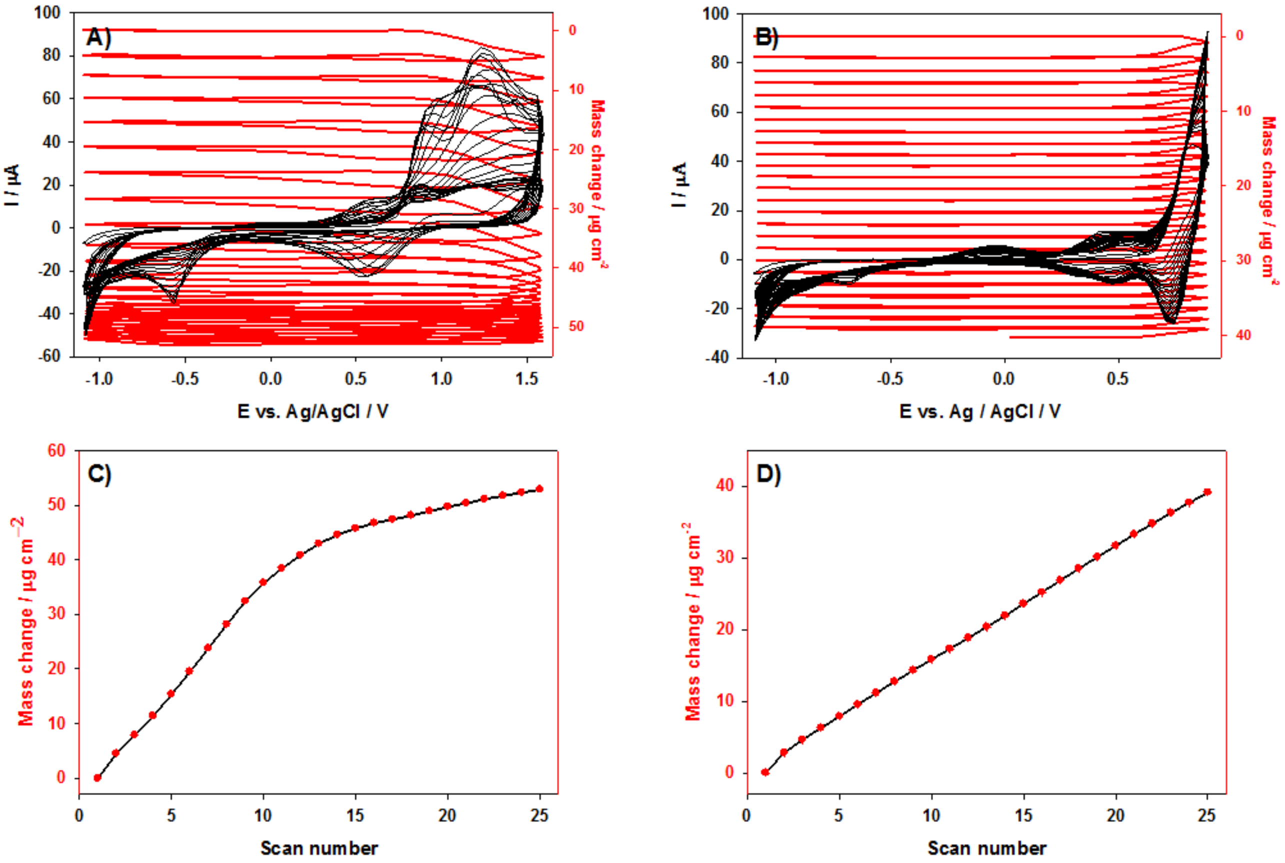

Figure 3.4. Successive cyclic voltammograms (25 scans) between A) -1.1 V and +1.6 V and B) -1.1 and +0.9 V electrochemical quartz crystal microbalance measurements (*Δm*) during the electropolymerization of 0.75 mmol L^{-1} **ZnT$_2$P** with 2.25 mmol L^{-1} py–C≡C–Ph–C≡C-py (ratio 1:3) in 1,2-$C_2H_4Cl_2$–CH_3CN (7/3) in the presence of 0.1 mol L^{-1} NBu_4PF_6. Working electrode: ITO (A = 0.2 cm^2) deposited on a 9.08 MHz AT-cut quartz crystal. *v* = 100 mVs^{-1}. Mass change (*Δm*) of the first 25 scans calculated from Sauerbrey's equation *versus* the number of scan n of C) **poly-ZnT$_2$P6** D) **poly-ZnT$_2$isoP6$^{\bullet}$**.

2.3. Cyclic voltammetric measurements of the films

2.3.1. Cyclic voltammetric investigations of the poly-ZnT$_2$P6 film.

Electroactive copolymers deposited by cyclic voltammetry (with various iterative scans number n) on ITO surfaces have been characterized by electrochemical methods. The cyclic voltammograms shown in Figure 3.5 have been recorded during a copolymer deposition on the ITO electrode surface at various iterative scan numbers n (n = 1, 2, 3, 5, 10, 15, 20, 25 cycles) between -1.1 V and +1.6 V. After the electropolymerization, the electrode was removed from the electrochemical cell, washed with CH_3CN and used as working electrode in a clean electrolytic solution containing only the solvent and the supporting electrolyte.

The first reduction wave observed at –0.88 V *vs.* SCE (peak I) is attributed to the reduction of the pyridinum and the formation of the pyridil radical. The anodic peak a may be explained by the oxidation of the intermediate isoporphyrin radical which is present as observed from the UV-visible-NIR spectra where the isoporphyrin copolymer was not fully converted to the polyporphyrin (incomplete oxidation of the intermediate isoporphyrin copolymer). The second oxidation wave II might correspond to the first oxidation of the porphyrin (Fig. 3.5B).

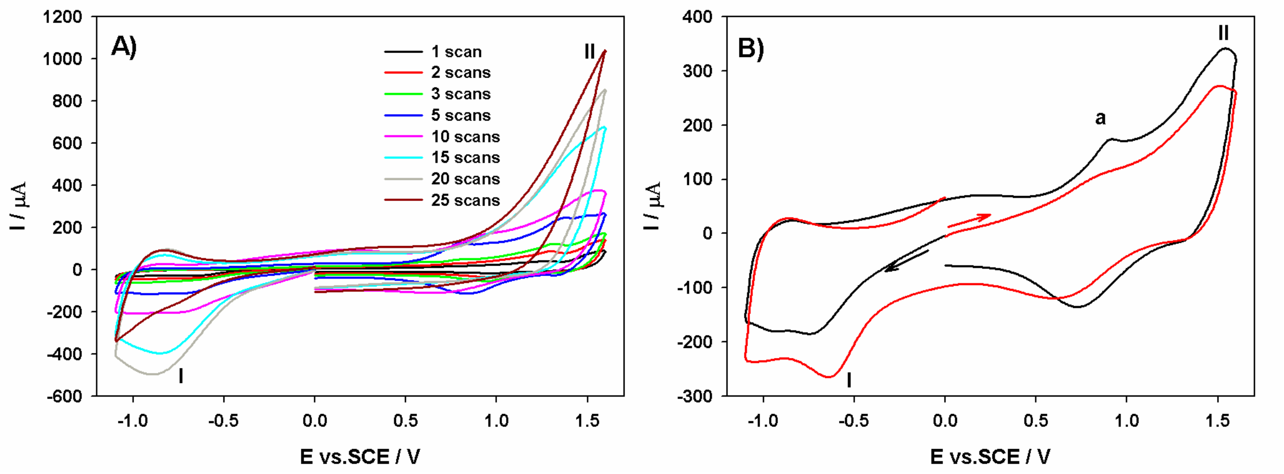

Figure 3.5. A) Cyclic voltammograms of **poly-ZnT2P6** obtained with py–C≡C–Ph–C≡C-py and **ZnT2P** after A) n = 1, 2, 3, 5, 10, 15, 20 and 25 scans and B) after 10 scans between -1.1 V and +1.6 V in $CH_3CN/1,2\text{-}C_2H_4Cl_2$ (3/7) with 0.1 M NBu_4PF_6. WE: ITO. S = 1 cm^2, v = 100 mV s^{-1}. Irreversible or quasi-reversible peaks not labelled in anodic part correspond to the oxidation of the π-ring of the macrocycle.

2.3.2. Permeability to Anionic and Neutral Probes of the Films.

The permeability of these films toward electrochemically active probe molecules has been also studied. Figure 3.6 shows the electrochemical response of the ferrocene or potassium ferricyanide ($Fe(CN)_6{}^{3-/4-}$) redox probe at ITO electrodes modified with films constituted of various numbers n of deposition cycles of **poly-ZnT2P6**.

In the case of $Fe(CN)_6{}^{3-/4-}$, for bare ITO electrode (not shown), the redox probe presents a quasi-reversible cyclic voltammetry (peak-to-peak separation 219 mV, full line), indicating that the probe diffuses freely to the ITO electrode surface and undergoes electron-transfer at the electrode. In contrast, in the presence of **poly-ZnT2P6** film which covered the ITO slide, it becomes more impermeable to the probe molecule when n is equal to 25 (Fig. 3.6B). Indeed, the peak current decreases when the number n of deposition cycles increases.

Similarly, using neutral ferocene redox probe, a quasi-eversible cyclic voltammetry (peak-to-peak separation 86 mV, not shown) is observed, indicating also that the probe diffuses freely to the ITO electrode (Fig. 3.6A). In the presence of **poly-ZnT2P6** films, it becomes more and more impermeable to ferrocene molecule when n increases. The peak current also decreases when the number n of deposition cycles reaches n = 25. Thus, the **poly-ZnT2P6** coated electrodes exhibit comparable behaviour with neutral ferocene or anionic potassium ferricyanide ($Fe(CN)_6^{3-/4-}$) redox probes.

The peak current for **poly-ZnT2P6** films deposited from 1 to 25 scans between -1.1 V and +1.6 V at modified ITO electrode have been scrutinized (in the dark) in 1 mmol L^{-1} ferrocene with $CH_3CN/1,2\text{-}C_2H_4Cl_2$ (3/7) (Fig. 3.6A) or in 1 mmol L^{-1} potassium ferricyanide with 0.5 mol L^{-1} Na_2SO_4 aqueous solution (Fig. 3.6B). The results indicated that the peak current of **poly-ZnT2P6** films increased from n=1 to n=3, and then decreased afterwards.

This follows the same trend of the photocurrent generation which will be discussed later. It suggests that the photocurrent efficiency is mainly dependent on the conductivity of the film, where the best performance for the photocurrent generation is for 3 iterative scans.

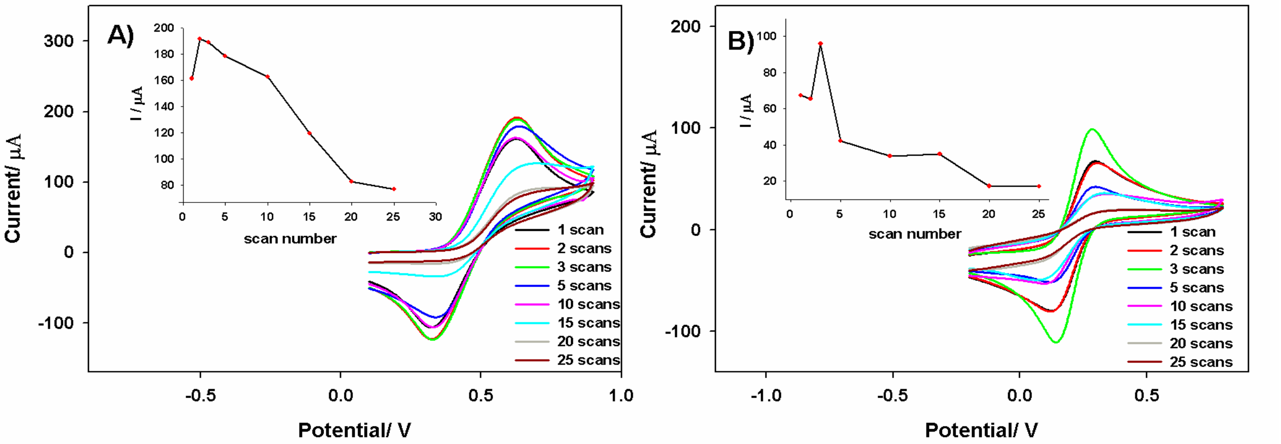

Figure 3.6. CVs of **poly-ZnT2P6** films deposited from 1 to 25 scans between -1.1 V and +1.6 V at modified ITO electrode in A) 1 mmol L^{-1} ferrocene with $CH_3CN/1,2\text{-}C_2H_4Cl_2$ (3/7) and B) 1 mmol L^{-1} potassium ferricyanide with 0.5 mol L^{-1} Na_2SO_4 aqueous solution.

2.3.3. Cyclic voltammetric investigations of the poly-ZnT$_2$isoP6$^\bullet$ film.

The cyclic voltammograms shown in Figure 3.7 have been recorded with a copolymer grown on the ITO electrode surface at various iterative scan numbers n (n = 1, 2, 3, 5, 10, 15, 20, and 25 cycles) between -1.1 V and +1.0 V forming **poly-ZnT$_2$isoP6$^\bullet$**. The electrode was then removed from the electrochemical cell, washed with CH_3CN and used as working electrode in a clean electrolytic solution containing only the solvent and the supporting electrolyte.

The first well defined, bell-shaped, reduction wave observed at –1.05 V *vs.* SCE (peak I) is attributed to the reduction of pyridinum in the copolymer films (Fig. 3.7 and Table 3.2). The anodic peak b may be explained after the reduction of the pyridinium at peak I by the presence of the radical coupling (intra- or inter-molecular reaction) between two radical pyridyl electrogenerated forming C-C bound and dipyridine.[20] Another explanation, after the reduction of the pyridinium generated the radical pyridyle, can be an intramolecular radical coupling between the radical pyridyl and the radical porphyrin which is still present giving the formation of the C-C bound between the radical pyridyl and the radical isoporphyrin forming one additional cycle with five carbons. In both case, peak b corresponds to the oxidation of this C-C bound (dipyridine) which regenerated the pyridinium as well as the isoporphyrin radical.

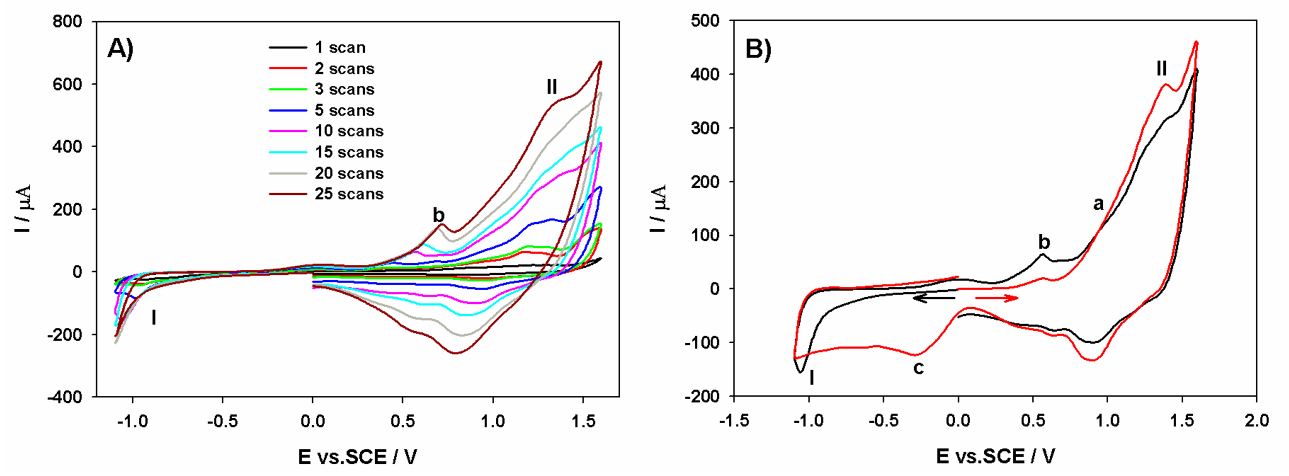

Figure 3.7. A) Cyclic voltammograms of **poly-ZnT$_2$isoP6$^\bullet$** obtained with py–C≡C–Ph–C≡C-py and **ZnT$_2$P** after A) n = 1, 2, 3, 5, 10, 15, 20 and 25 scans and B) after 10 scans between -1.1 V and +1.6 V in $CH_3CN/1,2\text{-}C_2H_4Cl_2$ (3/7) with 0.1 M NBu_4PF_6. WE: ITO. S = 1 cm^2, v = 100 mV s^{-1}. Irreversible peaks not labelled in anodic part correspond to the oxidation of the π-ring of the macrocycle.

Furthermore, **poly-ZnT$_2$isoP6$^\bullet$** films electropolymerized between by -1.1 V and 1.0 V, can be further oxidized between 1.0 V and 1.6 V (Fig. 3.7). Wave a is probably related to the oxidation the radical isoporphyrin **poly-ZnT$_2$isoP6$^\bullet$** generating the oxidized isoporphyrin **poly-ZnT$_2$isoP6$^+$** copolymer. Peak II may correspond to the further oxidation giving **poly-ZnT$_2$P6** copolymer followed by its oxidation.

However, the signal (peak II) is not unique and seem to be splitted into two close waves. The first signal may correspond to the oxidation of the isoporphyrin inducing the removal of the hydrogen and the rearromatization leading to the porphyrin. Thus, in such a case the second oxidation may be due to the oxidation of the resultant porphyrin leading to the π-radical cation porphyrin. This process is probably slow. Finaly, the presence of peak c is not clear and need further investigations.

Table 3.2. Electrochemical data for **ZnT$_2$P**, **poly-ZnT$_2$P6**, **poly-ZnT$_2$isoP6$^\bullet$**.

Compounds	**Ring oxidation**			**Reduction of spacer**		**Ring reduction**	
	Peak II	**peak a**	**peak b**	**peak I**	**peak c**		
ZnT$_2$P^a	1.08 (150)	0.79 (90)				-1.41 (160)	-1.84 (170)
poly-ZnT$_2$isoP6$^\bullet$	+1.39^{irr}	+0.93 (20)	+0.57^{irr}	-1.05^{irr}	-0.29^{irr}		
poly-ZnT$_2$P6	+1.51^{irr}	+0.80 (170)		-0.78^{irr}			

The given half-wave potentials are equal to $E_{1/2} = (E_{pa} + E_{pc})/2$. Under bracket: $\triangle E_p = |E_{pa} - E_{pc}|$.

3. Photocurrent generation

3.1. Photoelectrochemical properties of poly-ZnT$_2$P6

Figure 3.8A shows the typical current-potential curves of **poly-ZnT$_2$P6** thin films on ITO electrodes obtained in 5 mM I_2 / 0.5 M I^- aqueous solution under visible light illumination (full line). The photocurrent response in the potentiostatic mode at 0 V under on-off light illumination cycles is shown in Figure 3.8B. The equilibrium potential of I_3^-/I^- redox couple in solution is taken as reference potential at 0 V in the cyclic voltammograms. First, we can analyse the curves obtained in the absence of illumination (plotted with dashed lines in Figure 3.8A). For bare ITO electrode (blue curve), almost no Faradaic current is observed between -0.3 and 0.3 V, revealing a slow I^- oxidation and I_3^- reduction kinetics on ITO. However, the I^- oxidation and I_3^- reduction currents are significantly enhanced on the ITO modified by the presence of the copolymers (black curves in Figure 3.8A).

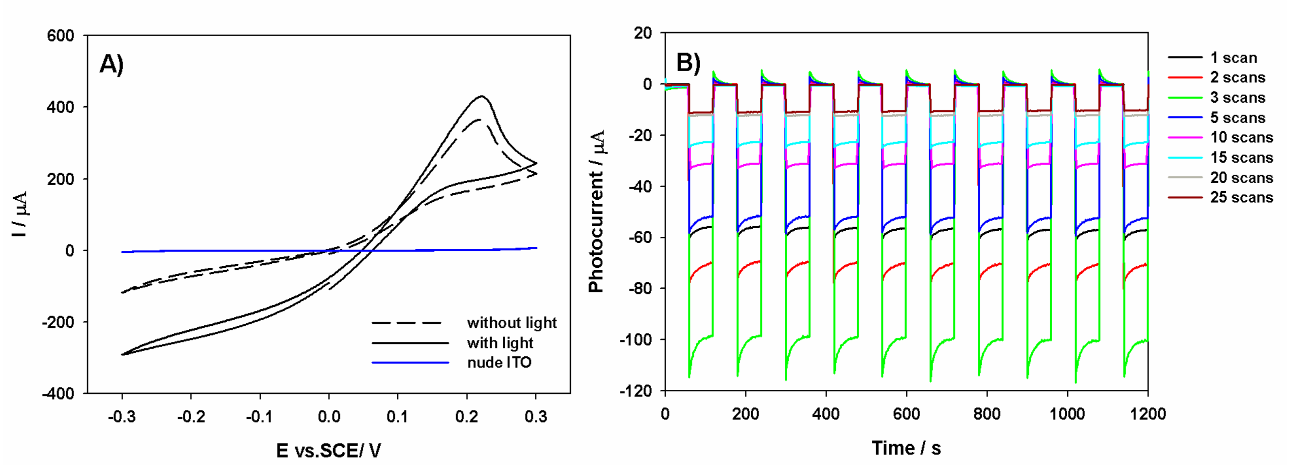

Figure 3.8. A) Current-potential curves of **poly-ZnT2P6** (obtained with n = 3 iterative scans between -1.1 V and +1.6 V) thin films on ITO electrodes obtained in 0.5 M I^- / 5 mM I_2 aqueous solution in the dark or under visible illumination. B) Photoelectrochemical response of **poly-ZnT2P6** films obtained with n = 1, 2, 3, 5, 10, 15, 20 or 25 iterative scans. Measurements has been done under on-off light illumination from a 300 W Xe arc lamp (with λ > 385 nm long pass filter) in I_3^- 5 mmol L^{-1} and I^- 0.5 mol L^{-1} aqueous solution. BIAS potential: 0.00 V *vs.* OCP.

Under visible light, the open circuit potential (OCP) increases of ca. 60 mV for the **poly-ZnT2P6** copolymers respectively. Above this potential, the I^- oxidation current becomes predominant due to the high I^- concentration in solution, impeding thus further increase of the photovoltage. For potentials below the OCP, a negative photocurrent is observed at 0 V for the **poly-ZnT2P6** copolymer thin film reaching ca. -98 µA cm^{-2}. The photovoltage response in the potentiostatic mode at 0 A under on-off light illumination cycles is displayed in Figure 3.9. The best photocurrent and phovoltage were obtained for the films prepared with 3 cycles (n = 3 iterative scans).

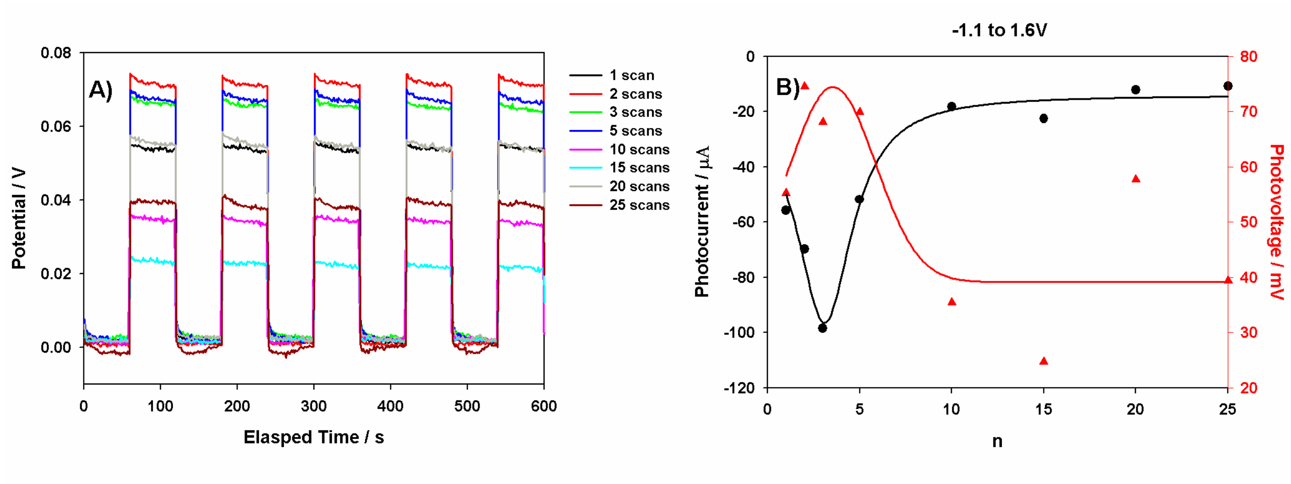

Figure 3.9. A) Photovoltage response of **poly-ZnT$_2$P6** films obtained with n = 1, 2, 3, 5, 10, 15, 20 or 25 iterative scans. Measurements has been done under on-off light illumination from a 300 W Xe arc lamp (with λ > 385 nm long pass filter) in I_3^- 5 mmol L^{-1} and I$^-$ 0.5 mol L^{-1} aqueous solution. BIAS current: 0.00 A. B) Photoelectrochemical response of **poly-ZnT$_2$P6** (photocurrent black line) and (photovoltage red line) obtained with py-C≡C-Ph-C≡C-py and **ZnT$_2$P** obtained with n = 1, 2, 3, 5, 10, 15, 20 and 25 iterative scans.

Various concentration of I_3^- have been tested (10 mmol L^{-1}, 5 mmol L^{-1}, and 2.5 mmol L^{-1}) with 0.5 mol L^{-1} I$^-$ (Fig. 3.S5). The results show that the mass transport of I_3^- is influencing the photocurrent for low I_3^- concentration, below 5 mM. Thus, when the concentration of triiodide was increased from 2.5 mmol L^{-1} to 5 mmol L^{-1}, the photocurrent increased. However, when higher concentration of triiodide (10 mmol L^{-1}) was used, decrease of photocurrent was observed and could be explained by the absorption of the visible light by the redox mediator that absorbs strongly the visible light leading to the strong decrease of the photons able to reach the film. Indeed, the modified ITO electrode is in the middle of the solution and not on the border of the cell.

3.2. Photoelectrochemical properties of poly-ZnT$_2$isoP6$^{\bullet}$

The current-potential curves measured under visible light illumination and potentiodynamic conditions are also plotted in Figure 3.10A (full line) for the **poly-ZnT$_2$isoP6$^{\bullet}$** copolymers. The photocurrent response in the potentiostatic mode at 0 V under on-off light illumination cycles is shown in Figure 3.10B. Under visible light, the open circuit potential increases of ca. 80 mV for the **poly-ZnT$_2$isoP6$^{\bullet}$** copolymers. For potentials below the OCP, a negative photocurrent is observed for both copolymers, the photocurrent at 0 V of the **poly-ZnT$_2$isoP6$^{\bullet}$** copolymer thin film reaching ca. -177 µA cm^{-2} (potentiostatic experiment).

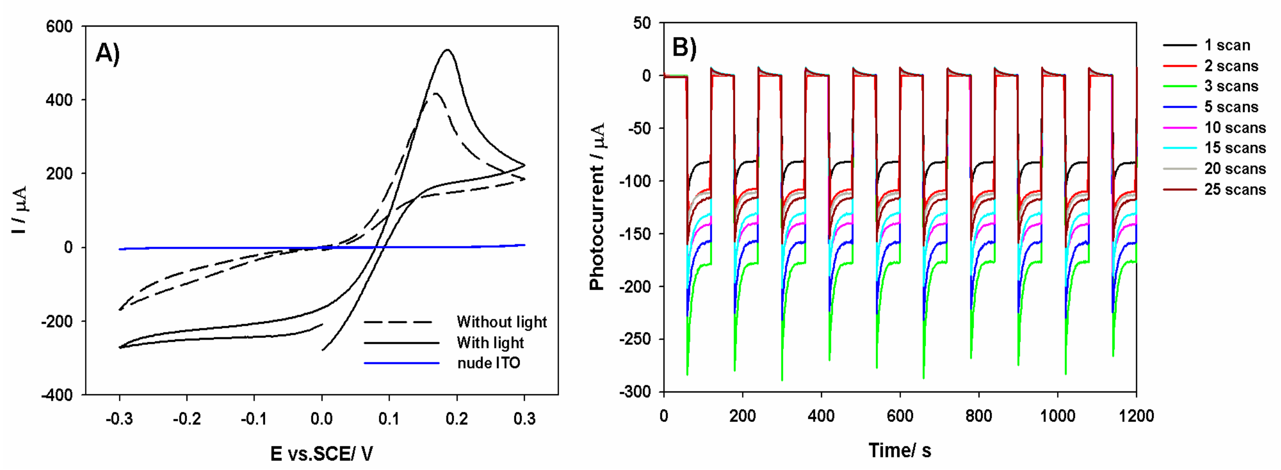

Figure 3.10. A) Current-potential curves of **poly-ZnT$_2$isoP6$^{\bullet}$** (obtained with n = 3 iterative scans between -1.1 V and +1.0 V) thin films on ITO electrodes obtained in 0.5 M I$^-$ / 5 mM I$_2$ aqueous solution in the dark or under visible illumination. B) Photoelectrochemical response of **poly-ZnT$_2$isoP6$^{\bullet}$** films obtained with n = 1, 2, 3, 5, 10, 15, 20 or 25 iterative scans. Measurements has been done under on-off light illumination from a 300 W Xe arc lamp (with $\lambda > 385$ nm long pass filter) in I$_3^-$ 5 mmol L^{-1} and I$^-$ 0.5 mol L^{-1} aqueous solution. BIAS potential: 0.00 V *vs.* OCP.

The better performance of isoporphyrin copolymer **poly-ZnT$_2$isoP6$^{\bullet}$** can be attributed to the broad and the splitting of Soret absorption band as well as the presence of the additional band in the NIR region which improves the light harvesting efficiency and then the photocurrent. For all the copolymers, the photocurrent level remains stable after several hours of on-off illumination cycles at 0 V (not shown) indicating that the copolymers are stable under photocurrent generation.

The magnitude of the photocurrent strongly depends on the number of potential scans n and then of the amount of copolymer film deposited, and the best performances being obtained for n=3 electropolymerization cycles. It is confirmed that higher photocurrents are obtained with the isoporphyrin copolymer **poly-ZnT$_2$isoP6$^{\bullet}$** as compared to polyporphyrin copolymer **poly-ZnT$_2$P6**. It may be explained in part by the better absorption of the whole light by **poly-ZnT$_2$isoP6$^{\bullet}$** that shows the spliting of the Soret bands as well as the presence of additional band in the NIR domain.

3.3. Eletcrochemical impedance spectroscopy

Further insights into the photoelectrochemical behaviour of the copolymer films as a function of n could be gained by electrochemical impedance spectroscopy, which is widely used in the investigation of dye sensitized solar cell. The Nyquist plots of a typical impedance spectra measured for **poly-ZnT$_2$isoP6$^{\bullet}$** and **poly-ZnT$_2$P6** at 0 V in 5 mM I$_3^-$ / 0.5 M I$^-$ aqueous solution are plotted in Figure 3.11 for various scan numbers. The charge transfer resistance R_{ct} of the I^-/I_3^- species at the ITO/solution interface and the charge resistance R_f within the film could be extracted from the experimental data. For the **poly-ZnT$_2$P6**, resistance at low frequency in the Nyquist plot first decreased from one to 2 scans which is due to a decrease of R_{ct}, and then increased with scan number due to a high film resistance. The results might explain the best photocurrent of **poly-ZnT$_2$P6** obtained after 3 cycles (film obtained with n = 3 iterative scans).

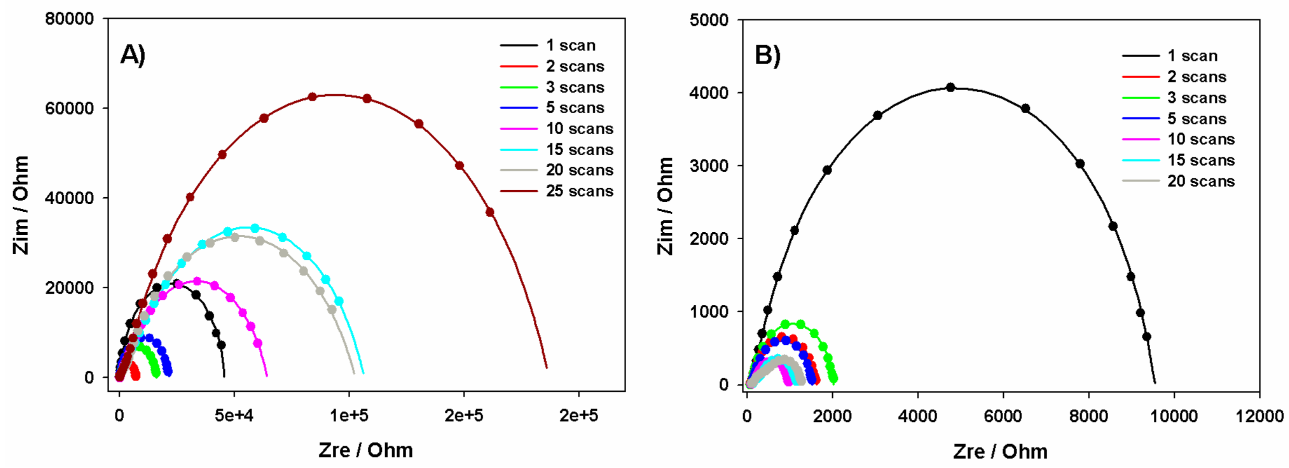

Figure 3.11. ESI Nyquist of A) **poly-ZnT$_2$P6** and B) **poly-ZnT$_2$isoP6$^\bullet$** with various scan number. Measurements have been done ***in the dark*** and in H_2O containing I_3^- 5 mmol L^{-1} and I^- 0.5 mol L^{-1}. BIAS potential: 0.00 V vs. OCP.

The evolution of R_{ct} and R_{ct_film} values as a function of n (number of iterative scan during the electropolymeriation) can be estimated from the fit of the experimental impedance spectra and is displayed in Figure 3.12 for the **poly-ZnT$_2$P6** and **poly-ZnT$_2$isoP6$^\bullet$** copolymers thin films. Overall, the charge transfer resistance R_{ct} at the ITO/copolymer interface decreases when n increases while the charge transfer resistance R_{ct_film} increases with the amount of copolymer deposited. For the **poly-ZnT$_2$isoP6$^\bullet$** copolymer, R_{ct} at ITO/copolymer decreases from ca. 10 kΩ for n=1 to ca. R_{ct} ~ 2000 Ω for n=3, confirming the enhancement of the I^-/I_3^- charge transfer kinetics when the copolymer is present on the ITO. After 5 scans, the Nyquist plots could not be fitted with a single resistance R_{ct} in parallel with a capacitance. This is attributed to the increasing thickness of the film. The charge transfer resistance R_{ct_film} could be estimated by using an equivalent circuit comprising the interfacial charge transfer resistance in parallel with the interfacial capacitance and the film charge transfer resistance in parallel with the film capacitance. R_{ct_film} rapidly increases with scan numbers indicating that the electronic and ionic transfer within the films becomes a limiting factor. For **poly-ZnT$_2$P6**, similar behavior is observed in Figure 3.12B.

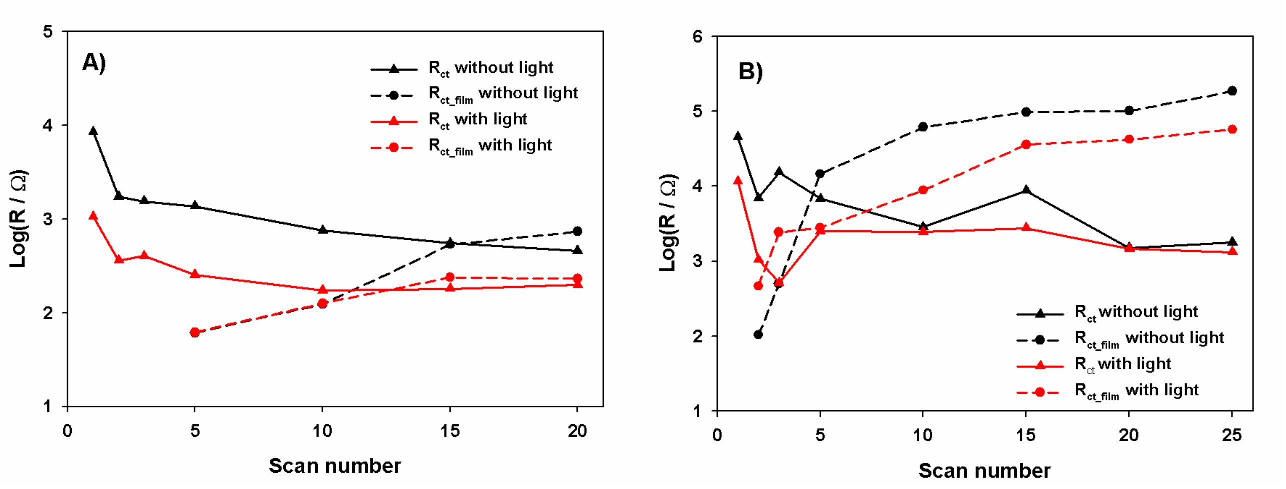

Figure 3.12. Plot of the Log(R) versus n (number of iterative scan, *v* = 100 mV s^{-1}, between -1.1 V and +1.0 V for **poly-ZnT$_2$isoP6$^\bullet$** A) and between -1.1 V and +1.6 V for **poly-ZnT$_2$P6** B) under one off light illumination and under one on light illumination.

3.4. Energy diagrams

Figure 3.13 and Figure 3.S6 represent the energy diagram corresponding to the photoreduction of I_3^- on the copolymer **poly-ZnT$_2$isoP6$^\bullet$** and **poly-ZnT$_2$P6** respectively.

The HOMO level energies of the **poly-ZnT$_2$isoP6$^\bullet$** and **poly-ZnT$_2$P6** species have been estimated from the first oxidation potential observed in the cyclic voltammograms, while the energy level of the dipyridinium species is given by the potential of the first reduction peak (Table 3.2). The LUMO levels of the excited **poly-ZnT$_2$isoP6$^\bullet$** and **poly-ZnT$_2$P6** species can be roughly estimated by subtracting the excitation energy of the Soret, Q as well as NIR bands from the HOMO level energies. The energy Level corresponding to the band in the NIR region has also been indicated in the energy diagram. Under illumination at 0 V, the photon absorption by the (iso)porphyrin entities generates an electron hole pair in the copolymer. The electron is transferred from the excited (iso)porphyrins to pyridinum which is the linker to form the radical pyridyle and then to the I_3^- reduced into I^-. The pyridinum acts as a relay for the electron transfer. The oxidized (iso)porphyrin is regenerated by an electron transfer from the ITO substrate.

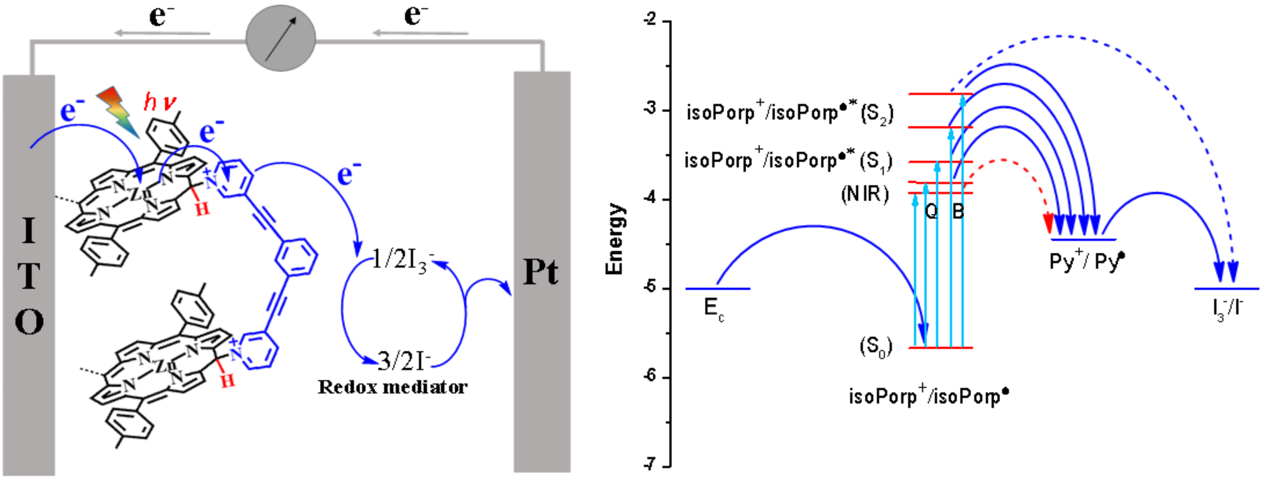

Figure 3.13. Schematic illustration of the energy level diagram for **poly-ZnT$_2$isoP6$^•$** showing electron transfer processes measured in H_2O containing I_3^- 5 mmol L^{-1} and I^- 0.5 mol L^{-1} (Py^+ = pyridinium, Porp = porphyrin).

4. Conclusions

The anodic electro-copolymerization of 5,15-ditolylporphyrin (**ZnT$_2$P**) with 3-(2-(3-(2-(pyridin-3-yl)ethynyl)phenyl)ethynyl)pyridine yielded two type of copolymer films depending of the potential applied. The polyporphyrin electroactive films **poly-ZnT$_2$P6** was obtained on ITO electrode surfaces during repetitive potential cycling between -1.1 V and 1.60 V *vs.* SCE while the poly-isoporphyrin radical copolymer **poly-ZnT$_2$isoP6$^•$** was obtained by electropolymerization between -1.1 V to 1.0 V. UV–visible absorption spectroscopy, and electrochemistry were used to fully characterize the resulting films. By electrochemical quartz crystal microbalance, the mass of two copolymers deposited onto the electrodes increased with scan numbers. The poly-isoporphyrin radical copolymer showed better photocurrent generation than the corresponding poly-porphyrin and be be explained by the splitting of the Soret band as well as the presence of additional band in the NIR region.

Due to the Covid-19, we have not time to study the inclusion of polyoxometalate or lacunary polyoxometalate inside such type of films. In such a case the triad D-A$_1$-A$_2$ will be obtained where the donor is the excited porphyrin and A$_1$ and A$_2$ are the polyoxometalate and the pyridinium linkers. In order to have robust material and to favorize the inclusion, the change of the nature of the metalloporphyrin is also required in order to have coordination interaction between porphyrin and POM.

It is also needed to characterize such copolymers by X-ray photoelectron spectroscopy and by atomic force microscopy.

As we have discussed in the chapter I, not only the pyridyl ligands could be used as nucleophiles to form porphyrin copolymer, also the polyoxometalate (POM) modified with at least two pendant pyridyl groups could be used to form hybrid copolymer with porphyrin and POM having pendant pyridyle groups. In the next chapter, one kind of hybrid polyiodometalate (PIM) wheresix pyridyl have been grafted (**PIM(py)$_6$**) will be used in order to try to form 3D material based on porphyrin or isoporphyrin and **PIM(py)$_6$**.

References

1. Z. Huo, A. Bonnefont, Y. Liang, R. Farha, M. Goldmann, E. Saint-Aman, H. Xu, C. Bucher, L. Ruhlmann. *Electrochimica Acta*, **2018**, 274, 177–191.
2. M. Boudiaf, Y. Liang, R. Lamare, J. Weiss, H. Ibrahim, M. Goldmann, E. Bentouhami, V. Badets, S. Choua, N. Le Breton, A. Bonnefont, L. Ruhlmann, *Electrochimica Acta*, **2019**, 309, 432–449.
3. A. Yokoyama, T. Kojima, K. Ohkubo, S. Fukuzumi, *Chem. Commun*, **2007**, 3997–3999.
4. A. Yokoyama, T. Kojima, K. Ohkubo, S. Fukuzumi, *Inorg. Chem*, **2010**, 49, 11190–11198.
5. A. Yokoyama, T. Kojima, K. Ohkubo, M. Shiro, S. Fukuzumi, *J. Phys. Chem. A*, **2011**, 115, 986–997.
6. Y. Mest, M. L'Her, N. H. Hendricks, K. Kim, J. P. Collman, *Inorg. Chem*, **1992**, 31, 835–847.
7. Y. Mest, C. Inisan, A. Laouénan, M. L'Her, J. Talarmin, M. El Khalifa, J. Saillard, *J. Am. Chem. Soc.* **1997**, 119, 6095–6106.
8. R. Guilard, F. Jérôme, J. Barbe, C. P. Gros, Z. Ou, J. Shao, J. Fischer, R. Weiss, K. M. Kadish, *Inorg. Chem*. **2001**, 40, 4856–4865.
9. J. Barbe, B. Habermeyer, T. Khoury, C. P. Gros, P. Richard, P. Chen, K.M. Kadish, *Inorg. Chem*. **2010**, 49, 8929–8940.
10. Karl M. Kadish, J. Shao, Z. Ou, R. Zhan, F. Burdet, J. Barbe, C. P. Gros, R. Guilard, *Inorg.Chem*. **2005**, 44, 9023−9038.
11. K. M. Kadish, J. Shao, Z. Ou, L. Frémond, R. Zhan, F. Burdet, J. Barbe, C. P. Gros, R. Guilard, *Inorg.Chem*. **2005**, 44, 6744−6754.
12. R. Guilard, C. P. Gros, J. Barbe, E. Espinosa, F. Jérôme, A. Tabard, *Inorg.Chem*. **2004**, 43, 7441−7455.
13. K. M. Kadish, Z. Ou, J. Shao, C. P. Gros, J. Barbe, F. Jérôme, F. Bolze, F. Burdet, R. Guilard, *Inorg. Chem*. **2002**, 41, 3990−4005.
14. J. T. Fletcher and M. J. Therien, *Inorg. Chem*. **2002**, 41, 331−341.
15. Z. N. Zahran, E. A. Mohamed and Y. Naruta, *Sci Rep* **2016,** 6**,** 24533. https://doi.org/10.1038/srep24533.
16. D. Sun, F. S. Tham, C. A. Reed, L. Chaker, P. D. W. Boyd, *J. Am. Chem. Soc.* **2002**, 124, 6604–6612.
17. A. L. Kieran, S. I. Pascu, T. Jarrosson, J. K. M. Sanders, *Chem. Commun.*, **2005**, 1276–1278.
18. K. Tashiro, T. Aida, J. Zheng, K. Kinbara, K. Saigo, S. Sakamoto, K. Yamaguchi, *J. Am. Chem. Soc.* **1999**, 121, 9477–9478.
19. Z. Huo, I. Azcarate, R. Farha, M. Goldmann. H. Xu, B. Hasenknopf, E. Lacôte, L. Ruhlmann, *J. Solid State Electrochem*, **2015**, 19, 2611–2621.
20. D. Schaming, S. Marggi-Poullain, I. Ahmed, R. Farha, M. Goldmann, J.-P. Gisselbrecht, L. Ruhlmann, *New J. Chem.*, **2011**, 35, 2534–2543

Chapter IV

Stable isoporphyrin copolymer prepared with pyridine end decorated molybdenum(II) halide cluster

Chapter IV: Stable isoporphyrin copolymer prepared with pyridine end decorated molybdenum(II) halide cluster

In former chapters 2 and 3, we have studied and performed the electropolymerization of copolymers of porphyrin or isoporphyrin using dipyridine ligand **Py-R-Py** (R = propanediyl, biphenyl, ethyne, benzene or even polyoxometalate) porphyrin **ZnT_2P**.[1] In our published work,[2-3] hybrid polyoxometalate-porphyrin copolymeric films were obtained by the electrooxidation of free base 5,15-ditolyl porphyrin (**H_2T_2P**) or zinc-*β*-octaethylporphyrin (**ZnOEP**) in the presence of POM modified with two pyridyl groups (**Py-POM-Py**).

In this chapter, our target is to electrosynthesize 3D copolymer using of **$PIM(py)_6$** (PIM = polyIodoMetalate) having 6 pendant pyridyl groups in the presence of **ZnT_2P** (Scheme 4.1). A novel hybrid supramolecular cluster-porphyrin system based on zinc-5,15-ditolyl-porphyrin (**ZnT_2P**) and pyridine end-decorated molybdenum(II) halide cluster (Bu_4N_2) $[\{Mo_6I_8\}(OOC\text{-}C_5H_4N)_6]$ can be obtained by electropolymerization. The mechanisms of preparation of these electroactive 3D copolymers are proposed and discussed. The material has been fully characterized and studied by UV-Vis-NIR spectroscopy, X-ray photoelectron spectroscopy, electrochemistry and ESR (Electron Spin Resonance). The photocurrent generation has been investigated under visible light and NIR light illumination. The impedance properties have been also examinated.

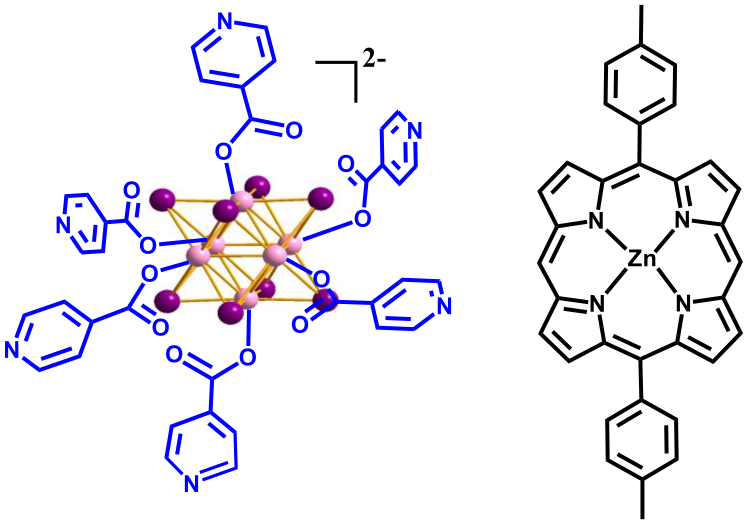

$PIM(py)_6$ **ZnT_2P**

Scheme 4.1. Structures of $[Mo_6I_8(pyCOO)_6]^{2-}$ (**$PIM(py)_6$**) and of **ZnT_2P**.

1. Introduction

Polyoxometalates (POMs) are a structurally diverse family of anionic metal-oxygen cluster anions constituted of metal elements in their highest oxidation states finding applications in analytical chemistry, medicine, homogeneous and heterogeneous catalysis, electronics and materials science.[4] In the case of hybrid POM-porphyrin systems, enhancement of photoelectric and nonlinear optical properties were observed, which makes them promising for the development of photoelectronic and optical devices.[5]

In the octahedral halide clusters of molybdenum(II) with the general formula $[\{Mo_6(\mu_3\text{-}X)_8\}L_6]^n$ ($X=Cl^-$, Br^-, I^-; L= inorganic or organic ligands; $\{Mo_6(\mu_3\text{-}X)_8\}^{4+}$ is the cluster core), the metal atom is associated with eight strongly bonded inner ligands X and six labile apical ligands L. Under excitation from the UV light to the green spectral regions, the clusters exhibit a broad red-NIR luminescence. Cluster of the type $\{Mo_6X_8\}^{4+}$ (X=Cl, Br, I) with L being O-donor, N-donor, C-, P-, and S-donor ligands have been reported.[6-15] The hybrid systems formed by the interaction of pyridine end-decorated Mo(II) halide clusters and porphyrin via metal-ligand coordination have been also reported by Maxim N. Sokolov group. However, large excess porphyrin was taken in order to be able to have six coordinated zinc porphyrin. Indeed, important excess of porphyrin is needed to induce coordination due to the steric hindrance as well as the low formation constant of pyridine subunits of **PIM(py)$_6$** to the zinc porphyrin.

In this chapter, we will show that electropolymerization will be one other way to use this **PIM(py)$_6$** cluster which will give 3D copolymer material. Indeed, covalent connections at the *meso* position of the porphyrin will induce lower steric hindrance in comparison of the coordiation.

2. Formation and characterization

2.1. Reactivity of $(Bu_4N)_2[Mo_6I_8(COOpy)_6]$

Firstly, the electrochemical behavior of $(Bu_4N)_2[Mo_6I_8(COOpy)_6]$ (**PIM(py)$_6$**) has been studied by cyclic voltammetry. Three different working electrodes have been used to study **PIM(py)$_6$** in solution: a glassy carbon electrode (GCE, d=3mm), a platinum electrode (Pt, s=1.0 cm^2) and an indium tin oxides electrode (ITO, s=1.0 cm^2).

PIM(py)$_6$ showed similar redox behavior on GCE and Pt electrodes as shown in Figure 4.1A and Figure 4.1B respectively. One reversible oxidation appeared near 1.32 V. The I_{pa}/I_{pc} is close to 1 and it was assumed to be the oxidation of $\{Mo_6I_8\}^{4+}/\{Mo_6I_8\}^{5+}$ according to the literature.[12] The small peaks (a, a$^{'}$, a$^{''}$) in Figure 4.1 are due to the absorption of **PIM(py)$_6$** on the electrodes (GCE, Pt or ITO) and corresponds to the "adsorption pre-peak" of oxidation of the adsorbed compound. In the case of Pt electrode for instance, the peak current a' increase linearly with the scan rate *v*, as shown in Figure 4.1D, which indicates that this wave is not control by the diffusion. It proves that such peak corresponds to the oxidation of the absorbed **PIM(py)$_6$** compound (adsorption peak). In contrast, I_{pa} or I_{pc} (anodic or cathodic peak current) of wave I (I$^{'}$ and I$^{''}$) increases linearly with the square root of the scan rate as shown in Figure 4S1. The results proved that the wave I corresponds to the diffusion-controlled redox processes (for scan rate higher than 100 mV/s in the case of GCE or Pt electrode).

However, in the case of ITO electrode, the anodic peak current $I^{''}_{pa}$ is always higher than the cathodic peak current $I^{''}_{pc}$, that means the cluster $\{Mo_6I_8\}^{5+}$ is not reduced completely on the reverse sweep as shown in Figure 4.1C. It may be due, this time to the absorption of the oxidized compound on the surface of the ITO electrode. In this case, it must be noticed that additional reduction peak is observed at -0.96 V in the cathodic domain. This additional peak may be due to the reduction of the adsorbed compound corresponding to the $\{Mo_6I_8\}^{4+}/\{Mo_6I_8\}^{3+}$ which is irreversible.

When a higher potential was reached in the anodic domain in the case of GCE electrode as shown in Figure 4.2A, one additional irreversible peak II is observed at 1.96 V. It may be due to the decomposition of the cluster core due to the fully oxidation of the Mo^{II} atoms.[13-15] Moreover, one irreversible peak (peak III) is also observed at -1.57 V and corresponds to the irreversible reduction of $\{Mo_6I_8\}^{4+}/\{Mo_6I_8\}^{3+}$ (Fig. 4.2B).

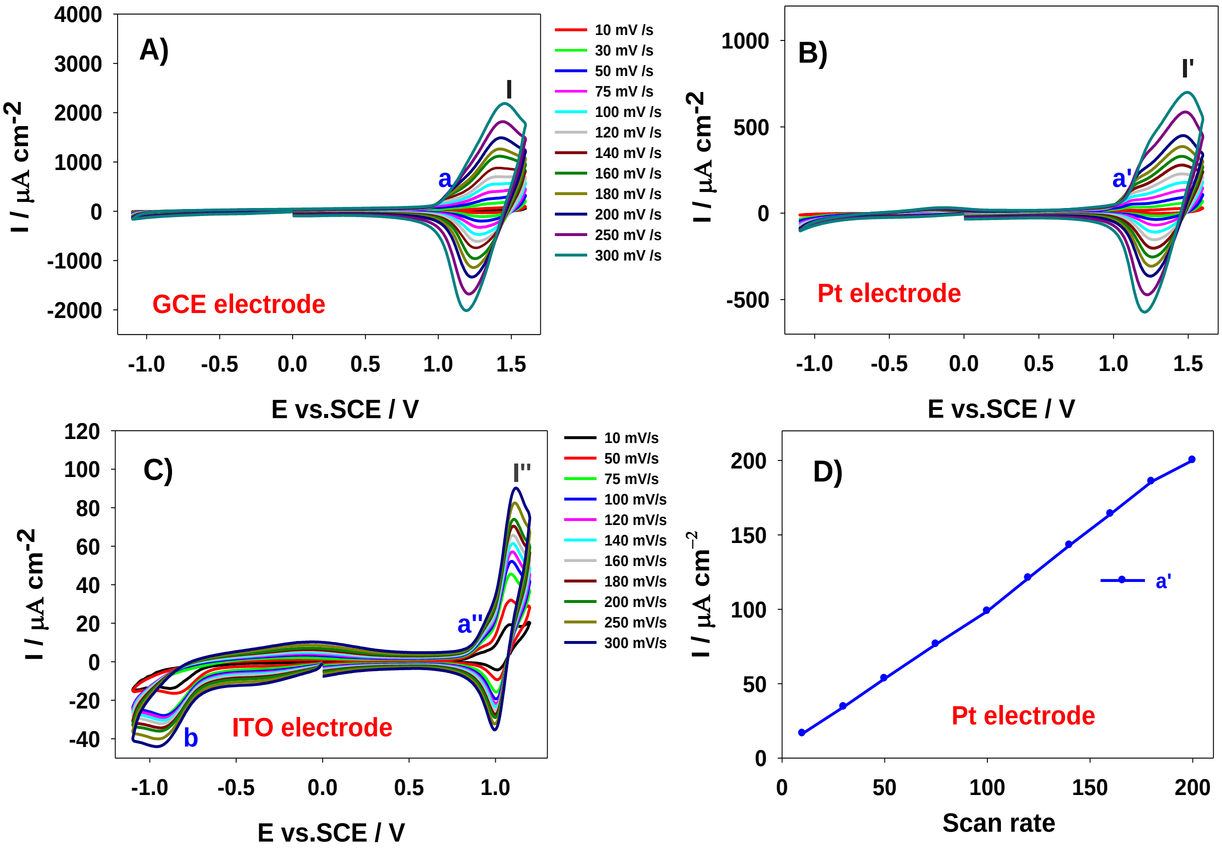

Figure 4.1. Cyclic voltammograms recorded of $(Bu_4N)_2[Mo_6I_8(pyCOO)_6]$ scans conducted *vs.* SCE between -1.1 V and +1.6 V on A) GCE electrode, B) Pt electrode, and between -1.1 V and +1.2 V on C) ITO electrode with increased scan rate in a 1,2-$C_2H_4Cl_2/CH_3CN$ (7/3) solution in the presence of NBu_4PF_6 (0.1 mol L^{-1}). (D) The relationship between scan rate and peak current of the peak a' in the case of Pt electrode.

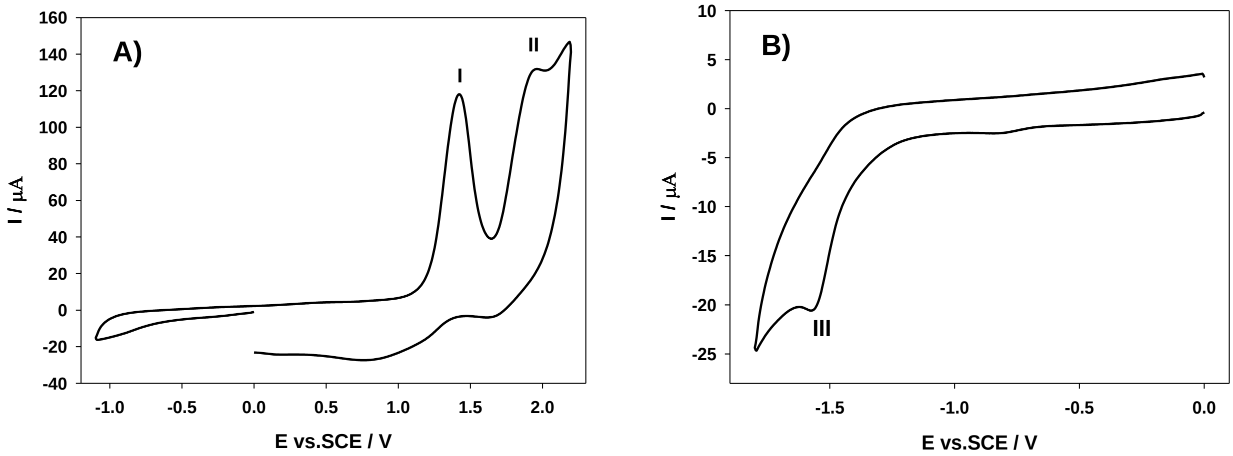

Figure 4.2. Cyclic voltammograms of cluster complexes of **PIM(py)₆** in 7/3 1,2-$EtCl_2/CH_3CN$ solution in the presence of NBu_4PF_6 (0.1 mol L^{-1}) on glassy carbon electrode (d = 3mm) (A) -1.1 V to 2.2 V (B) 0.0 V to -1.8 V. v = 100 mV s^{-1}.

The optical spectrum of **PIM(py)₆** is presented in Figure 4.3. With the increase of concentration of **PIM(py)₆**, the absorption intensity also increases as expected from the Beer-Lambert law. The absorption bands in UV region is due to the π–π* transitions in the aromatic terminal ligands. The broad and featureless absorption wavelength longer than 350 nm may due to the $\{Mo_6I_8\}^{4+}$ core-centered d−d transitions.[10] The result is consistent with the literature reported.[10, 12, 16, 17] The energy gap calculated form optical spectrum at 402 nm (3.08 eV) between HOMO and LUMO orbitals is close to the value calculated from the electrochemistry: 2.89 eV on GCE electrode (E_{ox} - E_{red}= 1.32 - (-1.57) = 2.89 eV).

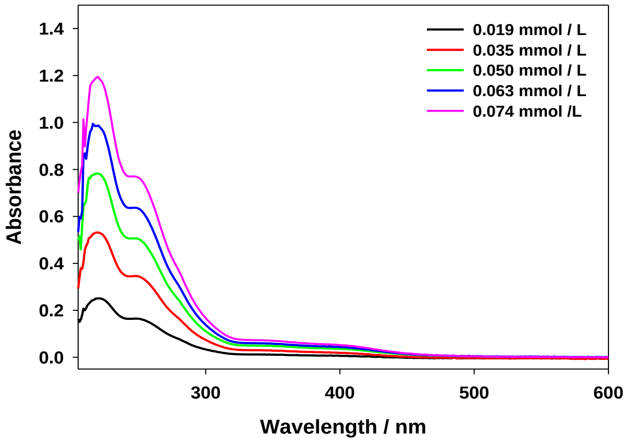

Figure 4.3. The UV-vis spectra of **PIM(py)$_6$** with different concentration in 7/3 dichloroethane/ acetonitrile.

2.2. Electropolymerization of isoporphyrin copolymers

The syntheses of the (iso)porphyrin copolymers need the attack of a dipyridyl ligand to an electro-generated π-radical cation porphyrin produced by iterative voltammetric scans (see pyridinum of red color in Scheme 4.2). The reactivity of oxidized porphyrins can be used to generate a wide range of poly-porphyrin or poly-isoporphyrin materials in the presence of **PIM(py)$_6$**. Thus, the pyridine end-decorated molybdenum halide cluster (**PIM(py)$_6$**) can combine with porphyrin through pyridyl ligands in order to form pyridinium linkers between porphyrin macrocycles.

During the electropolymerization of **ZnT$_2$P** in the presence of **PIM(py)$_6$**, when the anodic potential limit is +0.9 V, just after the first porphyrin-based oxidation potential, the π-radical cation $ZnT_2P^{+\bullet}$ is produced. At +0.9 V it must be noticed that the reversible oxidation of **PIM(py)$_6$** also occurred. We observed significant changes during the electropolymerization process. As shown in Figure 4.4A, in the anodic part, the intensity of the oxidation peak corresponding to the first oxidation of the porphyrin **ZnT$_2$P** as well as the reversible oxidation of **PIM(py)$_6$** continuously increases during the electropolymerization proving the formation of a new copolymer **poly-ZnT$_2$isoP$^•$/PIM(py)$_6$** in this potential range. The first reverse sweep toward negative potentials reveals only one quasi-reversible pyridinium-centered reduction near -1.0 V (peak I, Fig. 4.4A). This peak corresponds to the reduction of the pyridinium connected in the usual way to the isoporphyrin (py$^+$-Csp2).

Starting with the second scan, in the cathodic potential range, additional peak is observable and detected at ca. -0.7 V *vs.* SCE (peak a) as shown in Figure 4.4A. It has been attributed to reduction of the second pyrydinium unit connected to the isoporphyrin, on the *meso* carbon which still bear pyridinium and hydrogen (py$^+$(H)-Csp3).

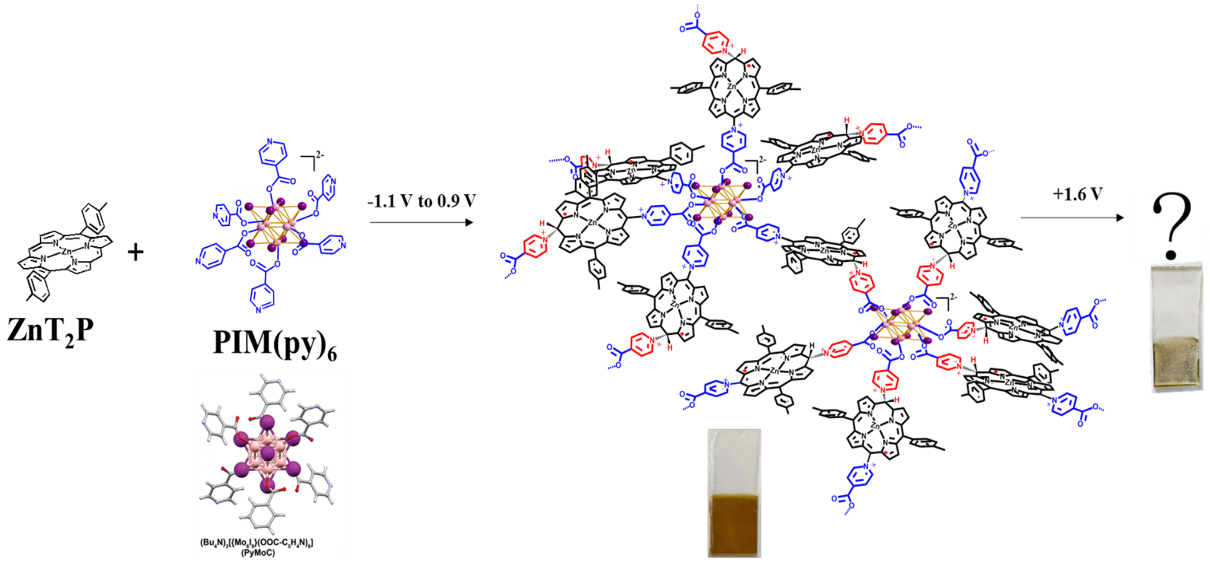

Scheme 4.2. The electropolymerization process of poly-isoporphyrin.

In the case of the electropolymerization of **ZnT$_2$P** in the presence of **PIM(py)$_6$**, using iterative scan between 1.6 V and -1.1 V, we observed that the oxidation peaks intensity increases and then decreased (Fig. 4.4B). In the cathodic potential range, the reduction peak observed at ca. -0.7 V *vs.* SCE (peak c) has been attributed to the irreversible reduction of the pyridinium spacers connected to the porphyrin subunits. In this case, the two pyridinium of the linkers are equal and reduced at the same time.

Definitely the choice of the anodic potential limit of 1.6 V is not a good point. Indeed, even if the first oxidation of the **PIM(py)$_6$** is reversible and does not perturb the electropolymerization, the oxidation at 1.6 V corresponds to the second wave of oxidation of **PIM(py)$_6$** which is irreversible. It problably induces the decomposition of the **PIM(py)$_6$** cluster during the electropolymerization. It can explain the rapid decrease of the current upon oxidation showing not homogeneous deposition (see photo of the film in Figure 4.4B).

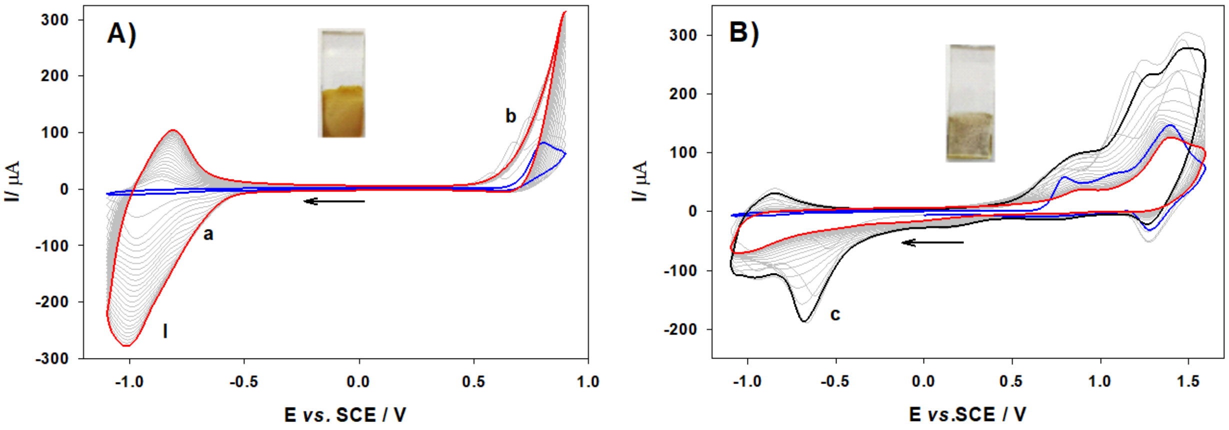

Figure 4.4. Cyclic voltammograms recorded during 25 iterative scans conducted between A) -1.1 V and +0.9 V/SCE and B) -1.1 V and +1.6 V *vs.* SCE in a 1,2-$C_2H_4Cl_2$/CH_3CN (7/3) solution of **ZnT_2P** (0.25 mmol L^{-1}) in the presence of **PIM(py)$_6$** (0.25 mmol L^{-1}) and NBu_4PF_6 (0.1 mol L^{-1}). WE: ITO. S = 1 cm^2. v = 100 mV s^{-1}. Blue curve: first scan (n=1). Red curve: final scan (n = 25). Black curve: highest reduction current.

2.3. Electrochemical Quartz Crystal Microbalance (EQCM) for copolymers deposition

The electrosynthesis of **poly-$ZnT_2isoP^{\bullet}$/PIM(py)$_6$** by electropolymerization with iterative scans between -1.1 and +0.9 V (Fig. 4.5) has been monitored *in-situ* by EQCM. Electropolymerization occurs upon the formation of the radical cation porphyrin $ZnT_2P^{+\bullet}$ in the presence of **PIM(py)$_6$**. The resonance frequency displays a significant decrease meaning an increase of the deposited mass during the electropolymeriation as shown in Figure 4.5A. The mass of the copolymer film increases with the number of potential cycle n (Fig. 4.5B). With the increasing of time, the mass change almost reached a plateau which means there is almost no film formed after 20 scans. After 5 iterative scans, 3.59 µg/cm^2 of poly-**$ZnT_2isoP^{\bullet}$/PIM(py)$_6$** is deposited. Assuming that the repeat unit is [3ZnT_2P-PIM] 6$TBAPF_6$ in the case of the pur 3D materials, the calculated surface coverage Γ is 0.56×10^{-9} mol.cm^{-2}. The theoretical values of mass change are calculated and given in Tables S1-S2.

For 5 iterative scans, the EQCM measurement indicates the deposition of Δm = 3.59 µg.cm^{-2} of the copolymer. This value is close to the value of the theoretic mass deposited calculated by the integration of the reduction wave I (reduction of the pyridinium spacers) which gives the value of Δm = 3.95 µg.cm^{-2} of copolymer deposited assuming that the repeat unit of the copolymer is one **PIM** and three **ZnT$_2$P** ([3ZnT$_2$P-PIM] 6TBAPF$_6$) (see Table 4.S2). Calculation assuming the 1D copolymer gives Δm = 6.9 µg.cm^{-2} (repeat unit: ([ZnT$_2$P-PIM] 2TBAPF$_6$)) which is very far from the value obtained by EQCM (Δm = 3.59 µg.cm^{-2}).

But, if the number of iterative scan is n = 25 scans in Table 4.S1, the mass deposited was Δm = 19.55 µg.cm^{-2}. In the case of the use of the repeat unit [3ZnT$_2$P-PIM] 6TBAPF$_6$, only Δm = 9.2 µg.cm^{-2} is calculated from the integration of the reduction wave of the pyridinium spacers (wave I). However, at this stage, the change of the slope has occured as shown in Figure 4.5B where inclusion into the film of solvent, **PIM(py)$_6$** and even **ZnT$_2$P** monomers as well as conducting salt occurred giving wrong calculations. Thus, in such a case our calculation is not valid because we don't know the quantity of solvent, monomers and conducting salt present in the film.

At n = 5, we are in the first part of the plot of the mass change (Δm) calculated from Sauerbrey's equation *versus* the number of scan n where only the copolymer is deposited (Fig. 4.5B). In this part of the curve, the calculation shows clearly the deposition of the 3D **poly-ZnT$_2$isoP$^{\bullet}$/PIM(py)$_6$** copolymer.

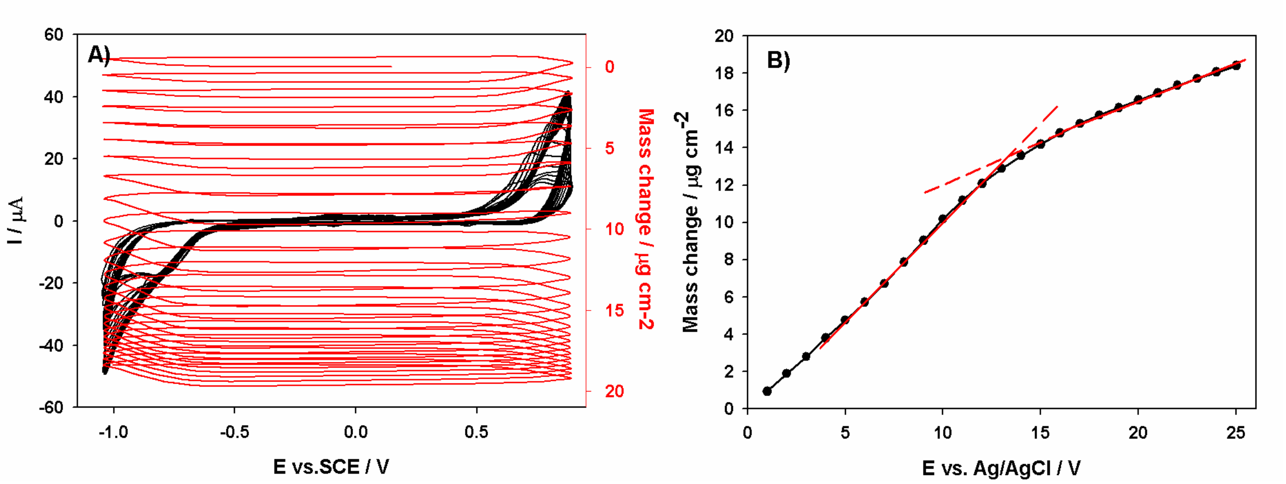

Figure 4.5. A) Consecutive cyclic voltammograms (first 25 scans) between -1.1 and 0.9 V and electrochemical quartz crystal microbalance measurements (Δm) for the first 25 scans during the formation of **poly-ZnT$_2$isoP$^{\bullet}$/PIM(py)$_6$** obtained by the electropolymerization of 0.25 mmol L^{-1} **ZnT$_2$P** with 0.25 mmol L^{-1} **PIM(py)$_6$** (0.25 mmol L^{-1}) in 1,2-$C_2H_4Cl_2$–CH_3CN (7/3) in the presence of 0.1 mol L^{-1} NBu$_4$PF$_6$. Working electrode: ITO (A = 0.2 cm^2) deposited on a 9.08 MHz AT-cut quartz crystal. v = 100 mVs^{-1}. B) Mass change (Δm) of the first 25 scans calculated from Sauerbrey's equation *versus* the number of scan n.

2.4. UV-vis-NIR spectroscopy

UV-visible-NIR spectra on ITO electrodes coated with the copolymer **poly-ZnT$_2$isoP$^\bullet$/PIM(py)$_6$** have been measured at various thickness (Fig. 4.6) where the absorption intensity of the chromophores increases with iterative scan number (Fig. 4.6B).

A typical UV-visible-NIR spectrum of **poly-ZnT$_2$isoP$^\bullet$/PIM(py)$_6$** obtained after electropolymerization between -1.1 and +0.9 V exhibited a broad split Soret absorption band at λ = 433 nm and λ= 473 nm. The bands were red-shifted by 18 and 58 nm respectively as compared to the **ZnT$_2$P** monomer (Table 4.1 and Fig. 4.6). The visible bands (Q bands), observed at 561 and 645 nm, are also red-shifted by 15 and 61 nm compared to **ZnT$_2$P** and an additional band at 875 nm in the NIR region is detected (Fig. 4.6A). These electropolymerized films have been found to be fully soluble in DMF. Analysis of **poly-ZnT$_2$isoP$^\bullet$/PIM(py)$_6$** in solution by UV-Vis-NIR absorption spectroscopy revealed comparable spectra than the ones recorded on the solid film (Fig. 4.7). The superposition of the UV-visible-NIR absorption spectra of **ZnT$_2$P** in solution and of the copolymer **poly-ZnT$_2$isoP$^\bullet$/PIM(py)$_6$** deposited on ITO are shown for comparison in Figure 4.7. It reveals that the Soret band, attributed to the main porphyrin-based π-π* electronic transition, is much broader, is split and more red-shifted for **poly-ZnT$_2$isoP$^\bullet$/PIM(py)$_6$** onto ITO electrode than for **ZnT$_2$P** (Table 4.1).

Table 4.1. UV–visible spectral data for **ZnT$_2$P in** CH_3Cl, **PIM(py)$_6$**, **poly-ZnT$_2$isoP$^\bullet$/PIM(py)$_6$**, **poly-ZnT$_2$P/PIM(py)$_6$** in 1,2-$EtCl_2$, on optical transparent ITO electrodes. Under bracket: molar extinction coefficient (ε /10^3 L.M.cm^{-1}).

Compound	**Soret band/nm**	**Q bands/nm**	**π-π*Band/nm**
ZnT$_2$P	415 (405.4)	546 (18.9), 584 (4.9)	
PIM[a]			220 (170.4), 246 (109.0), 344 (11.0), 402 (8.0)
poly-ZnT$_2$isoP$^\bullet$/PIM(py)$_6$[b]	433, 475	561, 645, 875	
poly-ZnT$_2$isoP$^\bullet$/PIM(py)$_6$[c]	417	547, 644	
poly-ZnT$_2$P/PIM(py)$_6$[d]	434	567, 607	

[a] in 1,2-$EtCl_2$/CH_3CN (7/3).
[b] Copolymers obtained by iterative scan between -1.1 V and +0.9 V *vs.* SCE onto ITO.
[c] Copolymers obtained by iterative scan between -1.1 V and +0.9 V *vs.* SCE in DMF.
[d] Copolymers obtained by iterative scan between -1.1 V and +1.6 V *vs.* SCE onto ITO.

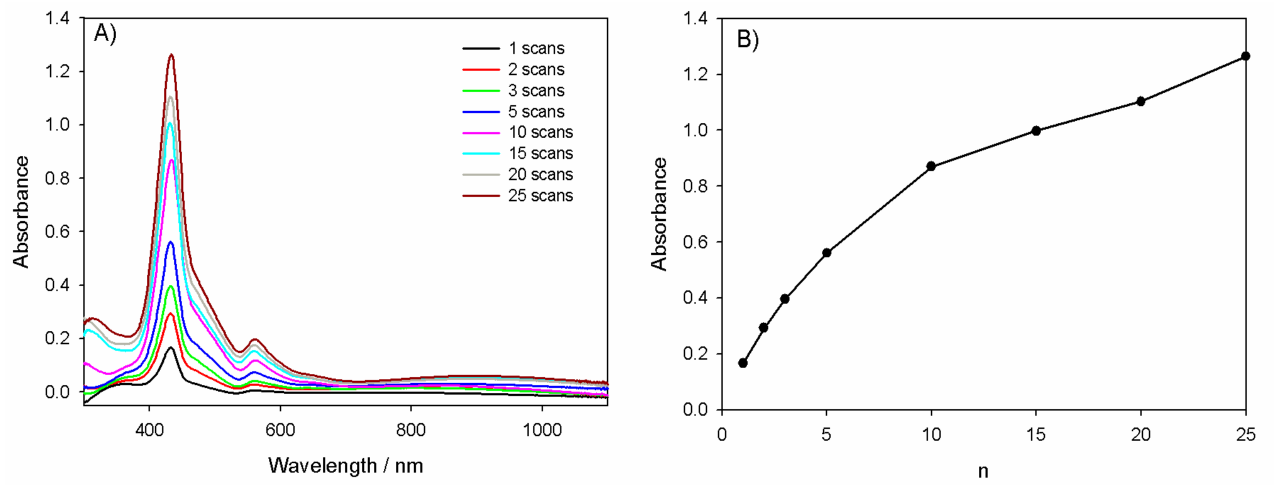

Figure 4.6. A) UV-visible-NIR absorption spectra of **poly-ZnT$_2$isoP$^{\bullet}$/PIM(py)$_6$** onto ITO with different numbers of iterative scans between -1.1 and +0.9 V *vs.* SCE (v = 100 mV s^{-1}). Only one side of the slide is covered by ITO. B) Plot of the absorbance measured at λ = 433 nm *versus* n the numbers of iterative scans.

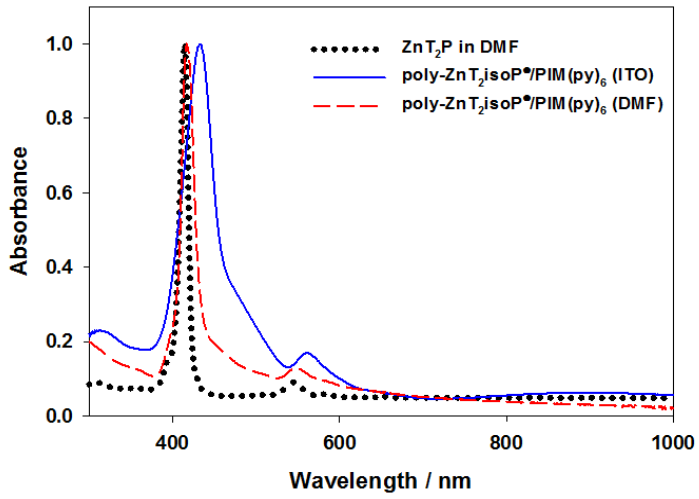

Figure 4.7. Normalized UV-Vis-NIR spectra of the ITO electrode modified with **poly-ZnT$_2$isoP$^{\bullet}$/PIM(py)$_6$**, obtained with 10 iterative scans between -1.1 and +0.9 V *versus* SCE at v = 100 mV s^{-1} (blue line), and **poly-ZnT$_2$isoP$^{\bullet}$/PIM(py)$_6$** (red line) and **ZnT$_2$P** (dark dotted line) in DMF solution.

The additional bands at 475 and 875 nm may be attributed to the isoporphyrin structure present in the copolymer. Similar bands have been already observed in the case of stable isoporphyrin monomer or copolymer as discussed in Chapters II and III. Interestingly, the broadening and the splitting of the Soret band as well as the presence of one additional band in the NIR between 750 nm and 1000 nm are expected to be advantageous to photovoltaic applications by extending the domain of solar light absorption.

2.5. Cyclic voltammetric investigations of the copolymeric films.

Electroactive copolymers deposited by cyclic voltammetry (n iterative scans) on ITO surfaces have been characterized by electrochemical methods. The cyclic voltammetry curves shown in Figure 4.8A have been recorded with a copolymers deposited on the ITO electrode surface for various number of scans (n = 1, 3, 5, 10, 15, 20 cycles) between -1.1 V and +0.9 V. The electrode was then removed from the electrochemical cell, washed with CH_3CN and used as working electrode in a clean electrolytic solution containing only the solvent and the supporting electrolyte (Fig. 4.8B).

Two successive waves are observed for **poly-ZnT$_2$isoP$^\bullet$/PIM(py)$_6$** during the cathodic scan (Table 4.2 and Fig. 4.8), the first being irreversible (peak a) and the second being quasi-reversible (peak I). The first irreversible wave (peak a) is detected at -0.72 V and is very close to the second reduction process (peak I). Peak a corresponds probably to the irreversible reduction of the pyridinium connected to the isoporphyrin close to the pendant hydrogen atom. It generates one radical which reacts rapidily via radical coupling. The peak b is due to the oxidation of resulting compound which regenerate the starting isoporphyrin radical.

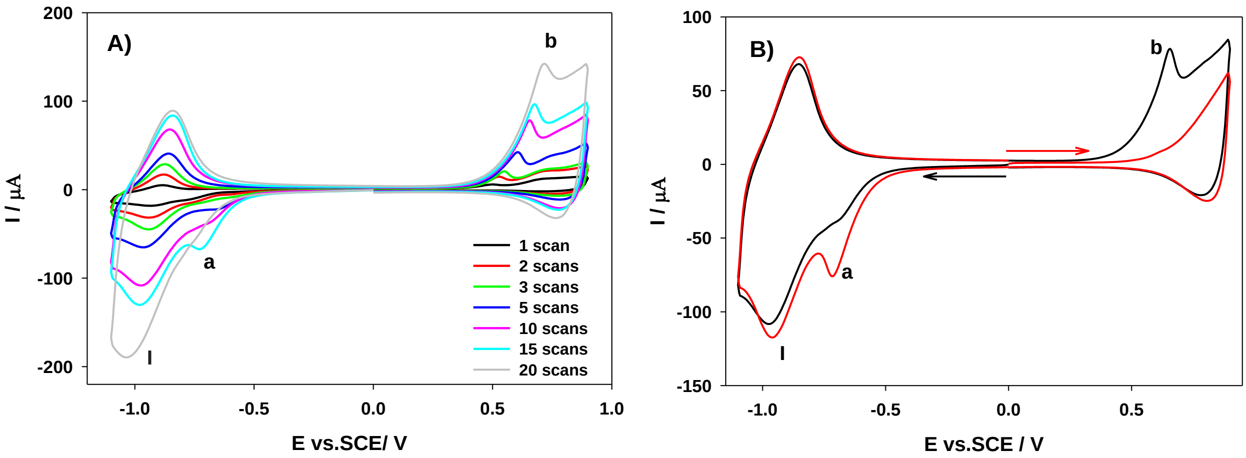

Figure 4.8. Left: cyclic voltammograms of **poly-ZnT$_2$isoP$^\bullet$/PIM(py)$_6$** obtained with **PIM(py)$_6$** and **ZnT$_2$P** after A) n = 1, 2, 3, 5, 10, 15 and 20 scans and B) after 10 scans between -1.1 V and +0.9 V in CH_3CN/1,2-$C_2H_4Cl_2$ (3/7) with 0.1 M NBu_4PF_6. WE: ITO. S = 1 cm^2, v = 100 mV s^{-1}.

When the upper potential chosen is 1.60 V, two oxidation waves appear at 1.10 V and 1.38 V as shown in Figure 4.S2. It can be explained by the formation of isoporphyrin cation via oxidation of the isoporphyrin radical followed by the oxidation of the porphyrin which can be formed by the release of the proton after the oxidation of isoporphyrin cation. Nevertheless, the films become weak and less colored when poly-isoporphyrin is oxidized using upper potential of 1.6 V. It probably indicates that the poly-porphyrin form maybe not stable under oxidation.

Table 4.2. Electrochemical data for **ZnT$_2$P**, **PIM(py)$_6$**, **poly-ZnT$_2$P/PIM(py)$_6$**, and **poly-ZnT$_2$isoP$^\bullet$/PIM(py)$_6$ in EtCl$_2$/CH$_3$CN** (7/3) solution.

Compounds	**Ring oxidation**			**Reduction of spacer**		**Ring reduction**	
			peak b	peak a	peak I		
ZnT$_2$P^a	1.08 (150)	0.79 (90)				-1.41 (160)	-1.84 (170)
PIM(py)$_6$	1.09 (117)				-0.96^{irr}		
poly-ZnT$_2$isoP$^\bullet$/PIM(py)$_6$	+1.38 (210)	+1.10 (200)	+0.76^{irr}	-0.76^{irr}	-0.92 (124)		

2.6. Electron spin resonance (ESR) spectroscopy

To confirm the presence of the organic radical, **poly-ZnT$_2$isoP$^\bullet$/PIM(py)$_6$** films onto ITO were prepared (25 iterative scans between -1.1 V and 0.9 V, v = 100 mV.s^{-1}).

Poly-ZnT$_2$isoP$^\bullet$/PIM(py)$_6$ was then removed from ITO after 25 cycles using DMF which was repeated three times. The obtained solutions were degassed in order to remove dioxygen and transferred to a capillary.

The ESR spectrum shown in Figure 4.9 reveals the presence of the radical of the isoporphyrin copolymer showing similar spectrum than discussed in chapter II associated with radical localized on the isoporphyrin subunits.

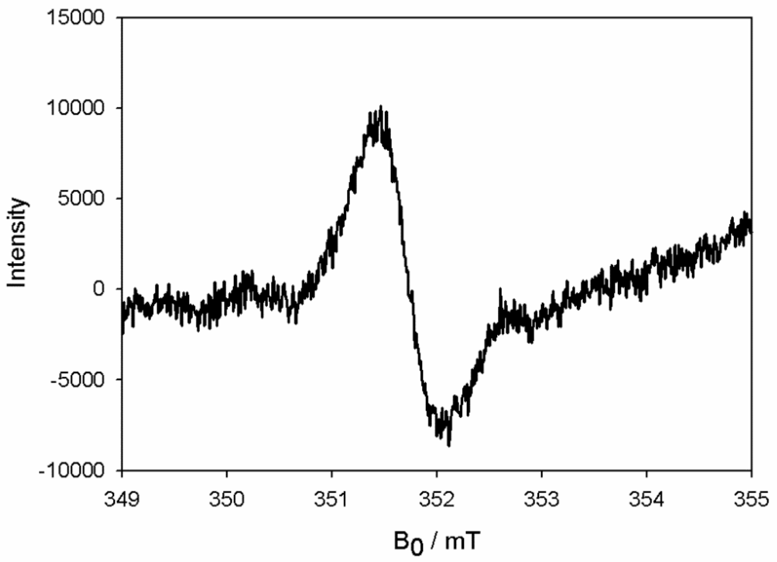

Figure 4.9. ESR spectrum of **poly-ZnT$_2$isoP$^•$/PIM(py)$_6$** in DMF at room temperature. The solution of **poly-ZnT$_2$isoP$^•$/PIM(py)$_6$** was prepared by washing with 160 µL of DMF three covered ITO obtained using 25 scans between -1.1 V and 0.9 V, *v* = 100 mV s^{-1}.

2.7. Film Morphology (Atomic Force Microscopy) of poly-ZnT$_2$isoP$^•$/PIM(py)$_6$ copolymer.

The films obtained by iterative scans between -1.1 V and +0.9 V were studied by scanning atomic force microscopy (AFM) (Fig. 4.10). Copolymer like tightly packed coils appears on the surface with an average diameter of ca. 20-50 nm, the height being around 5.0 nm for the film obtained after 1 iterative scan between -1.1 V and +0.9 V (Fig. 4.10). The rms surface roughness of the two films have been estimated at 20.0 nm for **poly-ZnT$_2$isoP$^•$/PIM(py)$_6$**, (calculated from an area of 0.08 µm^2 for Figure 4.10). The copolymer obtained after higher iterative scan number exhibited comparable morphology but showed in several positions some aggregation of the coils accompanied by a larger value of the rms surface roughness (400 nm for n = 15). The formation of coil aggregates might be related to the change of slope of the deposited mass, observed from EQCM measurements in Figure 4.5.

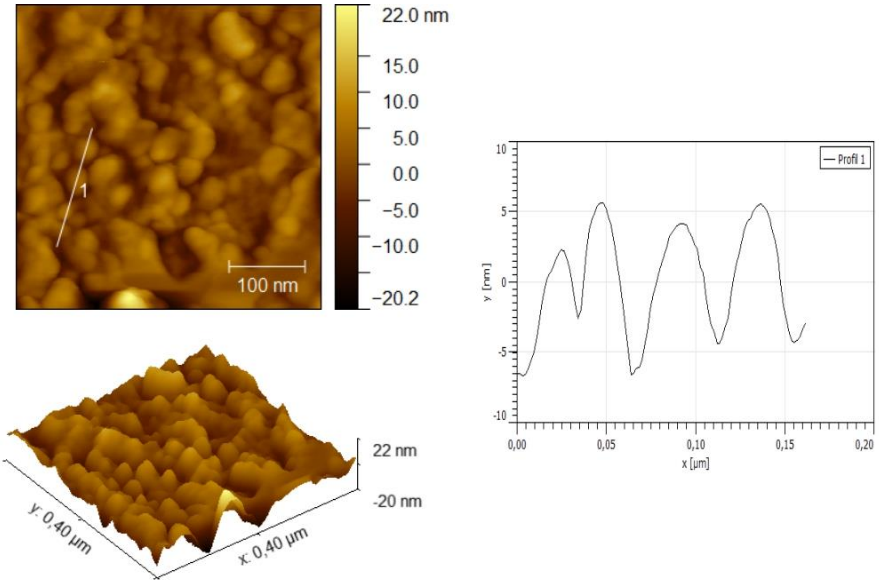

Figure 4.10. Left: tapping mode AFM topography of **poly-ZnT$_2$isoP$^\bullet$/PIM(py)$_6$** (deposition between -1.1 V and +0.9 V vs. SCE on ITO, n = 1). Right: section analysis of the aggregate marked by a white line.

2.8. X-ray photoelectron spectra (XPS) of copolymers

The copolymer films were also investigated by X-Ray photoelectron spectroscopy (Fig. 4.11). The analysis of the survey spectra of **poly-ZnT$_2$isoP$^\bullet$/PIM(py)$_6$** confirms the presence of the isoporphyrin radical subunits (Zn 2p3 at 1022.3 eV, N 1s, and C 1s peaks), and the presence of the **PIM** cluster subunits (Mo 3d and I 3d).[16,17] Furthermore, the signals for F 1s (686.6 eV) is also detected and corresponds to the incorporated counterion PF_6^- to equilibrate the pyridiniums charges. The C1s peaks are composed of three signals at 289.4 eV corresponding to the –C(O)OH- in the **PIM(py$^+$)$_6$**, 286.3 eV and 285.4 eV attributed to homo and hetero (connected to nitrogen) carbon atoms respectively. The N1s peaks reveal the presence of two chemically different nitrogens. The contributions at 401.3 eV and 398.5 eV are attributed to the iminic nitrogen and to the reduced pyridinium respectively. Finally, the peak localizated at 394.3 eV might result from the Molybdenum 3p 2/3 orbital.

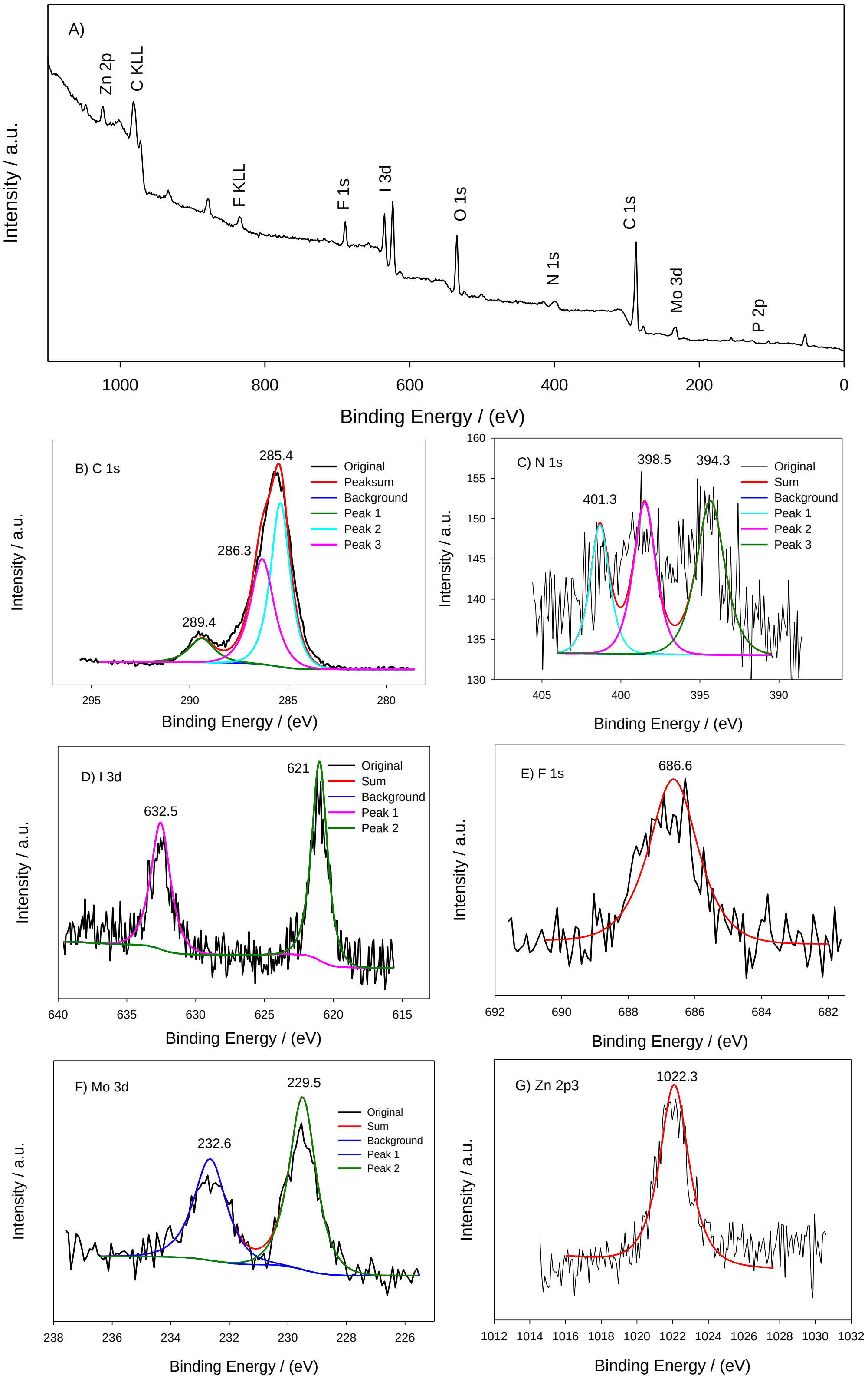

Figure. 4.11. XPS spectra of the modified ITO electrodes with **poly-ZnT$_2$isoP$^{\bullet}$/PIM(py)$_6$** obtained after 25 iterative scans between -1.1 V and 0.9 V *versus* SCE. XPS spectra (A), C 1s (B), N 1s (C), I 3d (D), F 1s (E), Mo 3d (F) Zn 2p3 (G).

3. Photoelectrochemical properties

3.1. Effect of the film thickness

Figure 4.12A shows the typical current-potential curves of **poly-ZnT$_2$isoP$^\bullet$/PIM(py)$_6$** thin films on ITO electrodes obtained in 5 mM I_2 / 0.5 M I^- aqueous solution.

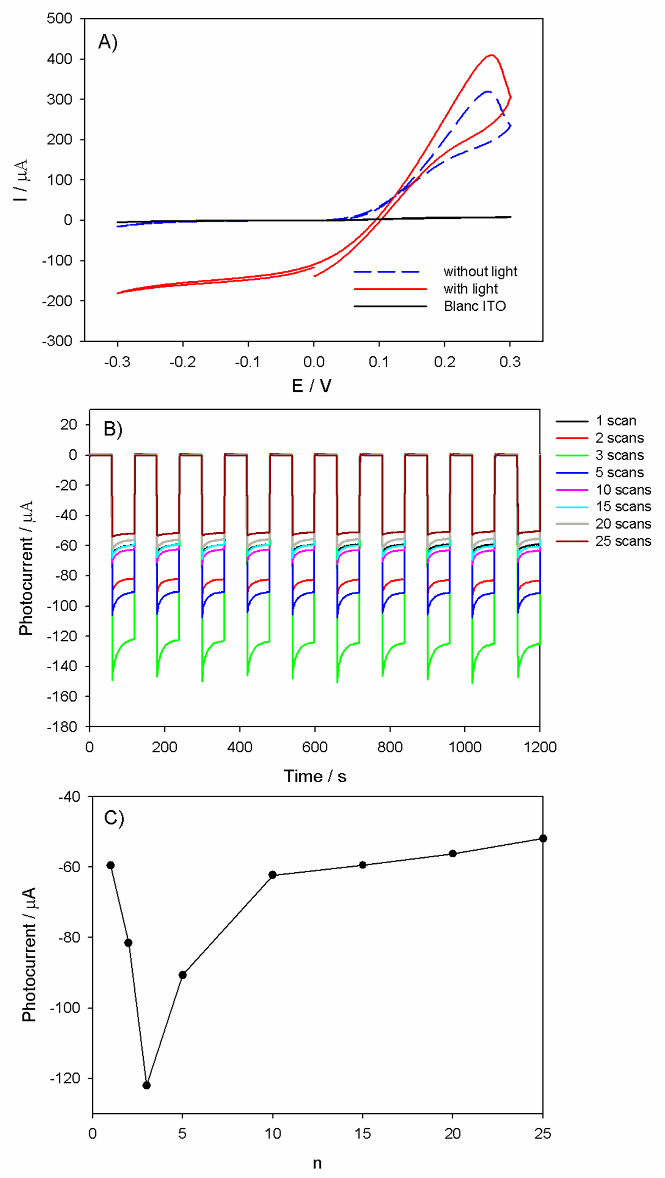

Figure 4.12. A) Current-potential curves of **poly-ZnT$_2$isoP$^\bullet$/PIM(py)$_6$** (obtained with n = 3 iterative scans between -1.1 V and +0.9 V thin films on ITO electrodes obtained in 0.5 M I^- / 5 mM I_2 aqueous solution in the dark or under visible illumination. B) and C) Photoelectrochemical responses of **poly-ZnT$_2$isoP$^\bullet$/PIM(py)$_6$** films obtained with n = 1, 2, 3, 5, 10, 15, 20 or 25 iterative scans. Measurements have been done under on-off light illumination from a 300 W Xe arc lamp (with $\lambda >$ 385 nm long pass filter) in I_3^- 5 mmol L^{-1} and I^- 0.5 mol L^{-1} aqueous solution. BIAS potential: 0.00 V *vs.* OCP.

The equilibrium potential of I_3^-/I^- redox couple in solution is taken as reference potential at 0 V in the cyclic voltammograms. For bare ITO electrode (black curve), almost no Faradaic current is observed between -0.3 V and 0.3 V, revealing the slow I^- oxidation and I_3^- reduction kinetics on ITO. However, the I^- oxidation and I_3^- reduction currents are significantly enhanced on the ITO modified by the copolymers (blue and red curves in Figure 4.12A).

The current-potential curves measured under UV-visible and NIR light illumination ($\lambda > 385$ nm using a long pass filter) and potentiodynamic conditions are also plotted in Figure 4.12A (red full line) for the **poly-ZnT$_2$isoP$^•$/PIM(py)$_6$** copolymers. The photocurrent response in the potentiostatic mode at 0 V under on-off light illumination cycles is shown in Figure 4.12BC. Under visible and NIR lights, the photocurrent at 0 V of the **poly-ZnT$_2$isoP$^•$/PIM(py)$_6$** copolymer thin film reaches ca. -120 µA cm^{-2} (measured from the potentiostatic experiment) or -150 µA cm^{-2} (measured from the cyclic voltammograms). To prove the contribution of NIR band for the photocurrent generation, one filter which could absorb the UV and visible light has been then used. As shown in Figure 4.13A, under only NIR light irradiation, the photocurrent of **poly-ZnT$_2$isoP$^•$/PIM(py)$_6$** films can reach -7.7 µA cm^{-2}. Compared with the visible and NIR light irradiation, the NIR band makes a contribution about 12% of the total photocurrent value. We must notice that the global photocurrent measured in Figure 4.13A with visible and NIR illumination is lower than the photocurrent obtained in Figure 4.12A. It is just because the film in Figure 4.13A is obtained with 10 iterative scans between -1.1 V and +0.9 V and not 3 iterative scan (Fig. 4.12A). The photocurrent is then near -60.0 µA cm^{-2} for n = 10 cycles.

It is known that NIR light can be used in phototherapy and be more permeable for the body, which makes a potential use of such isoporphyrin copolymer for further application in the photodynamic therapy.

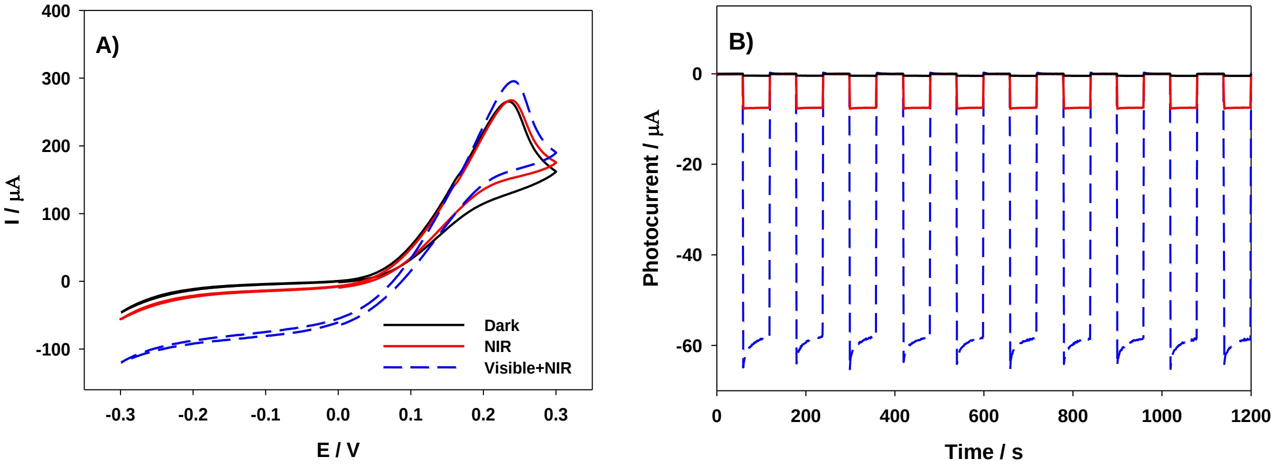

Figure 4.13. A) Current-potential curves of **poly-ZnT$_2$isoP$^{\bullet}$/PIM(py)$_6$** (obtained with n = 10 iterative scans between -1.1 V and +0.9 V thin films on ITO electrodes obtained in 0.5 M I^- / 5 mM I_2 aqueous solution in the dark or under visible plus NIR illumination or NIR illumination. B) Photoelectrochemical responses of **poly-ZnT$_2$isoP$^{\bullet}$/PIM(py)$_6$** films obtained under NIR and under visible plus NIR illumination.

3.2. Electrochemical Impedance spectroscopy

Further comprehensions into the photoelectrochemical behaviour of the copolymer films as a function of n could be gained by electrochemical impedance spectroscopy, which is widely used in the investigation of dye sensitized solar cell.[18] All the impedance spectra of the copolymer films **poly-ZnT$_2$isoP$^{\bullet}$/PIM(py)$_6$** obtained for various number of iterative cycle, n=1, 2, 3, 5, 10, 15 and 20 are given in Figure 4.14. The Nyquist diagrams exhibit only one semi-circle, which can be modelled by the charge transfer resistance R_{ct} of the I^-/I_3^- species at the ITO/solution interface in parallel with the interfacial capacitance C_i. The Nyquist and Bode plots of a typical impedance spectra measured for (**poly-ZnT$_2$isoP$^{\bullet}$/PIM(py)$_6$**) at 0 V in 5 mM I_3^- / 0.5 M I^- aqueous solution are plotted in Figure 4.15 for n = 10 iterative scans for the electropolymerization. Small slope at 100 Hz could be observed from the Bode plots due to the charge transfer resistance R_{ct_film}. As measured, the R_{ct_film} increased with scan number after 3 scans (film deposited using n = 3 iterative scans between -1.1 V and +0.9 V at v = 100 mVs^{-1}).

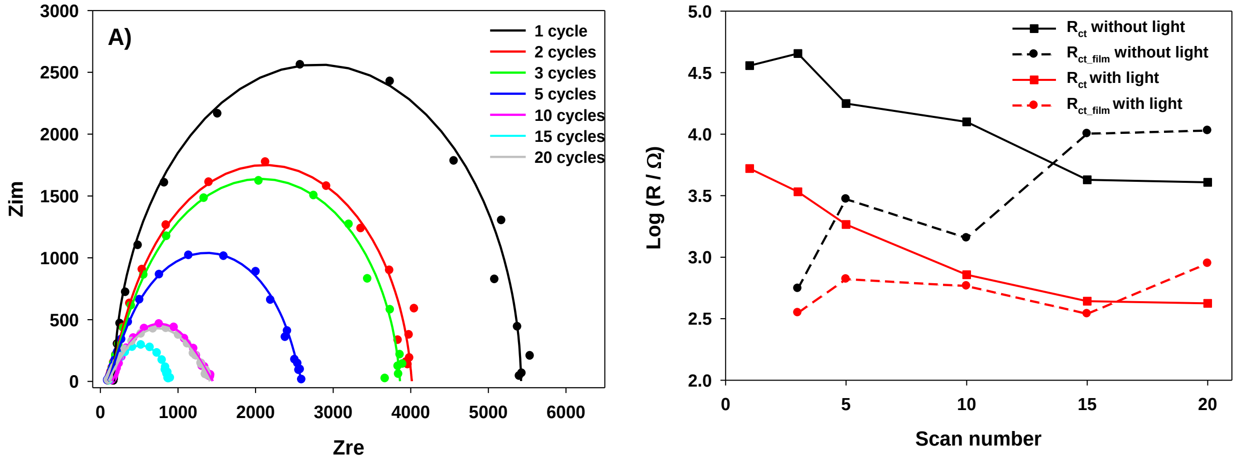

Figure 4.14. A) Nyquist curves of **poly-ZnT$_2$isoP$^{\bullet}$/PIM(py)$_6$** (obtained with iterative scans between -1.1 V and +0.9 V thin films on ITO electrodes obtained in 0.5 M I^- / 5 mM I_2 aqueous solution under light irradiation. B) Plot of the Log(R) *versus* n (number of iterative scan, *v* = 100 mV s^{-1}, between -1.1 V and +0.9 V for **poly-ZnT$_2$isoP$^{\bullet}$/PIM(py)$_6$**.

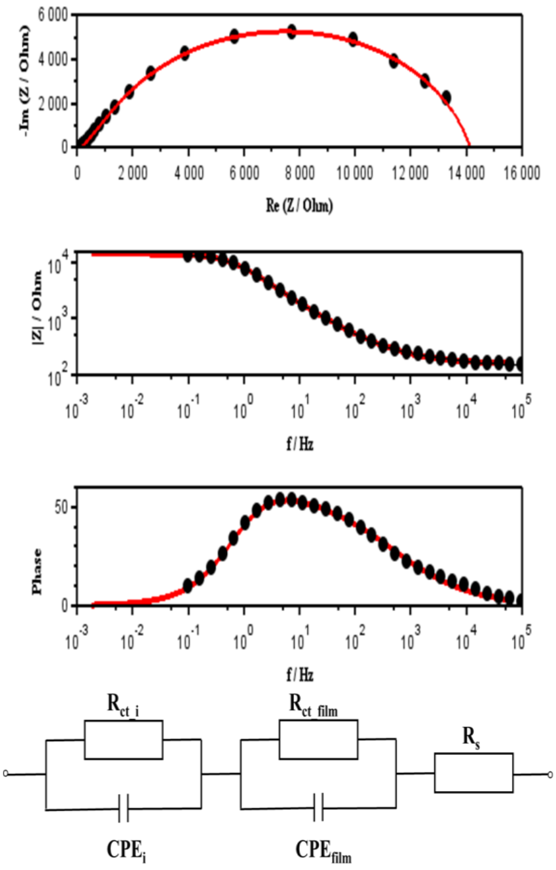

Figure 4.15. Nyquist and Bode curves of **poly-ZnT$_2$isoP$^{\bullet}$/PIM(py)$_6$** (obtained at 10 scans between -1.1 V and +0.9 V) thin films on ITO electrodes obtained in 0.5 M I^- / 5 mM I_2 aqueous solution without light. Bottom: equivalent circuit use for fit of experimental data.

3.3. Energy diagram

Figure 4.16 represents the energy diagram corresponding to the photoreduction of I_3^- on the copolymer **poly-ZnT$_2$isoP$^\bullet$/PIM(py)$_6$**. In the former research of our group,[2,3] the inclusion of polyoxometalates (POMs) was a benefit and helpful for increasing the photocurrent due to the electron transfer from the excited porphyrin of the copolymers to the pyridinum giving the radical pyridyl (py$^\bullet$), which in turn can give one electron to the POM moieties. This cascade of electron transfer will avoid the back recombination between the radical cation porphyrin and the radical pyridyl (py$^\bullet$).

The HOMO level energies of the **poly-ZnT$_2$isoP$^\bullet$/PIM(py)$_6$** have been estimated from the first oxidation potential observed in the cyclic voltammograms, while the energy level of the dipyridinium species is given by the potential of the first and second reduction peaks (Table 4.2). The LUMO levels of the excited **poly-ZnT$_2$isoP$^\bullet$/PIM(py)$_6$** species can be roughly estimated by subtracting the excitation energy of the Soret or Q bands from the HOMO level energies. The energy level corresponding to the band in the NIR region has also been indicated in the energy diagram. The energy level of the **PIM(py)$_6$/PIM(py)$_6^-$** at -3.78 eV can be calculated from the potential of reduction of **PIM(py)$_6$** (-4.50 -(-0.72) = -3.78 eV).

Under illumination at 0 V, the photon absorption by the (iso)porphyrin entities generates an electron hole pair in the copolymer. The electron is transferred from the excited isoporphyrins radical subunit, to the pyridinum subunit which is reduced to form the radical pyridyle py$^\bullet$ (dotted red arrow in Figure 4.16B). The pyridinium acts as a relay for the electron transfer. Then, the radical pyridyle py$^\bullet$ in turn can reduce I_3^- to form I^- which is reoxidized at the counter electrode. The oxidized isoporphyrin is regenerated by an electron transfer from the ITO substrate.

As the energy level of the NIR band associated to the isoporphyrin radical subunit is lower than the energy level of the couple Py$^+$/Py$^\bullet$, after non radiative relaxation, the electron also could be transferred directly from NIR energy level to the level I_3^-/I^- to reduce I_3^- to I^-, which could explain the non negligeable photocurrent generated by copolymer **poly-ZnT$_2$isoP$^\bullet$/PIM(py)$_6$** under NIR illumination. In such a case, **PIM(py)$_6$** play not role to the electron transfer.

However, it must be noted that the **PIM(py)$_6$** can also accept electron from the excited isoporphyrins radical subunit giving the reduced form **PIM(py)$_6^-$** but only in the case of the levels

S2 (Soret bands) as well as the more energetic level S1 corresponding to the Q band as shown in Figure 4.16 (blue arrows). In such a case, the reduced **PIM(py)$_6$**$^-$ can in turn gives one electron to the pyridium subunit to form the radical pyridyle Py$^{\bullet}$. Finally, the Py$^{\bullet}$ can exchange electron with I_3^- giving I^- which is reoxidized at the counter electrode.

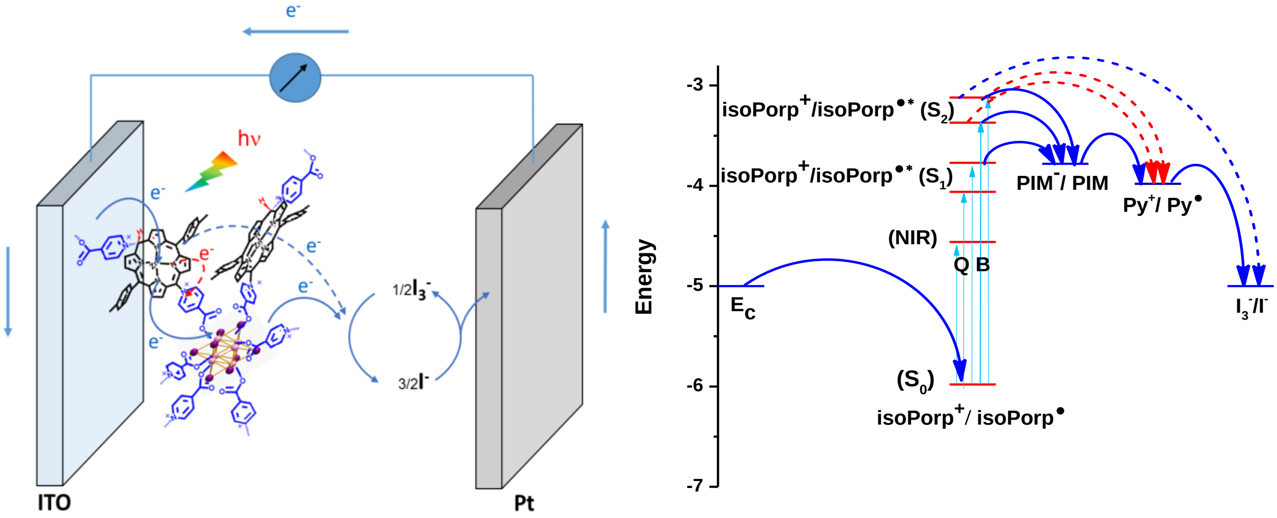

Figure 4.16. Schematic illustration of the energy level diagram for **poly-ZnT$_2$isoP$^{\bullet}$/PIM(py)$_6$** showing electron transfer processes in H_2O containing I_3^- 5 mmol L^{-1} and I^- 0.5 mol L^{-1} (Py^+ = pyridinium, Porp = porphyrin) under light irradiation.

4. Conclusions

In summary, copolymer films have been prepared by the electro-oxidation of 5,15-ditolylporphyrin (**ZnT$_2$P**) in the presence of polyiodometalate with 6 pendant pyridyl ligands $(Bu_4N)_2[Mo_6I_8(pyCOO)_6]$. Electrogenerated radical cation porphyrin is a powerful electrophile which can rapidly react to form copolymer containing stable isoporphyrins (**poly-ZnT$_2$isoP$^{\bullet}$/PIM(py)$_6$**). The existence of the cation radical of the isoporphyrin was proved by electron spin resonance spectroscopy. The achieved copolymers were characterized by UV-Vis-NIR spectroscopy, Atomic Force Microscopy and X-ray photoelectron spectroscopy. Electrochemical properties of these copolymers have been discussed and studied.

The photocurrent measurements under visible-NIR light irradiation show that **poly-ZnT$_2$isoP$^{\bullet}$/PIM(py)$_6$** thin films exhibit significantly performance. However, the photovoltaic performances reach an optimum depending on the number of electropolymerization potential scan n. The best performances are obtained for n = 3. Therefore, the control of the thickness of the copolymer films is of great importance to optimize the generation of photocurrent under visible illumination. Furthermore, the results proved that the NIR band played an important role for photocurrent measurement.

Poly-ZnT$_2$isoP$^\bullet$/PIM(py)$_6$ in the solid state could be stored for over several months and even one year without any degradation under ambient conditions in air. The stability is still good in DMF solution. Further investigations are underway in order to understand more about this remarkable stability. Other type of stable isoporphyrin radical are in preparation in our laboratory.

In the final chapter, the diphosphane ligand will be used for the first time to generate stable isoporphyrin radical copolymers. Various type of diphosphane lignand will be used for this study.

References

1. A. Giraudeau, L. Ruhlmann, L. El-Kahef, M. Gross, *J. Am. Chem. Soc*. **1996**, 118, 2969–2979.

2. Z. Huo, D. Zang, S. Yang, R. Farha, M. Goldmann, B. Hasenknopf, H. Xu, L. Ruhlmann, *Electrochim. Acta*, **2015**, 179, 326–335.

3. Z. Huo, I. Azcarate, R. Farha, M. Goldmann. H. Xu, B. Hasenknopf, E. Lacôte, L. Ruhlmann, *J. Solid State Electrochem*, **2015**, 19, 2611–2621.

4. D.-L. Long, R. Tsunashima, L. Cronin, *Angew Chem. Int. Ed. Engl*. **2010**, 49, 1736–1758.

5. M. Santoni, G. S. Hanan, B. Hasenknopf, *Coord. Chem. Reviews*, **2014**, 281, 64–85.

6. M. N. Sokolov, M. a. Mihailov, E. V. Peresypkina, K. a. Brylev, N. Kitamura and V. P. Fedin, *Dalton Trans*., **2011**, 40, 6375–6377.

7. M. A. Mikhailov, K. A. Brylev, A. V. Virovets, M. R. Gallyamov, I. Novozhilov, M. N. Sokolov, *New J. Chem.*, **2016**, 40, 1162–1168.

8. C. Felip-León, C. Arnau del Valle, V. Pérez-Laguna, M. Isabel Millán-Lou, J. F. Miravet, M. Mikhailov, M. N. Sokolov, A. Rezusta-López, F. Galindo, *J. Mater. Chem. B*, **2017**, 5, 6058–6064.

9. A. Beltrán, M. Mikhailov, M. N. Sokolov, V. Pérez-Laguna, A. Rezusta, M. J. Revillo and F. Galindo, *J. Mater. Chem. B*, **2016**, 4, 1–5.

10. M. A. Mikhailov, K. A. Brylev, P. A. Abramov, E. Sakuda, S. Akagi, A. Ito, N. Kitamura and M. N. Sokolov, *Inorg. Chem*., **2016**, 55, 8437–8445.

11. M. V. Volostnykh, M. A. Mikhaylov, A. A. Sinelshchikova, G. A. Kirakosyan, A. G. Martynov, M. S. Grigoriev, D. A. Piryazev, A. Yu. Tsivadze, M. N. Sokolov, Y. G. Gorbunova, *Dalton Trans.*, **2019**, 48, 1835–1842.

12. K. Kirakci, P. Kubát, M. Dusek, K. Fejfarová, V. Šícha, J. Mosinger, K. Lang, *Eur. J. Inorg. Chem*. **2012**, 3107–3111.

13. K. Kirakci, P. Kubát, M. Kuceráková, V. Šícha, H. Gbelcová, P. Lovecká, P. Grznárová, T. Ruml, K. Lang, *Inorganica Chimica Acta*, **2016**, 441, 42–49.

14. J. A. Jackson, C. Turro, M. D. Newsham, and D. G. Nocera, *J. Phys. Chem*. **1990**, 94, 4500–4507.

15. L. Riehl, A. Seyboldt, M. Ströbele, D. Enseling, T. Jüstel, M. Westberg, P. R. Ogilbyc, H.-J. Meyer, *Dalton Trans.,* **2016**, 45, 15500–15506.

16. Y. A. Vorotnikov, O. A. Efremova, I. N. Novozhilov, V. V. Yanshole, N. V. Kuratieva, K. A. Brylev, N. Kitamura, Y. V. Mironov, M. A. Shestopalov, *J. Mole. Struc.* **2017**, 1134, 237–243.

17. A. Fuhrmann, A. Seyboldt, A. Schank, G. Zitzer, B. Speiser, D. Enseling, T. Jüstel, H. Meyer, *Eur. J. Inorg. Chem.* **2017**, 4259–4266.

18. A. D. Mironova, M. A. Mikhajlov, T. S. Sukhikh, K. A. Brylev, A. L. Gushchin, I. V. Eltsov, D. V. Stass, E. I. Goryunov, V. K. Brel, M. N. Sokolov, *Z. Anorg. Allg. Chem.*, **2019**, 645, 1135–1140.

19. R. Ramirez-Tagle, R. Arratia-Perez, *Chem. Phys. Lett.* **2008**, 460, 438−441.

20. O. A. Efremova, Y. A. Vorotnikov, K. A. Brylev, N. A. Vorotnikova, I. N. Novozhilov, N. V. Kuratieva, M. V. Edeleva, D. M. Benoit, N. Kitamura, Y. V. Mironov, M. A. Shestopalov, and A. J. Sutherland, *Dalton Trans.*, **2016**, 45, 15427–15435.

21. K. Kirakci, P. Kubát, M. Kuceráková, V. Šícha, H. Gbelcová, P. Lovecká, P. Grznárová, T. Ruml, K. Lang, *Inorg. Chim. Acta*, **2016**, 441, 42–49.
22. S. A. BEST and R. A. WALTON, *Inorganic Chemistry*, **1979**, 18, 484–488.
23. B. Fabre, S. Cordier, Y. Molard, C. Perrin, S. Ababou-Girard, C. Godet, *J. Phys. Chem. C*, **2009**, 113, 17437–17446.

Chapter V

Stable isoporphyrin copolymer prepared with di(phenylphosphane)

Chapter V: Stable isoporphyrin copolymer prepared with di(phenylphosphane)

As already described, the pyridine or dipyridine ligand could react with the π-radical cation of **$ZnT_2P^{+\bullet}$** which form isoporphyrin copolymer in the case of the use of bipyridyl ligand.

As alreay published, porphyrin dimer and trimer have been prepared with diphosphonium bridges connected at the *β*-positions of the tetraphenyl porphyrin of zinc, **ZnTPP** by electrochemical synthesis. However, the various type of dimers have been obtained only from **ZnTPP** in the presence of various type of diphosphane (called also diphosphine) ligand such as bis(diphenylphosphino)acetylene, bis(diphenylphosphino)alkyl, and 1,2-bis(diphenylphosphino)benzene. It must be noted that no electropolymer has been obtained till now due to the easy oxidation of the diphosphane ligand.

In this chapter, the four different diphosphine ligand, namely 1,2-bis(diphenylphosphino)ethene, 1,2-bis(diphenylphosphino)benzene, 1,2-bis(diphenylphosphino)ethyne and 1,2-bis(diphenylphosphino)propane have been tested as nucleophiles to prepare isoporphyrin copolymer in the presence of **ZnT_2P**. The copolymers have been obtained with success and have been characterized by UV-vis-NIR spectroscopy, X-ray photoelectron spectroscopy (XPS), electrochemical quartz crystal microbalance (EQCM). The photoelectrocatalytic properties have been also examined and studied under illumination.

1. Introduction

Over the years, several extended porphyrin structures have been prepared and studied with a particular interest in the dependence of the geometric factors on their physical properties. The structural flexibility is determined by the nature of the bridge. To observe efficient interactions between the different chromophores, a large variety of bridging chains have been used as spacers in the building of dimers, but only a few papers were devoted to phosphanylporphyrins. Electrochemistry has been shown to be an appropriate synthetic tool in the coupling of porphyrins.

Phosphorus ligands are useful nucleophiles and could nucleophilic attack the π cation radicals of metalloporphyrins. In a direct one-pot electrochemical reaction, the bis(dipheny1phosphino)acetylene ligand acts as a nucleophile allowing the synthesis of diporphyrins with a diphosphonium spacer bridged directly at their meso positions. The group of Ruhlmann described the efficient synthesis of various diphosphonium-bridged porphyrins using more or less rigid diphosphanes with variable length.[1-3] However, such compounds are easily oxidized which can limit the use of such ligands for the electrosynthesis which is conditioned by the applied potential as well as the potential of the first oxidation of the porphyrin.

In this chapter, we still use the ditolyl porphyrin of zinc, **ZnT$_2$P**, and expect to prepare stable isoporphyrin copolymers in the presence of diphosphanes such as 1,2-bis(diphenylphosphino)ethene and 1,2-bis(diphenylphosphino)benzene.

2. Formation and characterization

2.1. Electropolymerization of isoporphyrin copolymers

As already reported, in the presence of various diphosphanes, the second oxidation step of the tetraphenyl porphyrin of zinc (**ZnTPP**) became irreversible and a new cathodic peak appeared, as observed in the reduction of electrochemically generated isoporphyrins.[4-7]

In the case of the increase of the potential near the second oxidation of the **ZnTPP** porphyrin, it induces the oxidation of the di(phenylphosphane) which is fully converted to the di(phenylphosphane oxide) without formation of the copolymer of porphyrin. If using **ZnTPP**, no copolymer is obtained if we applied the potential at the first oxidation of the **ZnTPP** where only the dimer of porphyrin with diphosphonium spacer is obtained. It must noted that at this potential (first oxidation of the porphyrin), the oxidation of the diphosphane ligand does not occur. This isprobably due to the steric hindrance of the **ZnTPP** porphyrin which leads to the slower kinetic of the nucleophilic attack which avoid the isoporphyrin copolymer formation.

Thus, in the presente chapter, we will test the ditolyl porphyrin of zinc, **ZnT$_2$P** used in the other chapters. This porphyrin shows two side occupied by hydrogen at the *meso* and β positions, leading to the decrease of the steric hindrance. Thus, oxidation of the porphyrin around the first oxidation of **ZnT$_2$P** should be more favorable to generate copolymers of isoporphyrin.

Indeed, irreversible oxidation waves have been measures for 1,2-bis(diphenylphosphino)ethene and 1,2-bis(diphenylphosphino)benzene as shown in Figure 5.S1 showing the instabiliy at higher potential.

The oxidation wave at 1.0 V corresponds to a one-electron oxidation of **ZnT_2P** which generated the corresponding π-radical cation porphyrin **$ZnT_2P^{+\bullet}$**. It is known that electrolysis at this potential (first oxidation of the porphyrin) induces the formation of the monosubstituted porphyrin via an ECEC process. The $E_1C_NE_2C_B$ process is involved to form the monosubstituted porphyrin where the first step corresponds to generation of the π-radical cation porphyrin **$ZnT_2P^{+\bullet}$** by oxidation (E_{ox1} step). The second step is the nucleophilic attack of the phosphane group –$P(Ph_2)$- which forms one isoporphyrin (C_N step). Then, this intermediate isoporphyrin can be in turn oxidized (E_{ox2} step) inducing the removal of the hydrogen and the rearomatisation of the porphyrin (C_B step) as shown in Scheme 5.1.

At this stage, we have already obtained the monosubstituted porphyrin with one phosphonium covalently connected to the porphyrin and one pendant phosphane which is still active for nucleophilic attack. At that time, the oxidation of the monosubstituted porphyrin will generate the π radical cation porphyrin (E_{ox3} step) which can react itself (nucleophilic attack of the pendant phosphane group –$P(Ph_2)$-) forming isoporphyrin radical copolymer (C_N step) with diphosphonium spacers (Scheme 5.1). This isoporphyrin copolymer can be further oxidized (E_{ox4} step) giving the corresponding polyporphyrin after the release of H^+(C_B step).

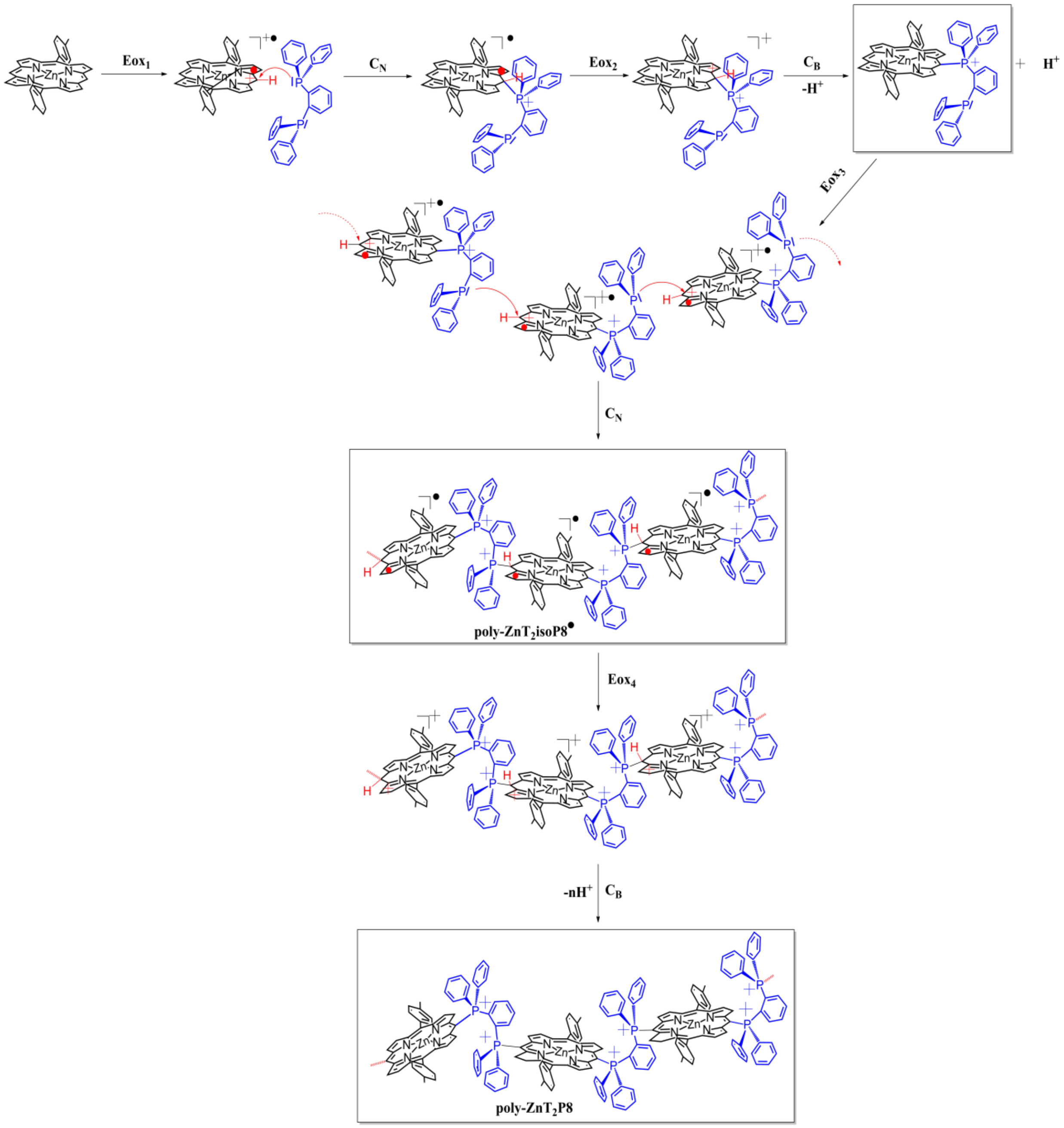

Scheme 5.1. The electropolymerization mechanism proposed to form the poly-isoporphyrin with **ZnT$_2$P** and 1,2-bis(diphenylphosphino)benzene.

Cyclic voltammograms during electropolymerization of **ZnT$_2$P** in the presence of bis(diphenylphosphino)ethene or 1,2-bis(diphenylphosphino)benzene are shown in Figure 5.1.

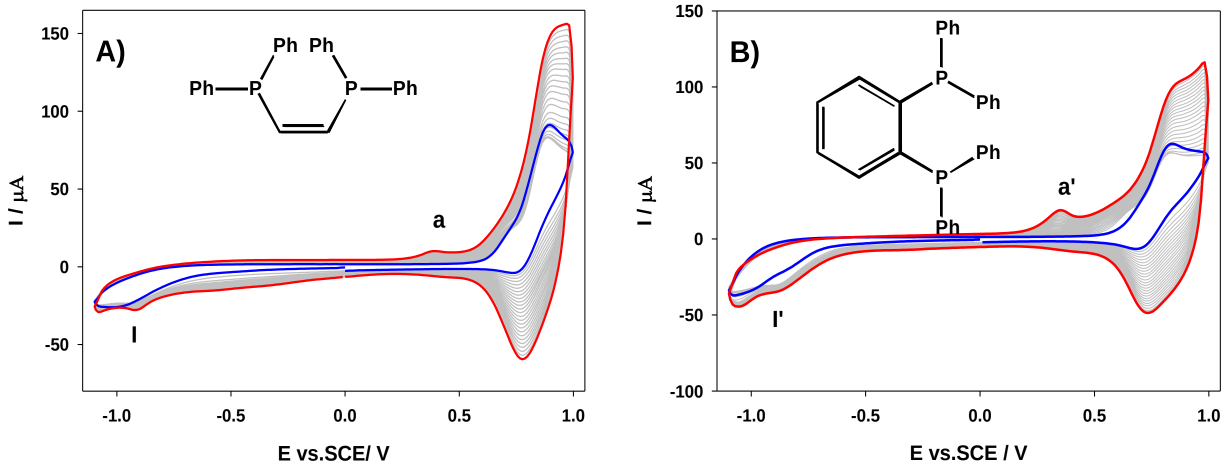

Figure 5.1. Cyclic voltammograms recorded during 25 iterative scans conducted between -1.1 V and +1.0 V/SCE in the presence of **ZnT$_2$P** (0.25 mmol L^{-1}) with A) 0.25 mmol L^{-1} 1,2-bis(diphenylphosphino)ethene and B) 0.25 mmol L^{-1} 1,2-bis(diphenylphosphino)benzene, in a 1,2-$C_2H_4Cl_2/CH_3CN$ (7/3) solution and NBu_4PF_6 (0.1 mol L^{-1}). WE: ITO. S = 1 cm^2. v = 100 mV s^{-1}. Blue curve: first scan (n=1). Red curve: final scan (n = 25).

The reduction peak I or I' are not well defined and are due to the reduction of the phosphonium -$P(Ph)_2^+$- connected between the isoporphyrin **ZnT$_2$P$^\bullet$** subunits.

Thus, under 1.0 V, the di(phenylphosphane) ligand could react with the π-radical cation porphyrin **ZnT$_2$P$^{+\bullet}$** to form at the end poly-isoporphyrin radical copolymers as discussed below. After 25 iterative scans, the oxidation waves continue to increase showing the growth of copolymer materials (Figure 5.1). Finally, brown deposited films could be observed on the ITO surface.

2.2. EQCM for the copolymer deposition

The electrosynthesis of **poly-ZnT$_2$isoP7$^\bullet$** prepared from **ZnT$_2$P** and 1,2-bis(diphenylphosphino)ethene) and **poly-ZnT$_2$isoP8$^\bullet$** prepared from **ZnT$_2$P** and 1,2-bis(diphenylphosphino)benzene) has been monitored *in-situ* by EQCM (Fig. 5.2). According to the Sauerbrey's equation, the decrease of resonance frequency in Figure 5.3 corresponds to the increase of deposited mass. Electropolymerization occurs in the presence of diphosphane ligand and **ZnT$_2$P** via the oxidation. The mass of the copolymer film increased with the increase of number of potential cycle n (Fig. 5.3). After 25 iterative scans, 7.81 µg/cm^2 of **poly-ZnT$_2$isoP7$^\bullet$** and 11.46 µg/cm^2 of **poly-ZnT$_2$isoP8$^\bullet$** are deposited. The repeat unit are ($isoZnT_2P\text{-}^+PPh_2\text{-}C{=}C\text{-}PPh_2^+\cdot 2PF_6^-$) and ($isoZnT_2P\text{-}^+PPh_2\text{-}Ph\text{-}PPh_2^+\cdot 2PF_6^-$) for **poly-ZnT$_2$isoP7$^\bullet$** and **poly-ZnT$_2$isoP8$^\bullet$**. The calculated surface coverages Γ are 8.36×10^{-9} $mol.cm^{-2}$ and 11.78×10^{-9} $mol.cm^{-2}$, respectively. From the EQCM measurements, the mass deposited of poly-isoporphyrin copolymer obtained is higher in the case of 1,2-bis(diphenylphosphino)benzene which means that this ligand shows better reactivity toward the nucleophilic attack than 1,2-bis(diphenylphosphino)ethene. It may be due to the higher flexibility of the disphosphane 1,2-bis(diphenylphosphino)ethene where with possible Z/E isomerization under illumination. Such isomerization is impossible on the case of the rigid 1,2-bis(diphenylphosphino)benzene.

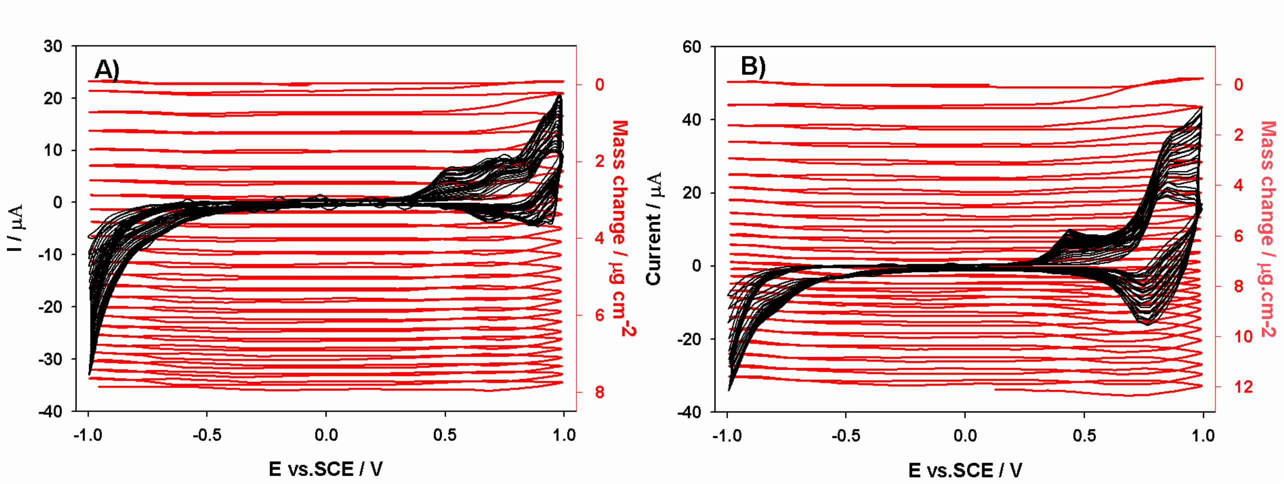

Figure 5.2. Electrochemical quartz crystal microbalance measurements (*Δm*) and consecutive cyclic voltammograms (first 25 scans) between (A) -1.0 and 1.0 V of **poly-ZnT$_2$isoP7$^\bullet$** (B) -1.0 and 1.0 V of **poly-ZnT$_2$isoP8$^\bullet$** obtained by the electropolymerization of 0.25 mmol L^{-1} **ZnT$_2$P** with 0.25 mmol L^{-1} 1,2-bis(diphenylphosphino)ethene and 1,2-bis(diphenylphosphino)benzene ligand respectively in 1,2-$C_2H_4Cl_2$–CH_3CN (7/3) in the presence of 0.1 mol L^{-1} NBu_4PF_6. Working electrode: ITO (A = 0.2 cm^2) deposited on a 9.08 MHz AT-cut quartz crystal. *v* = 100 mV s^{-1}.

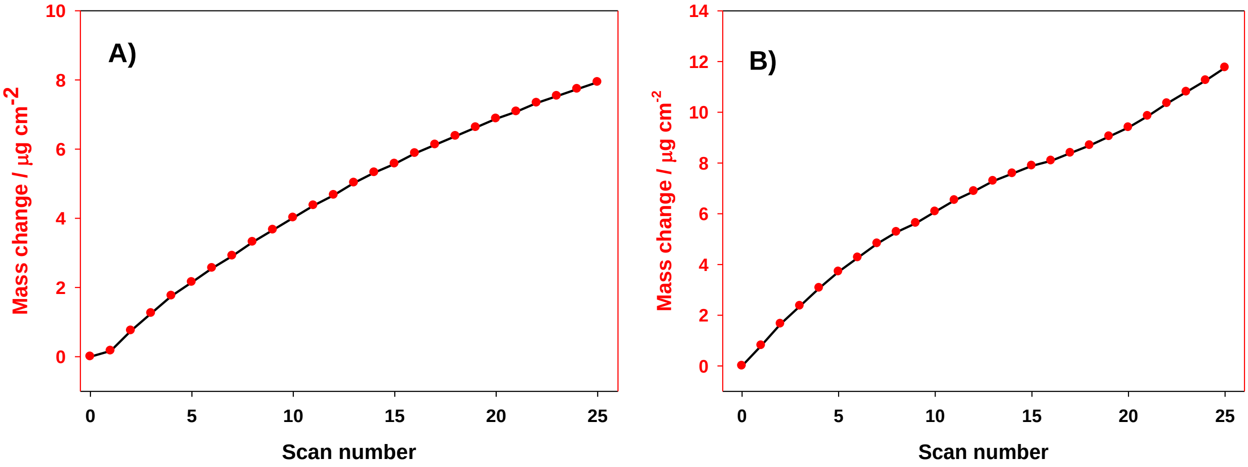

Figure 5.3. Mass change (*Δm*) of the first 25 scans calculated from Sauerbrey's equation versus the number of scan n of (A) **poly-ZnT$_2$isoP7$^\bullet$** and (B) **poly-ZnT$_2$isoP8$^\bullet$** prepared from **ZnT$_2$P** and 1,2-bis(diphenylphosphino)ethene and 1,2-bis(diphenylphosphino)benzene ligands respectively.

2.3. UV-vis spectroscopy

Figure 5.4 showed UV-visible-NIR spectra on ITO electrodes coated with the poly-isoporphyrin measured at various thickness. The optical spectra of the diphosphane ligand, namely 1,2-bis(diphenylphosphino)ethene and 1,2-bis(diphenylphosphino)benzene are also showed in Figure 5.S2. The absorption intensity increases with the iterative scan number showing similar trend with EQCM results (Fig. 5.4C).

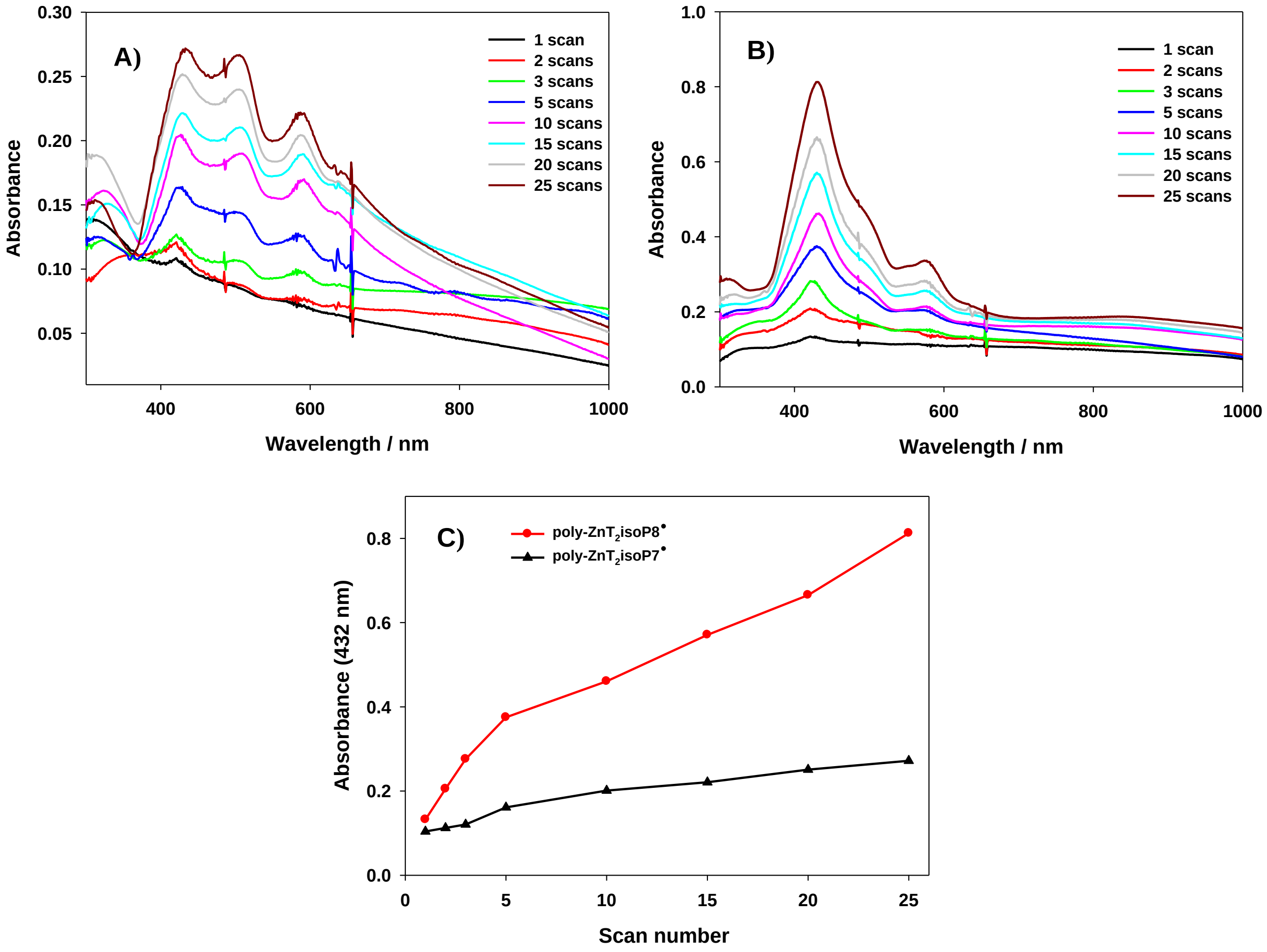

Figure 5.4. UV-visible-NIR absorption spectra of (A) **poly-ZnT$_2$isoP7$^•$** and (B) **poly-ZnT$_2$isoP8$^•$** prepared from **ZnT$_2$P** and 1,2-bis(diphenylphosphino)ethene) and 1,2-bis(diphenylphosphino)benzene ligands respectively onto ITO with different numbers of iterative scans (v = 100 mV s^{-1}). C) Plot of the absorbance measured at λ = 432 nm *versus* n the numbers of iterative scans of **poly-ZnT$_2$isoP7$^•$** and **poly-ZnT$_2$isoP8$^•$**.

A typical UV-visible-NIR spectrum of **poly-ZnT$_2$isoP7$^•$** obtained after electropolymerization between -1.1 and +1.0 V exhibited a split of the Soret absorption band at λ = 432 nm and λ= 505 nm. The bands were red-shifted by 18 and 90 nm respectively compared to the **ZnT2P** monomer (Table 5.1). The visible bands (Q bands), observed at 587 and 633 nm, are also red-shifted by 41 and 49 nm as compared to **ZnT2P**. The presence of the additional band in the NIR region is difficult to detect because it isvery weak and broad even after 25 iterative cycles (n = 25; n : number of iterative cycle during the electropolymerization) as shown in Figure 5.4A. In the case of **poly-ZnT2isoP8●**, Soret absorption bands are localized at λ = 432 nm and λ = 497 nm while Q bands are detected at 574 nm, 632 nm. In this case, large NIR band can be detected with the maximum of absorption near 805 nm. This bathochromic shift of the Soret and Q bands may result from the electron withdrawing effect of the positive charge on the diphosphonium dications spacers. These results indicated excitonic interactions between isoporphyrins rings as well as the presence of the radical isoporphyrin subunit (NIR band detected in the case of **poly-ZnT2isoP8●**). These interactions would thus favor a presence of the two subunits namely the diphosphonium spacer and the isoporphyrin.[2] The weak absorption band in NIR region may be explained by important delocalization of the radicals of isoporphyrin subunit through the disphosphonium spacers.

Table 5.1. UV–visible spectral data for ZnT2P in CH_3Cl, 1,2-bis(diphenylphosphino)ethene and 1,2-bis(diphenylphosphino)benzene, **poly-ZnT2isoP7●**, **poly-ZnT2isoP8●** on optical transparent ITO electrodes. Under bracket: molar extinction coefficient (ε /10^3 L.M.cm^{-1}).

Compound	Soret band/nm	Q bands/nm	π-π^*Band/nm
ZnT2P	415 (405.4)	546 (18.9), 584 (4.9)	
1,2-bis(diphenylphosphino)ethene[a]			214 (44.9) 257 (19.7)
1,2-bis(diphenylphosphino)benzene[a]			214 (58.7), 278 (17.9)
poly-ZnT2isoP7● [b]	432, 505	587, 633, 810	
poly-ZnT2isoP8● [c]	432, 497	574, 632, 805	

[a] in 1,2-$EtCl_2$/CH_3CN (7/3).

[b] Copolymers obtained by iterative scan between -1.1 V and +1.0 V *vs.* SCE onto ITO.

[c] Copolymers obtained by iterative scan between -1.1 V and +1.0 V *vs.* SCE onto ITO.

2.4. Cyclic voltammetric measurements of the films

The cyclic voltammetry (CV) of electroactive copolymers deposited on ITO surfaces have been studied for various iterative scans number n (n = 1, 3, 5, 10, 15, 20, 25 cycles) using electrolytic solution containing only the mixed solvent $CH_3CN/1,2\text{-}C_2H_4Cl_2$ (3/7) and the supporting electrolyte NBu_4PF_6.

In the case of copolymer where isoporphyrin was substituted by diphosphonium linker, an electron-withdrawing group, the macrocycle was harder to oxidize, so compared to the corresponding unsubstituted porphyrin **ZnT$_2$P** (Table 5.2 and Figure 5.5). For **poly-ZnT$_2$isoP7$^\bullet$**, the reversible waves at 0.86 V is probably due to the oxidation of the radical isoporphyrin leading to the oxidized isoporphyrin (**poly-ZnT$_2$isoP7$^+$**). We can observe also the presence of an additional irreversible peak a or a' at 0.42 V which can be explained by the irreversible reduction of the phosphonium giving first one radical which can form the covalent C-P bound with the radical of the isoporphyrin (peak I or I') by radical coupling. The radical coupling can be intra- or even intermolecular. The irreversible oxidation peak a or a' can be attributed to the oxidation of the C-P forming after the radical coupling leading to the regeneration of the radical isoporphyrin and the phosphonium. Similar results were observed in the case of the use of dipyridyl ligands.

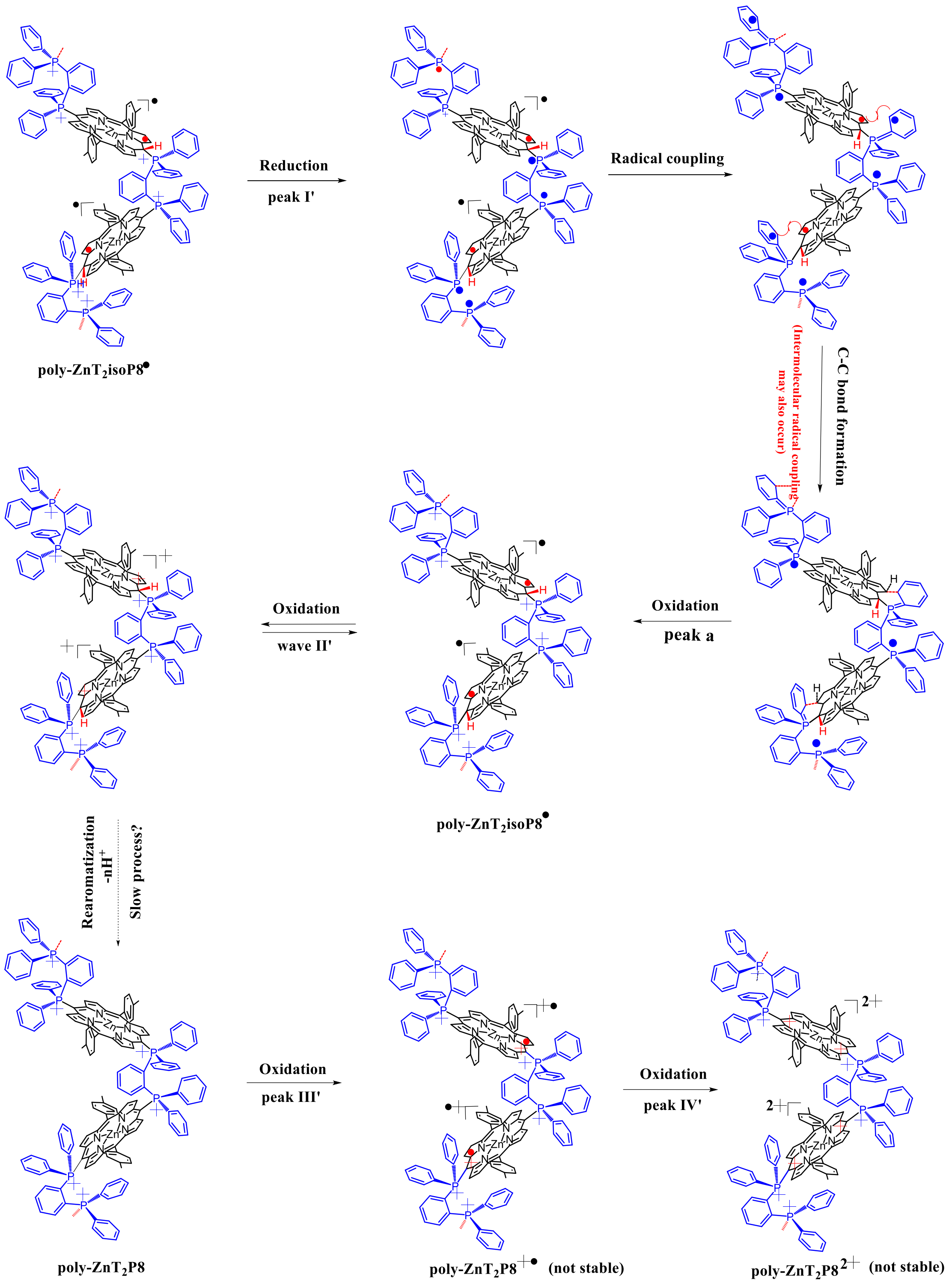

Scheme 5.2. Proposed mechanism explaining the redox reactivity of **poly-ZnT$_2$isoP8$^\bullet$**.

Poly-ZnT$_2$isoP8$^\bullet$ film shows similar electroactive properties as shown in Figure 5.5B.

Furthermore, in the case of the two copolymers, if the films are further oxidized to 1.6 V, the hydrogen atoms located on the *meso*-carbon can be released to form polyporphyrin as shown in former chapters. However, in the case of these two copolymers, we have observed partial decomposition of the film suggesting that during the oxidation at 1.6 V (Table 5.2 and Figure 5.S3). Thus, in resume, the intermediate radical poly-isoporphyrin copolymers with diphosphonium bridges are stable. But further oxidation at 1.6 V leads to the important decomposition of the copolymer due to the oxidation of the porphyrin subunits to form the π-radical cation and the dication (first and second irreversible oxidation). Please note that the irreversible oxidation potentials do not depend on the type of diphosphonium spacers.

The pictures of isoporphyrin copolymer films on the ITO before and after oxidized to 1.6 V are shown in Figure 5.S3.

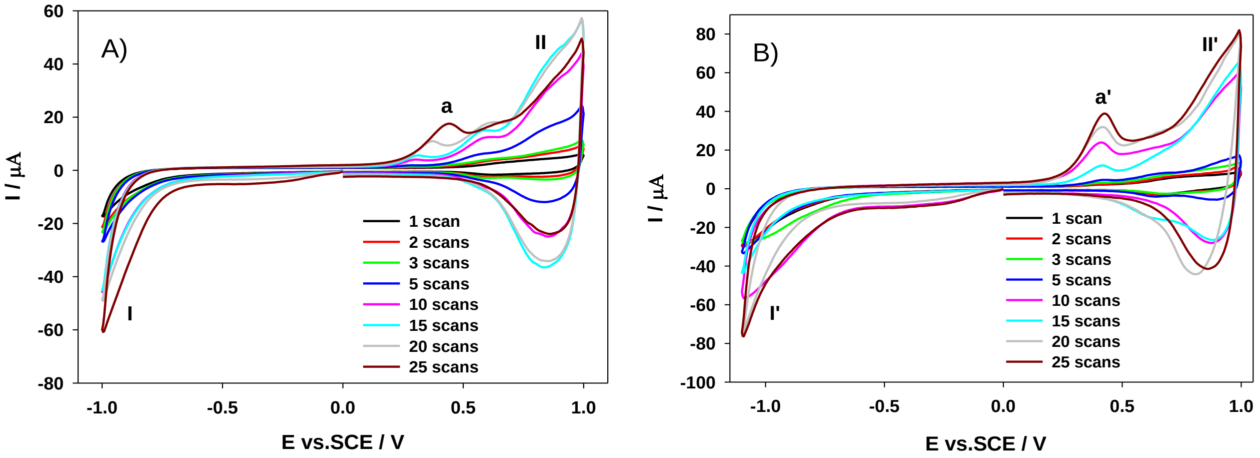

Figure 5.5. cyclic voltammograms of (A) **poly-ZnT$_2$isoP7$^\bullet$** between -1.0 V and +1.0 V obtained from 1,2-bis(diphenylphosphino)ethene) and (B) **poly-ZnT$_2$isoP8$^\bullet$** between -1.1 V and +1.0 V obtained from 1,2-bis(diphenylphosphino)benzene respectively after n = 1, 3, 5, 10, 15 and 20 scans in $CH_3CN/1,2-C_2H_4Cl_2$ (3/7) with 0.1 M NBu_4PF_6. WE: ITO. S = 1 cm^2, v = 100 mV s^{-1}. Irreversible peaks not labelled in anodic part correspond to the oxidation of the π-ring of the macrocycle.

In the Figure 5.S3, the **poly-ZnT$_2$isoP7$^\bullet$** and **poly-ZnT$_2$isoP8$^\bullet$** show two intense irreversible oxidation waves around 1.2 V and 1.4 V, which can be due to the first and the second oxidation of the porphyrin subunits which results in a change inthe color of films from brown to light green with nearly complete dispearing. During these oxidation, the film seems to be not stable showing partial decomposition.

Table 5.2. Electrochemical data for **ZnT$_2$P**, 1,2-bis(diphenylphosphino)ethene) and 1,2-bis(diphenylphosphino)benzene, **poly-ZnT$_2$isoP7$^{\bullet}$** and **poly-ZnT$_2$isoP8$^{\bullet}$**.

Compounds	**Ring oxidation**				**Oxidation of the diphosphane**	**Reduction of spacer**	**Ring reduction**	
	peak IV(IV')	**peak III(III')**	**peak II (II')**	**peak a**		**peak I (I')**		
ZnT$_2$P^a		1.08 (150)					-1.41 (160)	-1.84 (170)
1,2-bis(diphenylphosphino)ethene)			1.37^{irr}		1.37^{irr}			
1,2-bis(diphenylphosphino)benzene			1.68^{irr}		1.68^{irr}			
poly-ZnT$_2$isoP7$^{\bullet}$	1.39^{irr}	1.15^{irr}	0.86 (40)	$+0.42^{irr}$		-0.91^{irr}		
poly-ZnT$_2$isoP8$^{\bullet}$	1.40^{irr}	1.17^{irr}	0.85 (80)	$+0.38^{irr}$		-0.87^{irr}		

^{a} Potentials in V *vs.* SCE were obtained from cyclic voltammetry in 1,2-$C_2H_4Cl_2$ with 0.1 mol L^{-1} $TBAPF_6$. Scan rate = 100 mV s^{-1}. Working electrode: ITO, S = 1 cm^2.

The given half-wave potentials are equal to $E_{1/2} = (E_{pa} + E_{pc})/2$. Under bracket: $\triangle E_p = |E_{pa} - E_{pc}|$.

2.5. X-ray photoelectron spectroscopy

The X-Ray photoelectron spectroscopy of **poly-ZnT$_2$isoP8$^{\bullet}$** was also investigated as shown in Figure 5.6. The analysis of the survey spectra confirms the presence of the isoporphyrin and diphosphonium subunits. (Zn 2p3 at 1022.0 eV, N 1s, and C 1s peaks), while the signals for F 1s (686.7 eV) and for P 2p (136.8 eV) electrons stem from the incorporated counterion PF_6^- to equilibrate the phosphonium charges. Note that only one signal is detected for the P 2p signal localized at 136.8 eV. This signal is coming from the counterions PF_6^-counteranions. Additional measurements are under work in order to detect the signal of the phosphorus atoms of the diphosphonium spacers.

The C1s peaks are composed of two signals, 286.5 eV and 285.0 eV attributed to homo and hetero (connected to nitrogen) carbon atoms respectively. The N1s peaks reveal the presence of three chemically different nitrogens due to the porphyrin, the countercation tetrabutylammonium and solvent molecules inside the film. The small signals detected at 139.9 eV may due to the Zn 3s. Finally, O 1s (532.5 eV, 530.7 eV) signal comes from ITO as well as from the H_2O adsorbed on the copolymer surface.

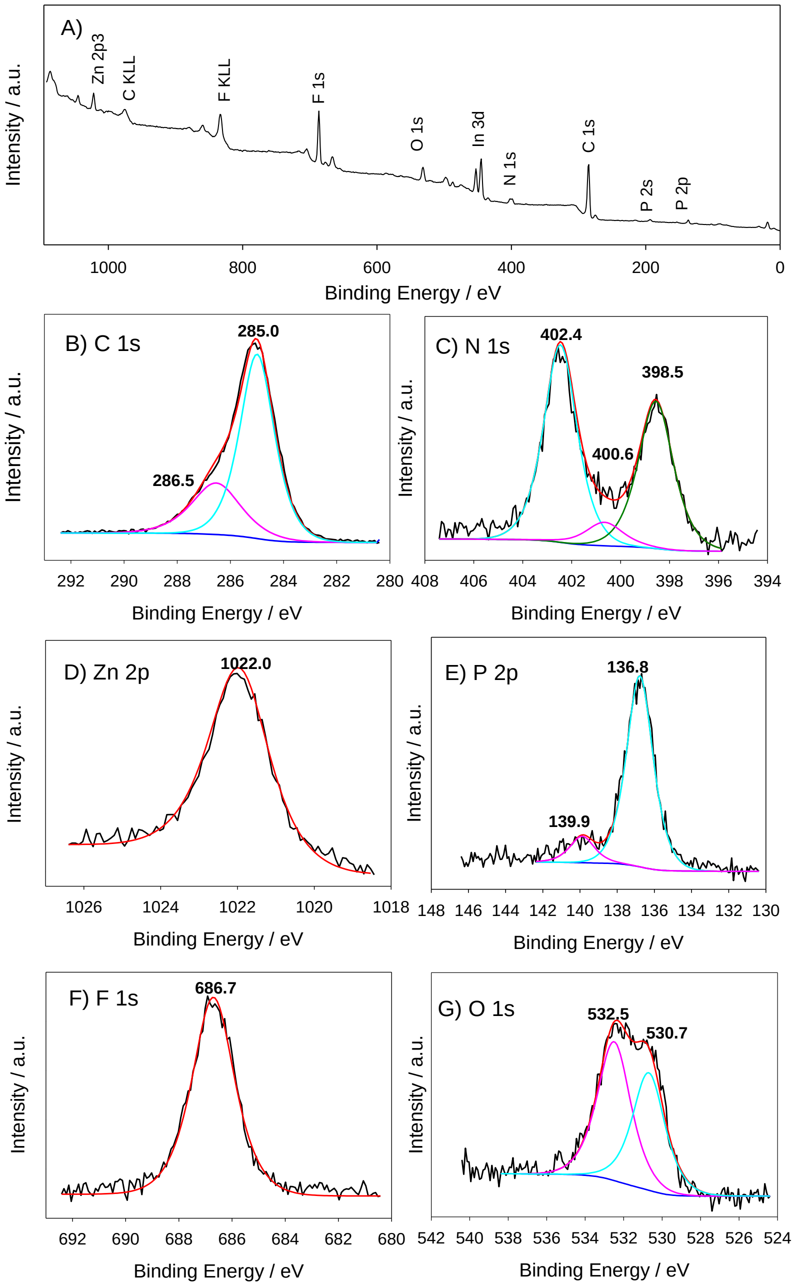

Figure 5.6. XPS spectra of the modified ITO electrodes with **poly-ZnT$_2$isoP8$^\bullet$** obtained with 1,2-1,2-bis(diphenylphosphino)benzene after 25 iterative scans between -1.1 V and 1.0 V *versus* SCE. XPS full spectra (A), C 1s (B), N 1s (C), Zn 2p (D), P 2p (E), F 1s (F) O 1s (G).

3. Photocurrent generation

3.1. Effect of the film thickness

Figure 5.7A shows the typical current-potential curves of **poly-ZnT$_2$isoP7$^{\bullet}$** and **poly-ZnT$_2$isoP8$^{\bullet}$** thin films on ITO electrodes obtained in 5 mM I_3^- / 0.5 M I^- aqueous solution.

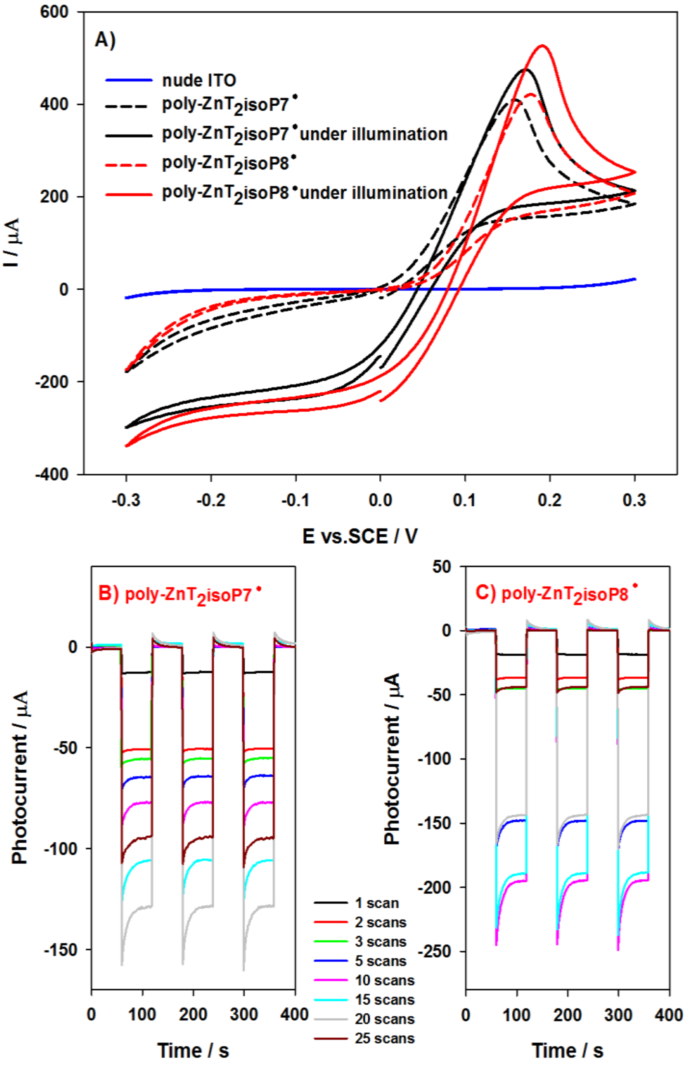

Figure 5.7. A) Current-potential curves of **poly-ZnT$_2$isoP7$^{\bullet}$** (obtained with n = 20 iterative scans between -1.0 V and +1.0 V) and **poly-ZnT$_2$isoP8$^{\bullet}$** (obtained with n = 10 iterative scans between -1.1 V and +1.0 V) thin films on ITO electrodes in 0.5 M I^- / 5 mM I_2 aqueous solution in the dark or under visible illumination. B) and C) Photoelectrochemical response of **poly-ZnT$_2$isoP7$^{\bullet}$** and **poly-ZnT$_2$isoP8$^{\bullet}$** films obtained with n = 1, 2, 3, 5, 10, 15, 20 or 25 iterative scans. Measurements has been done under on-off light illumination from a 300 W Xe arc lamp (with $\lambda > 385$ nm long pass filter) in I_3^- 5 mmol L^{-1} and I^- 0.5 mol L^{-1} aqueous solution. BIAS potential: 0.00 V *vs.* OCP.

The equilibrium potential of I_3^-/I^- redox couple in solution is taken as reference potential at 0 V in the cyclic voltammograms. First, we analyse the curves obtained without light illumination (ploted with dashed lines in Figure 5.7A).

For bare ITO electrode (blue curve), almost no Faradaic current is observed between -0.3 and 0.3 V, revealing the slow I^- oxidation and I_3^- reduction kinetics on ITO electrode. However, the I^- oxidation and I_3^- reduction currents are significantly enhanced on the ITO modified by the copolymers (black and red curves in Figure 5.7A). The anodic peak potential is negatively shifted by ca. 0.1 V on **poly-ZnT$_2$isoP7$^\bullet$** as compared to **poly-ZnT$_2$isoP8$^\bullet$** suggesting that the I^- oxidation kinetics is significantly faster on the **poly-ZnT$_2$isoP7$^\bullet$** modified electrode.

Under visible light illumination, the current-potential curves measured are plotted in Figure 5.7A (full line) for the **poly-ZnT$_2$isoP7$^\bullet$** and **poly-ZnT$_2$isoP8$^\bullet$** copolymers respectively. Under irradiation the current magnitude increased and the difference between light on and light off corresponds to the photocurrent. Thus, I_3^- was a little bit easier to be reduced under visible illumination. The photocurrent response in the potentiostatic mode at 0 V under on-off light illumination cycles is shown in Figure 5.7BC (under visible light for 1 min followed by the dark for 1 min). The magnitude of the photocurrent strongly depends on the number of iterative scans n used for the electropolymerization and then of the amount of copolymer film deposited as displayed in Fig. 5.7BC. For the best photocurrent value of both **poly-ZnT$_2$isoP7$^\bullet$** (20 scans) and **poly-ZnT$_2$isoP8$^\bullet$** (10 scans) samples, the amount of deposited copolymer on ITO substrate is approximately the same (ca. 6.5 µg/cm^2), thus enabling the comparison of their (photo)electrochemical properties. Under visible light, the open circuit potential increases of ca. 40 and 80 mV for the **poly-ZnT$_2$isoP7$^\bullet$** and **poly-ZnT$_2$isoP8$^\bullet$** copolymers respectively. Above this potential, the I^- oxidation current becomes predominant due to the high I^- concentration in solution, impeding thus further increase of the photovoltage. For potentials below the OCP, a negative photocurrent is observed for both copolymers, the photocurrent at 0 V of the **poly-ZnT$_2$isoP7$^\bullet$** copolymer thin film reaching ca. -127 µA cm^{-2} and -194 µA cm^{-2} (potentiostatic experiment) of **poly-ZnT$_2$isoP8$^\bullet$** for approximately the same amount of electrodeposited copolymer.

The values of photocurrent for different scan numbers are shown in Figure 5.8. The best photocurrent generation of copolymers was obtained for 20 iterative scans for **poly-ZnT$_2$isoP7$^\bullet$** and 10 (or 15) iterative scans in the case of **poly-ZnT$_2$isoP8$^\bullet$**. To explain the results, the charge transfer resistance at the electrode/solution interface R_{ct} as well as the charge transfer resistance within the film R_{ct_film} have been measured by electrochemical impedance spectroscopy.

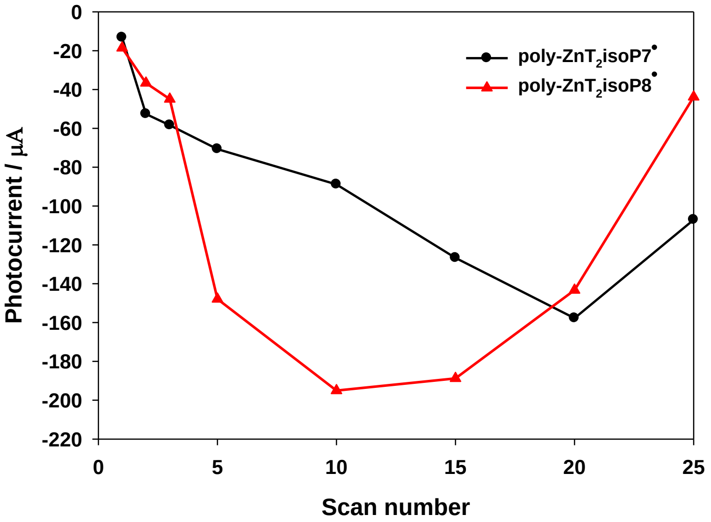

Figure 5.8. Photoelectrochemical response of (A) **poly-ZnT$_2$isoP7•** (black line) and (B) **poly-ZnT$_2$isoP8•** (red line) obtained with n = 1, 2, 3, 5, 10, 15, 20 and 25 iterative scans.

3.2. Electrochemical Impedance Spectroscopy

The electrical properties of copolymer films were studied by electrochemical impedance spectroscopy (EIS), which is widely used in the investigation of dye sensitized solar cell. The Nyquist plots of a typical impedance spectra measured for **poly-ZnT$_2$isoP7•** and **poly-ZnT$_2$isoP8•** obtained from **ZnT$_2$P** and 1,2-bis(diphenylphosphino)ethene) or 1,2-bis(diphenylphosphino)benzene respectively at 0 V in 5 mM I_3^- / 0.5 M I^- aqueous solution, *versus* various iterative scan numbers (n=1, 2, 3, 5, 10, 15, 20 and 25) used for the electropolymerization, are plotted in Figure 5.9 showing semi-circles typical for a parallel combination of a charge transfer resistance with a capacitance. The diameter of the semi-circle of the Nyquist plot on X axis corresponds to the charge transfer resistance R_{ct}. When n increases above 10, a second semi-circle appears at high frequency and is attributed to the charge transfer processes within the copolymer film with charge transfer resistance in the film R_{ct_film} in parallel with C_{ct_film} the capacitance of the film. The values R_{ct} and R_{ct_film} with light on and off are plotted in Figure 5.10.

Compared with Figure 5.8, the photocurrent response depends on the number of deposition scans. The magnitude of the photocurrent increased from n = 1 to n = 10 or 15, and then decreased when n > 10 (n corresponds to the iterative scans use for the deposition for **poly-ZnT$_2$isoP7•**). The same trend is observed for **poly-ZnT$_2$isoP8$^\bullet$**. It must be noted that under light illumination, the charge transfer resistance decreased when n increases compared to the dark (with no light illumination condition). In resume, the charge transfer resistance (R_{ct}) decreases with the increase of the iterative scan number n showing that the film is catalyzing the charge transfer between the I_3^-/I^- redox mediator and the electrode. For n <15, the whole isoporphyrin thin film is in good electrical contact with the ITO substrate and is able to participate to the photocurrent generation. It explains the increase of photocurrent *versus* n the number of iterative scan between n=1 to n=15. Above 15 scans, the appearance of a second semi-circle in the impedance spectra reveals that the increasing thickness of the film is hindering the electronic and/or ionic charge transfer within the copolymer film. The appearance of this second impedance loop seems to be correlated with the decrease of the photocurrent. In comparison to the copolymers obtained with dipyridine ligands, the copolymer films of **poly-ZnT$_2$isoP7$^\bullet$** and **poly-ZnT$_2$isoP8$^\bullet$** are thinner, less tight and less colored which is in line with the smaller R_{ct_film} values.

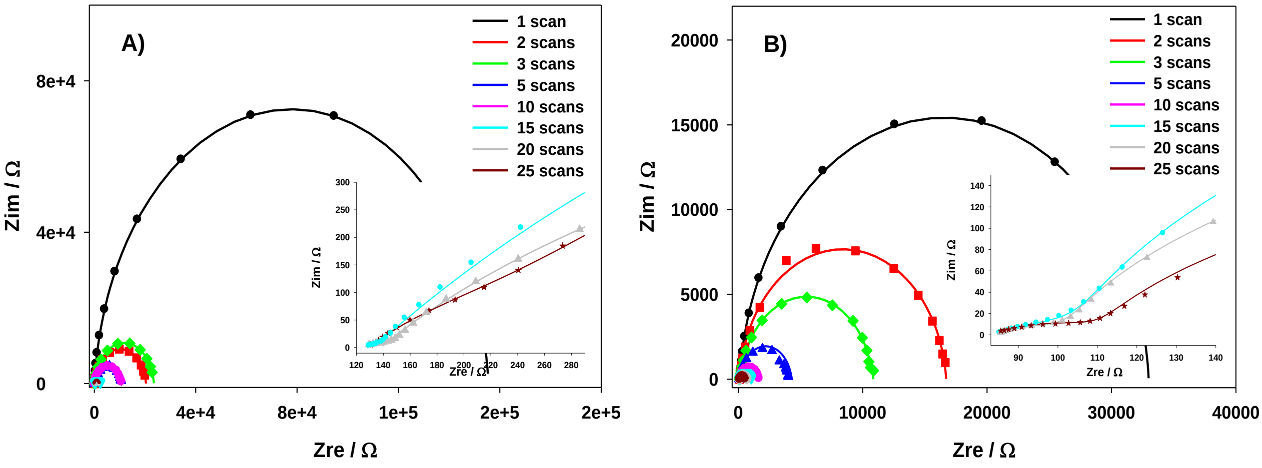

Figure 5.9. ESI Nyquist of A) **poly-ZnT$_2$isoP7$^\bullet$** and B) **poly-ZnT$_2$isoP8$^\bullet$** obtained from 1,2-bis(diphenylphosphino)ethene) and 1,2-bis(diphenylphosphino)benzene respectively. Measurements has been done in the dark and in H_2O containing I_3^- 5 mmol L^{-1} and I^- 0.5 mol L^{-1}. BIAS potential: 0.00 V *vs.* OCP. Insert figures are the zoom of second semi-cycle of Niquist plot obtained at n = 15-25 scans.

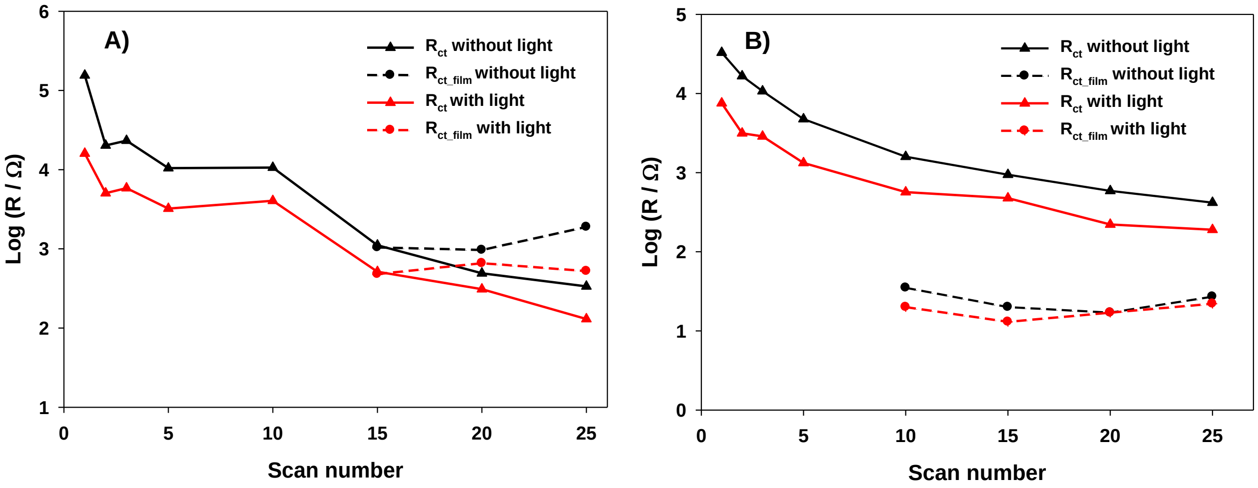

Figure 5.10. Plot of the Log(R) *versus* n (number of iterative scan, v = 100 mV s^{-1}) for (A) **poly-ZnT$_2$isoP7$^{\bullet}$** and (B) **poly-ZnT$_2$isoP8$^{\bullet}$** obtained from 1,2-bis(diphenylphosphino)ethene) and 1,2-bis(diphenylphosphino)benzene respectively. Measurements has been done in H_2O under on (red line) and off light (black line) illumination from a 300W Xe arc lamp (with λ > 385 nm long pass filter) in containing I_3^- 5 mmol L^{-1} and I^- 0.5 mol L^{-1}. BIAS potential: 0.00 V *vs.* OCP. (R_{ct} = charge transfer resistance at the I^-/I_3^- species at the ITO/solution interface (triangle plot with solid line), R_{ct_film} = the charge transfer resistance of films (square plot with dotted line).

3.3. Energy diagram

To investigate the electron transfer mechanism in the system, the energies of the relevant electronic states have been estimated. In the case of copolymer **poly-ZnT$_2$isoP7$^{\bullet}$**, an energy level diagram can be built using the oxidation potential of isoporphyrin subunit and the reduction potential of phosphonium subunits, together with the optical absorption spectra of copolymer films (Fig. 5.11). It describes the thermodynamics for spectral sensitization of the ITO electrode. The LUMO levels of the excited **poly-ZnT$_2$isoP7$^{\bullet}$** and **poly-ZnT$_2$isoP8$^{\bullet}$** species can be roughly estimated by subtracting the excitation energy of the Soret or Q bands from the HOMO level energies. The levels of the excited isoporphyrin, isoPorp^{+}/Porp*, are calculated from the absorption spectra of the film and the wavelength of the B, Q and NIR bands. The ground state isoporphyrin (isoPorp$^{+\bullet}$/Porp) is calculated from the oxidation potential of the isoporphyrin giving for instance in the absolute scale –5.60 eV for the **poly-ZnT$_2$isoP7$^{\bullet}$** film. The energy level of I_3^-/I^- on the absolute scale is –5.00 eV. The energy Level of **poly-ZnT$_2$isoP8$^{\bullet}$** corresponding to the band in the NIR region has also been indicated in the energy diagram (Fig. 5.S4). Under illumination at 0 V, the photon absorption by the (iso)porphyrin entities generates an electron hole pair in the copolymer. The electron is transferred from the excited (iso)porphyrins to the phosphonium subunit acting as a relay for the electron transfer forming the radical phosphane. This radical phosphane gives in turn the electron to the I_3^- which is reduced into I^- which is reoxidized at the counter-electrode. The oxidized (iso)porphyrins are regenerated by an electron transfer from the ITO substrate. The I_3^- reduction is in competition with the recombination of the photogenerated electron-hole pair. Thus, fast electron transfer kinetics between the ITO and the oxidized (iso)porphyrins and/or between the excited (iso)porphyrins and the I_3^- are crucial for the efficient photocurrent generation.

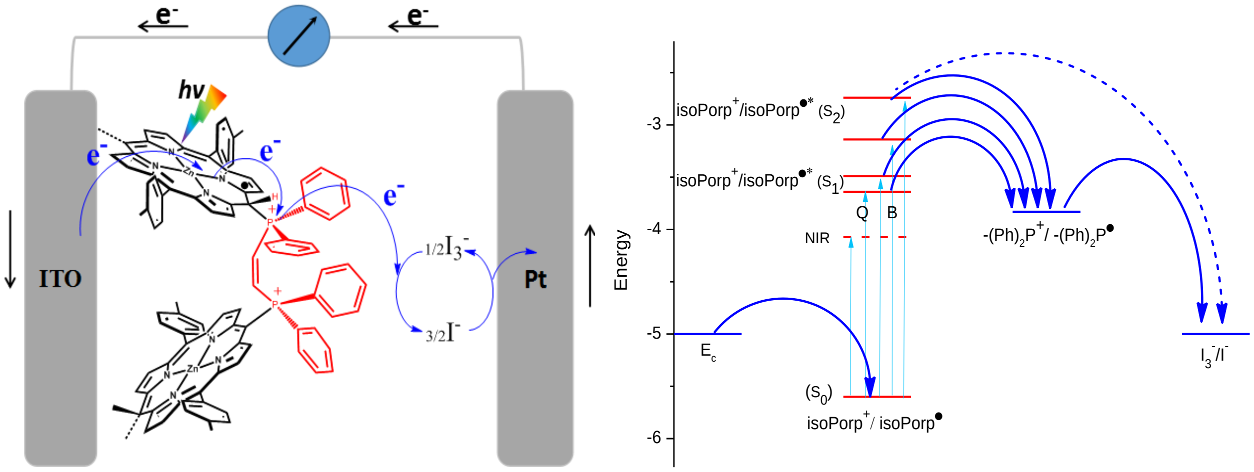

Figure 5.11. Schematic illustration of the energy level diagram for **poly-ZnT$_2$isoP7$^\bullet$** showing electron transfer processes in H_2O containing I_3^- 5 mmol L^{-1} and I^- 0.5 mol L^{-1} (**-(Ph)$_2$P$^+$** = di(phenylphosphonium), Porp = porphyrin).

4. The electropolymerization of two other kinds di(phenylphosphane) ligands

As showed in Figure 5.12, during the electropolymerization of **ZnT$_2$P** in the presence of 1,2-bis(diphenylphosphino)ethyne, the oxidation current decreased with the number of iterative scans, which seems to mean that no copolymer is formed. At the end of the process, no copolymer was deposited on the surface of the ITO electrode.

On the contrary, in the case of **ZnT$_2$P** in the presence of 1,3-bis(diphenylphosphino)propane, the current increased during the iterative scan indicating the copolymer formation which is deposited on the ITO electrode. The oxidation behavior of diphosphanes are shown in Figure 5.S5.

One explanation can be the delocalization of the positive charge of the first phosphonium connected through the triple bond which deactivate the non-binding doublet of the second phosphane ligand. In such a case, the nucleophilicity is not enough to be able to attack the π-radical cation porphyrin and then to generate the isoporphyrin copolymer.

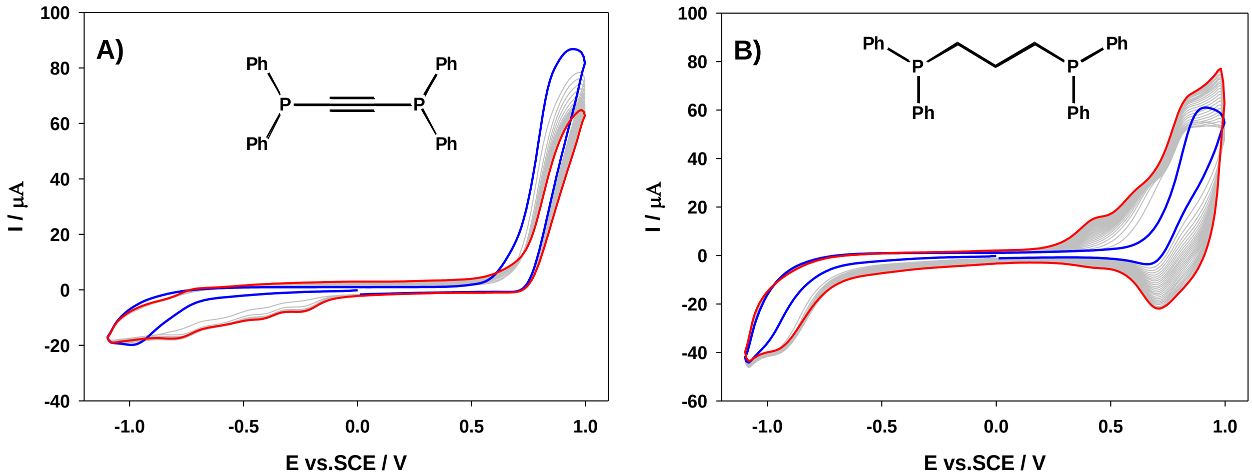

Figure 5.12. Cyclic voltammograms recorded during 25 iterative scans conducted between -1.1 V and +1.0 V/SCE in a 1,2-$C_2H_4Cl_2$/CH_3CN (7/3) solution of **ZnT_2P** (0.25 mmol L^{-1}) in the presence of A) 1,2-bis(diphenylphosphino)ethyne (0.25 mmol L^{-1}) and B) 1,3-bis(diphenylphosphino)propane (0.25 mmol L^{-1}). WE: ITO. S = 1 cm^2. v = 100 mV s^{-1}. Blue curve: first scan (n=1). Red curve: final scan (n = 25).

The UV-vis-NIR spectra of copolymers films formed with **ZnT_2P** in the presence of 1,3-bis(diphenylphosphino)propane is shown in Figure 5.13. The absorption intensity increased with the iterative scan number chosen for the electropolymerization showing the deposition of the isoporphyrin radical copolymer versus n. We observed again the typical splitting of the Soret band and the red shift of the Soret and Q bands typical for the formation of isoporphyrin copolymer with diphosphonium linkers. One not well resolved NIR can be detected for n = 10 iterative scans.

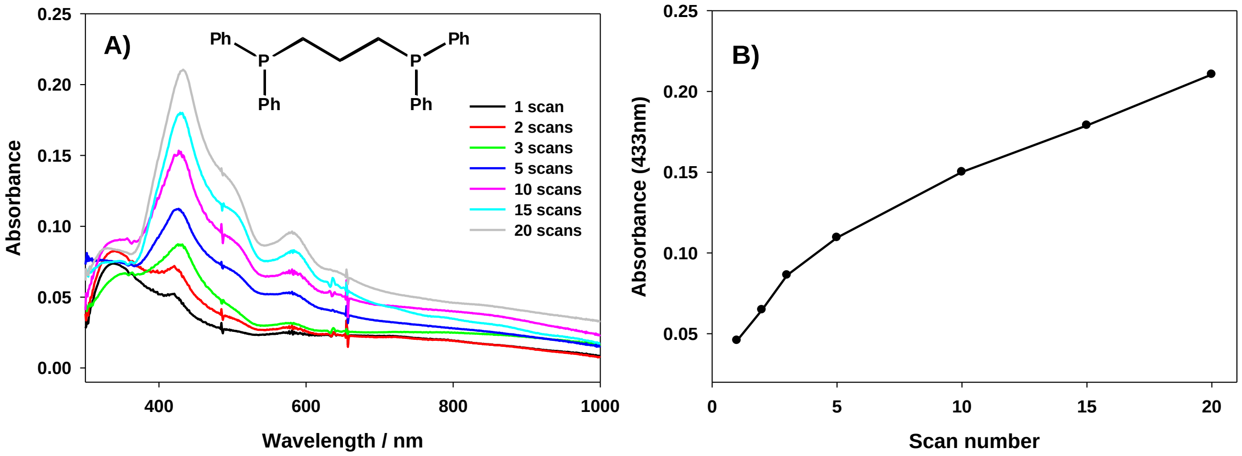

Figure 5.13. A) UV-visible-NIR absorption spectra of poly-isoporphyrin formed with **ZnT$_2$P** in the presence of 1,3-bis(diphenylphosphino)propane onto ITO with different numbers of iterative scans between -1.0 and +1.0 V *vs.* SCE (v = 100 mV s^{-1}). Only one side is covered by ITO. B) Plot of the absorbance measured at λ = 433 nm *versus* n the numbers of iterative scans.

The photocurrent measurements as well as the impedance measurements are in progress and will be completed for the submission of one paper.

Due to the COVID-19 pandemic, the EPR spectra of the film in DMF solution has also not yet been measured. It is needed to prove the presence of the radical isoporphyrin. It will be completed as soon as possible. The morphology of the copolymer by AFM will be also studied a little later and is not introduce in the manuscript of the thesis due to the same reason.

5. Conclusion

In summary, copolymer films have been prepared by the electro-oxidation of 5,15-ditolylporphyrin (**ZnT$_2$P**) in the presence of various type of di(phenylphosphane) ligands. Electrogenerated radical cation porphyrin is a powerful electrophile which can rapidly react to form copolymer containing stable isoporphyrin subunits (**poly-ZnT$_2$isoP$^•$**). The achieved copolymers were characterized by UV-Vis-NIR spectroscopy, and X-ray photoelectron spectroscopy. Mechanisms of electrochemical routes to these electroactive copolymers have been discussed as well as the description of the unusual redox properties of copolymers containing stable isoporphyrin.

The photocurrent measurements under visible-NIR light irradiation show that **poly-ZnT$_2$isoP8$^•$** thin films exhibit significantly better performance than **poly-ZnT$_2$isoP7$^•$**. However, the photovoltaic performances reach an optimum depending on the number of electropolymerization potential scan n.

The best performances for **poly-ZnT$_2$isoP7$^\bullet$** and **poly-ZnT$_2$isoP8$^\bullet$** are obtained for n =20 and 10 respectively. Therefore, the control of the thickness of the copolymer films is of great importance to optimize the generation of photocurrent under visible illumination. The copolymer in the solid state could be stored for over several months and even one year without any degradation under ambient conditions in air. Further investigations are underway in order to understand more about this remarkable stability.

References

1. L. Ruhlmann, A. Giraudeau, *Chem Commun*, **1996**, 17, 2007–2008.
2. L. Ruhlmann, A. Giraudeau, *Eur J Inorg Chem*, **2001**, 13, 659–668.
3. L. Ruhlmann, M. Gross, A. Giraudeau, *Chem Eur J*, **2003**, 9, 5085–5096.
4. A. S. Hinman, B. J. Pavelich, S. Pons, A. E. Kondo, *J. Electroanal. Chem.* **1987**, 234, 145–162.
5. A. El-Kasmi, D. Lexa, P. Maillard, M. Momenteau, J. M. Savéant, *J. Am. Chem. Soc.* **1991**, 113, 1586–1595.
6. K. M. Kadish, R. K. Rhodes, *Inorg. Chem*. **1981**, 20, 2961–2996.
7. K. M. Barkigia, M. W. Renner, H. Xie, K. M. Smith, J. Fajer, *J. Am. Chem. Soc*. **1993**, 115, 7894–7899.

Conclusion générale

Objectif de la présente thèse était d'étudier les copolymères de porphyrines et les copolymères d'isoporphyrines préparés avec différents types de ligand. Les ligands peuvent être subdivisés en deux groupes : les ligands de type dipyridyle et les ligands de type diphénylphosphine.

Après une description de la chimie et des propriétés physico-chimiques des porphyrines, des isoporphyrines et des polyoxométallate et la description de l'état de l'art des hybride poprhyrin – polyoxométallate, le chapitre II a porté sur l'électrosynthèse de nouveaucopolymères d'isoporphyrine radicalaire stables avec des espaceurs dipyridiums. Ceux-ci peuvent être obtenu à un potentiel appliqué de+1,0 V en présence de la 5,15-ditolylporphyrine de zinc **ZnT$_2$P** et d'un ligand dipyridiles. Les analogues polypoprhyrins sont obtenus en poussant le potentiel vers +1,6 V. Les ligands 1,1"-(1,3-propanediyl)bis-4,4'-bipyridinium hexafluorophosphate (bpy$^+$-(CH$_2$)$_3$–$^+$bpy · 2PF$_6^-$) et 4,4'-bipyridyl ont été utilisés. Des copolymères radicalaires d'isoporphyrine ont été caractérisés par spectroscopie RPE confirmant la présence des centres radicaux isoporphyrines. En spectroscopie d'absorption UV-visible-NIR, le copolymère d'isoporphyrine radicalaire a également montré deux bandes d'absorptions additionnelles par rapport au copolymère à base de porphyrines : une nouvelle bande d'absorption dans le domaine visible (dédoublement de la bande Soret) et une nouvelle bande d'absorption dans la région du proche infrarouge. L'absorption de la lumière plus importante (absorbance dans le domaine du visible plus élevée et absorption dans le NIR) des copolymères d'isoporphyrine radicalaires permet de générer un photocourant plus efficace que pour les copolymères de porphyrine parents obtenus en poussant le potentiel d'oxydation à 1,6 V *vs.* ECS. L'excitation au niveau de cette nouvelle bande NIR dans le cas du copolymère d'isoporphyrine radicalaire conduit, en milieux aérés (présence de $^3O_2$), à la formation de l'état singulet du dioxygène $^1O_2$ qui est la première étape pour l'utilisation de tels matériaux pour le traitement de cancer par photothérapie. Dans ce chapitre, trois autres types de ligands dipyridyle ont également été utilisés et les copolymères d'isoporphyrine radicalaires correspondants ont tous été préparés avec succès.

Dans le chapitre III, un nouveau ligand du type la 3-(2-(3-(2-(pyridin-3-yl)éthynyl)phényl)éthynyl)pyridine a été proposé pour former un copolymère de porphyrines face à face (c’est-à-dire cofaciale). De nombreux facteurs ont été étudiés pour obtenir de meilleures conditions de formation de ce copolymère lors de l'électropolymérisation, comme le rapport entre la concentration de la porphyrine et du ligand dipyridile et les concentrations de la porphyrines et de la 3-(2-(3-(2-(pyridin-3-yl)éthynyl)phényl)éthynyl)pyridine. Ce nouveau copolymère a montré une efficacité intéressante et importante pour la génération de photocourant sous éclairage dans le domaine du visible. En perspective à ce travail, de manière ultérieure, divers types de polyoxométalates seront insérés dans un tel copolymère cofacial, en utilisant différents types de polyoxométalate (POM par exemple du type Anderson, Keggin, Dawson) avec des tailles, géométrie et charge différentes.

Dans le chapitre IV, l’emplois d’un cluster du type polyiodométalate (PIM) substitué par six ligands pyridyle pendant : **PIM(py)$_6$**, a permis comme attendu l’obtention d’un copolymère isoporphyrine / PIM par électropolymérisation. Le copolymère a montré des propriétés électrochimiques et photoélectrochimiques intéressantes. La seconde vague d’oxydation du **PIM(py)$_6$** qui est reversible coïncide avec le potentiel de seconde oxydation de la porphyrine générant le dication porphyrine. Une électropolymerisation à un potentiel au delà de 1,0 V a été ainsi délicate du fait de la formation d’un copolymère à base de porphyrine peu stable. Cependant, le copolymère d'isoporphyrine radicalaire (**poly-ZnT$_2$isoP🔒 / PIM(py)$_6$**) a été obtenu avec succès par balayages itératifs entre -1,1 V à 0,9 V, ce qui a permis d’éviter d’oxydation au niveau de la seconde oxydation irréversible du **PIM(py)$_6$**. Cela a permis de former avec succès des copolymères radicalaires isoporphyrine stables. Les mesures en microscopie électrochimiques à microbalance de quartz a permis de montrer la formation d’un polymère 3D.

La spectroscopie RPE a confirmé la présence du radical porphyrines dans les films à base de **poly-ZnT$_2$isoP🔒 / PIM(py)$_6$**.

Enfin, dans le dernier chapitre V, des ligands du type diphosphine, qui peuvent également agir comme nucléophiles à l’instar de la bipyridine, ont été utilisés avec succès pour former et synthétiser un nouveau type de copolymères d'isoporphyrine radicalaire avec différents types d'espaceurs du type diphosphonium. Les copolymères peuvent être obtenus par exemple par électrooxydation de **ZnT$_2$P** en présence de 1,2-bis(diphénylphosphino)éthène (**poly-ZnT$_2$isoP7🔒**) ou de 1,2-bis (diphénylphosphino)benzène (**poly-ZnT$_2$isoP8🔒**). Une bonne efficacité pour la génération de photocourant sous éclairage visible a été obtenue. Les performances photovoltaïques dépendent du nombre de cycles itératifs utilisés lors de l'électropolymérisation, c’est-à-dire de l’épaisseur du dépôt obtenu. De tels résultats ouvrent une nouvelle voie pour former des copolymères originaux avec de nouvelles propriétés intéressantes pour la photo (électro)catalyse.

D'autres recherches dans le futur seront axées sur l'inclusion de POM dans ce type de copolymères porphyrine / isoporphyrine développés par exemple dans le chapitre III.

En outre, la différence des densités de photocourant pour les copolymères obtenus à partir de **ZnT$_2$P** et de divers types de ligands devait être étudiée plus en détail en fonction par exemple de l’intensité d’absorption de photosensibilisateur ou de l’épaisseur des films.

Appendix of Chapter II: Stable porphyrin/isoporphyrin copolymers prepared with viologen or double viologen spacers

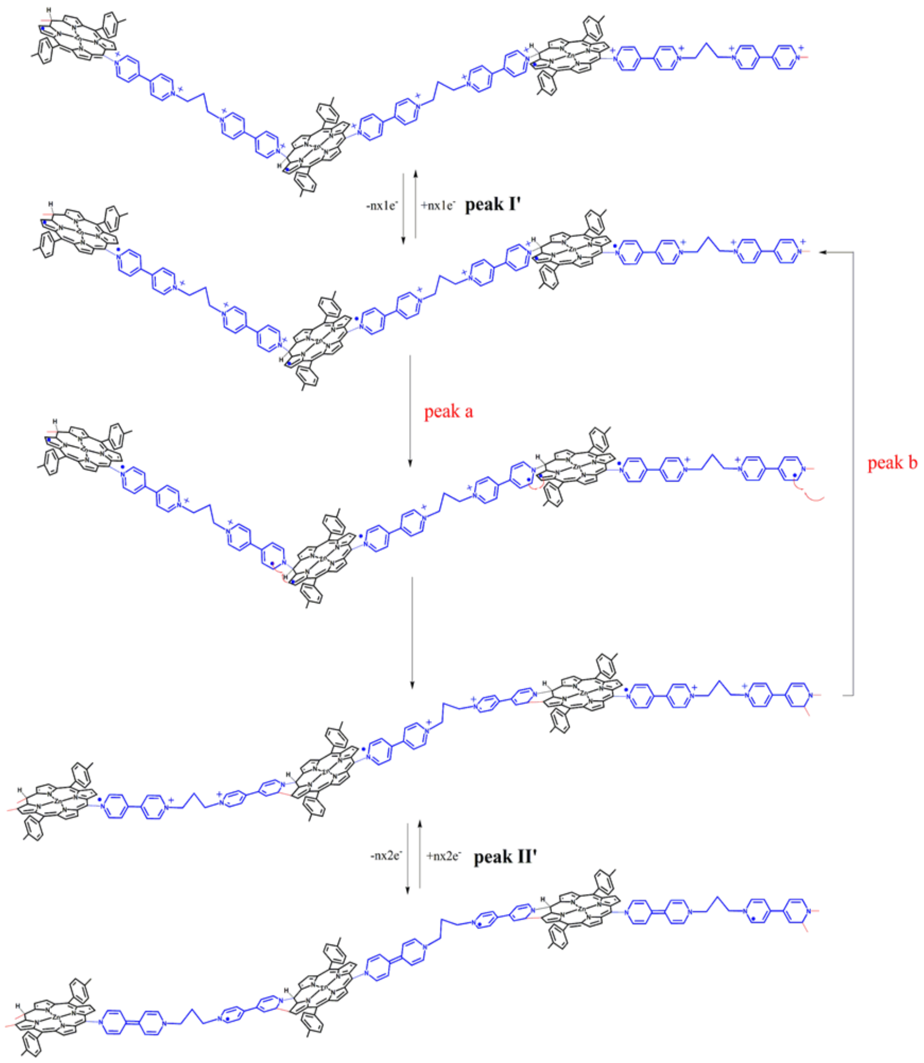

Scheme 2.S1. Proposed mechanism explaining the redox reactivity of **poly-ZnT$_2$isoP$^{\bullet}$**.

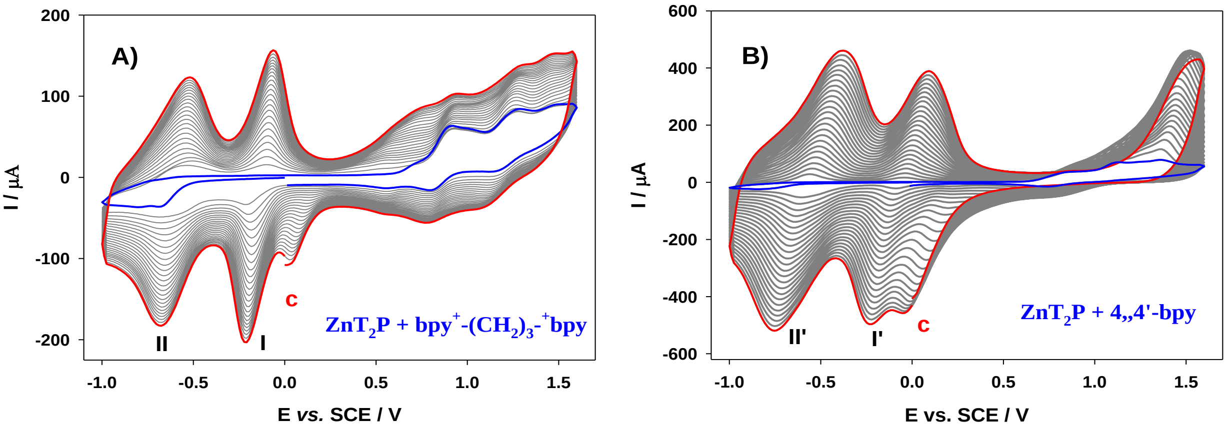

Figure 2.S1. Cyclic voltammograms recorded during 25 iterative scans conducted between −1.0 V and +1.6 V *vs.* SCE in a 1,2-$C_2H_4Cl_2/CH_3CN$ (7/3) solution and NBu_4PF_6 (0.1 mol L^{-1}) of **ZnT$_2$P** (0.25 mmol L^{-1}) in the presence of A) bpy$^+$–(CH$_2$)$_3$–$^+$bpy·2PF$_6^-$ (0.25 mmol L^{-1}) and B) 4,4'-bpy (0.25 mmol L^{-1}). WE: ITO. S = 1 cm^2. v = 100 mV s^{-1}. Blue curve: first scan (n=1). Red curve: final scan (n = 25).

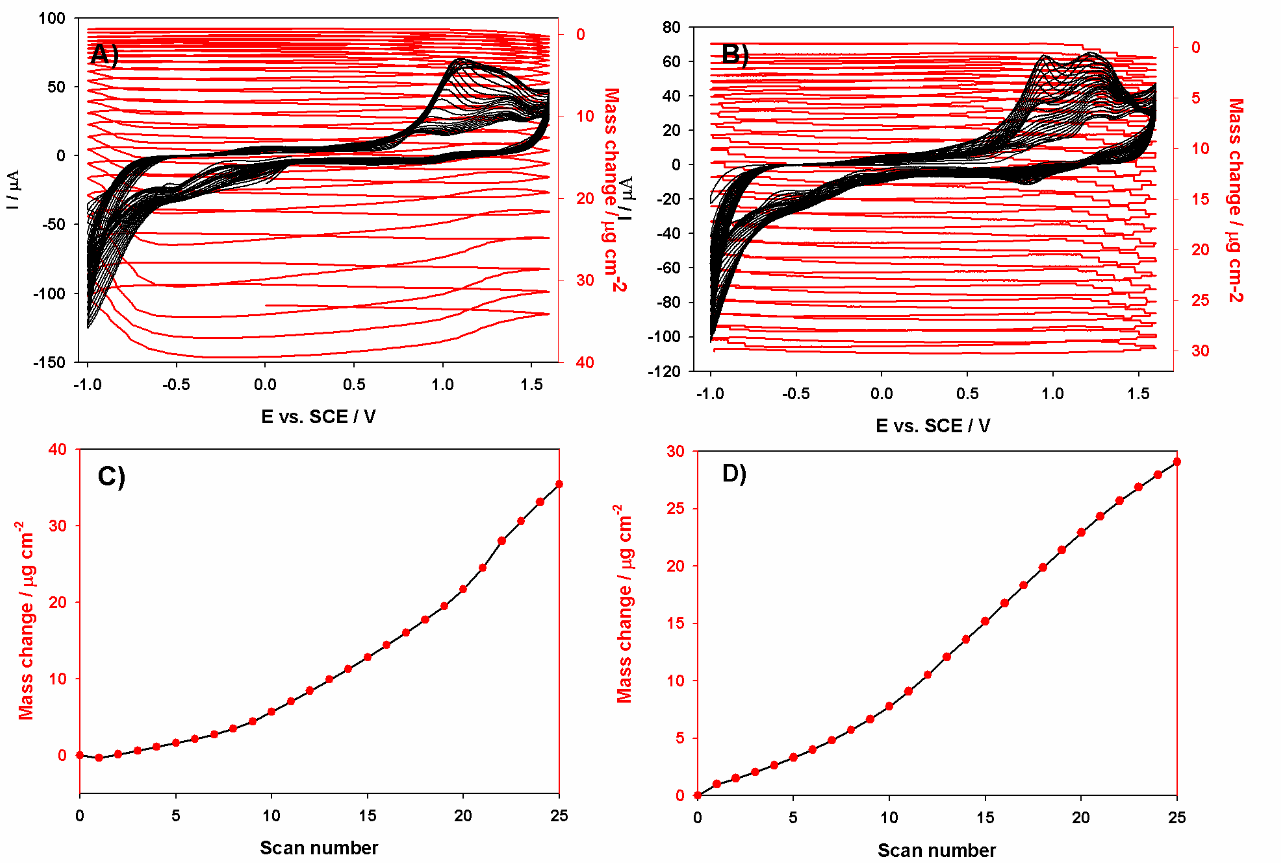

Figure 2.S2. Consecutive cyclic voltammograms (first 25 scans) between -1.0 V and +1.6 V and electrochemical quartz crystal microbalance measurements (*Δm*) during the formation of A) **poly-ZnT$_2$P1$^\bullet$** obtained by the electropolymerization of 0.25 mmol L^{-1} **ZnT$_2$P** with 0.25 mmol L^{-1} bpy$^+$–(CH$_2$)$_3$–$^+$bpy·2PF$_6^-$ and B) **poly-ZnT$_2$P2$^\bullet$** obtainedof ZnT$_2$P with 0.25 mmol L^{-1} 4,4'-bpy in 1,2-$C_2H_4Cl_2$–CH_3CN (7/3) in the presence of 0.1 mol L^{-1} NBu_4PF_6. Working electrode: ITO (A = 0.2 cm^2) deposited on a 9.08 MHz AT-cut quartz crystal. v = 100 mV s^{-1}. Mass change (*Δm*) of the first 25 scans calculated from Sauerbrey's equation *versus* the number of scan n of **poly-ZnT$_2$P$^\bullet$** with 0.25 mmol L^{-1} C) bpy$^+$–(CH$_2$)$_3$–$^+$bpy·2PF$_6^-$ and D) 4,4'-bpy.

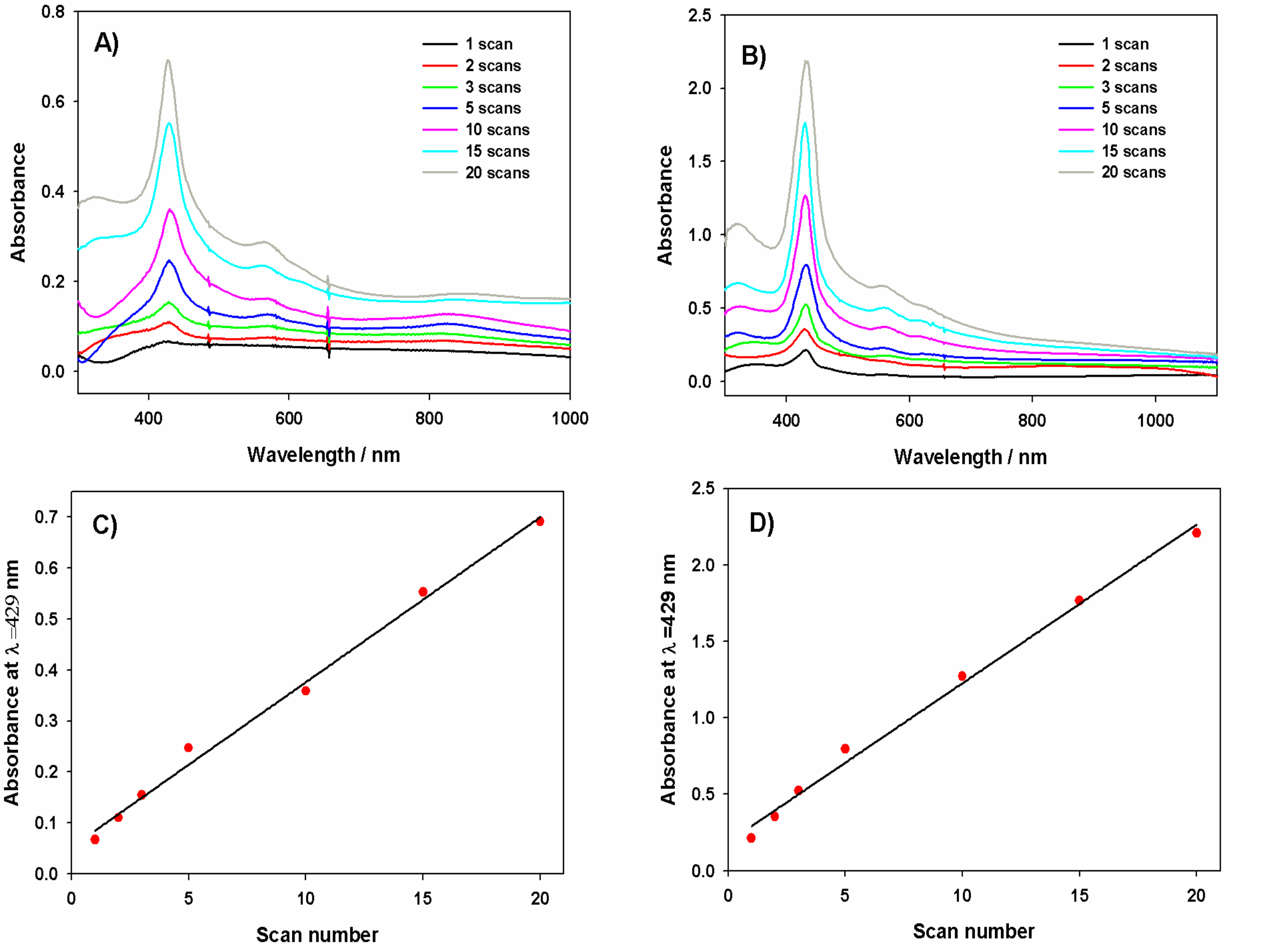

Figure 2.S3. UV-visible-NIR absorption spectra of A) **poly-ZnT$_2$P1$^{\bullet}$** and B) **poly-ZnT$_2$P2$^{\bullet}$** onto ITO with different numbers of iterative scans between -1.0 and +1.6 V *vs.* SCE (v = 100 mV s^{-1}). Only one side is covered by ITO. Plot of the absorbance measured of C) **poly-ZnT$_2$P1$^{\bullet}$** and D) **poly-ZnT$_2$P2$^{\bullet}$** at λ = 430 nm *versus* n the numbers of iterative scans.

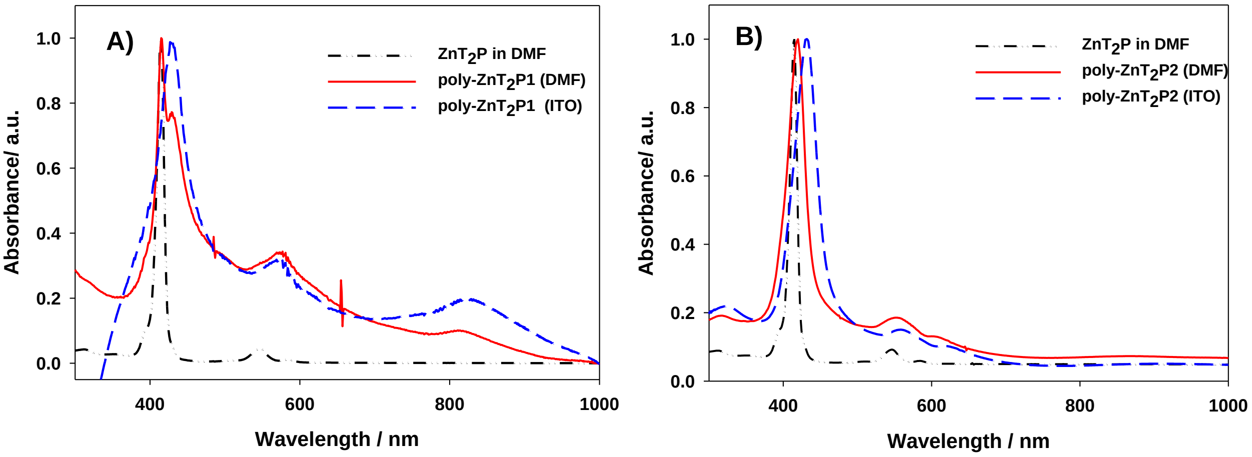

Figure 2.S4. Normalized UV-Vis-NIR spectrawith A) **poly-ZnT$_2$P1$^{\bullet}$**, B) **poly-ZnT$_2$P2$^{\bullet}$** modified obtained with 10 iterative scans between -1.0 and +1.6 V *versus* SCE at v = 100 mV s^{-1} in DMF solution (red solid line), and on the ITO electrode (blue dash line) and **ZnT$_2$P** (dark dash-dotted line) in DMF solution.

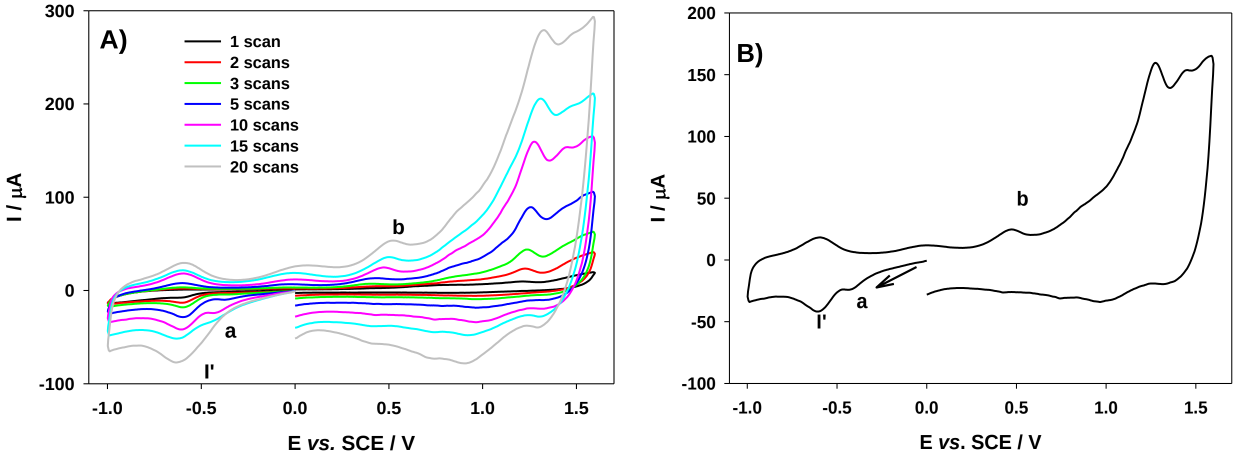

Figure 2.S5. Cyclic voltammograms of **poly-ZnT$_2$P2$^{\bullet}$** obtained with 4,4’-bpy and **ZnT$_2$P** after A) n =1, 2, 3, 5, 10, 15 and 20 scans and B) after 10 scans between -1.0 V and +1.0 V in CH_3CN/1,2-$C_2H_4Cl_2$ (3/7) with 0.1 M NBu_4PF_6. WE: ITO. S = 1 cm^2, v = 100 mV s^{-1}.

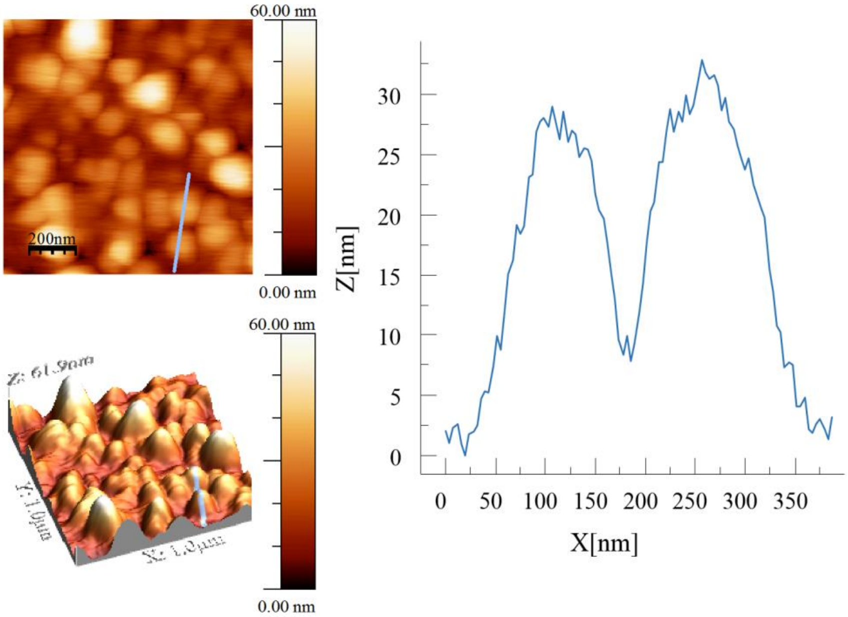

Figure 2.S6. Left: Tapping mode AFM topography of **poly-ZnT$_2$P1** (deposition between -1.0 V and +1.6 V vs. SCE on ITO, n = 20). Right: section analysis of the aggregate marked by a blue and green lines.

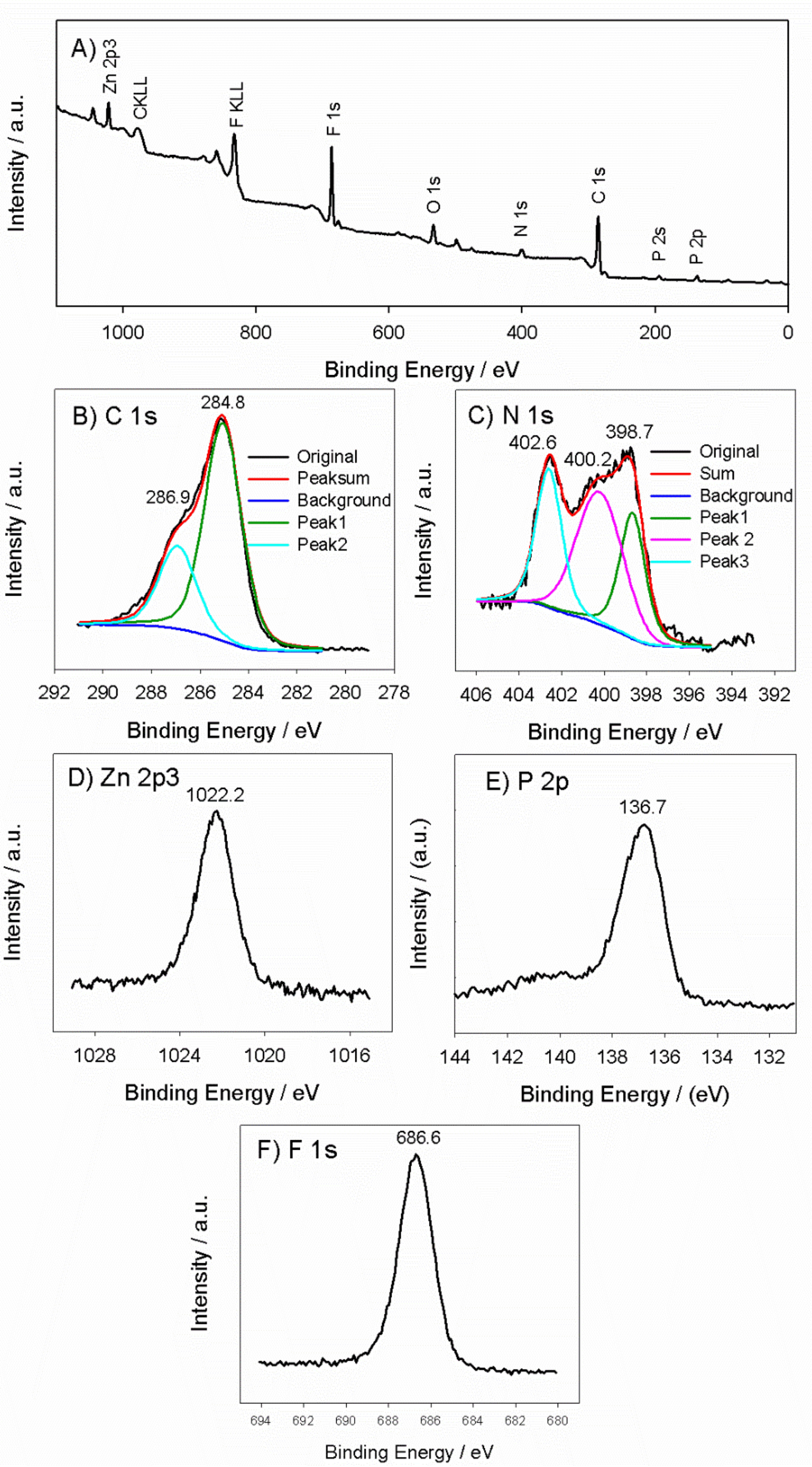

Figure 2.S7. XPS spectra of the modified ITO electrodes **poly-ZnT$_2$P1** on ITO (achieved from ZnT$_2$P and (bpy$^+$-(CH$_2$)$_3$-$^+$bpy).2PF$_6^-$) obtained after 25 iterative scans between -1.0 and 1.0 V *versus* SCE. XPS spectra (A), C 1s (B), N 1s (C), Zn 2p3 (D), P 2p3 (E), F 1s (F).

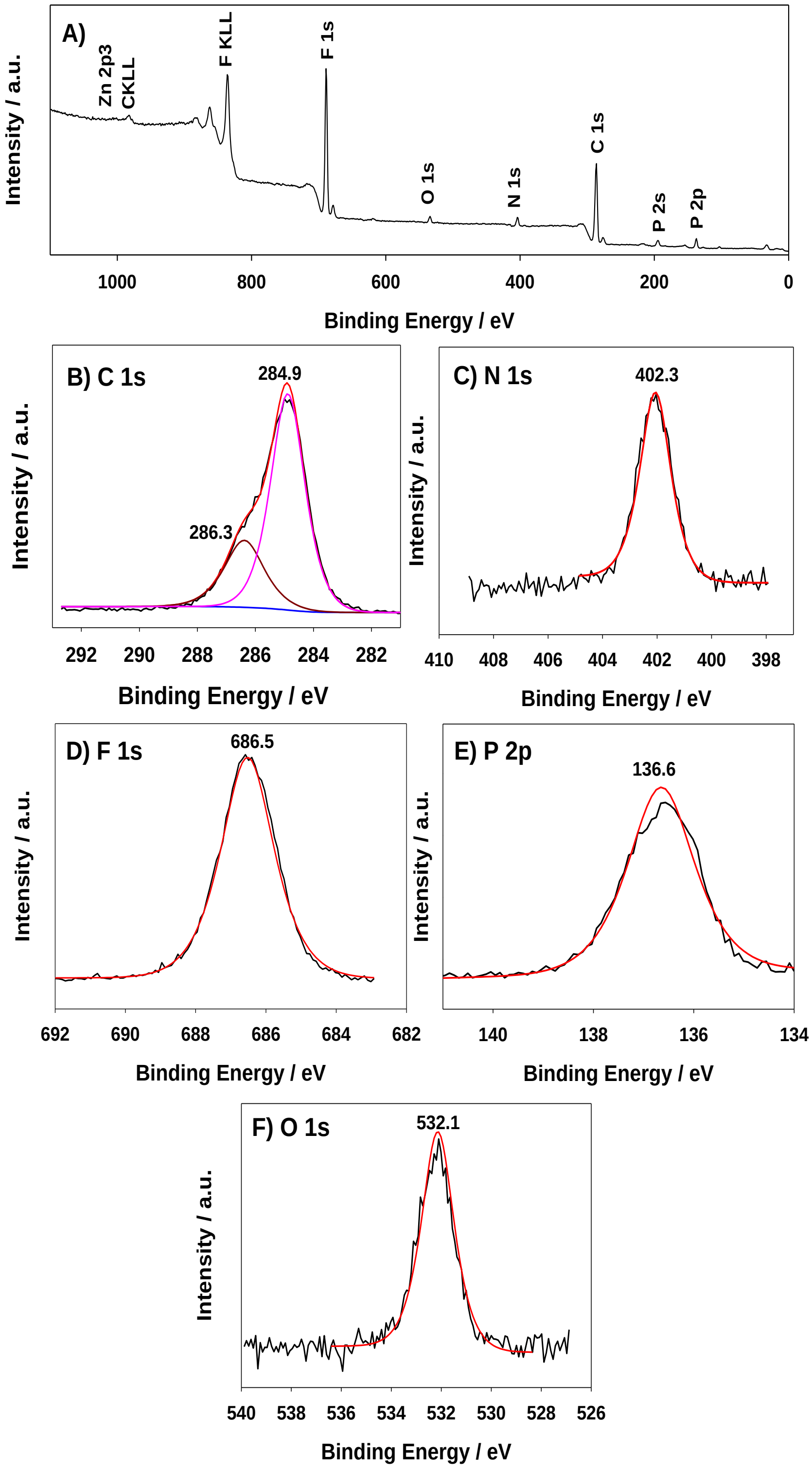

Figure 2.S8. XPS spectra of the modified ITO electrodes **poly-ZnT$_2$isoP2$^\bullet$** on ITO (achieved from ZnT$_2$P and 4,4'-bpy obtained after 25 iterative scans between -1.0 and 1.0 V *versus* SCE. XPS spectra (A), C 1s (B), N 1s (C), F 1s (D), P 2p (E), O 1s (F).

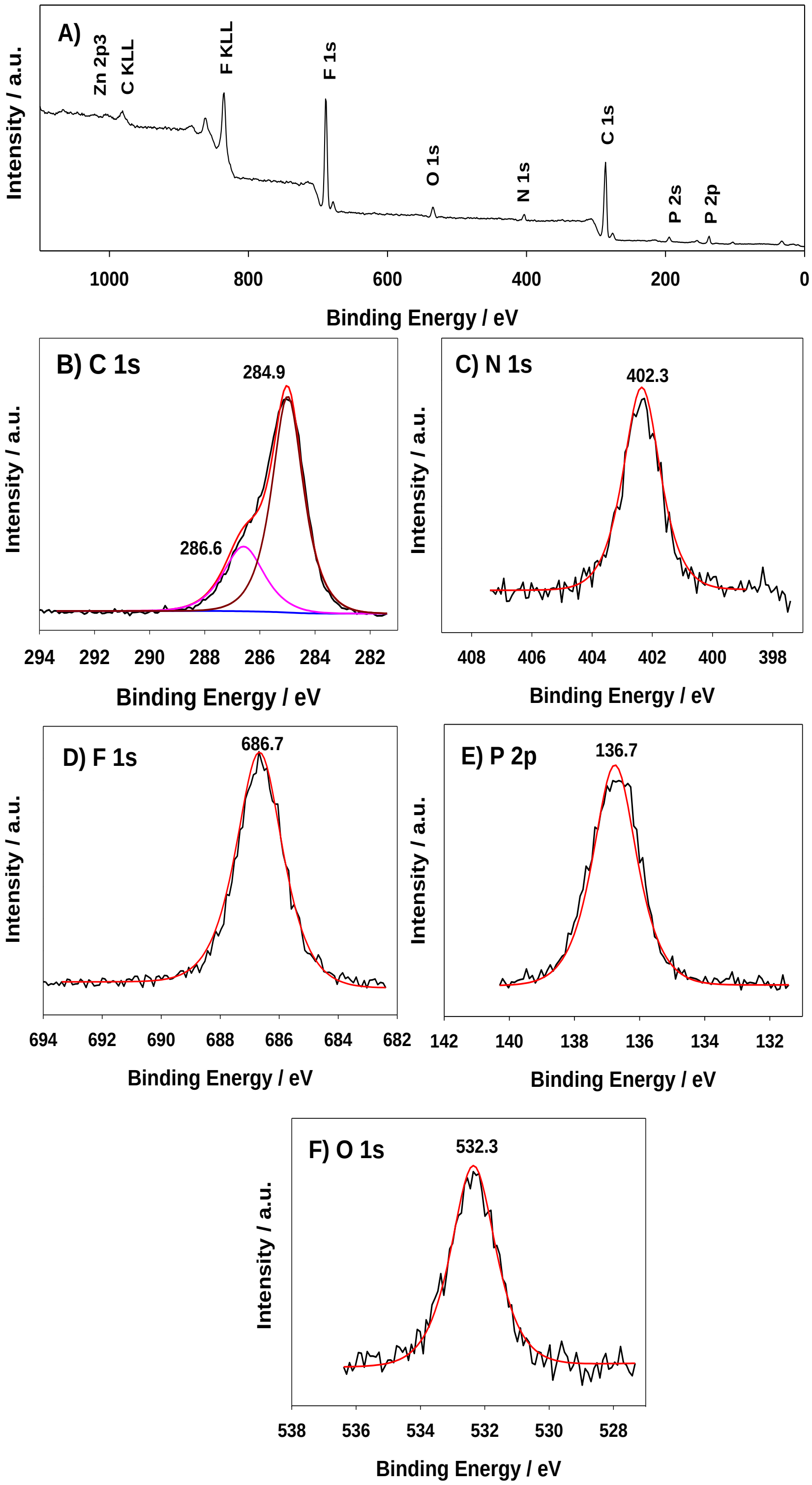

Figure 2.S9. XPS spectra of the modified ITO electrodes **poly-ZnT$_2$P2** on ITO (achieved from ZnT$_2$P and 4,4'-bpy obtained after 25 iterative scans between -1.0 and 1.0 V *versus* SCE. XPS spectra (A), C 1s (B), N 1s (C), F 1s (D), P 2p3 (E), O 1s (F).

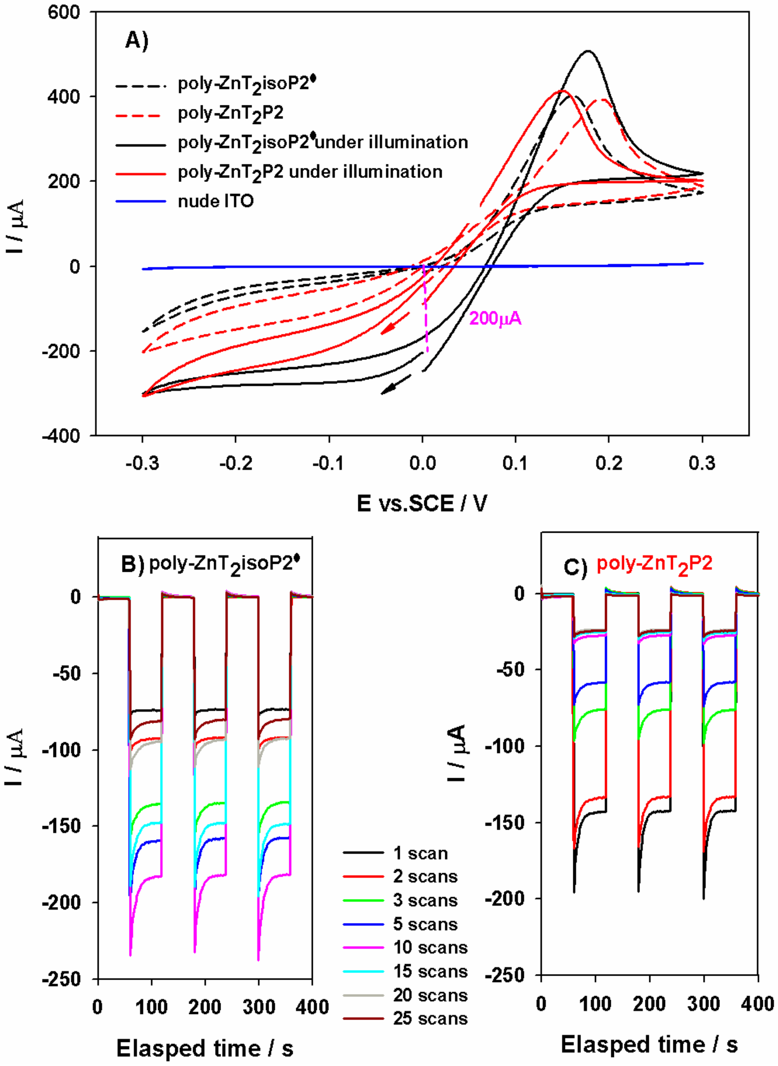

Figure 2.S10. A) Current-potential curves of **poly-ZnT$_2$isoP2$^\bullet$** (obtained with n = 10 iterative scans between -1.0 V and +1.0 V) and **poly-ZnT$_2$P2** (obtained with n = 10 iterative scans between -1.0 V and +1.6 V) thin films on ITO electrodes obtained in 0.5 M I^- / 5 mM I_2 aqueous solution in the dark or under visible illumination. B) and C) Photoelectrochemical response of **poly-ZnT$_2$isoP2$^\bullet$** and **poly-ZnT$_2$P2** films obtained with n = 1, 2, 3, 5, 10, 15, 20 or 25 iterative scans. Measurements has been done under on-off light illumination from a 300 W Xe arc lamp (with $\lambda >$ 385 nm long pass filter) in I_3^- 5 mmol L^{-1} and I^- 0.5 mol L^{-1} aqueous solution. BIAS potential: 0.00 V *vs.* OCP.

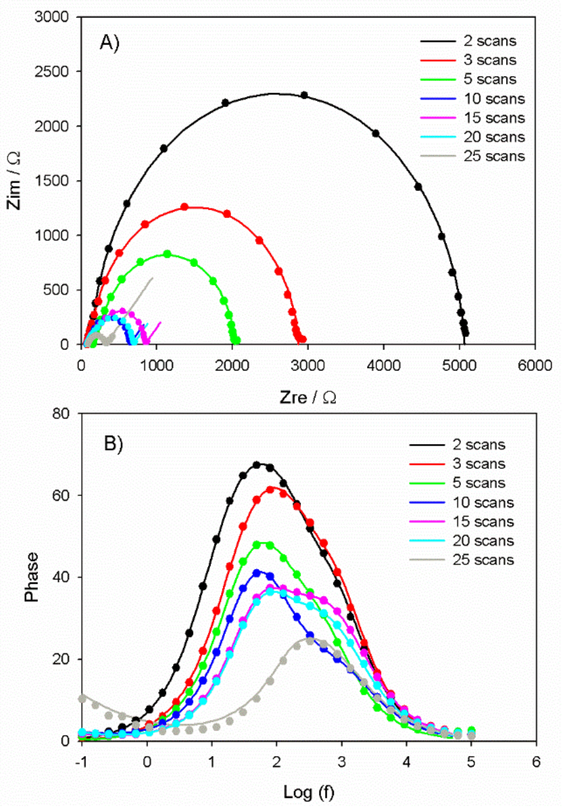

Figure 2.S11. A) ESI Nyquist and B) Bode plots (phase *vs.* frequency (f)) of **poly-ZnT$_2$isoP1$^\bullet$** . Measurements has been done ***in the dark*** and in H_2O containing I_3^- 5 mmol L^{-1} and I^- 0.5 mol L^{-1}. BIAS potential: 0.00 V vs. OCP.

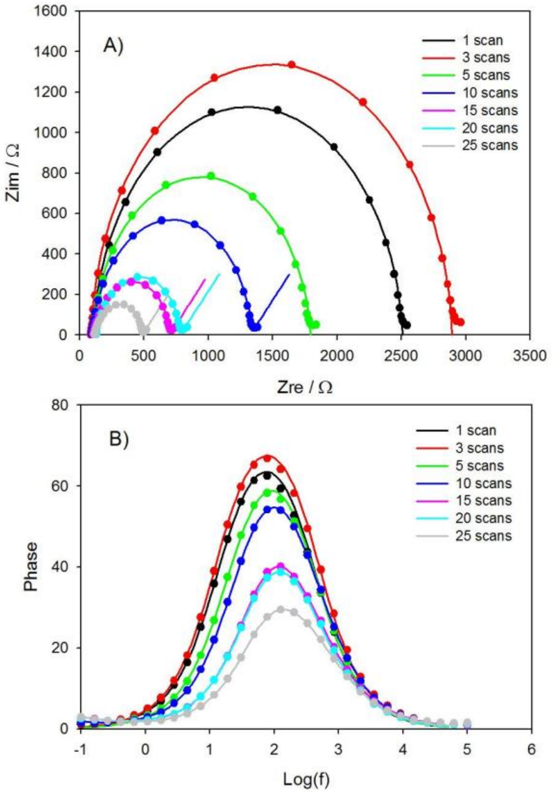

Figure 2.S12. A) ESI Nyquist and B) Bode plots (phase *vs.* frequency (f)) of **poly-ZnT$_2$P1** . Measurements has been done ***in the dark*** and in H_2O containing I_3^- 5 mmol L^{-1} and I^- 0.5 mol L^{-1}. BIAS potential: 0.00 V vs. OCP.

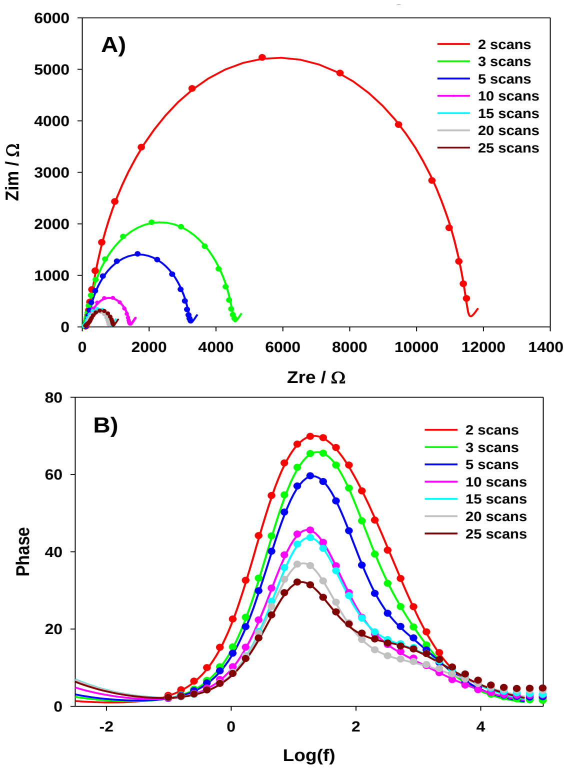

Figure 2.S13. A) ESI Nyquist and B) Bode plots (phase *vs.* frequency (f)) of **poly-ZnT$_2$isoP2$^{\bullet}$** Measurements has been done ***in the dark*** and in H_2O containing I_3^- 5 mmol L^{-1} and I^- 0.5 mol L^{-1}. BIAS potential: 0.00 V vs. OCP.

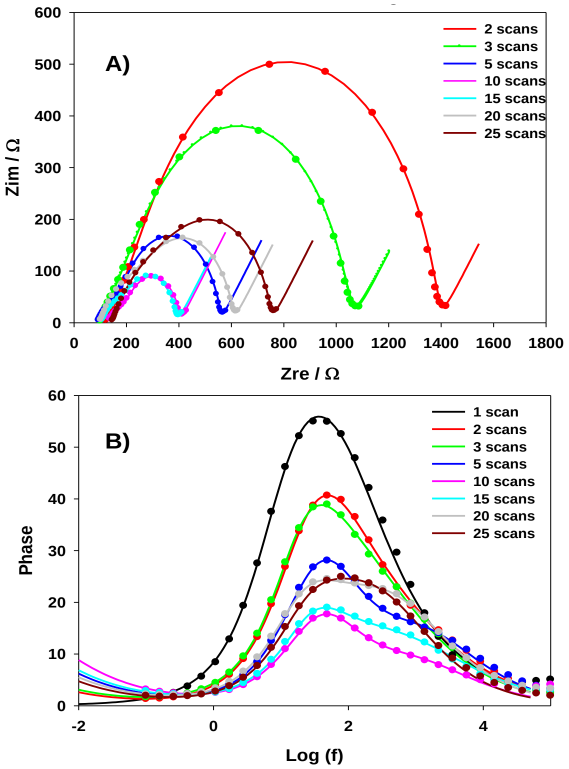

Figure 2.S14. A) ESI Nyquist and B) Bode plots (phase *vs.* frequency (f)) of **poly-ZnT$_2$P2$^{\bullet}$** . Measurements has been done ***in the dark*** and in H_2O containing I_3^- 5 mmol L^{-1} and I^- 0.5 mol L^{-1}. BIAS potential: 0.00 V vs. OCP.

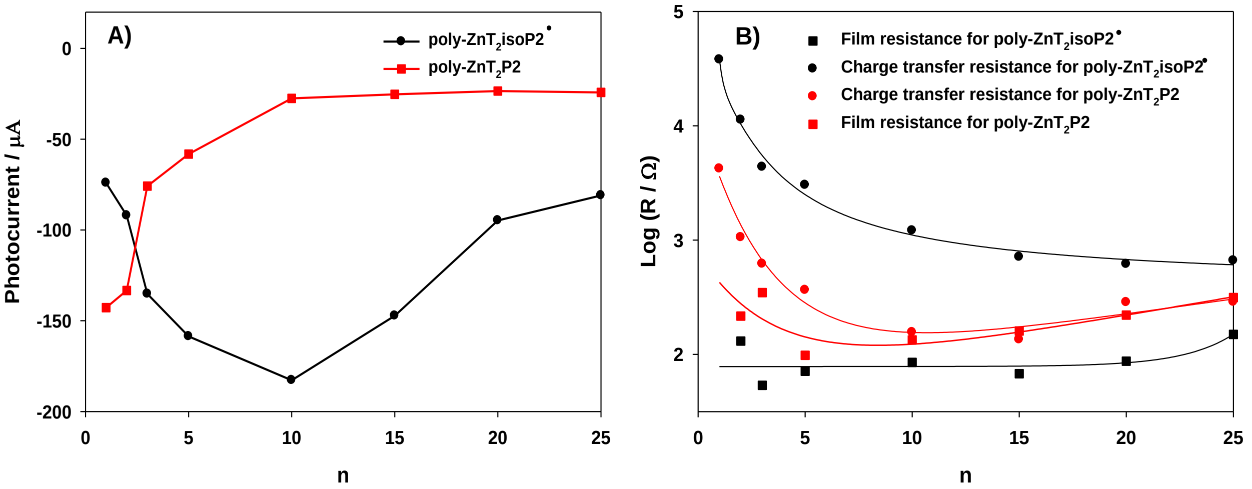

Figure 2.S15. A) Photoelectrochemical response of **poly-ZnT$_2$isoP2$^\bullet$** (black line) and **poly-ZnT$_2$P** (red line) obtained with 4,4'-bpy and **ZnT$_2$P** obtained with n = 1, 2, 3, 5, 10, 15 and 20 iterative scans. B) Plot of the Log(R) versus n (number of iterative scan,v = 100 mV s^{-1}, between -1.0 V and +1.0 V for **poly-ZnT$_2$isoP2$^\bullet$** and between -1.0 V and +1.6 V for **poly-ZnT$_2$P2** Measurements has been done in H_2O under one off light illumination from a 300W Xe arc lamp (with λ > 385 nm long pass filter) in containing I_3^- 5 mmol L^{-1} and I^- 0.5 mol L^{-1}. BIAS potential: 0.00 V *vs.* OCP.

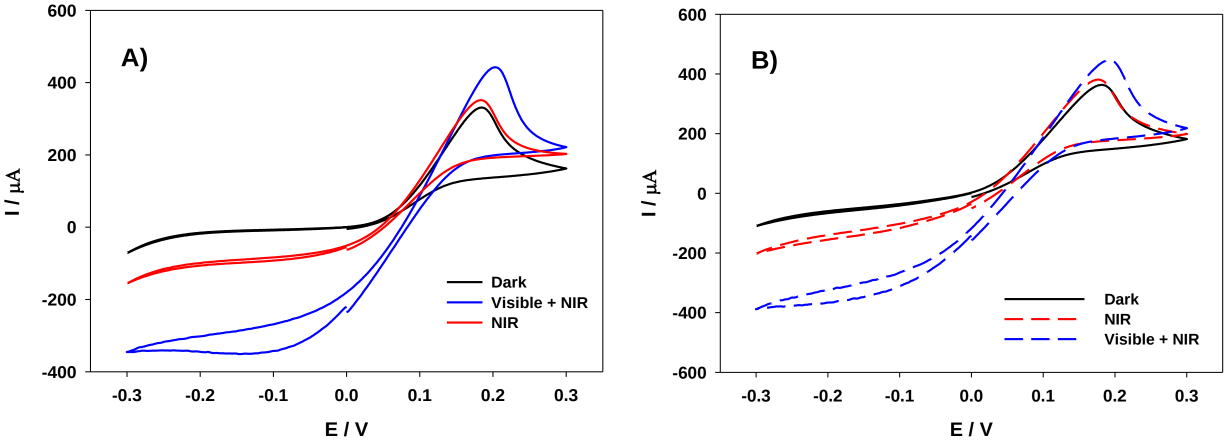

Figure 2.S16. Current-potential curves of A) **poly-ZnT$_2$isoP1$^\bullet$** and B) **poly-ZnT$_2$isoP2$^\bullet$** (obtained with n = 10 iterative scans between -1.0 V and +1.0 V) under one off light or near-infrad light or visible-NIR light illumination.

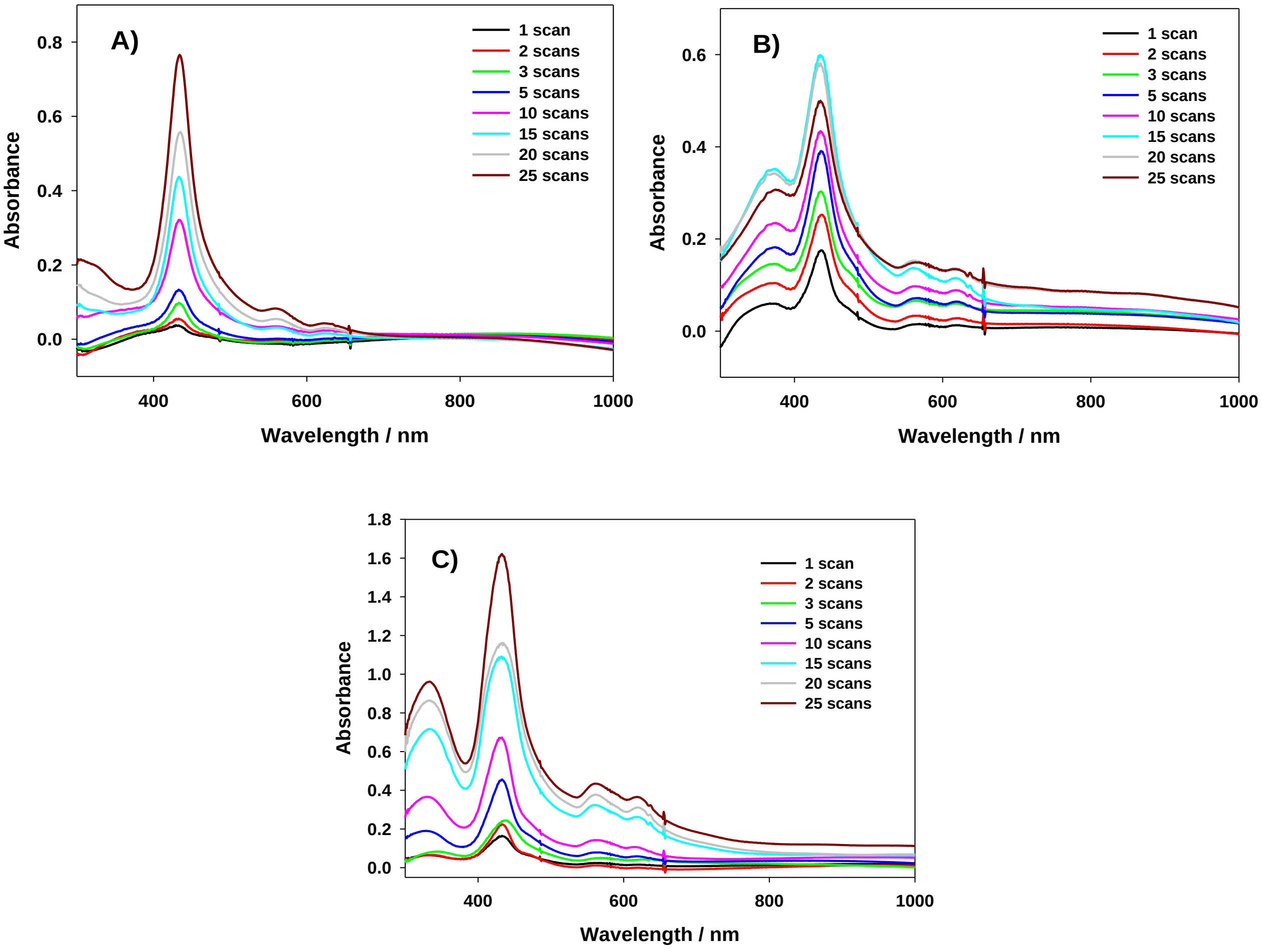

Figure 2.S17. UV-visible-NIR absorption spectra of copolymer **poly-ZnT$_2$P3, poly-ZnT$_2$P4** and **poly-ZnT$_2$P5** prepared between -1.0 V and 1.0 V in the presence of **ZnT$_2$P** (0.25 mmol L^{-1}) and (A) py-C≡C-py (0.25 mmol L^{-1}) (B) py-Ph-py (0.25 mmol L^{-1}) and (C) py-Ph-Ph-py (0.25 mmol L^{-1}) respectively onto ITO with different numbers of iterative scans. Only one side is covered by ITO.

Appendix of Chapter III: Stable porphyrin/isoporphyrin copolymers prepared with bipyridyl ligands

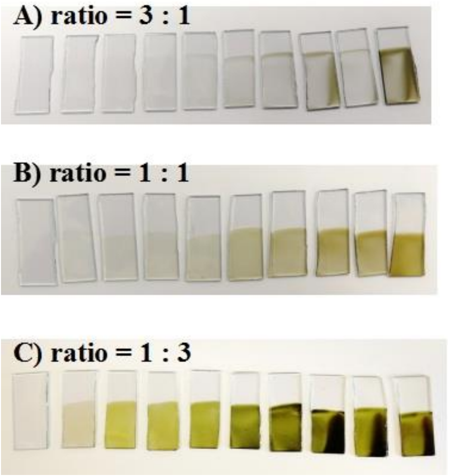

Figure 3.S1. The films obtained by electropolymerization with different ratio of concentration between **ZnT$_2$P** and py-C≡C-Ph-C≡C-py (3:1, 1:1, 1:3) under various scan numbers (0, 1, 2, 3, 5, 10, 15, 20, 25, 30 scans) between -1.1 V and 1.6 V. Scan rate = 100 mV s^{-1}.

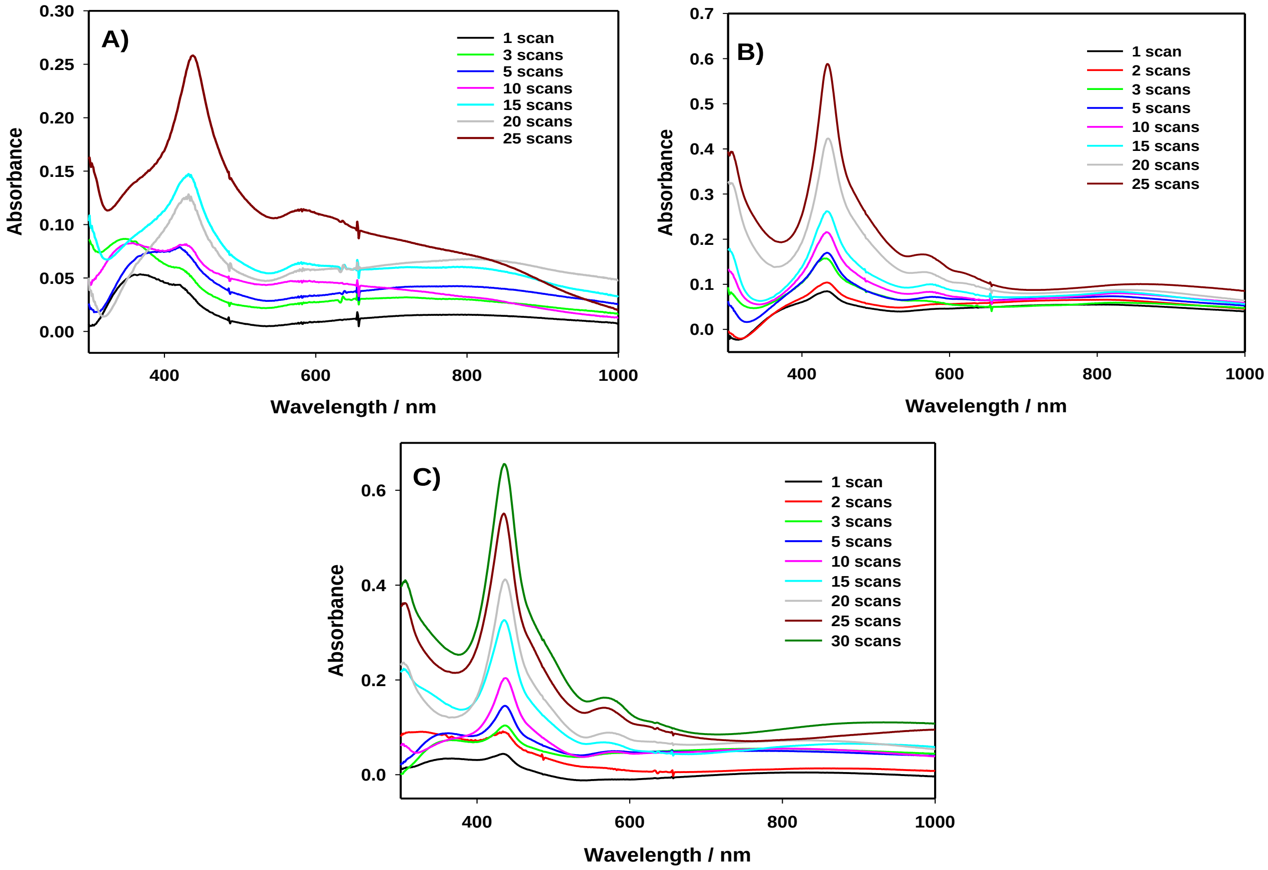

Figure 3.S2. UV-vis-NIR spectrum of porphyrin copolymers films obtained with different scan numbers of 0.25 mmol L^{-1} **ZnT$_2$P** in the presence of A) 0.08 mmol L^{-1} py-C≡C-Ph-C≡C-py (ratio 1:3), B) 0.25 mmol L^{-1} py-C≡C-Ph-C≡C-py (ratio 1:1), C) 0.75 mmol L^{-1} py-C≡C-Ph-C≡C-py (ratio 3:1) between -1.1 V and 1.6 V.

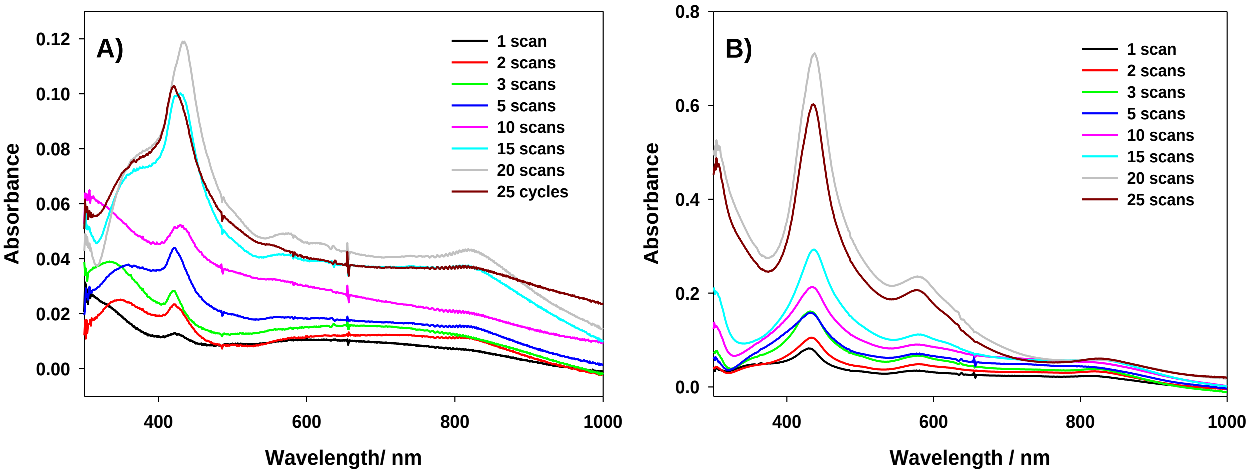

Figure 3.S3. UV-vis-NIR spectrum of porphyrin copolymers films obtained with different scan numbers of 0.75 mmol L^{-1} **ZnT$_2$P** in the presence of A) 0.25 mmol L^{-1} py-C≡C-Ph–C≡C-py (ratio 3:1). B) 0.75 mmol L^{-1} py-C≡C-Ph–C≡C-py (ratio 1:1) between -1.1 V and 1.6 V. Scan rate = 100 mV s^{-1}.

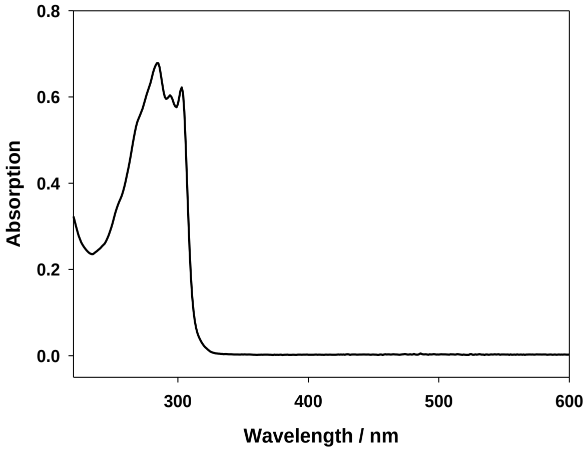

Figure 3.S4. UV-vis-NIR spectrum of 0.15 mmol L^{-1} py-C≡C-Ph–C≡C-py in 1,2-EtCl$_2$/CH$_3$CN (7/3).

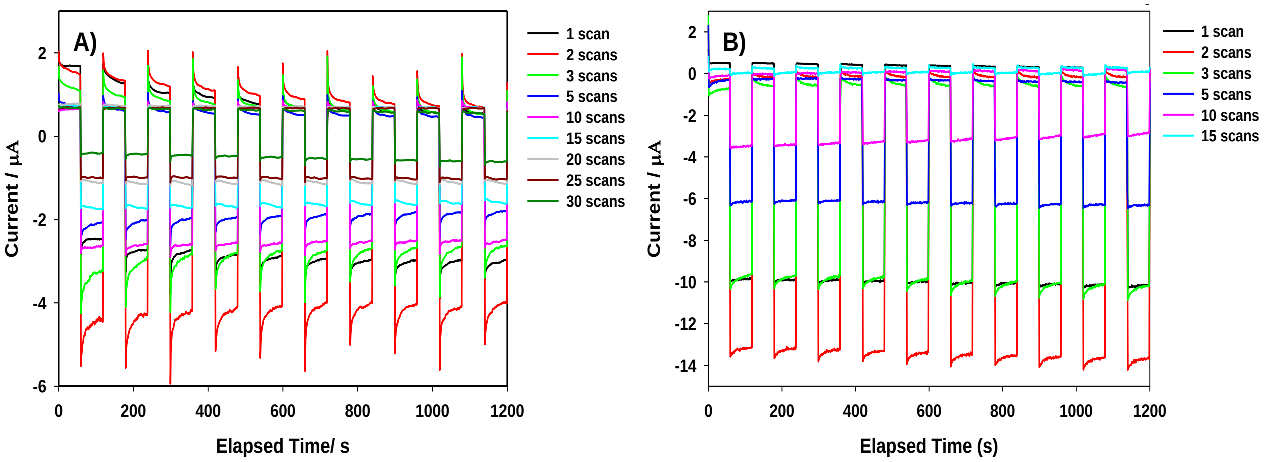

Figure 3.S5. Photoelectrochemical response of **poly-ZnT$_2$P6** films obtained from -1.1 V and 1.6 V (scan rate = 100 mV/s) under on-off light illumination from a 300 W Xe arc lamp (with λ > 385 nm long pass filter) in A) I$_3^-$ 0.25 mmol L^{-1} and I$^-$ 0.5 mol L^{-1} aqueous solution and B) I$_3^-$ 10 mmol L^{-1} and I$^-$ 0.5 mol L^{-1} aqueous solution. BIAS potential: 0.00 V *vs.* OCP.

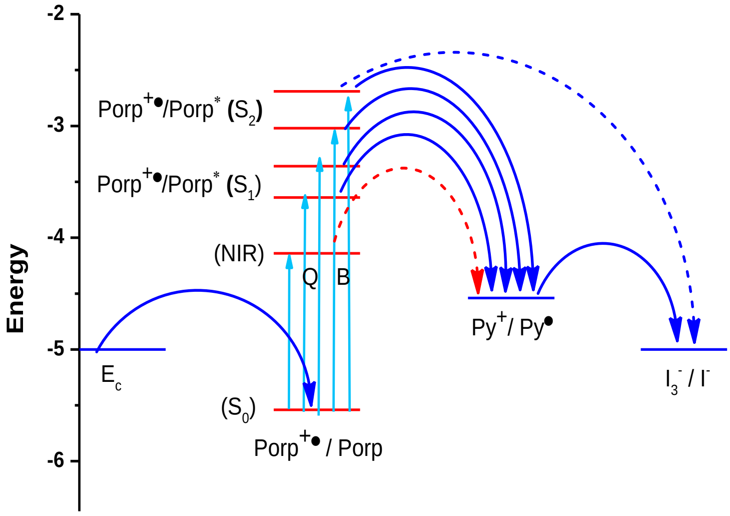

Figure 3.S6. Schematic illustration of the energy level diagram for **poly-ZnT₂P6** obtained from -1.1 V and 1.6 V showing electron transfer processes in H_2O containing I_3^- 5 mmol L^{-1} and I^- 0.5 mol L^{-1} (Py^+ = pyridinium, Porp = porphyrin).

Appendix of Chapter IV: Stable isoporphyrin copolymer prepared with pyridine end decorated molybdenum(II) halide cluster

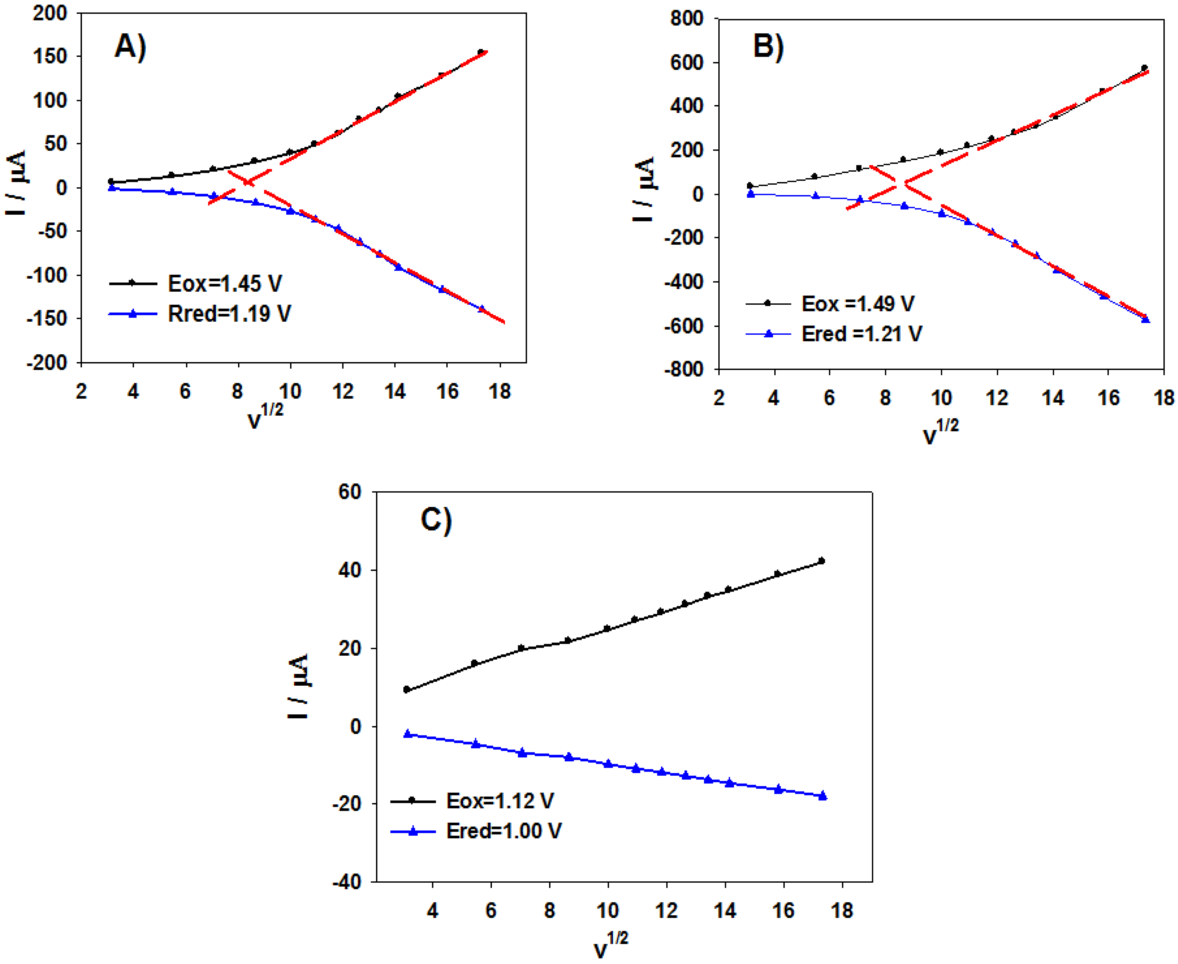

Figure 4.S1. The relationship between current of the first wave of oxidation I, I’ or I’’ on A) GCE electrode, B) Pt electrode, C) ITO electrode and square root of scan rate.

Table 4.S1. Theoretically value of mass change for **poly-$ZnT_2isoP^{\bullet}$/PIM(py)$_6$** obtained **at 20 scans** (EQCM: **Δm = 16.54 µg. cm^{-2}**) ($Q_{red\text{-}cv}$ = 8.15*10^{-4}C)

Structure	Ratio	Molecular Mass	n	Δm (µg.cm^{-2})
1D	**1PIM + 1 porphyrin + 2TBA + 2PF_6^- - 1H^+ (2325 + 552 + 243*2 + 144*2-1)** **(2 porphyrin-py$^+$)**	**3650**	**2**	**15.4**
1D and coordination	1PIM + 2 porphyrins + 2TBAPF_6^- - 1H^+ (2 porphyrin-py$^+$ + 1 py-Zn coordination)	4202	2	18.0
3D	1PIM + 3 porphyrins + 2TBA+6PF_6^- - 3H^+ (6 porphyrin-py$^+$)	5328	6	7.5
	1PIM + 3 porphyrins + 2TBA+4PF_6^- - 2H^+ (4 porphyrin-py$^+$ + 1 py-Zn coordination)	5041	4	10.6
	1PIM + 2 porphyrins + 2TBA+4PF_6^- - 2H^+ (4 porphyrin-py$^+$)	4489	4	9.4

Δm = MQ/nFA
M is the molecular mass of repeat units (g/mol)
Q is the charge (C) calculated from the CV (integration of the pyridinium reduction waves of the copolymer films obtained from -1.1 V to 0.9 V).
n = electron number corresponding to the reduction of the py$^+$ groups.
F = Faraday's constant 96485 C/ mol.
A = electrode surface (1 cm^2).

Table 4.S2. Theoretically value of mass change for **poly-ZnT$_2$isoP$^{\bullet}$/PIM(py)$_6$** obtained **at 3 scans** (EQCM: **Δm = 2.79 µg.cm^{-2}**) ($Q_{red\text{-}cv}$ = 3.04*10^{-4}C)

Structure	Ratio	Molecular Mass	n	Δm (µg.cm^{-2})
1D	1PIM + 1 porphyrin + 2TBA + 2PF$_6^-$ - 1H$^+$ (2325 + 552 + 243*2 + 144*2-1) (2 porphyrin-py$^+$)	3650	2	5.8
1D and coordination	1PIM + 2 porphyrins + 2TBAPF$_6^-$ - 1H$^+$ (2 porphyrin-py$^+$ **+ 1 py-Zn coordination)**	4202	2	6.7
3D	**1PIM + 3 porphyrins + 2TBA+6PF$_6^-$ - 3H$^+$** **(6 porphyrin-py$^+$)**	**5328**	**6**	**2.8**
	1PIM + 3 porphyrins + 2TBA+4PF$_6^-$ - 2H$^+$ (4 porphyrin-py$^+$ + 1 py-Zn coordination)	5041	4	4.0
	1PIM + 2 porphyrins + 2TBA+4PF$_6^-$ - 2H$^+$ (4 porphyrin-py$^+$)	4489	4	3.5

$\Delta m = MQ/nFA$
M is the molecular mass of repeat units (g/mol)
Q is the charge (C) calculated from the CV (integration of the pyridinium reduction waves of the copolymer films obtained from -1.1 V to 0.9 V).
n = electron number corresponding to the reduction of the py$^+$ groups.
F = Faraday's constant 96485 C/ mol.
A = electrode surface (1 cm^2).

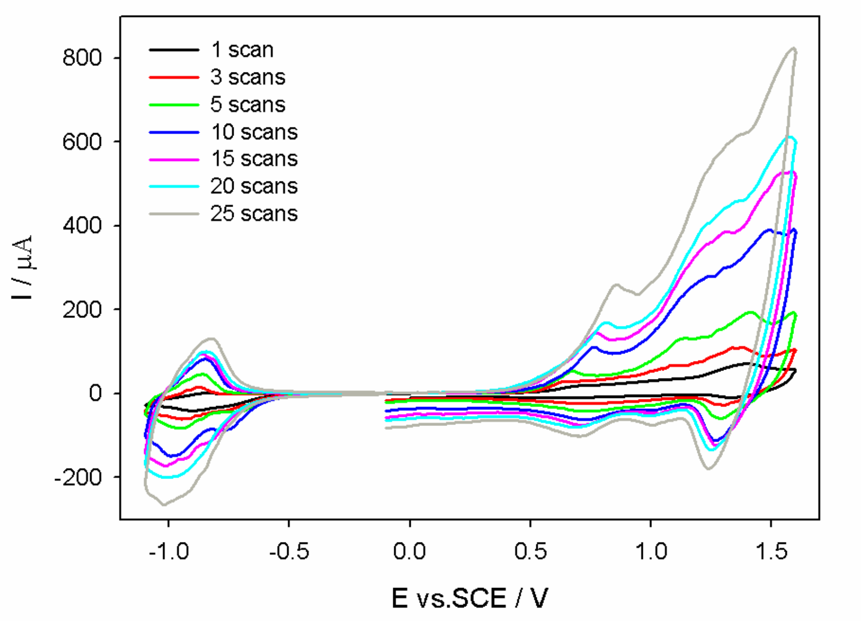

Figure 4.S2. Cyclic voltammograms of **poly-ZnT$_2$isoP$^{\bullet}$/PIM(py)$_6$** obtained with **PIM(py)$_6$** and **ZnT$_2$P** after n = 1, 2, 3, 5, 10, 15 and 20 scans between -1.1 V and +0.9 V in $CH_3CN/1,2\text{-}C_2H_4Cl_2$ (3/7) scan from -1.1 V to 1.6 V with 0.1 M NBu_4PF_6. WE: ITO. S = 1 cm^2, v = 100 mV s^{-1}.

Appendix of Chapter V: Stable isoporphyrin copolymer prepared with di(phenylphosphane)

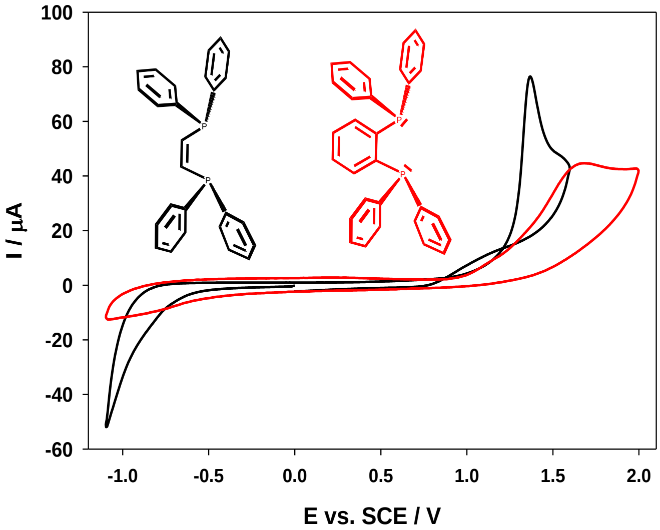

Figure 5.S1. Cyclic voltammograms of 0.25 mmol L^{-1} 1,2-bis(diphenylphosphino)ethene and 1,2-bis(diphenylphosphino)benzene in $CH_3CN/1,2-C_2H_4Cl_2$ (3/7) with 0.1 M $TBAPF_6$. WE: ITO. S = 1 cm^2. v = 100 mV.s^{-1}.

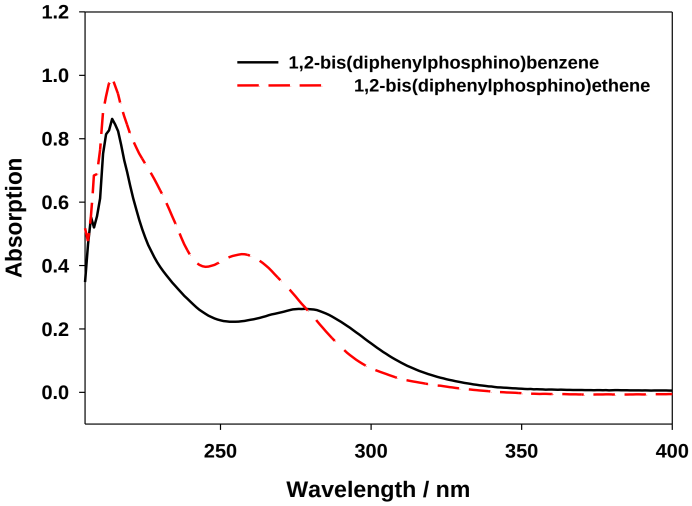

Figure 5.S2. UV-vis-NIR spectrum of 0.22 mmol L^{-1} 1,2-bis(diphenylphosphino)ethene and 0.15 mmol L^{-1} 1,2-bis(diphenylphosphino)benzene in CH_2Cl_2.

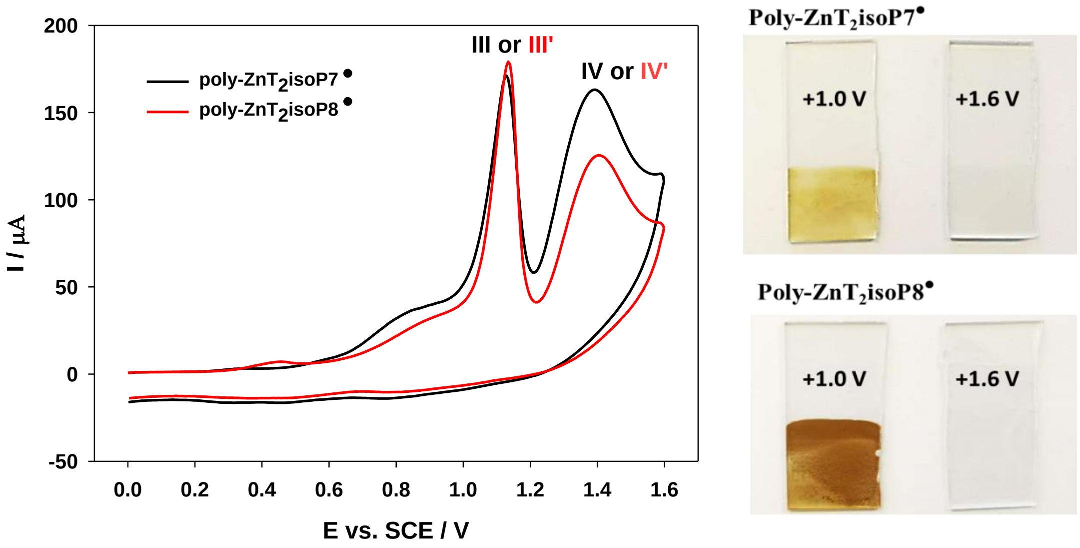

Figure 5.S3. Left) Cyclic voltammograms of **poly-ZnT$_2$isoP7$^\bullet$** and **poly-ZnT$_2$isoP8$^\bullet$** obtained after n = 10 scans using iterative scan between -1.1 V and +1.0 V in $CH_3CN/1,2-C_2H_4Cl_2$ (3/7) with 0.1 M $TBAPF_6$. WE: ITO. S = 1 cm^2. ν = 100 mV.s^{-1}. Right) Figure of **poly-ZnT$_2$isoP7$^\bullet$** and **poly-ZnT$_2$isoP8$^\bullet$** copolymer films deposited at 25 scans between -1.1 and 1.0 V on the ITO and after oxidized to 1.6 V on the ITO.

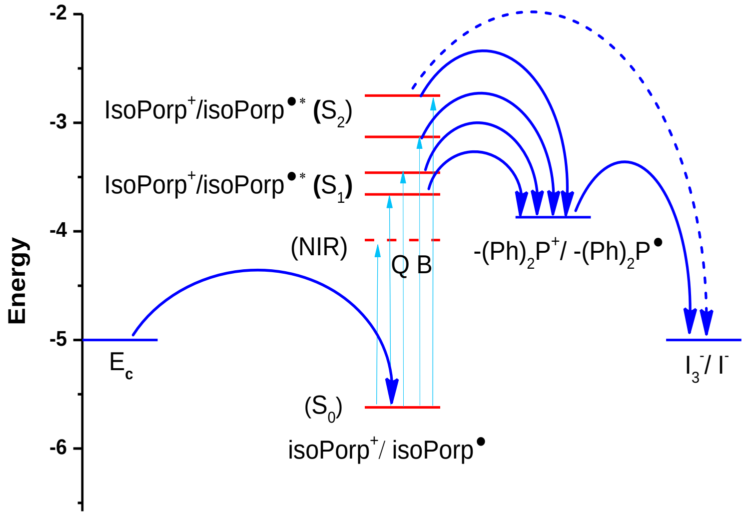

Figure 5.S4 Schematic illustration of the energy level diagram for **poly-ZnT$_2$isoP8$^\bullet$** showing electron transfer processes in H_2O containing I_3^- 5 mmol L^{-1} and I^- 0.5 mol L^{-1} ($-(Ph)_2P^+$ = di(phenylphosphane), Porp = porphyrin).

Table 5.S1. Theoretically value of mass change for **poly-ZnT$_2$isoP7$^\bullet$** and **poly-ZnT$_2$isoP8$^\bullet$**.

Repeat unit	Molecular Mass (g/mol)	Δm / Δm$_{EQCM}$ 3 scans (μg/cm^2)	Δm / Δm$_{EQCM}$ 5 scans (μg/cm^2)	Δm / Δm$_{EQCM}$ 10 scans (μg/cm^2)	Δm / Δm$_{EQCM}$ 20 scans (μg/cm^2)
isoZnT$_2$P-$^+$PPh$_2$-C=C-PPh$_2^+$ • 2PF$_6^-$	1236	1.18 / 0.77	1.86 / 1.74	3.54 / 3.69	7.26 / 6.66
isoZnT$_2$P-$^+$PPh$_2$-Ph-PPh$_2^+$ • 2PF$_6^-$	1286	1.72 / 1.76	2.70 / 3.15	5.00 / 5.82	9.49 / 9.18

Δm = MQ/nFA
M is the molecular mass of repeat units (g/mol)
Q is the charge (C) calculated from the reduction waves of CV of copolymer films obtained from -1.10 V to 1.0 V.
n = electron number 3
F = Faraday's constant 96485 C/ mol
A = electrode surface (1 cm^2)

The Q value comes from the integration of the wave corresponding to the oxidation process +0.5 V to +1.0 V during electropolymerization. The formation of the monosubstituted intermediate ZnT$_2$P-$^+$PPh$_2$-C=C-PPh$_2^+$ obtained from **ZnT$_2$P** and PPh$_2$-C=C-PPh$_2$ needs the exchanged of two electron as well as the release of one proton H$^+$. Finally, the formation of isoporphyrin radical copolymer need one more electron per isoporphyrin unit.

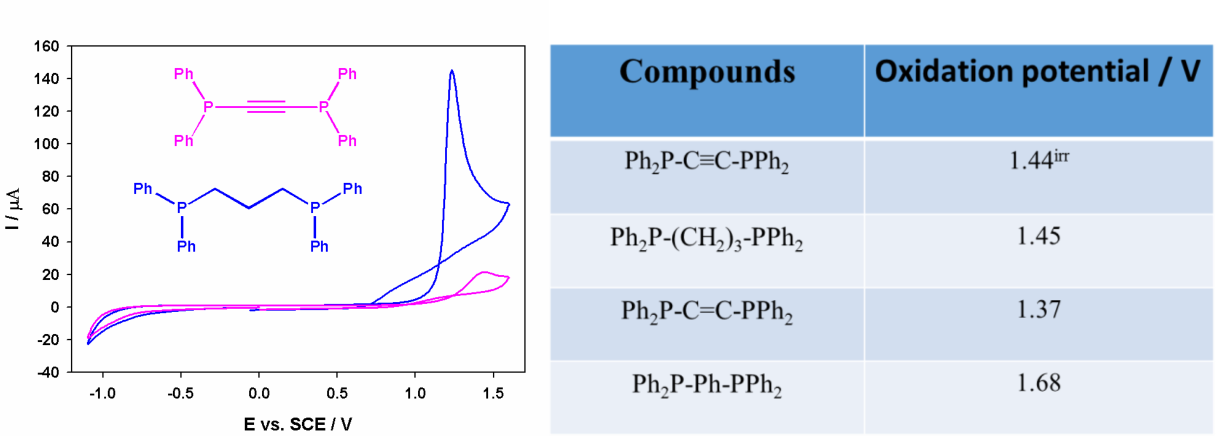

Compounds	Oxidation potential / V
Ph$_2$P-C≡C-PPh$_2$	1.44^{irr}
Ph$_2$P-(CH$_2$)$_3$-PPh$_2$	1.45
Ph$_2$P-C=C-PPh$_2$	1.37
Ph$_2$P-Ph-PPh$_2$	1.68

Figure 5.S5. Left : Cyclic voltammograms of 0.25 mmol L^{-1} 1,2-bis(diphenylphosphino)ethyne and 1,3-bis(diphenylphosphino)propane in CH$_3$CN/1,2-C$_2$H$_4$Cl$_2$ (3/7) with 0.1 M TBAPF$_6$. WE: ITO. S = 1 cm^2. v = 100 mV s^{-1}. Right: Oxidation potential of 0.25 mmol L^{-1} different diphosphane in CH$_3$CN/1,2-C$_2$H$_4$Cl$_2$ (3/7) with 0.1 M TBAPF$_6$.

Representation of the ligands and copolymers studied

Chapter II

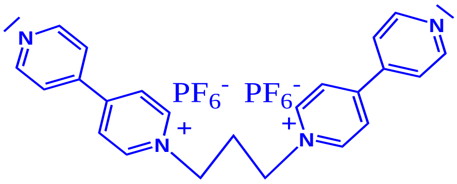

bpy$^+$-(CH$_2$)$_3$-bpy$^+$ 2PF$_6^-$

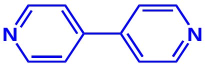

4,4'-bipyridine

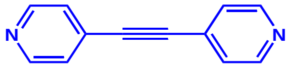

1,2-di(pyridin-4-yl)ethyne

1,4-di(pyridin-4-yl)benzene

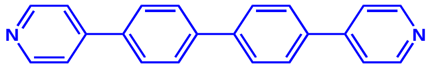

4,4'-di(pyridin-4-yl)-1,1'-biphenyl

Chapter III

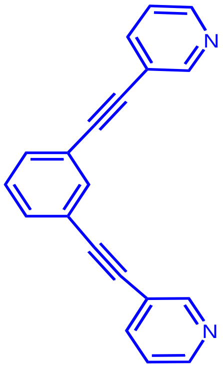

1,3-bis(pyridin-3-ylethynyl)benzene

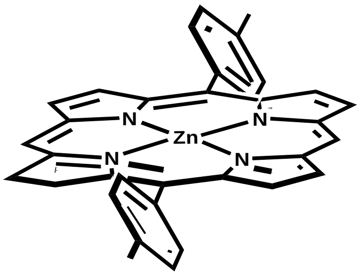

ZnT$_2$P

Chapter IV

Chapter V

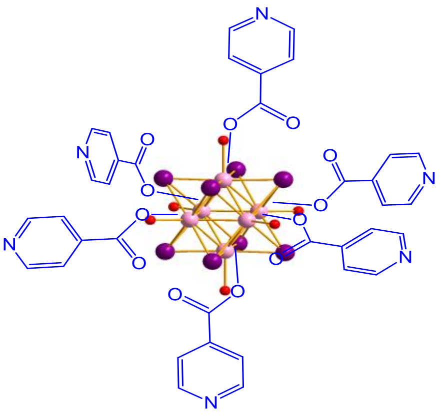

PIM

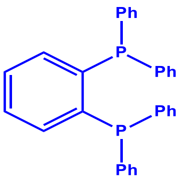

1,2-bis(diphenylphosphino)benzene

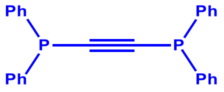

1,2-bis(diphenylphosphino)ethyne

1,3-bis(diphenylphosphino)propane

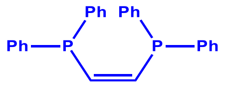

(*Z*)-1,2-bis(diphenylphosphino)ethene

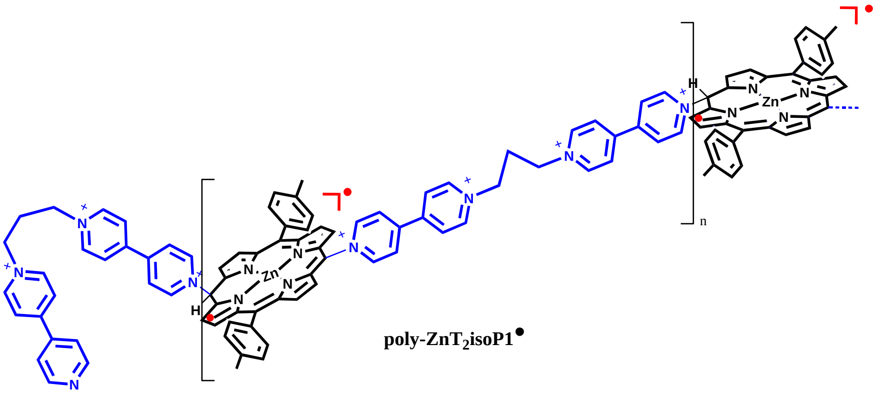

poly-ZnT$_2$isoP1$^\bullet$

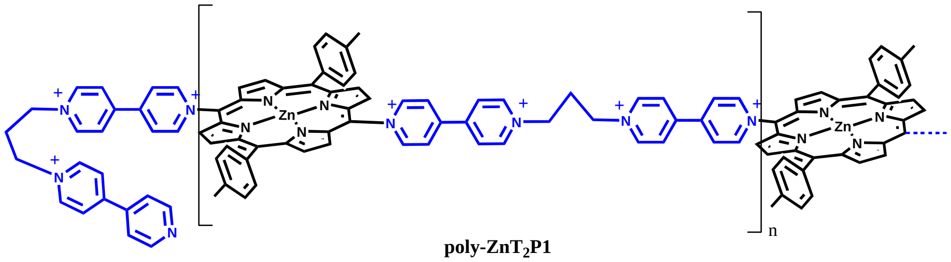

poly-ZnT$_2$P1

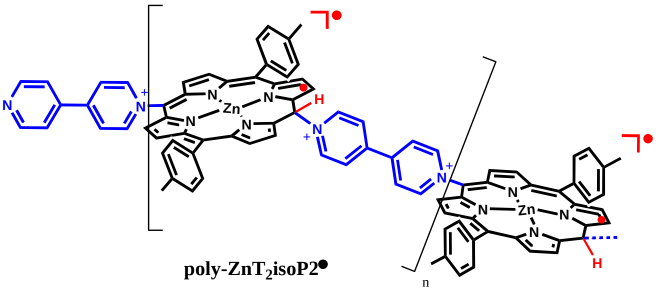

poly-ZnT$_2$isoP2$^\bullet$

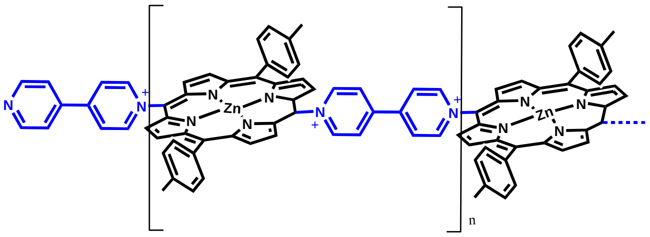

poly-ZnT$_2$P2

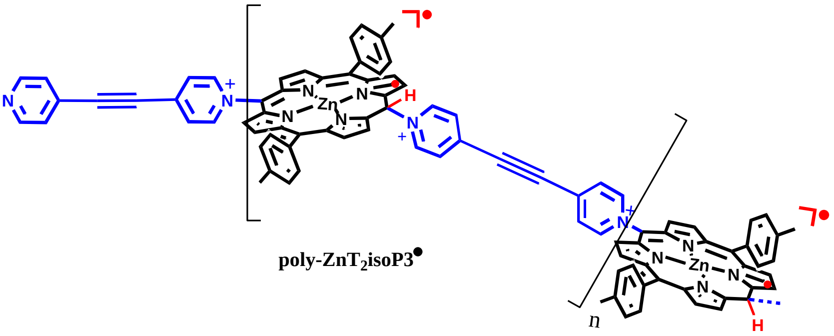

poly-ZnT$_2$isoP3$^\bullet$

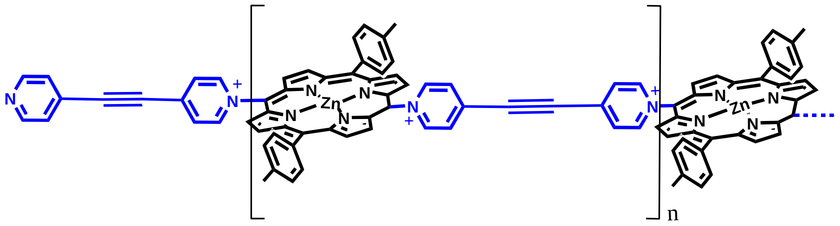

poly-ZnT$_2$P3

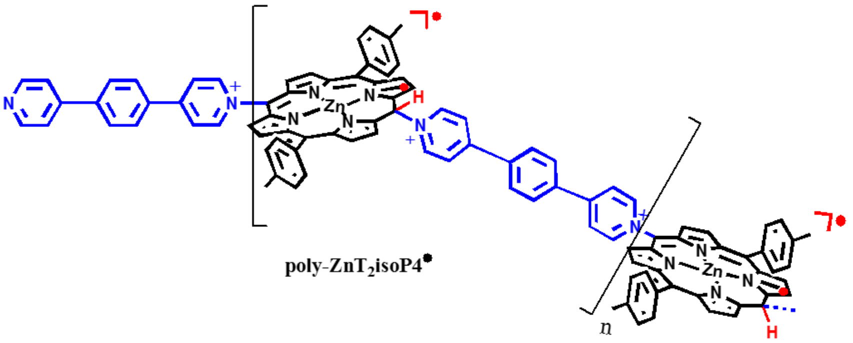

poly-ZnT$_2$isoP4$^\bullet$

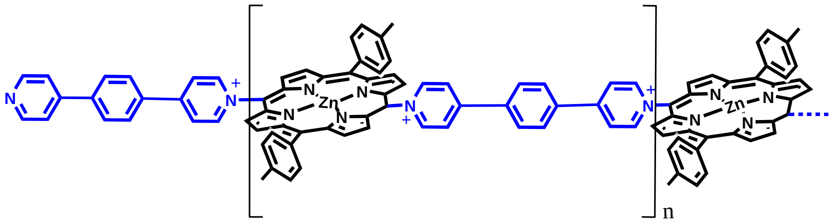

poly-ZnT$_2$P4

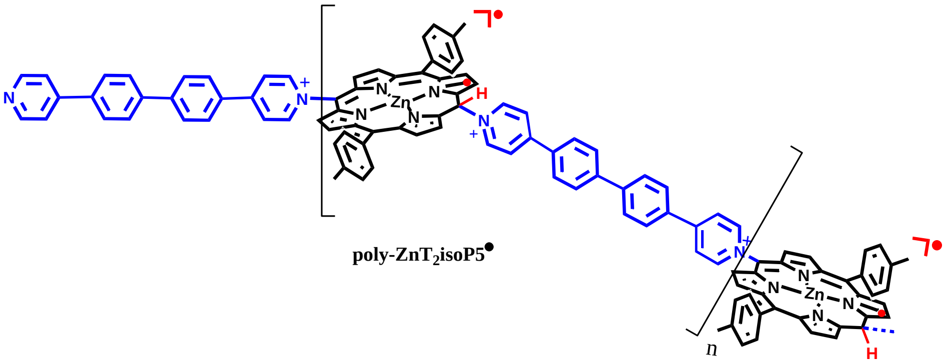

poly-ZnT$_2$isoP5$^\bullet$

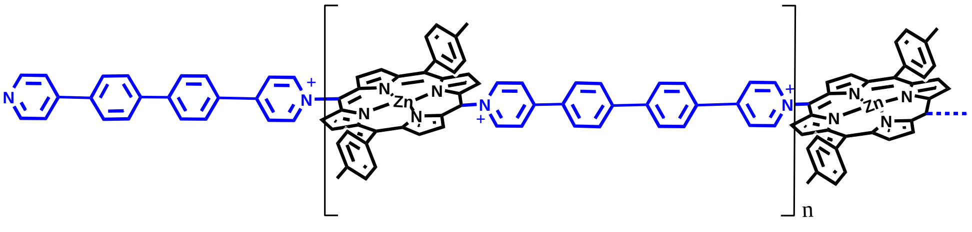

poly-ZnT$_2$P5

Chapter III

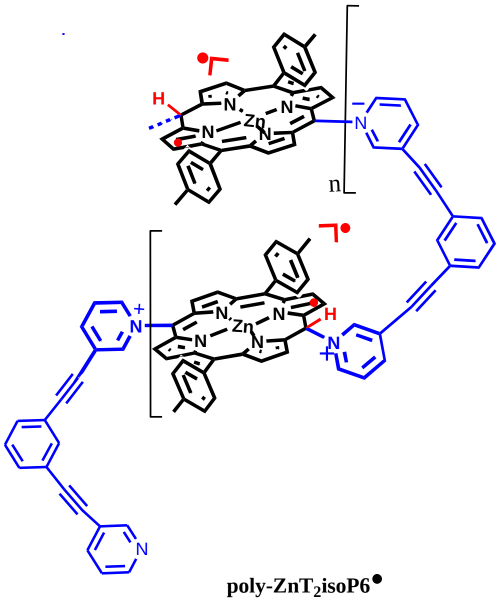

poly-ZnT$_2$isoP6$^{\bullet}$

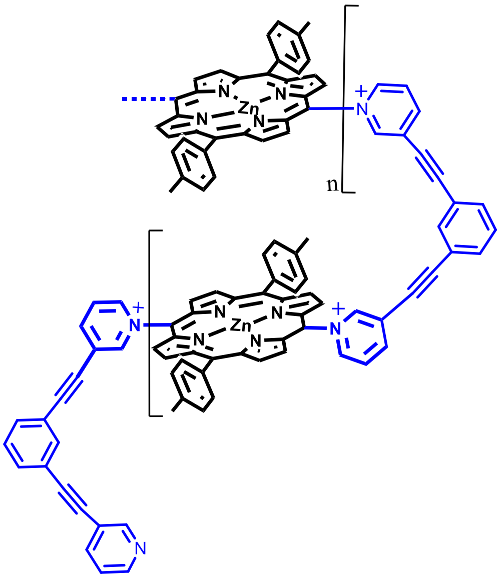

poly-ZnT$_2$P6

Chapter IV

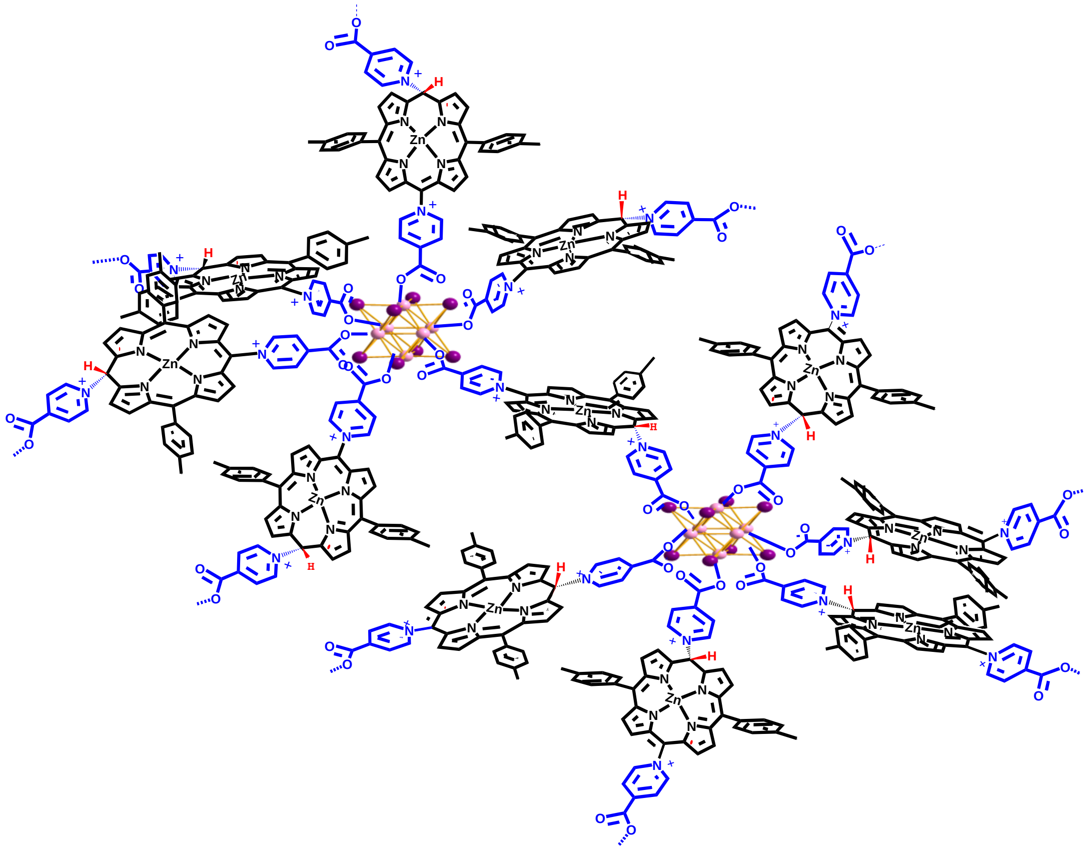

poly-ZnT$_2$isoP$^{\bullet}$/PIM(py)$_6$

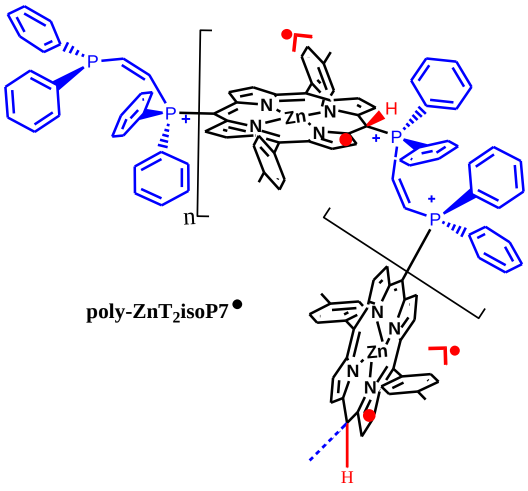

poly-ZnT$_2$isoP7$^\bullet$

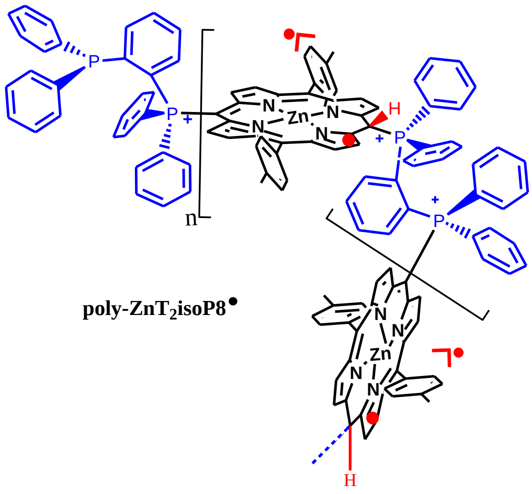

poly-ZnT$_2$isoP8$^\bullet$

LISTE DES PRÉSENTATIONS :

Présentation de posters :

1. LIA-CLUSPOM Conference (5-8 Juin 2018 à Gif-sur-Yvette, France).
La conférence ***LIA-CLUSPOM*** est issue de la participation de **L**aboratoires **I**nternationaux **A**ssociés créé par le CNRS en 2014, associant l'Institut des Sciences Chimiques de Rennes (ISCR), l'Institut Lavoisier de Versailles (ILV) et l'Institut Nikolaiev de Chimie Inorganique (NIIC, Russie). L'objectif principal du LIA-CLUSPOM est le développement d'une chimie innovante résultant de la construction d'un pont entre la chimie des clusters (***CLUS***) et des composés du type polyoxométallate (***POM***).
Titre : Supramolecular assemblies obtained using polyoxometalates and copolymer of porphyrin: formation and photovoltaic properties
Author: **Yiming LIANG**, Antoine Bonnefont, Zhaohui Huo et Laurent Ruhlmann

2) Supramolecular Chemistry of Nitrogen Ligands (29-30 Juin 2018 in Strasbourg).
Titre : Photovoltaic properties of supramolecular assemblies obtained by incorporation of Preysler's type polyoxometalate in a polycationic copolymer of porphyrin
Yiming LIANG, Antoine Bonnefont, Zhaohui Huo et Laurent Ruhlmann

3) 9th Barrande-Vltava French-Czech Chemistry Meeting (27 – 28 aout 2018 à Strasbourg).
Titre : "Supramolecular assemblies obtained using polyoxometalates and copolymer of porphyrin: formation and photovoltaic properties"/
Yiming LIANG, Antoine Bonnefont, Zhaohui Huo et Laurent Ruhlmann

4) "Stable metallo-isoporphyrin copolymer: electrochemical mechanism and photovoltaic properties", 71st Annual Meeting of the International Society of Electrochemistry (30 Aout- 4 Septembre 2020, conference en ligne) – Prix du meilleur poster.
Yiming LIANG, Antoine Bonnefont, Laurent Ruhlmann

5) "Investigation on the Photoelectrochemical Properties of Covalently Grafted None-noble Metal Polyoxometalates-porphyrin Copolymer", 71st Annual Meeting of the International Society of Electrochemistry (30 Aout- 4 Septembre 2020, conference en ligne).
J. Wang, **Y. Liang**, C. Boudon, V. Badets, A. Bonnefont, L. Ruhlmann.

Présentation orales :

1) International Workshop on Electrochemistry of Electroactive Materials WEEM-2019 (June 16 - 21, 2019, Borovets Resort, Bulgaria) with **a poster with 2 minutes oral-presentation**.
Titre : Stable isoporphyrin/porphyrin copolymer: mechanism of the electrochemical routes and photovoltaic properties
Auteurs : **Yiming LIANG**, Antoine Bonnefont et Laurent Ruhlmann

2) 71st Annual Meeting of the International Society of Electrochemistry (30 Aout- 4 Septembre 2020, conference en ligne)
Titre : Hybrid (iso)porphyrin – polyoxometalate copolymer for photo(electro)chemical applications: from flat to mesoporous ITO electrodes
Auteurs : L. Ruhlmann, **Yiming LIANG**, Z. Huo, A. Bonnefont,

5) Autres Conférences avec une présentation orale (15+5 min) :

- **Yiming LIANG**, Antoine Bonnefont et Laurent Ruhlmann, « Electrosynthesis of stable metallo-isoporphyrin/metalloporphyrin copolymer », 3rd Mapyro Symposium (14 Novembre 2019) à Lyon. (15+5 min)

- **Yiming LIANG**, Antoine Bonnefont et Laurent Ruhlmann, «Electrosynthesis and photovoltaic properties of stable metallo-isoporphyrin/metalloporphyrin copolymer », Journées scientifiques de l'UMR 7177 (29 octobre 2019) à Strasbourg. (15+5 min)

- **Yiming LIANG**, Antoine Bonnefont, and Laurent Ruhlmann, « Electrosynthesis and photochemical properties of stable metallo-isoporphyrin copolymer », Journée des doctorants en chimie (3 décembre 2019) à Strasbourg. (15+5 min)

LISTE DES PUBLICATIONS (en rapport avec les travaux de thèse) :

1. "Photovoltaic properties of supramolecular assemblies obtained by incorporation of Preysler's type polyoxometalate in a polycationic copolymer of porphyrin", Z. Huo, A. Bonnefont, **Y. Liang**, R. Farha, M. Goldmann, E. Saint-Aman, H. Xu, C. Bucher, L. Ruhlmann. *Electrochimica Acta*, **2018**, *274*, 177-191

2. "Stable isoporphyrin copolymer: Electrochemical mechanism and behavior and photovoltaic properties", M. Boudiaf,* **Y. Liang**,* R. Lamare, J. Weiss, A. Bonnefont, L. Ruhlmann, *Electrochimica Acta*; **2019**, *309*, 432-449.
** L'ensemble des auteurs ont contribué de manière égale à ce travail.*

3. "Photocurrent Generation from Visible Light Irradiation of Covalent Polyoxometalate-Porphyrin Copolymer" accepté à Electrochimica Acta.
Z. Huo, **Y. Liang**, S. Yang, D. Zang, R. Farha, M. Goldmann, H. Xu, A. Bonnefont, G. Izzet, A. Proust, L. Ruhlmann* ", submitted.

Université de Strasbourg

EDSC
École Doctorale des Sciences Chimiques

Yiming LIANG

Matériaux hybrides polyoxométallate – (iso)porphyrine : dispositifs photovoltaïques et photo(électro)catalyse

Résumé

Dans le cadre de la thèse, la fonctionnalisation de positions méso d'une porphyrine avec des ligands du type dipyridyle a été réalisée de manière à obtenir des copolymères d'(iso)porphyrines radicalaires par électropolymérisation. Des copolymères du type poly-isoporphyrine et poly-porphyrine peuvent être ainsi obtenus par électro-oxydation aux potentiels de +1,0 V / ECS ou de 1,6 V / ECS respectivement. La spectroscopie RPE a confirmé la présence du radical pour les copolymères à base d'isoporphyrines. Les spectres optiques des polyisoporphyrines ont montré un dédoublement de la bande d'absorption Soret et la présence d'une bande additionnelle dans le proche IR. Une réponse photoélectrique plus efficace pour les polyisoporphyrines comparés aux polyporphyrines a été observée et a été expliquée en partie par les propriétés optiques du matériau absorbant plus dans le domaine du visible et du proche IR. L'excitation de cette nouvelle bande proche IR pour le copolymère isoporphyrine radicalaire conduit, en milieux aérés en présence de $^3O_2$, à la formation de l'état singulet du dioxygène ($^1O_2$). Cela montre que ce type de matériau peut être prometteur par exemple pour des applications en photothérapie. Un copolymère 3D à base d'isoporphyrines a également été obtenu à l'aide d'un cluster du type polyiodométallate portant six groupement pyridyles pendants (PIM(py)$_6$). Des copolymères à base d'isoporphyrines avec des espaceurs diphosphoniums ont également été préparés avec succès.

Mots clés : Porphyrine, isoporphyrine, dipyridyle, photocourants, oxygène singulet, électropolymérisation, cluster, viologène, dipyridiniumn, diphosphonium

Résumé en anglais

The purpose of this thesis was to functionalize the meso position of a porphyrin with ligands using electropolymerization. Polyisoporphyrin and polyporphyrin can be obtained at applied potential of 1,0 V vs SCE or of 1,6 V vs SCE respectively. ESR spectroscopy confirmed the presence of the radical only inside polyisoporphyrin films. The optical spectra of polyisoporphyrins showed a splitting of Soret band and additional Near IR band which produce more efficient photocurrent response than polyporphyrins. Excitation of this new NIR band for the isoporphyrin radical copolymer lead, in the aerated media (presence of $^3O_2$), to the formation of the singlet state $^1O_2$ which is the first step for the use of such materials for the phototherapy cancer treatment. Moreover, the same conditions were used to introduce pyridyl decorated octahedral halide clusters given a 3D copolymer with isoporphyrin macrocycles. Polyisoporphyrin copolymer with diphosphonium spacers were also obtained with success.

Keywords : Porphyrin , isoporphyrin, dipyridyl, photocurrent, singlet oxygen, electropolymerization, octahedral halide clusters, viologen, dipyridinium, diphosphonium.